VILNIUS UNIVERSITY
CENTER FOR PHYSICAL SCIENCES AND TECHNOLOGY

Marijonas
TUTKUS

Single-molecule fluorescence microscopy for protein dynamics studies

Doctoral dissertation

Natural sciences,
Physics [N 002]

VILNIUS 2019

This dissertation was implemented between 2014 and 2018 at the Center for Physical Sciences and Technology.

The research was supported by the Research Council of Lithuania with scholarships that were granted for academic accomplishments twice: for the year 2015 and for the year 2017, and with financial support for the research visit to the University of Bordeaux (France) for two weeks during the first semester in 2018.

Academic supervisor:
Prof. habil. dr. Leonas Valkūnas (Center for Physical Sciences and Technology, natural sciences, physics – N 002). 2017-11-01 – 2018-09-30.
Dr. Gediminas Trinkūnas (Center for Physical Sciences and Technology, natural sciences, physics – N 002). 2014-10-01 – 2017-10-31.

This doctoral dissertation will be defended in a public/closed meeting of the Dissertation Defence Panel:
Chairman – Prof. habil. dr. Vytautas Balevičius (Vilniaus University, natural sciences, physics, N 002).
Members:
Ass. prof. dr. Johannes Hohlbein (Wageningen UR, natural sciences, physics, N 002),
Prof. dr. Gediminas Niaura(Center for Physical Sciences and Technology natural sciences, physics, N 002),
Prof. dr. Valdas Šablinskas (Vilniaus University, natural sciences, physics, N 002),
Dr. Aurimas Vyšniauskas (Center for Physical Sciences and Technology, natural sciences, physics, N 002).

The dissertation shall be defended at a public meeting of the Dissertation Defence Panel at 15:00 on 5th of July 2019 in Room A101 of the Center for Physical Sciences and Technology.

Address: Saulėtekio av. 3, Room No., Vilnius, Lithuania
Tel. +37052649211; e-mail: office@ftmc.lt

The text of this dissertation can be accessed at the libraries of the Center for Physical Sciences and Technology, Vilnius University, as well as on the website of Vilnius University: www.vu.lt/lt/naujienos/ivykiu-kalendorius

VILNIAUS UNIVERSITETAS
FIZINIŲ IR TECHNOLOGIJOS MOKSLŲ CENTRAS

Marijonas
TUTKUS

Pavienių molekulių fluorescencinė mikroskopija baltymų dinamikos tyrimams

Daktaro disertacija

Gamtos mokslai,
Fizika [N 002]

VILNIUS 2019

Disertacija rengta 2014– 2019 metais Fizinių ir technologijos mokslų centre.

Mokslinius tyrimus rėmė Lietuvos mokslo taryba paskirdama stipendija už akademinius pasiekimus dukart: 1už 2015 metus ir už 2017 metus, bei paskirdama finansavimą doktoranto mokslinei išvykai į Bordo Universitetą (Prancūzija) 2018 metų pirmąjį semestrą.

Mokslinis vadovas:
Prof. habil. dr. Leonas Valkūnas (Fizinių ir technologijos mokslų centras, gamtos mokslai, fizika – N 002). 2017-11-01 – 2018-09-30.
Dr. Gediminas Trinkūnas (Fizinių ir technologijos mokslų centras, gamtos mokslai, fizika – N 002). 2014-10-01 – 2017- 10 – 31.

Gynimo taryba:
Pirmininkas – **prof. habil. dr. Vytautas Balevičius** [Vilniaus universitetas, gamtos mokslai, fizika, N 002].
Nariai:
ass. prof. dr. Johannes Hohlbein [Vageningeno universitetas, gamtos mokslai, fizika, N 002],
prof. dr. Gediminas Niaura [Fizinių ir technologijos mokslų centras, gamtos mokslai, fizika, N 002],
prof. dr. Valdas Šablinskas [Vilniaus universitetas, gamtos mokslai, fizika, N 002],
dr. Aurimas Vyšniauskas [Fizinių ir technologijos mokslų centras, gamtos mokslai, fizika, N 002].

Disertacija ginama viešame Gynimo tarybos posėdyje 2019 m. liepos mėn. 5 d. 15:00 val. Fizinių ir technologijos mokslų centro A101 auditorijoje. Adresas: Saulėtekio al. 3, A101, Vilnius, Lietuva, tel. +37052649211 ; el. paštas office@ftmc.lt.

Disertaciją galima peržiūrėti Fizinių ir technologijos mokslų centro, Vilniaus universiteto bibliotekose ir VU interneto svetainėje adresu: https://www.vu.lt/naujienos/ivykiu-kalendorius

Contents

INTRODUCTION

Conformational dynamics of proteins are essential for their functioning objectives, which are possible due to the inherent flexibility of protein structure. As a result of such flexibility, different conformational states become responsible for a different role[1], allosteric effects[2], propagation pathways for action (catalysis, target recognition, stability, etc.), disfavoring or recognition of binding partners[3]. They also enable the cell to respond to changing environmental conditions. A prominent example of such response is the feedback adaptation to external light conditions in plant photosynthesis also known as the non-photochemical quenching (NPQ) process, in which the conformational dynamics of light-harvesting pigment-protein complexes (LHCs) of plants is directly involved[4].

Conformational dynamics of proteins links biology with physics[5], and especially with the single-molecule fluorescence (SMF) spectroscopy. These methods are so valuable because conformational dynamics of protein are typically hidden in an ensemble type of measurements and can only be revealed with the aid of the SM methods. Various fluorescence-based methods have been developed for measuring the dynamics of biomolecules at the nanoscale. Indeed, application of the SM Förster resonance energy transfer (smFRET) method for studies of biomolecule dynamics was the most successful. This relatively simple method broadened understanding of many biological systems[6]. There were also other molecular "rulers" developed for probing shorter distance ranges than those accessible by the smFRET. These include protein-induced fluorescence enhancement (PIFE), and fluorescence quenching either by a dark quencher or a metal ion[7]. Also, other methods for probing dynamics of biomolecules based on fluorescence properties such as polarization have been successfully employed[8]. However, all these strategies require labeling of the biomolecule of interest and this is not a trivial task[9]. The other proteins, such as the photosynthetic light-harvesting pigment-protein complexes LHCs (major and minor antenna proteins), are natively fluorescent and this property was employed many times to study the behavior of these proteins at the SM level using various techniques[10,11].

Every protein, regardless of whether it is located in lipid membranes (membrane proteins) or found in the cytosol (water-soluble proteins), undergoes conformational dynamics. The mentioned classes of proteins are different regarding their native environment and involved in different aspects of cellular life. In this work we chose to investigate the following representatives from two different classes – transmembrane pigment-protein complexes from photosystem II of plants (commonly used abbreviation is

LHCII) and water-soluble proteins interacting with nucleic acids – DNA Restriction endonucleases (REases).

LHCII is the major light-harvesting antenna located in thylakoid membranes of green plants and is the key player of the photosynthesis regulation as a result of the NPQ process. The link between conformation dynamics and fluorescence changes on the SM level for the LHCII has been demonstrated several times[12]. However, knowledge of the carotenoid composition effect on the fluorescence variability (and thus conformational dynamics) of single LHCII complexes is minimal. Therefore we decided to employ for the first time an extremely sensitive TIRF microscopy setup for investigation of the LHCII isolated from the native source and various mutants. Also, we investigated the role of the peripheral carotenoid site of LHCII in the fluorescence quenching upon the change in pH and detergent concentration (high light conditions) at the SM and ensemble levels.

The second protein type, REases are typically situated in the cytosol of bacteria and serve as a defense mechanism against viruses. There have been many SM level studies of DNA-interacting proteins published that successfully revealed the conformational dynamics of these proteins. However, more complex DNA-interacting proteins, consisting of several domains or having many different states are still not sufficiently explored mainly because it is hard to label them or their investigation requires dedicated methods. In this work, we showed that simultaneous measurement of two SM signals allows revealing of previously obscured protein dynamics of DNA-interacting proteins. First, we studied DNA-Ecl18kI restriction endonuclease complex dynamics. Results of these experiments revealed three possible conformations of the DNA-protein complex and associated dynamics[13]. In further experiments, we also examined tetrameric REase – NgoMIV, the protein that interacts with DNA heterogeneously and in a protein concentration dependent manner[14].

In addition to the above mentioned experimental work, we also developed two new methods dedicated to studies of transmembrane pigment-protein complexes and DNA-interacting proteins. One of them allowed us to study truly liposome reconstituted LHCII at the single-liposome level[15]. This methodology is an advancement because previously employed assays did not provide the possibility to check whether studied LHCII is truly reconstituted in liposomes[16]. In addition, our method allows immobilization of proteoliposomes on a modified (passivated against nonspecific interactions) surface without affecting liposomes and with a possibility to access the liposome sizes directly. Another method that we developed permitted immobilization of biotinylated DNA on surface structures – nanoscale lines of streptavidin fabricated on a glass coverslip, and stretching the immobilized DNA fragments along the buffer flow. This facilitated visualization of DNA-protein interactions at the SM level. The review also covers the methodological advancements regarding microscopy setup, and the sample preparation is described. The literature review presented in this thesis also includes the description of the SMF methods developed so far and also those employed explicitly in our research work.

Our results on SM conformational dynamics studies of protein-pigment complexes and DNA-interacting proteins provided essential insights into each field of research. Also, both of our developed methods were successfully applied and will be useful for future studies of various DNA-interacting proteins and other pigment-protein complexes or their assemblies. Thus, the final part of the literature review presented in this thesis provides a discussion of the future perspective of our research.

1. GOALS OF THE RESEARCH WORK

To understand conformational dynamics involved in different processes of cellular life, we chose to study representatives from two different classes of proteins – transmembrane pigment-protein complexes (LHCII) and cytosolic DNA Restriction endonucleases. These two classes of proteins have been studied at the ensemble level, but have been very infrequently or never before studied at the SM level. Specific features, such as LHCII carotenoid composition, which may alter its conformational dynamics and NPQ process, were not studied systematically at the SM level. Also, conformational changes involved in DNA-REase complex dynamics are not fully understood and may vary between different types of REases. Thus the goals of this research work are:

- To understand the role of the carotenoids in fluorescence quenching of LHCII,
- Reveal and characterize DNA-protein complex dynamics at the SM level of two different types of REases.

2. TASKS OF THE RESEARCH WORK

We employed a similar method of measurement – SMF microscopy – for all measurements, but we needed a different strategy of sample preparation for different experiments. For LHCII we used detergent solubilization and liposome reconstitution, while for REases studies we employed labeling and immobilization of DNA substrate containing binding sites for the REase. To achieve these goals we identified the following tasks:

- To develop and apply fluorescence microscopy methods for studying conformational dynamics of the LHCII with various carotenoid composition in detergent micelles at the SM level.

○ To develop and apply methods allowing us to reveal and characterize DNA-protein complex dynamics of two different REases at the SM level.

3. STATEMENTS OF THE THESIS

○ Simultaneous measurement of FRET and tethered fluorophore motion allowed us to reveal previously hidden conformational dynamics of DNA-protein complexes of two different REases.

○ Carotenoid composition of the peripheral LHCII site affects neither quenching extent nor conformational dynamics of this protein. However, LHCII mutant, which contains zeaxanthin as the only carotenoid, had altered conformational dynamics and was highly quenched.

○ SMF microscopy methods and surface tethering of fluorescently labeled LHCII proteoliposomes revealed a considerable amount of liposome-free LHCII and a broad heterogeneity of LHCII density in the proteoliposomes.

4. NOVELTY AND RELEVANCE

Various fluorescence based methods have been developed for measuring the dynamics of biomolecules at nanoscale. DNA-interacting proteins were extensively studied using the smFRET method. Nonetheless, a combination of different SM signals helped to reveal previously obscured dynamics of these kinds of proteins. LHCII and other pigment-protein complexes were studied at the SM level using confocal microscopy under relatively intensive excitation conditions. However, there are practically no studies published, in which LHCII would be studied at the SM level using TIRF setup. This setup is beneficial because of extremely high SNR, that enables studying even highly quenched pigment-protein complexes under relatively low excitation conditions. Overall, for our proteins-of-interest we applied a similar method of measurement – SMF microscopy – but we needed a different strategy of sample preparation for each experiment. Thus novelty and relevance of our research work was several-fold:

○ TIRF microscopy was applied for the first time to study conformational dynamics of LHCII at the SM level under very low-light intensity conditions. These experiments revealed a previously hidden effect of carotenoids on conformational dynamics of LHCII at the SM level.

○ A new method – combination of smFRET and fluorophore motion in the evanescent field – was developed and applied to study DNA – Ecl18kI REase complex dynamics. This method allowed us to discriminate all possible different conformations of DNA – Ecl18kI complexes and their dynamics that were previously obscured. A similar strategy was employed for the first time to reveal two different modes of DNA – NgoMIV complex dynamics.

LITERATURE OVERVIEW

1. THE DYNAMICS OF PROTEINS ARE GOVERNING LIFE

The cell is the most fundamental single unit of a living organism. It is known that mammalian cells are composed out of lipid bilayer – the membrane, which is surrounding the cytosol, in which there are different organelles – nucleus, endoplasmic reticulum, mitochondria, etc. However, these organelles are large assemblies of biological molecules – lipids, nucleic acids and proteins, that function to build structures of the cell, maintain gradients, ensure protection, etc. To perform any of these tasks, biological molecules and, in particular proteins (3D folded biopolymers), must change their conformation – perform *conformational dynamics* – or in other words be able to move. Therefore since the first single-molecule (SM) level experiments involving biological molecules, it is becoming more apparent that conformational dynamics is a prerequisite for protein function.

Most often proteins are found to exist in a conformational equilibrium at some “ground” state (conformation), which is typically observed in X-ray crystallography or cryo-electron microscopy[3]. Some proteins are more flexible and have wider conformational distribution, which is often called conformational landscape[17,18]. In the conformational landscape, states are separated by barriers, whose heights are dependent on thermodynamics and protein function (e.g., allosteric modulation, direct recognition, etc.). These features of the conformational landscape became more evident after the information from modeling[19], experiments (mainly NMR)[20], and theoretical studies[21] was obtained. Now it is commonly agreed that the conformation of a specific protein within an ensemble changes over time, meaning that all conformations pre-exist, and the shift of the population of proteins into one or another side of the conformational landscape (“dynamic conformational distribution”) reflects the functioning of the cells’ mechanisms[22]. A prominent example of conformational landscape modulation involvement in the protein function is so-called allosteric modulation, when an effector binds to a protein, the protein changes its conformation and becomes activated or deactivated.

Another aspect of protein dynamics which is involved in cellular functioning, is motion. There are two basic types of protein motion: diffusion or directed movement. However, these moving proteins (molecular machines) are asynchronous and have multiple kinetic pathways through intermediate states. Therefore knowledge of the protein motion can be revealed only when suitable experimental methods are combined with the

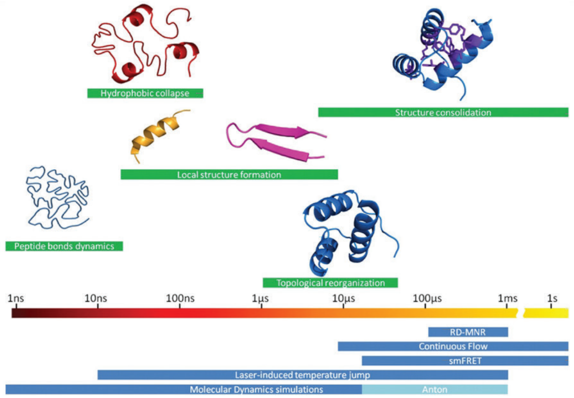

Figure 1: Timescales of different conformational dynamics modes involved in proteins' function. Below there are methods listed that are used to probe these different modes. Reprinted with the permission from: V. Munoz, M. Cerminara. When fast is better: protein folding fundamentals and mechanisms from ultrafast approaches. Biochemical Journal, 2016, 473 (17), 2545-2559.

structural information. This is the reason why methods that allow revealing mechanistic details of this relationship currently attract a lot of attention.

As mentioned in the introduction, the conformational dynamics of biological molecules undergoing biochemical reactions or interactions can be revealed using relatively novel single-molecule (SM) fluorescence and force spectroscopy and microscopy techniques (Fig. 1)[23]. Such measurements rely on molecular rulers of distance or angle. This field of studies has grown rapidly because there are various proteins (cytoskeletal motor proteins, rotary motors, nucleic acids motors[24]), that function differently and, therefore, requires the development of new and more dedicated SM level techniques. Their strength is the ability to monitor individual molecules in real-time with nanometer or pN precision. This helps to access unique information – distribution functions of parameters like state duration (even at non-equilibrium), resolve heterogeneities and record time trajectories of parameters, that would otherwise be hidden in ensemble measurements[23]. This is especially important in cases where multiple proteins are interacting or where conformational dynamics have many degrees of freedom. Today these methods have become almost a mainstream tool in biophysics for *in vitro* and *in cellulo*[25–27]studies, due to extremely stable fluorophores, efficient biomolecule labeling techniques and sensitive detection methods[28].

2. MEASUREMENTS AT THE ENSEMBLE LEVEL

Proteins in the solution are dynamic, and it is nearly impossible to use X-ray crystallography or similar ensemble level techniques to characterize the conformational dynamics. Thus various experimental ensemble types of approaches: nuclear magnetic resonance (NMR), electron paramagnetic resonance (EPR), small angle X-ray scattering (SAXS), cryo-electron microscopy (cryo-EM), fluorescence spectroscopy and FRET, in combination with computational methods are employed to reveal proteins' conformational dynamics[29]. Theoretical methods such as REMD[30] and metadynamics[31], that allow accessing structural and thermodynamic properties of proteins, are also employed to get better understanding about underlying conformations. However, to show the kinetic rates and conformational dynamics one has to use Markovian state models in combination with the MD simulations[32].

NMR and EPR spectroscopy are one of the most widely used tools for the conformational dynamics studies of various proteins. That is because they allow revealing large-amplitude conformational dynamics at an extremely high resolution[33]. To probe conformational dynamics of a protein with EPR one has to label the protein of interest with spin labels at desired positions. This labeling is less challenging compared to the effort needed to label a protein with a FRET dye pair. Once the protein is labeled, it can be examined with the EPR spectroscopy. This measurement involves many factors: reports the distribution of structured domains orientations, conformational flexibility of disordered regions, local environment, the presence of secondary structure and conformational dynamics[34,35]. On the other hand, SAXS does not require any labeling of the protein, and it reports dimensions of domains or movements. Therefore information obtained from SAXS can help to understand the results of NMR or EPR spectroscopy better[36].

To obtain more information about the protein studied the NMR and SAXS data has to be fitted. There are many algorithms developed for that purpose: the Flexible-Meccano and Ensemble Optimization Method (EOM), ASTEROIDS, BSS-SAXS, ENSEMBLE[3]. For these algorithms, initial guesses and constraints come from the NMR and SAXS measurements. During simulation algorithms typically generate a bunch of conformations and perform a comparative analysis to tell which of them matches the constraints the best[37].

To monitor longer time scale movements molecular dynamics simulations are often employed. Constraints and initial conditions for these simulations are provided from the NMR, EPR or X-ray crystallography studies. NMR, EPR and high-resolution X-ray crystallography often are employed in combination, because they are very complimentary – one can provide only a part of the full picture[38]. However, these two techniques alone are not always able to provide the information needed to characterize the activity of more complex proteins. In such cases, low-resolution X-ray data combined with bulk or single-molecule kinetic data can be helpful.

Bulk FRET or simple fluorescence spectroscopy methods were used to study the dynamics of biological molecules and systems for a long time[39–43]. Bulk steady-state and time-resolved fluorescence polarization anisotropy measurements are employed to determine the size, shape, flexibility, and rotation of biomolecules. The tricky part of these experiments is the interpretation of results and performing proper controls because dynamic or static heterogeneity in the sample affects the interpretation drastically. Also the stability of the measurement systems becomes crucial because intensity of the fluorescent probe attached to the protein may show very few changes compared to the noise level.

3. MEASUREMENTS AT THE SINGLE-MOLECULE LEVEL

SM spectroscopy and microscopy methods: AFM and optical tweezers[44], SM FRET (smFRET) and fluorescence[43,45], nowadays are work horses for quantitative studies of protein conformational dynamics and heterogeneities[46]. These studies require nanometer precision and overcoming thermal fluctuations surrounding the molecules. Now, this is possible at ~0.3 nm precision with the shortest time resolution of ~1 ms[24].

Advantages of SM measurements over typical ensemble measurements are several: 1) they allow direct monitoring of a physical parameter describing action of a single biomolecule in a real-time, 2) do not require a synchronization of an ensemble of biomolecules and, therefore, multi-step, multi-state and by default non-synchronizable processes of biomolecule action can be monitored, 3) allow selecting or separating non-homogeneous populations of the process under study, 4) have the possibility to identify and differentiate between static and dynamic heterogeneity, 5) allow identifying transient kinetics controlled intermediate states and characterizing the complex mechanisms, 6) biological processes are intrinsically single-molecule processes, at least in their early state, 7) protein interaction mechanisms – induced fit, conformational selection, or combined – can be identified. Here the main SM methods will be discussed.

3.1 Single-molecule force spectroscopy methods

Single-molecule force spectroscopy methods – AFM, optical or magnetic tweezers – work in two modes – constant force and constant velocity. They provide information on forces needed for folding and unfolding of a protein, energy landscape, mechanical properties, and conformational dynamics[46,47]. During these experiments either both ends or one end of a single biomolecule are captured with the probe (AFM cantilever or a bead) and by moving the probe force is applied to the biomolecule[48].

In AFM studies deflection of the sensitive probe is monitored with a high precision, and this allows quantifying forces. Ultrafast scanning AFM can be employed to acquire movies of protein (e.g., molecular motors like myosin) conformational dynamics and provide evidence of dynamic molecular behavior[49]. In optical or magnetic tweezer experiments molecules are typically tethered between a surface and a bead, that can be captured in the trap[50].

There are two basic types of optical tweezers – double- and single-trap. Double optical trap allows capturing molecules conjugated on both ends with beads. In this way, the molecule does not face the surface effect. While, the single optical trap requires immobilization of the biomolecule by one end on a surface, and the other end of the molecule is then attached to the bead.

The magnetic tweezer setup enables applying torque to a surface-immobilized nucleic acid molecule, and in this way it is more beneficial than the optical trap. More information and reviews on the SM force methods can be found elswhere[48,50,51].

3.2 Single-molecule fluorescence spectroscopy methods

Observed fluorescence in SMF measurements depends on the population of molecules in the excited state. Fluorescence itself is a radiative decay from the electronic excited state to the ground state, that occurs after absorption of a photon. Actually, after excitation a molecule can undergo radiative (fluorescence) or non-radiative decay. Fluorescence intensity and lifetime depends on these process[52]. The fluorescence intensity over absorbance is proportional to the fluorescence quantum yield (QY). The fluorescence quantum yield is proportional to the radiative decay rate over the sum of all rates leading to the population loss from the fluorescent state. Thus changes in fluorescence intensity, lifetime or polarization are employed for SMF detection.

Another important aspect of SMF measurement is background-free detection[53]. However, signal-to-noise (SNR) in the SMF experiments is lower than in ensemble because of a smaller number of molecules observed. Thus optimization of SNR is a crucial aspect of SMF measurement, and there are several aspects of such optimization: the sample, the optical setup, and the detectors.

SMF methods employ wide-field epifluorescence, confocal or total internal reflection fluorescence (TIRF) microscopy modes. Excitation sources are either constant wave (CW) or pulsed lasers and fluorescence emission is collected using high numerical aperture (NA) objectives. Background level in these measurements is minimized because of the specific features of TIRF or confocal modes. In the wide-field epifluorescence the background is typically suppressed by blocking the stray light[54].

Size of a single fluorophore that in optical microscopy images appears as a point spread function (PSF), is limited by the diffraction (~λ / 2×NA), but its center position can be defined more precisely using PSF fitting[55]. This method belongs to the rapidly evolving class of super-resolution methods and can achieve a minimum resolution of ~2 nm, but typically is ~20 nm (because of the limited photon budget). However, these methods are rarely employed for conformational dynamics studies of proteins[24].

SM fluorescence-based measurements employed for protein conformational dynamics studies rely on unique properties of absorption and emission transition dipoles of the fluorescent probe attached to the protein. Changes in fluorophore orientation can also be detected by measuring changes of its dipole orientation via SM fluorescence polarization anisotropy (smFPA). To perform smFPA, one has to determine the transition dipoles of absorption and emission by the aid of polarized excitation or analyzing their emission (e.g recording two signals of fluorescence emission after the polarization beam-splitter)[56]. These can be employed to calculate fluorescence polarization trajectories using the equation written below,

$$P(t)=(I_1(t)-f*I_2(t))/(I_1(t)+f*I_2(t))$$

where f is a weighting factor to normalize both channels[57]. Histograms of dipole orientation of rigidly attached fluorophore can provide information on the distribution of states and time traces can reveal the angular motion of the biomolecule, binding events, and enzyme activity. The first smFPA measurements were performed on the actin-myosin system when labeled actin filaments were moving, and the myosins were immobilized on the glass surface[58]. smFPA was also heavily employed for studying conformational dynamics of ATP synthase[59]. These experiments directly demonstrated the rotary motion of the F_1-ATPase subunit, the conformational fluctuation of the F_0 subunit[60–62], and the motor axis[63].

Fluorescence correlation spectroscopy (FCS) of diffusing molecules is another long-standing SMF technique that is still often applied to study biomolecules[64]. It uses correlation analysis of fluorescence intensities from a very diluted solution of fluorescently labeled biomolecules. This analysis provides information on various processes with very high time resolution, but with a relatively short observation time-frame. That is because molecules are only detectable while they are diffusing through the confocal volume, which has diffraction limited size. A method allowing extension of the observation time-frame was developed recently[65]. It is called recurrence analysis of single particles (RASP). The RASP method uses the fact that the same molecule has a higher probability of entering the focal volume after it escapes from it than the new molecule to come.

smFRET – a method that is based on fluorophores' sensitivity to the presence of other nearby fluorophores and quenchers, was developed and applied many times to study biomolecules. This method allows measuring distances and distance dynamics between a single pair of dyes attached to a biomolecule either using fluorescence emission intensities or by fluorescence lifetime[28,66,67]. FRET efficiency (E) is associated with the donor-acceptor distance (R) by this formula

$$E = \left(1 + \left(R / R_0\right)^6\right)^{-1},$$

where R_0 is the Forster radius. R_0 for a typical FRET pair – Cy3 and Cy5 is ~ 5.6 nm[68]. Thus the range of distances accessible by smFRET is from 2 nm to 10 nm, which is compatible with the size of biological molecules. FRET efficiency also depends on the orientation between dipoles of fluorophores[69].

smFRET in combination with other SM methods allows simultaneous monitoring of proteins' conformational dynamics and, for example, their activity or manipulation of molecules[70]. To fully understand the behavior of complex biomolecules or biosystems probing of several observables is often necessary. Therefore smFRET employing three or four colors was developed[71,72]. Three-color smFRET can measure up to three different pairwise distances, four-color – up to six, and by alternating-laser excitation (ALEX) it is possible to deconvolve all of the distances[73]. Recently it has been shown that it is possible to increase precision and to achieve better distance to FRET efficiency correlation by combining the smFRET with computer modeling, X-ray structures, fluorophore accessible volume calculations, and additional physical parameters such as anisotropy[6,74,75].

4. TRANSMEMBRANE PIGMENT-PROTEINS

Photosynthesis is a process that provides energy for life on Earth. It begins in a sophisticated transmembrane pigment-proteins network, where solar energy is absorbed and transferred further to perform charge separation reaction in the reaction centers. This process occurs under fluctuating physiological conditions that result in massive heterogeneity of molecular freedom, that exists inside the cell. However, under low-light conditions (~1 kW/m^2) it operates in a unity efficiency[76]. This heterogeneity, in turn, creates heterogeneity in the energy landscape of proteins, which is related to their function. It is clear that this heterogeneity changes the energy barriers and, therefore, affects energy transport.

To understand the processes mentioned above, it is the best to employ SM techniques, because they allow monitoring of spectroscopic parameters and have a unique power to reveal heterogeneity that is typically lost in the ensemble averaging[53]. The first time SM methods were applied to study light-harvesting complexes was in the year 1999[77]. These experiments involved different types of antenna proteins originating from various sources of bacteria and higher plants. Also these methods revealed how the identified molecular basis of heterogeneity affects the excited state manifold, and the conformational dynamics exhibited by the LH2[78]. Additionally, these methods have been widely applied to study the LHCII (the major light-harvesting complex from green plants), and these studies were exploring multiple functional roles of this protein, especially the effect of the high-light and low-light conditions[11,79–81].

Typical photosynthetic systems are composed of reaction centers (RC) and antenna proteins. Reaction centers are conserved between different organisms different organisms. However observing fluorescence from the RC is a difficult task, because the electron transfer chain products are quenching the excited states. In contrast, monitoring the fluorescence form antenna proteins (transmembrane pigment-protein complexes) has been a relatively easy task. These proteins function as a scaffold, which positions and orders the embedded pigments, enabling efficient and directional energy flow. That helps to increase local concentration, prevents self-quenching of the pigments and results in higher solar absorption[82,83]. Also, this results in significant pigment-pigment and pigment-protein interactions, that are related to the energies of the excited states and drive the energy transport[84]. These interactions are heterogeneous because they are affected by the structural differences among the conformational substates, that are accessible in the RT[85]. Chl variants and carotenoids are the main building blocks that compose most of the pigment-protein complexes. Chls (including bacteriochlorophyll – BChl) are porphyrins with a stable/planar structure, having a long excited state lifetime suitable for primary light-harvesting and energy transfer. Carotenoids are polyenes with a long and dynamic structure, which is suitable for accessory light-harvesting, that rapidly transfers energy to the chlorophylls. Also, they perform photo-protection, because energy from generated triplet states is transferred to the carotenoids, and even they have an extremely short excited state lifetime[86].

SM level studies of such transmembrane pigment-proteins have been primarily performed with fluorescence-based techniques. These studies revealed heterogeneities in: conformational dynamic, characteristics of the excited states and the energy transfer process[53]. SM spectroscopy also helped to study the spectral diffusion process – changes in excited state energies (fast processes) due to the dynamic protein environment (slow) in which pigments are embedded. These measurements allow identifying separate conformational substates and transitions between them, that can be visualized using the potential energy landscape. High barriers in these landscapes represent slow dynamics that give discrete peak positions (sharp spectra), and low barriers – and enables fast dynamics, which gives broadened absorption and fluorescence spectra. However, proteins often have a continuum of barrier heights, and the distinction between slow and fast dynamics is often unclear[87].

In SM studies changes in fluorescence emission on the time-scale of seconds are typical for conformational substates with a high potential barrier[88]. This was observed with LH2 complex (bacterial antenna), where the fluorescence spectrum at room temperature (RT) showed a temporal change in peak position on a seconds time-scale[89]. Such measurements reveal slow dynamics related to the discrete peak position. Under cryogenic conditions, it is possible to access better resolution of the conformational substates especially those of fast dynamics (low energy), because the fast dynamics are slowed down and the spectral lines become narrower[90]. Thus by combining cryogenic conditions and SM spectroscopy one can obtain the spectral characteristics of the embedded pigments.

LH2 and LH1 antenna from purple bacteria are most widely studied using SM spectroscopy because of their exceptional photo-stability. These proteins exist in membrane structures called chromatophores, whose structure and composition vary depending on the species and growth conditions. However, chromatophores in general have a number of LH2 proteins surrounding the LH1, which contains the RC in its core[91,92]. It is known that the LH2 network performs the initial absorption step, transfers the energy to LH1, and then LH1 transfers energy to RC. In this path, excitons move energetically downhill, but there is a barrier to reach the RC[78]. The BChl molecules in LH2, of the well-studied species *R. acidophula,* form two concentric rings, that give rise to two absorption maxima – B800 and B850[93]. In the B800 ring, BChls are weakly coupled and in the B850, strongly coupled[94]. Typically the B850 ring is modeled as a circular aggregate with excited states delocalized over the entire ring. However, thermal fluctuations destroy the delocalization and introduce confinement of the excited states. The above mentioned photo-stability and the fact that inhomogeneity in the excited state energies of the LH2 is an order of magnitude higher than in the other photosynthetic complexes make it a perfect target for SM studies[85].

The SM spectrum of the LH2 B800 band allows monitoring changes in the local environment and, therefore, dynamics of the landscape. The SM spectrum of B800 displayed three sizes of spectral fluctuations: large jumps (0.001-0.01 s^{-1}), small spectral changes, which after a number of measurements resulted in averaged line width (0.03-1 s^{-1}), and rapid fluctuations in the individual spectrum, which led to broadening of each peak (>1 s^{-1})[87]. These types of dynamics were interpreted as the protein dynamics between the three tiers in the potential energy landscape. This experiment demonstrated that SM spectroscopy is an excellent tool for monitoring the local potential surface and dynamics that would be otherwise obscured.

In higher plants similar to the purple bacteria, the general scheme of light-harvesting is the same – energy migrates through a local network of LH proteins, to reach the dedicated RCs, which performs the charge separation reaction, except that in the higher plants there are two photosystems – Photosystem I (PSI) and photosystem II (PSII), that are located in the thylakoid membrane of the chloroplasts (Fig. 2). PSII is typically found in the stacked regions of the thylakoid (known as grana), while PSI is found at the periphery of the membrane (stroma lamellae)[95]. Light-harvesting protein I (LHCI) is located in the PSI, and Light-harvesting protein II (LHCII) in PSII. Both of these proteins have been extensively studied at the SM level. LHCII is a trimeric protein, and in each monomer contains eight Chl *a*, six Chl b and four carotenoids[82]. In this protein energy is fast (fs-ps) transferred from carotenoids to Chl *b* to Chl *a*, and then the fluorescence occurs from the Chl *a* band. SM level studies have revealed the role of conformational dynamics of LHCII on the photoprotective process – non-photochemical quenching (NPQ). This process enables regulation of the electron transport chain so that the amount of excitation energy does not exceed the capacity of the RC[96]. There are several time components of the NPQ process, and the short-time component, involving excess energy dissipation, is related to the LHCs. This was rationalized by the aid of modeling and SM research, to

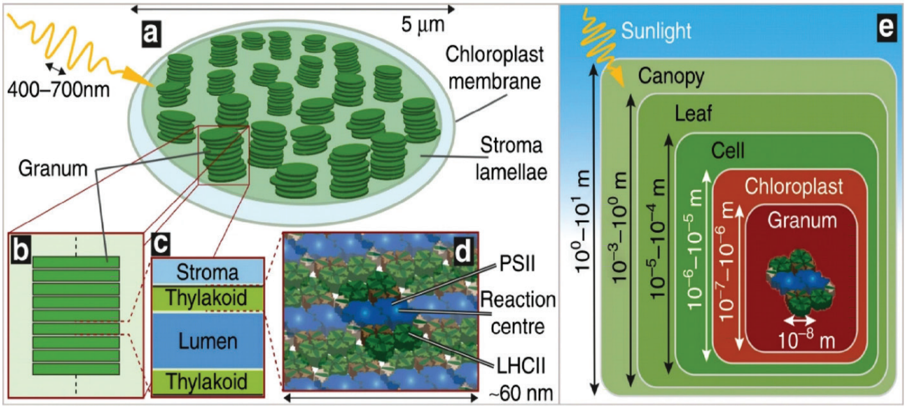

Figure 2: Illustration of a higher-plant chloroplast depicting the outer and inner thylakoid membranes. Reprinted with permission from: A. Capretti, et al. Nanophotonics of higher-plant photosynthetic membranes. Light: Science & Applications. 2019, 8:5.

happen by the conformational changes of the LHCs that produce energy-transfer, charge-transfer, or Chl-carotenoid excited states[97].

The blinking mentioned above of isolated SM LHCII and other pigment-proteins will likely influence the efficiency of light-harvesting. The question is whether this blinking is involved in NPQ. There are several possibilities, and the most commonly accepted is that the conformation change of antenna complexes open up non-radiative decay channels via the carotenoid pigments[98]. As indicated by many SMF experiments the SM blinking phenomena of antenna complexes is influenced by the changes in protein conformation or environment[11,99].

Using SMF, LHCII and related protein conformational changes were probed under high light and low light conditions. It has been shown using the ABEL trap and confocal setup, which measures lifetime and the intensity of fluorescence, that LHCII has several distinct populations[11]. Different conformational states of LHCII were rationalized to be responsible for them: the unquenched state, and two partially quenched states. The lifetime and intensity changed proportionally, and, therefore, quenching was related to a non-radiative decay process of the emissive state. Since the emissive state is close to the carotenoid, thus the quenched state was assigned to the conformation where Chl-carotenoid distance decreases. Also one of the partially quenched states becomes more probable under high light conditions, suggesting that it may be related to photoprotection. Additional experiments with cross-linked versions of antennae proteins and also other protein antenna added more confidence that these states are related to the changes in protein conformation[100].

The dark state – entirely quenched – of LHCII was proposed to arise from a conformational change and serve as the state responsible for NPQ[12]. This state was explored at the SM level using various buffer conditions, that mimic the effects of high light (low pH and low detergent concentration). Under those conditions mimicking high light and also under different zeaxanthin composition, the probability of the dark state increases and red-shifted states appear (excitonic/charge transfer type)[12,101]. In contrast, fluorescence change of homologous minor peripheral antenna complexes in PSII (CP24, CP26, CP29) showed a different response to the same change in environment. Therefore it was suggested that LHCII is the main NPQ player, because of a strong abundance of partially quenched states[98]. Also, there were several SM level studies published on the Lhca, that at room temperature characterized emission spectra, that changed depending on the multimeric composition of the complex[88,102]. Additionally, these experiments revealed that different conformations are stabilized in Lhcb and Lhca.

Additional information on protein conformational changes' relation with the fluorescence intensity states was gained by measuring SM spectral diffusion over time (spectral traces)[103]. These traces can be described by a random walk model, which is dependent on the potential energy surface/landscape[104]. Thus the protein fluctuations affect the pigment transition energies, and that is manifested in changes of fluorescence intensity and spectrum. Also SM measurements of the mutant version of LHCII – A2, that is lacking two Chl (a611 and a612), revealed that the delocalized Chl cluster a610-a611-a612 functions as a robust terminal emitter domain in the WT protein. This terminal emitter is less susceptible to the fluctuating environment.

To mimic a natural-like environment, the LHCII complexes were isolated using styrene-maleic acid, which produces a nanodisk of lipids around the protein[105]. SM fluorescence intensity and lifetime measurements of such samples demonstrated that the protein in nanodisks seems to be in the native trimeric structure. It is harder to investigate the LHCII reconstituted in liposomes at the SM level because of high possibility to have multiple copies of LHCII per liposome. However, by a combination of bulk and SM measurements, the fluorescence properties of the LHCII in liposomes can be investigated for the number of LHCs per liposome[16]. The same fluorescence lifetime as in native state was found in liposomes with a small number of LHCII. In contrast, when multiple copies of LHCII per liposome are present, they fluorescence yield is reduced. However, in these experiments, liposomes were not labeled and, therefore, it was not clear whether the studied LHCII was indeed liposome reconstituted. Later, we have shown that a substantial fraction of LHCII remains liposome free, and it is critical to use liposome -protein co-localization techniques when studying LHCII in proteoliposomes[15]. Also, the surface modification that was employed in the previous study could affect the results.

SMF experiments have revealed the energy transfer pathways between monomers constituting LHCII antenna[81]. Results of these experiments showed that each monomer within the trimer contains an emissive state, but not one monomer serving as the trap/terminal state in the energy transport pathway. In addition to that, results showed that each monomer functions relatively independently and there is little energy transfer between the monomers. It is known that in these proteins the energy landscape is relatively flat, but despite this, the absorbed energy somehow reaches the reaction center. This suggests that energy transfer through the complex is constrained, but not entirely dictated by energetics.

5. DNA-INTERACTING PROTEINS

Protein-DNA interactions are typically associated with the changes in proteins' or DNA conformation and static or dynamic heterogeneities[106].

These processes, which are vital for normal cell development, are hard to study in ensemble measurements because of spatial, temporal, and energetic heterogeneous dynamics, which often involves multiple steps and multiple conformations[107]. SMF methods are well suited for studying such processes and can reveal a detailed mechanistic picture[57,108]. This is particularly interesting because DNA-interacting proteins are often working as molecular machines.

A significant effort has been made over the past decade to employ the newest SM techniques to study DNA-protein interactions *in vitro* and *in cellulo*. Currently, *in vitro* studies are often preferred because of better SNR and also fewer limitations in manipulating and stimulating the system[109]. However, these methods are sensitive enough even to detect SM inside the living cell[110]. In particular the smFRET method is a powerful tool, that has been extensively applied[109]. The smFRET method is described in detail in the methods section of this thesis.

Cellular machines involved in genetic regulation and processing were intensively studied employing the SMF methods. Rep helicase motion on DNA was monitored with the aid of smFRET and revealed repetitive cycles of translocation on the single-stranded DNA until the double-stranded DNA block[111]. Later smFRET study of donor labelled REP helicase and acceptor labelled DNA revealed ATP fueled translocation towards the double stranded junction and consecutive protein conformational change[111,112]. Another DNA interacting protein, FtsK translocase, was studied with different SMF method – DNA curtains[113]. These studies revealed translocation along DNA with the possibility to bypass, push or dislodge other DNA-bound proteins in the way of translocation. The ribosome is an essential nucleic acid interacting protein – motor, that was extensively studied using smFRET[114–117]. The distance between two FRET pair labeled tRNAs inside the ribosome was measured and these measurements provided evidence for differences in distances when correct, and incorrect tRNAs are present[115,118]. Another insight gained from smFRET studies of the ribosome was the highly coordinated translocation of the ribosome along the messenger RNA, which suggested that ribosome works as a Brownian ratchet[119]. Four-color smFRET, by monitoring dynamics of tRNA and l1 stalk domain, revealed that these dynamics are not tightly coupled and the elongation factor has an effect on them[120,121].

DNA polymerase is an enzyme whose function is to copy DNA using template DNA and mononucleotides based on the base pairing between the template and the nucleotide from solution. This protein is one of the most studied DNA-interacting proteins regarding conformational dynamics at the SM level.

One of the first smFRET studies of FRET acceptor-labeled DNA polymerase revealed donor-labeled DNA synthesis: incorporation of nucleotides at the base pair level and several conformations of the complex related to the nucleotide insertion[122]. Several later studies focused on duration of DNA-polymerase complex interaction with a DNA template and different nucleotides using smPIFE – protein induced fluorescence enhancement[123,124]. It was discovered that complementary deoxynucleotides stabilize the complex more than complementary ribonucleotides. However, all non-complementary nucleosides were destabilizing the complex.

The next step in DNA polymerase research at the SM level was probing dynamics of the flexible part of the polymerase - "fingers". To monitor these movements, the fingers domain was labeled with a FRET donor and an acceptor was placed on the thumb domain[125]. These studies revealed that polymerase could perform conformational changes between opened and closed conformations and distribution of these conformations depended on the complex (correct DNA vs. without DNA substrate). This suggested that the closing of the "fingers" is not necessarily an indication of correct nucleotide incorporation. Additional support to that statement was provided from related studies of complexes with DNA and nucleotides (both deoxy- and ribo-), that showed mean FRET efficiency of the polymerase, just slightly higher than that of the open conformation[125–127]. This was an indication of the intermediate conformation of the polymerase that allows polymerase to detect, not correct, nucleotide before the "fingers" close entirely.

The further set of smFRET studies investigated the dynamics of transitions between these three identified states and found evidence of dynamics subpopulations and with the aid of decreased fidelity polymerase mutants, were able to confirm that the major fidelity checkpoint is the partially closed state[126,128].

Additionally, the exonuclease domain activity of the polymerase was studied by the smFRET. These studies of labeled polymerase and labeled DNA revealed binding of the polymerase to the template DNA and also switching between polymerase pol and exo domains bind to the DNA[127,129]. The internal mismatches in DNA increased the rate of the domain switching that makes sense because DNA is undergoing conformational dynamics to remove the wrongly inserted nucleotides. This study also revealed that any of the nucleotides (correct or incorrect) could accelerate the domain switching of polymerase bound to the template terminus with a wrongly paired primer. All these findings taken together emphasize the importance of conformational ensemble control in gene expression.

RNA polymerase is an essential protein involved in the process of protein synthesis using the DNA template. This protein is known to start transcription (production of RNA from the DNA template) with the initial stage and the processive state which follows. smFRET method – FRET pair labeled DNA in complex with RNA polymerase and ribonucleotides – revealed the start of transcription that was manifested by the increase in FRET efficiency due to bent DNA. These results confirmed the "DNA scrunching" model and rotational motion of one polymerases' domain for the initiation of the transcription[130–132]. Later studies with the RNA polymerase and its specificity factor on FRET pair labeled DNA revealed the repetitive opening-closing transitions, that were related to presence or absence of the specificity factor[133]. It was necessary to rationalize these motions in order to determine how much ATP is present in the cell and also to select the correct sequence to start the RNA synthesis. Also a version smFRET – quenchable FRET – was used to determine the rate constants of formation of the open complex (the transcription bubble) formation[134]. The RNA polymerase was labeled with a FRET pair – donor on the mobile part and acceptor on the immobile[135]. This labeled construct without any substrate showed three FRET efficiency populations: open (dominant in this study), closed and collapsed states. A single-stranded DNA polymerase was also mainly in the opened state, while with the double-stranded DNA protein complex was mostly in the closed conformation.

Type III DNA restriction endonuclease was investigated at the SM level using magnetic tweezers. These experiments revealed that the restriction endonuclease is using ATP for its helicase domain to translocate on DNA using 1D diffusion to find both of its targets[136]. Exoribonuclease Rrp44 that digests RNA molecules was studied using smFRET, and it turned out that this enzyme in complex with RNA works as a mechanical spring, converting chemical energy into storable mechanical energy. This enzyme unwinds RNA in steps of four bases, but the motion is occurring due to consumption of energy that occurs in the digestion of each nucleotide[137]. The smFRET method was applied to probe equilibrium protein structural fluctuations and enzyme-substrate interaction during DNA cleavage by the nonspecific staphylococcal nuclease[138]. smFRET was also used to monitor the freely diffusing molecules – DNA endonuclease and DNA substrate – in solution and allowed studying intramolecular distances or identification of subpopulations of states in a heterogeneous ensemble[139].

6. METHODS EMPLOYED IN THIS RESEARCH WORK

In this research we mainly used the TIRF microscopy and also confocal microscopy. The TIRF microscopy setup was equipped with several CW laser sources, a 1.4 NA objective, custom-made dual-view module, and an EMCCD camera. The confocal mode was established on the same microscopy setup as the TIRF, except that the beam was not focused onto the back focal plane of the objective. The sample scanning in the confocal mode was achieved by the XY piezo scanner, and the fluorescence emission was registered on two APD detectors (the dual-vie principle). The full description of the setup is in the materials and methods part of each publication. Our glass coverslip surfaces were modified using silane and PEG to allow specific and functional biomolecule immobilization. The acquired single-molecule signals were analyzed using a custom-written analysis package – TEA_MT, that is available online (igorexchange.com). Here various aspects of employed microscopy setups, surface preparation and data analysis will be described in more detail.

6.1 TIRF and confocal microscopy

In this work we used confocal and TIRF (special case of wide-field) microscopy modes, that are typically employed for SMF methods (Fig. 3). First the TIRF microscopy will be described and then the confocal. Working principles and the recent advancements are also listed.

TIRF microscopy allows circumventing the short observation time faced in the single-molecule confocal experiments, due to fast diffusion through the focal volume problem[67,140]. Also, it reduces the background fluorescence from out of focus fluorophores, faced in the wide-field epifluorescence mode, because of the shallow excitation field[68]. Immobilization of molecules is often required for camera-based methods such as TIRF microscopy, and this allows monitoring molecules in a massively parallel manner.

The principle of TIRF is explained by the Snell law – $\sin\theta_2 / \sin\theta_1 = n_1/n_2$, which states that light at the interface of two media (1, 2) of different refraction indices (n), is totally reflected if media 2 has a greater refractive index and incidence light angle (θ) is equal to or greater than the critical angle – $\theta_{crit} = \arcsin(n_2/n_1)$. Once light, totally reflected from the surface of the sample is created, evanescent field, penetrating into the sample, also appears. Intensity of this field decays exponentially within a few hundred nanometer from the surface in Z direction, and this penetration depth depends on the angle of incidence – the higher the angle the lower the penetration[141]. This shallow excitation field allows reducing the background fluorescence level and enables using higher concentration/ density of labelled molecules, than the confocal microscopy. The challenge that also exists in the confocal method is the photo-physics of single dye molecules, because fast bleaching or blinking of various time scales (triplet, radical states, etc.) limits the photon budget of the dye molecule. But as mentioned, this can be overcome with the aid of triplet state quenchers, self-healing fluorophores and oxygen scavenger systems[142–146].

The TIRF microscope set-up can either use prism or objective of high numerical aperture (NA) for directing the light into the sample. Prism type TIRF is becoming less frequently used nowadays. Therefore we also used

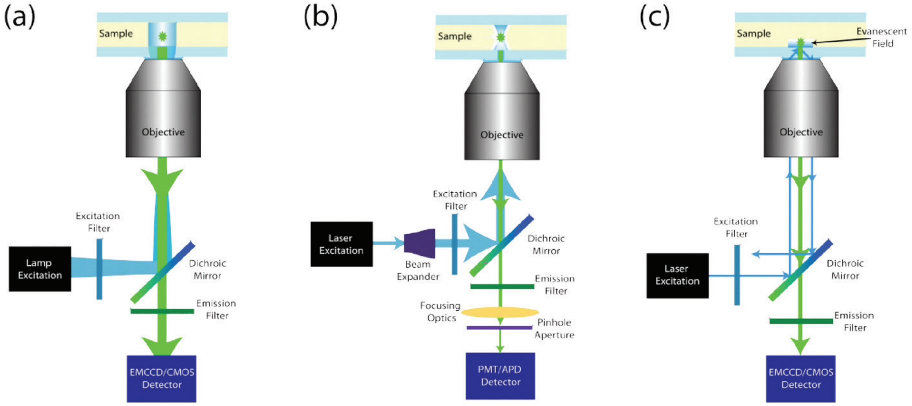

Figure 3: Excitation modes used in SM fluorescence microscopy. A) Epi-illumination, B) Confocal, C) TIRF. Reprinted with the permission from: J. M. Moran-Mirabal. Advanced-Microscopy Techniques for the Characterization of Cellulose Structure and Cellulose-Cellulase Interactions. Cellulose – Fundamental Aspects, 2013.

the objective based TIRF system, in which the excitation beam has to be focused on the back focal plane of the objective. The excitation light is typically directed to the objective with the aid of dichroic mirror, which can be single or multi-band to enable several laser excitations without the need of chaining the dichroic. Also now there is a possibility to use a micro-mirror system, which is dichroic free and ensures an extremely flat reflection surface and, therefore, produces perfect beam quality. This results in a parallel collimated beam exiting the objective with a desired angle, which can be adjusted by moving the beam sideways from the center of the objective. The beam diameter is limited with an aperture, so that only the visible area of the sample would be illuminated. The sample is placed on top of the objective on the x-y positioning stage. The objective is typically also placed on a motorized or motorized and piezo combined Z stage, which helps to keep the objective in focus by tracking the additional infrared laser reflection from the sample. The fluorescence emission from sample is also collected with the same objective, and having a high NA objective helps to collect as much light as possible from the nearby the surface existing fluorophore, which has the odd shape of the emission profile. To block the excitation light the collected emission is then passed through the dichroic mirror and the emission filter. Next this light is spectrally separated into donor component and acceptor component by a dichroic beamsplitter and directed to a different half of a single camera (dual-view scheme) or into a separate camera (dual-camera scheme). Then one half of the camera or the first camera is called the donor channel, and the other half or the second camera is called the acceptor channel.

Confocal microscopy is typically employed for probing the interior of the biological specimen or molecules diffusing in a solution. This microscopy mode allows achieving rapid and multi-parameter detection (intensity, lifetime, polarization, spectra)[147]. The principal difference between the wide-field and the confocal modes is the use of a pinhole. This item is positioned in in the path of the excitation beam, that is focused onto the focal plane of the objective at the diffraction limit to illuminate a small volume (~1 femto L). The collected fluorescence emission travels through the same optical path and is cleaned from the out-of -focus background light by the same pinhole. So only the fluorescence from the focal spot is detected with high SNR[148]. The APD detector (high sensitivity and low dark noise) allows for detection of weak signals. This setup also allows acquisition of a 3D image by moving a sample by piezo stage or the laser by galvonometric scanners[149,150]. The major advantage of the confocal microscopes is that they make point observations when a molecule is located on the focal spot so that it is the main source of the fluorescence in the area. Therefore confocal microscopes are the most common technique for SMF studies on photosynthetic systems. By combining the confocal setup with time-correlated single photon counting (TCSPC) systems, one can measure fluorescence lifetimes on the scale of nanoseconds from single-molecules[151]. Also it is possible to measure the fluorescence spectrum from a single molecule using this setup and a CCD spectrometer placed instead of an APD[152]. By inserting a polarizer into the excitation of the emission path of the confocal setup and rotating it, it is possible to estimate the angle of the transition dipole moment of a single molecule[153].

Because of the sensitivity that is a prerequisite for SM fluorescence (intensity, lifetime, and spectrum) monitoring the detectors is the main aspect of the system. Therefore the development of highly sensitive (high quantum efficiency (QE)) and low noise (dark noise and readout noise) level detectors with suitable time resolution and pixel dimensions (APD, CCD and CMOS cameras) opened the door for various SM level studies[154,155]. There are two main classes of detectors: single element and array. Single element detectors are used in confocal microscopy, and they have high QE and high time resolution. The same detectors with pulsed lasers are used in a confocal setup for TCSPC experiments to measure fluorescence lifetime. Array detectors allow accessing the spatial distribution of the photons, but typically they are not used for lifetime data detection. In wide-field epifluorescence and TIRF techniques they record images of fluorescence intensity or in confocal-fluorescence spectra.

Single-element detectors – APD and PMT – are typically used to measure fluorescence intensity and lifetime in the confocal mode. In the early experiments of single-molecule fluorescence detection PMTs were used[156].

These detectors have ~ 30% QE (lower for near-IR range), have temporal resolution of ~ 100 ps, and have a large active area of the detector element. Further experiments were performed using the single-photon-counting avalanche diodes (SPADs)[157]. Those have very high QE (~70%), temporal resolution similar to the PMTs, but their detection area is much smaller.

Array detectors allow paralleling detection of single-molecules signals, while having lower time resolution. Also they, in combination with the dispersion optics, provide a possibility of spectral acquisition. The CCD camera is the most abundant 2D array detector and is available in various frame rates, pixel sizes and counts, QE, dynamic ranges, and noise levels. For SMF the CCD camera with ~90% of QE (back-illuminated versions) and low noise (either cooled or intensified versions) is used. The intensified CCD camera includes electron-bombarded CCD and electron-multiplication CCD (EMCCD). Cooling of CCD chip to -75^0C and below allows reducing the thermal noise significantly and then long-term accumulation of photo-induced charges with low read-out noise becomes possible. EMCCD is surely the most abundant camera used for SMF experiments. This is because EMCCD allows multiplying the signal several thousand times on each CCD chip before analog-to-digital conversion, and that helps to overcome the read-out noise[158]. However the EMCCD has the same basic structure as the regular cooled CCD camera: a back-illuminated CCD chip, cooling, and analog-to-digital converter. The only difference is that EMCCD has a so-called EM gain register, which enables signal amplification using impact ionization. The lowest possible frame rate using binning of the EMCCD is ~0.1ms. The complementary metal-oxide semiconductor (CMOS) camera is an alternative technology that now is becoming a new work horse for the SMF. The difference between CCD and CMOS technology is that each pixel of the CMOS camera has an independent analog-to-digital converter, which allows rapid read-out of data (10 μs resolution)[159]. The QE of CMOS is lower than that of CCD. Additionally CMOS are cheaper than EMCCD, especially of those industry-grade CMOS cameras[155].

6.2 Single-molecule FRET

The smFRET method was used in this work. It employs the principle of FRET (discovered by Förster in 1946), that is essentially the distance-dependent non-radiative energy transfer from donor to acceptor fluorophore (FRET pair) via dipole-dipole interaction. FRET is possible if: 1) the spectra of donor emission and acceptor absorption overlap, 2) the FRET pair is in close proximity, 3) relative orientation of the FRET pair transition dipole moments allow transfer of energy[52]. FRET efficiency (E_{FRET}) can be expressed mathematically by this formula:

$E_{FRET} = k_T / (k_D+k_T) = 1 - (\tau_T/\tau_D) = 1 / (1+(R/R_0)^6)$, where k_D is the fluorescence emission rate of donor only, and k_T is the rate of energy transfer between the pair. These rates are determined by fluorescence lifetime measurements of donor only – τ_D and of donor with acceptor in close prioximity – τ_T. The E_{FRET} is inversely proportional to the sixth power of the distance between the FRET pair, and depends on the Förster radius – R_0 (distance at which 50% of energy transfer occurs). So R_0 is dependent on the properties of the pair, their relative orientation and can be evaluated given donor only quantum yield, refractive index of medium, orientation factor (typically = 2/3, which is valid as long as one of the dyes is freely rotating[160]), and the spectral overlap integral, which is calculated knowing the molecular extinction coefficient of the acceptor and the emission spectrum of the donor.

The important aspect of smFRET is the downscaling of the sample concentration and, therefore, detection of a low number of photons emitted from a single dye becomes important. However dilution of the sample to very low concentrations, means that the number of events studied at a given time will also be lowered, therefore to collect good statistics the experiment must be run for very long periods of time[109,161,162]. Thus a good working concentration of the investigated sample must be chosen experimentally, to avoid overlapping single molecules, but also to have enough statistics.

For sample excitation typically only the donor exciting laser is employed. If the donor is excited with this laser, it can emit some photons, that can be recorded in the donor channel (I^D_D) or transfer part of its energy to the acceptor in close proximity, then acceptor starts to emit fluorescence, which is recorded in the acceptor channel (I^A_D). This allows calculating apparent FRET efficiency:

$E_{FRET}{*} = I^A_D / (I^D_D + I^A_D)$,

which value reflects probability of FRETing. Most of the typically employed FRET pairs have a broad spectrum of emission and, therefore, it is hard to spectrally separate the fluorescence of the donor from the acceptor entirely. This is one of the reasons why registered E_{FRET}* will be non zero. Another reason is the instrument dependent detection efficiency differences for different dyes. All these aspects can be corrected and then E_{FRET}*, represents the true FRET efficiency[163].

It is also possible to employ two laser systems (donor exciting and acceptor exciting lasers) for excitation of the acceptor and donor separately by alternating laser excitation (ALEX)[163,164]. In this scheme one frame or time point is registered with the donor and the next with the acceptor exciting laser and this alternation is repeated as long as needed. If the acceptor is present and also active on the molecule one would be able to see that during excitation with the acceptor exciting laser. That is why ALEX, due to the stochiometry parameter:

$S = (I^{A}_{D} + I^{D}_{D}) / (I^{A}_{D} + I^{D}_{D} + I^{A}_{A})$,

helps to solve the problem of discrimination of molecules which are labelled with both dyes (S~0.5) from those which have only a donor (S=1), but do not have an acceptor or vice versa (S=0). The possibility to plot E_{FRET} versus S of acquired signals opened new and easy ways for sorting the results, without the need of careful signal selection.

6.3 Single-molecule microscopy data analysis

SMF experiments typically allow acquiring great quantity of data. However only a part of that data is meaningful or important. Therefore automated analysis algorithms and programming skills, because analysis procedures must be optimized for each experiment (there is no standard SM microscopy analysis software *per se*), became very important in this field[165]. However there are several common approaches to SMF data analysis.

From SMF experiments we can access changes in fluorescence intensity of a single emitter, also temporal characteristics, spectrum and polarization. Analysis of the fluorescence intensity (often time-averaged), which is the most straightforwardly detected parameter, allows investigation of molecular inhomogeneity, conformational dynamics and other parameters. In such analysis detected photons are integrated over a time window to determine an average intensity level of a molecule. This is easily achievable with the confocal setup, where one focuses the excitation beam on a molecule and records a signal. In the wide-field microscopy one acquires an image from which single-molecule signals have to be extracted. First molecules – fluorescent spots have to be detected[166]. That is typically achieved by the thresholding of an image and then detecting clusters of interconnected pixels having values above the threshold. Also recently a phasor-based approach for single-molecule localization has been applied[167]. Then, once fluorescent spots are detected, this extraction can be achieved in two principally different ways: by the region of interest integration or the 2D Gaussian fitting. The Gaussian fitting is time consuming, but better because it does not require local background correction of the extracted signal. In this research work the 2D Gaussian fitting was mainly used for SMF signal extraction[13].

The time-average fluorescence intensity extraction has one major drawback related to the dynamics rate of the system under study. Dynamics are manifested in the acquired SM signals as fast blinking, and a longer time-window may obscure these events. It has been shown that increasing the time-window leads to artifacts in further analysis[168]. However this is a nice way to increase signal-to-noise level of the signal. An alternative method provides a way to characterize physical parameters – state intensity, state duration (on and off times), and transitions – from the photon stream. There are several methods published, that allow accessing this information and they rely on different approaches: a generalized likelihood ratio test, T-test, step detection, Kalafut-Visscher algorithms, changes in SD and average intensity of a box-car[10,169–171]. This type of analysis allowed accessing dynamics down to the microsecond time scale[172]. In this research work we used the custom-written intensity change point detection algorithm, that is similar to the previously published algorithm[10,13]. The main difference is that the scanning window size is constant and we also applied the t-test for verification of the putative change point. Such analysis typically focuses on the millisecond-minutes time scales and in many different SM systems the obtained behavior of the probability distribution of the state dwell times exhibited an inverse power law[99,173].

6.4 Sample preparation for single-molecule microscopy

A single-molecule must undergo thousands of cycles of excitation and emission to allow collection of a sufficient number of photons for detection and analysis. That is related to the absorption cross-section (~1 Å^2), fluorescence QY, and the photobleaching QY (the inverse of it is the number of excitation cycles before bleaching) of the fluorescent molecule under study. The first parameter is related to the excitability of the molecule, and the latter two define the strength of the emitter. Some molecules (fluorophores, photosynthetic complexes) are better suited in that respect, the others are worse[174,175]. For example chlorophylls have an extinction coefficient ~ 70000 cm^{-1} M^{-1}, and the fluorescence QY~0.1, while phycobiliproteins have fluorescence QY ~0.98. The photobleaching is photo-degradation of a fluorescent particle and it is hypothesized to occur via radical formation or via photo-oxidative process, mediated by reactive intermediates generated from the triplet state[145]. In SMF experiments photobleaching QY is minimized by addition of triplet state scavengers or reducing and oxidizing species (ROXS), and by oxygen removal, either through scavengers or deoxygenation with argon or nitrogen[142,176,177]. Recent advancement in this field by covalent conjugation a triplet state quencher with a dye molecule enabled generation of self-healing fluorophores[178]. The average number of photons before bleaching is given by the ratio of the fluorescence QY and photobleaching QY, and for a typical molecular dye it is ~10^6 photons[140]. The longer the photo-bleaching of the dye is the better, because this extends the observation time and enables studies of the biological systems. In the photosynthetic complexes the pigments with more rigid structure of the tetrapyroles give rise to a longer excited state lifetime (~ ns). In many systems these pigments are found in close proximity to the carotenoids and the triplet states have a high efficiency of transfer from the Chl to the carotenoid. This prevents the triplet-state-mediated photobleaching and reduces the photobleaching QY, that may be important in natural photoprotection[179].

To ensure the signal extraction from a single-molecule during the experiment, dilute samples, in which molecules are separated spectroscopically or spatially (> diffraction limit), have to be used[180]. Recently super-resolution microcopy methods opened the doors for SM levels studies beyond the diffraction limit[181]. However the most straightforward approach is to use dilute samples of the fluorescently labeled molecules, and traditionally these samples were prepared by immobilizing single molecules at a picomolar concentration onto a surface. There are a number of ways to immobilize biological molecules on a glass surface. The simplest is to encast the sample in a polymer matrix, such as the poly(vinyl) alcohol (PVA), by spin-coating a thin film from a solution of sample mixed with the polymer. Other methods require modification of the glass surface. The most simple way is to modify the glass surface with the poly-L-lisine (PLL) and then biological molecules will anchor on such surface via nonspecific interactions. This method was also employed in this research work for detergent solubilized LHCII immobilization. Both PVA and PLL immobilization of pigment-proteins may introduce perturbations to the structure of the protein[182]. Nonetheless PLL modification is a method which works well and was used countless times for SM research of LHCII.

More dedicated surface modification methods for tethering biomolecules on the surface include: blocking with proteins, polyethylene glycol modification (PEGylation), lipid bilayers, liposomes[183], micro-fluidic approaches[184], and DNA curtains[185]. Surface blocking with nonspecific proteins such as BSA is a very popular method, but it is not very effective against preventing nonspecific absorption[112]. PEGylation is often much more effective than BSA covering. There are two generally used ways to make PEGylated surfaces – using amino-reactive PEG and aminosilane modified glass, or PLL-PEG conjugates, that adsorb on a clean glass surface. The inclusion of Biotinylated PEG into these preparations allows functional anchoring of other biotinilyated molecules via streptavidin or related protein. In this research glass surface silanization with aminosilane and amino reactive PEG modification was used for DNA-protein interaction SM level studies. Lipid bilayers provide a similar environment as the cell, and, therefore, are compatible with various proteins. Bilayers can be functionalized by the introduction of a small portion of chemically modified lipids (e.g. biotinylated), and that enables functional anchoring of other biotinylated molecules. These bilayers are relatively simple to prepare by injecting liposomes on a clean glass surface[186]. Biomolecules can also be encapsulated or reconstituted (transmembrane proteins) into the liposomes. These liposomes can then be immobilized on a BSA covered or PEGylated surface via biotinylated lipid and neutravidin interaction[15,187]. Recently a new technology called DNA curtains was developed[188]. It enables SM level studies of protein-DNA interactions, with a faster collection of statistically significant data and without disturbance of the functional activity of proteins. In these DNA curtains molecules are anchored to a bilayer of freely diffusing lipids. Then immobilized DNA molecules can be organized along the leading edges of barriers using buffer flow. This tool was extensively exploited for fabrication of various types of DNA curtains, that have been employed for studying various DNA interacting proteins.

smFRET and other fluorescence trajectories (intensity vs. time) are often limited in time and resolution, because of a low number of photons that can be measured in a given time. This has now improved due to the use of chemical additives in solution or covalent conjugation of these chemicals to the fluorophores[146] and also oxygen removal systems (oxygen scavengers)[176,189]. They reduce probability of the triplet state and other dark states, and thus increase the number of photons that can be measured in a given time, and also prolongs the observation time (bleaching time) of a single fluorophore. The solution surrounding the biomolecules should be controlled as well. Some additives such as reducing agents like TCEP or a detergent, that are needed for a transmembrane protein, may affect the photo-physics. In this research we have mainly used the Glucose Oxidase and Catalase oxygen scavenger system with the triplet state quencher Trolox. It has been demonstrated multiple times that this system works well for the Cy3/Cy5 FRET pair labelled biomolecules[142]. For LHCII measurements we used the same oxygen scavenger systems without the Trolox. This systems is known to affect the buffer pH, but as long as buffer capacity is high enough and the experiment does not last too long, the buffer pH is affected minimally[190].

CONCLUSIONS

Advancement of fluorescence microscopy techniques is significant for other fields of research – biotechnology, molecular biology, etc. They are also employed to address fundamental problems of life sciences, because of the possibility to probe bio-molecular processes and structure harmlessly, often non-invasively and in real time[191]. In the past 20 years, smFRET has become the mainstream tool for studying conformational dynamics of biomolecules and especially DNA-interacting proteins[24,27]. Currently, to obtain more information about the system under study, various versions of simultaneous monitoring of smFRET and other fluorescence parameters have emerged. They were useful for sorting out different populations of biomolecule species in the sample or reaction intermediates both for immobilized and for freely diffusing molecules.

The work presented in this thesis is devoted to conformational dynamics studies of biomolecules from two different fields: DNA-interacting proteins and transmembrane pigment-protein complexes. Both of these were studied at the single-molecule level using fluorescence microscopy techniques. Besides conformational protein studies, in this research work, we have also developed new technology and two methods. The developed technology is useful for studying DNA interacting proteins at the single-molecule level. The first developed method is helpful for studying conformational dynamics of DNA interacting proteins and their complexes. The second developed method is useful for functional studies of truly liposome reconstituted transmembrane pigment-protein complexes at the single-liposome level in a native-like environment.

In this research, we for the first time used simultaneous smFRET and tethered fluorophore motion in the evanescent field for monitoring interaction dynamics of Ecl18kI REase and DNA[13]. In this experiment, FRET pair labeled biotinylated DNA fragments, containing two target sites for Ecl18kI, were immobilized on a modified glass coverslip surface via biotin – neutravidin-biotin linkage. In the presence of Ca^{2+} ions Ecl18kI was binding DNA reversibly, and this resulted in repetitive DNA looping. The protein formed two types of DNA loops (parallel and un-parallel), and this novel SM methodology allowed us to reveal all possible different DNA-protein complex conformations and their kinetics, that were previously hidden[192]. Also we monitored DNA-protein complex dynamics of NgoMIV REase (stable tetramer) at the SM level. For these experiments we employed the same strategy of labeling biotinylated DNA, containing two target sites for NgoMIV, with a FRET pair and immobilizing it on the neutravidin covered surface[14]. Previously conformational dynamics of this protein-DNA complex were also studied at the SM level, but the studies were not able to provide a deeper understanding. This problem arose mainly because of the faced issues of significant aggregation of protein[193]. This protein can form a single type of DNA loop, but despite this fact, in our experiments we recorded two different FRET levels and at least two different types of single-molecule dynamics: slow and fast. This heterogeneity was hypothesized to occur because two copies of the protein can bind to a single DNA fragment, and then one protein forms a DNA loop, while the other scans DNA and searches for a target site. This lead to **the first statement of the thesis**: simultaneous measurement of FRET and tethered fluorophore motion allowed us to reveal previously hidden conformational dynamics of DNA-protein complexes of two different REazes.

In this research, we studied WT, and several mutant LHCII versions, that were solubilized in detergent micelles and immobilized on the PLL modified glass coverslip surface[101]. TIRF microscopy in contrast to confocal, which was previously employed for similar studies, has better SNR and also provides the possibility to collect data in a massively parallel manner. Mutant LHCIIs, that we studied, had various carotenoid compositions. Our results showed that distinct carotenoids affect the conformation dynamics as well as the mean intensity of the fluorescent state, but properties of the quenched conformation remain unchanged. Additionally it was not clear whether the peripheral carotenoid site in LHCII is involved in the quenching process. Here we compared SM level results of Vio- or Zea-enriched LHCII (in the peripheral site) with the bulk level results. This comparison showed that the quenching levels were higher in bulk than at the SM level. This inconsistency was rationalized to occur due to aggregation of LHCII in bulk measurements upon the change in environmental conditions, while aggregation in the SM experiments was prevented due to immobilization. The kinetics of quenching induction were faster for Zea- than for Vio-enriched LHCII, but the total level of fluorescence decrease was the same. Faster kinetics of quenching induction most likely occurs due to a faster aggregation rate in Zea-enriched LHCII samples. This leads to **the second statement of the thesis**: carotenoid composition of the peripheral LHCII site affects neither quenching extent nor conformational dynamics of this protein. However, LHCII mutant, which contains zeaxanthin as the only carotenoid, had altered conformational dynamics and was highly quenched.

Studies of isolated LHCII complexes in a native-like environment are important because they allow precise controlling of lipid composition, protein to lipid ratio, membrane curvature, pH gradient, etc. It is possible to achieve this goal by reconstitution of LHCII into the nanodisk system[194] or even better – liposomes[16]. In this thesis, we employed functional surface tethering of fluorescently labeled LHCII proteoliposomes. These experiments revealed that a substantial fraction of LHCII remains liposome-free in proteoliposome samples even after gradient centrifugation, and it is critical to use liposome-protein co-localization techniques when studying LHCII in proteoliposomes[15]. Also, the surface modification that was employed in the previous study could affect the results. This leads to **the third statement of the thesis:** SMF microscopy methods and surface tethering of fluorescently labeled LHCII proteoliposomes revealed a considerable amount of liposome-free LHCII and a broad heterogeneity of LHCII density in the proteoliposomes.

ABBREVIATIONS

a.a. - amino acid
AFM – Atomic force microscopy
ALEX – Alternating-laser excitation
ATP – Adenosine tri-phosphate
APD – Avalanche photo detector
BVA – Burst variance analysis
Bchl – Bacterio-chlorophyll
bp – Base pair
CAP – Catabolite activator protein
Cryo-EM – cryo-electron microscopy
CW – Constant wave
Chl – Chlorophyll
DNA – Deoxyribonucleic acid
dsDNA – Double-stranded deoxyribonucleic acid
dNTP – Deoxyribonucleoside tri-phosphate
EMCCD – Electron-multiplication CCD
FRET – Förster resonance energy transfer
FPS – FRET-restrained positioning and screening
IDP – Intrinsically disordered proteins
LHC – Light-harvesting complex
LHCI – Light-harvesting complex I
LHCII – Light-harvesting complex II
MFD – Multi-parameter fluorescence detection
NA – Numerical aperture
NMR – Nuclear magnetic resonance
NPS – Nano-positioning system
PDA – Probability distribution analysis
PIFE – Protein-induced fluorescence enhancement
PMT – Photomultiplier tube
Pol – Polymerase
PSF – Point spread function
quFRET – Quenchable Förster resonance energy transfer

RASP – Recurrence analysis of single particles
RC – Reaction center
RNA – Ribonucleic acid
RNAP – RNA polymerase
RNase – Ribonuclease
RT – Room temperature
rNTP – Ribonucleoside tri-phosphate
smFRET – Single-molecule Förster resonance energy transfer
SMS – Single-molecule spectroscopy
SMF – SM fluorescence
SSB – Single-stranded DNA binding protein
ssDNA – Single-stranded deoxyribonucleic acid
TIRF – Total internal reflection fluorescence
TBP – TATA box binding protein
TF – Transcription factor
tRNA – Transport RNA
QY – Quantum yield
QE – Quantum efficiency

BIBLIOGRAPHY

1. Tsai, C. J., Ma, B. & Nussinov, R. Protein-protein interaction networks: how can a hub protein bind so many different partners? *Trends in Biochemical Sciences* **34**, 594–600 (2009).
2. Ma, B. & Nussinov, R. Enzyme dynamics point to stepwise conformational selection in catalysis. *Current Opinion in Chemical Biology* **14**, 652–659 (2010).
3. Wei, G., Xi, W., Nussinov, R. & Ma, B. Protein Ensembles: How Does Nature Harness Thermodynamic Fluctuations for Life? the Diverse Functional Roles of Conformational Ensembles in the Cell. *Chem. Rev.* **116**, 6516–6551 (2016).
4. Giovagnetti, V. & Ruban, A. V. The evolution of the photoprotective antenna proteins in oxygenic photosynthetic eukaryotes. *Biochem. Soc. Trans.* **46**, 1263–1277 (2018).
5. Nussinov, R. & Wolynes, P. G. A second molecular biology revolution? The energy landscapes of biomolecular function. *Phys. Chem. Chem. Phys.* **16**, 6321 (2014).
6. Craggs, T. D. & Kapanidis, A. N. Six steps closer to FRET-driven structural biology. *Nat. Methods* **9**, 1157–1158 (2012).
7. Hwang, H. & Myong, S. Protein induced fluorescence enhancement (PIFE) for probing protein–nucleic acid interactions. *Chem. Soc. Rev.* **43**, 1221–1229 (2014).
8. Warshaw, D. M. *et al.* Myosin conformational states determined by single fluorophore polarization. *Proc Natl Acad Sci U S A* **95**, 8034–8039 (1998).
9. Jäger, M., Nir, E. & Weiss, S. Site-specific labeling of proteins for single-molecule FRET by combining chemical and enzymatic modification. *Protein Sci.* **15**, 640–646 (2006).
10. Krüger, T. P. J., Ilioaia, C. & van Grondelle, R. Fluorescence Intermittency from the Main Plant Light-Harvesting Complex:

Resolving Shifts between Intensity Levels. *J. Phys. Chem. B* **115**, 5071–5082 (2011).

11. Schlau-Cohen, G. S. *et al.* Single-molecule identification of quenched and unquenched states of LHCII. *J. Phys. Chem. Lett.* **6**, 860–867 (2015).
12. Krüger, T. P. J., Ilioaia, C., Johnson, M. P., Ruban, A. V. & Van Grondelle, R. Disentangling the low-energy states of the major light-harvesting complex of plants and their role in photoprotection. *Biochim. Biophys. Acta - Bioenerg.* **1837**, 1027–1038 (2014).
13. Tutkus, M., Marciulionis, T., Sasnauskas, G. & Rutkauskas, D. DNA-Endonuclease Complex Dynamics by Simultaneous FRET and Fluorophore Intensity in Evanescent Field. *Biophys. J.* **112**, 850–858 (2017).
14. Tutkus, M., Sasnauskas, G. & Rutkauskas, D. Probing the dynamics of restriction endonuclease NgoMIV-DNA interaction by single-molecule FRET. *Biopolymers* **107**, e23075 (2017).
15. Tutkus, M. *et al.* Fluorescence Microscopy of Single Liposomes with Incorporated Pigment-Proteins. *Langmuir* **34**, 14410–14418 (2018).
16. Natali, A. *et al.* Light-harvesting Complexes (LHCs) cluster spontaneously in membrane environment leading to shortening of their excited state lifetimes. *J. Biol. Chem.* **291**, 16730–16739 (2016).
17. Tsai, C. J., Buyong, M., Sham, Y. Y., Kumar, S. & Nussinov, R. Structured disorder and conformational selection. *Proteins: Structure, Function and Genetics* **44**, 418–427 (2001).
18. Frauenfelder, H., Sligar, S. & Wolynes, P. The energy landscapes and motions of proteins. *Science (80-.).* **254**, 1598–1603 (1991).
19. McCammon, J. A., Gelin, B. R. & Karplus, M. Dynamics of folded proteins. *Nature* **267**, 585–590 (1977).
20. VENYAMINOV, S. Y., RAJNAVÖLGYI, É., MFDGYESI, G. A., GERGELY, J. & ZÁVODSZKY, P. The Role of Interchain Disulphide Bridges in the Conformational Stability of Human Immunoglobulin

G1 Subclass: Hydrogen−Deuterium Exchange Studies. *Eur. J. Biochem.* **67**, 81–86 (1976).

21. Cooper, A. Thermodynamic fluctuations in protein molecules. *Proc. Natl. Acad. Sci.* **73**, 2740–2741 (1976).

22. Kumar, S., Ma, B., Tsai, C.-J., Sinha, N. & Nussinov, R. Folding and binding cascades: Dynamic landscapes and population shifts. *Protein Sci.* **9**, 10–19 (2008).

23. Weiss, S. Measuring conformational dynamics of biomolecules by single molecule fluorescence spectroscopy. *Nat. Struct. Biol.* **7**, 724–729 (2000).

24. Kim, H. & Ha, T. Single-molecule nanometry for biological physics. *Reports Prog. Phys.* **76**, 016601 (2013).

25. Schütz, G. J., Kada, G., Pastushenko, V. P. & Schindler, H. Properties of lipid microdomains in a muscle cell membrane visualized by single molecule microscopy. *EMBO J.* **19**, 892–901 (2000).

26. Schütz, G. J. *et al.* 3D Imaging of Individual Ion Channels in Live Cells at 40 nm Resolution. *Single Mol.* **1**, 25–31 (2000).

27. Sustarsic, M. & Kapanidis, A. N. Taking the ruler to the jungle: Single-molecule FRET for understanding biomolecular structure and dynamics in live cells. *Curr. Opin. Struct. Biol.* **34**, 52–59 (2015).

28. Weiss, S. Fluorescence spectroscopy of single biomolecules. *Science (80-.).* **283**, 1676–1683 (1999).

29. Bhabha, G., Biel, J. T. & Fraser, J. S. Keep on moving: Discovering and perturbing the conformational dynamics of enzymes. *Acc. Chem. Res.* **48**, 423–430 (2015).

30. Sugita, Y. & Okamoto, Y. Replica-exchange molecular dynamics method for protein folding. *Chem. Phys. Lett.* **314**, 141–151 (1999).

31. Laio, A. & Gervasio, F. L. Metadynamics: A method to simulate rare events and reconstruct the free energy in biophysics, chemistry and material science. *Reports Prog. Phys.* **71**, (2008).

32. Lane, T. J., Shukla, D., Beauchamp, K. A. & Pande, V. S. To milliseconds and beyond: Challenges in the simulation of protein folding. *Current Opinion in Structural Biology* **23**, 58–65 (2013).

33. Jensen, M. R., Zweckstetter, M., Huang, J.-R. & Blackledge, M. Exploring free-energy landscapes of intrinsically disordered proteins at atomic resolution using NMR spectroscopy. *Chem. Rev.* **114**, 6632–6660 (2014).

34. Mulder, F. A. A. & Filatov, M. NMR chemical shift data and ab initio shielding calculations: emerging tools for protein structure determination. *Chem. Soc. Rev.* **39**, 578–590 (2010).

35. Tolman, J. R. & Ruan, K. NMR residual dipolar couplings as probes of biomolecular dynamics. *Chemical Reviews* **106**, 1720–1736 (2006).

36. Sibille, N. & Bernadó, P. Structural characterization of intrinsically disordered proteins by the combined use of NMR and SAXS. *Biochem. Soc. Trans.* **40**, 955–962 (2012).

37. Huang, J. R. *et al.* Transient electrostatic interactions dominate the conformational equilibrium sampled by multidomain splicing factor U2AF65: A combined NMR and SAXS study. *J. Am. Chem. Soc.* **136**, 7068–7076 (2014).

38. Ward, A. B., Sali, A. & Wilson, I. A. Integrative Structural Biology. *Science (80-.).* **339**, 913–915 (2013).

39. Sternberg, S. H., LaFrance, B., Kaplan, M. & Doudna, J. A. Conformational control of DNA target cleavage by CRISPR–Cas9. *Nature* **527**, 110–113 (2015).

40. Stryer, L. & Haugland, R. P. Energy transfer: a spectroscopic ruler. *Proc. Natl. Acad. Sci. U. S. A.* **58**, 719–26 (1967).

41. Clegg, R. M. Fluorescence resonance energy transfer and nucleic acids. in *Methods in Enzymology* **211**, 353–388 (1992).

42. Jares-Erijman, E. A. & Jovin, T. M. FRET imaging. *Nat. Biotechnol.* **21**, 1387–1395 (2003).

43. Michalet, X., Weiss, S. & Jäger, M. Single-molecule fluorescence studies of protein folding and conformational dynamics. *Chem. Rev.* **106**, 1785–1813 (2006).

44. Žoldák, G. & Rief, M. Force as a single molecule probe of multidimensional protein energy landscapes. *Current Opinion in Structural Biology* **23**, 48–57 (2013).

45. Schuler, B. & Hofmann, H. Single-molecule spectroscopy of protein folding dynamics—expanding scope and timescales. *Curr. Opin. Struct. Biol.* **23**, 36–47 (2013).

46. Deniz, A. A. Deciphering Complexity in Molecular Biophysics with Single-Molecule Resolution. *J. Mol. Biol.* **428**, 301–307 (2016).

47. Woodside, M. T. & Block, S. M. Reconstructing Folding Energy Landscapes by Single-Molecule Force Spectroscopy. *Annu. Rev. Biophys.* **43**, 19–39 (2014).

48. Ritchie, D. B. & Woodside, M. T. Probing the structural dynamics of proteins and nucleic acids with optical tweezers. *Curr. Opin. Struct. Biol.* **34**, 43–51 (2015).

49. Kodera, N., Yamamoto, D., Ishikawa, R. & Ando, T. Video imaging of walking myosin v by high-speed atomic force microscopy. *Nature* **468**, 72–76 (2010).

50. Greenleaf, W. J., Woodside, M. T. & Block, S. M. High-Resolution, Single-Molecule Measurements of Biomolecular Motion. *Annu. Rev. Biophys. Biomol. Struct.* **36**, 171–190 (2007).

51. Walter, N. G. & Bustamante, C. Introduction to Single Molecule Imaging and Mechanics: Seeing and Touching Molecules One at a Time. *Chem. Rev.* **114**, 3069–3071 (2014).

52. Lakowicz, J. R. *Principles of Fluorescence Spectroscopy*. *Principles of Fluorescence Spectroscopy* (Springer US, 2006). doi:10.1007/978-0-387-46312-4

53. Kondo, T., Chen, W. J. & Schlau-Cohen, G. S. Single-Molecule Fluorescence Spectroscopy of Photosynthetic Systems. *Chem. Rev.*

117, 860–898 (2017).

54. Sase, I., Miyata, H., Corrie, J. E., Craik, J. S. & Kinosita, K. Real time imaging of single fluorophores on moving actin with an epifluorescence microscope. *Biophys. J.* **69**, 323–328 (1995).

55. Yildiz, A. & Selvin, P. R. Fluorescence Imaging with One Nanometer Accuracy: Application to Molecular Motors. *Acc. Chem. Res.* **38**, 574–582 (2005).

56. Tan, X., Hu, D., Squier, T. C. & Lu, H. P. Probing nanosecond protein motions of calmodulin by single-molecule fluorescence anisotropy. *Appl. Phys. Lett.* **85**, 2420–2422 (2004).

57. Lu, H. P. Single-molecule protein interaction conformational dynamics. *Curr. Pharm. Biotechnol.* **10**, 522–31 (2009).

58. Sase, I., Miyata, H., Ishiwata, S. & Kinosita, K. Axial rotation of sliding actin filaments revealed by single-fluorophore imaging. *Proc. Natl. Acad. Sci. U. S. A.* **94**, 5646–50 (1997).

59. Boyer, P. D. THE ATP SYNTHASE—A SPLENDID MOLECULAR MACHINE. *Annu. Rev. Biochem.* **66**, 717–749 (1997).

60. Noji, H., Yasuda, R., Yoshida, M. & Kinosita, K. Direct observation of the rotation of F1-ATPase. *Nature* **386**, 299–302 (1997).

61. Yasuda, R., Noji, H., Kinosita, K. & Yoshida, M. F1-ATPase is a highly efficient molecular motor that rotates with discrete 120 degree steps. *Cell* **93**, 1117–24 (1998).

62. Sambongi, Y. *et al.* Mechanical rotation of the c subunit oligomer in ATP synthase (F0F1): direct observation. *Science* **286**, 1722–4 (1999).

63. Häsler, K., Engelbrecht, S. & Junge, W. Three-stepped rotation of subunits γ and ε in single molecules of F- ATPase as revealed by polarized, confocal fluorometry. *FEBS Lett.* **426**, 301–304 (1998).

64. Kulzer, F. & Orrit, M. SINGLE-MOLECULE OPTICS. *Annu. Rev. Phys. Chem.* **55**, 585–611 (2004).

65. Hoffmann, A. *et al.* Quantifying heterogeneity and conformational dynamics from single molecule FRET of diffusing molecules: Recurrence analysis of single particles (RASP). *Phys. Chem. Chem. Phys.* **13**, 1857–1871 (2011).

66. McKinney, S. A., Joo, C. & Ha, T. Analysis of Single-Molecule FRET Trajectories Using Hidden Markov Modeling. *Biophys. J.* **91**, 1941–1951 (2006).

67. Hohlbein, J., Gryte, K., Heilemann, M. & Kapanidis, A. N. Surfing on a new wave of single-molecule fluorescence methods. *Phys. Biol.* **7**, 031001 (2010).

68. Roy, R., Hohng, S. & Ha, T. A practical guide to single-molecule FRET. *Nat. Methods* **5**, 507–16 (2008).

69. Badali, D. & Gradinaru, C. C. The effect of Brownian motion of fluorescent probes on measuring nanoscale distances by Förster resonance energy transfer. *J. Chem. Phys.* **134**, 225102 (2011).

70. Comstock, M. J. *et al.* Direct observation of structure-function relationship in a nucleic acid-processing enzyme. *Science (80-.).* **348**, 352–354 (2015).

71. Hohng, S., Joo, C. & Ha, T. Single-Molecule Three-Color FRET. *Biophys. J.* **87**, 1328–1337 (2004).

72. DeRocco, V. C., Anderson, T., Piehler, J., Erie, D. A. & Weninger, K. Four-color single-molecule fluorescence with noncovalent dye labeling to monitor dynamic multimolecular complexes. *Biotechniques* **49**, 807–816 (2010).

73. Lee, N. K. *et al.* Three-Color Alternating-Laser Excitation of Single Molecules: Monitoring Multiple Interactions and Distances. *Biophys. J.* **92**, 303–312 (2007).

74. Muschielok, A. *et al.* A nano-positioning system for macromolecular structural analysis. *Nat. Methods* **5**, 965–971 (2008).

75. Muschielok, A. & Michaelis, J. Application of the nano-positioning system to the analysis of fluorescence resonance energy transfer

networks. *J. Phys. Chem. B* **115**, 11927–11937 (2011).

76. Blankenship, R. E. The Basic Principles of Photosynthetic Energy Storage. in *Molecular Mechanisms of Photosynthesis* 1–10 (Blackwell Science Ltd, 2002). doi:10.1002/9780470758472.ch1

77. Bopp, M. A., Sytnik, A., Howard, T. D., Cogdell, R. J. & Hochstrasser, R. M. The dynamics of structural deformations of immobilized single light-harvesting complexes. *Proc. Natl. Acad. Sci.* **96**, 11271–11276 (2002).

78. Cogdell, R. J., Gall, A. & Köhler, J. The architecture and function of the light-harvesting apparatus of purple bacteria: From single molecules to in vivo membranes. *Q. Rev. Biophys.* **39**, 227–324 (2006).

79. Kruger, T. P. J., Wientjes, E., Croce, R. & van Grondelle, R. Conformational switching explains the intrinsic multifunctionality of plant light-harvesting complexes. *Proc. Natl. Acad. Sci.* **108**, 13516–13521 (2011).

80. Bopp, M. A., Jia, Y., Li, L., Cogdell, R. J. & Hochstrasser, R. M. Fluorescence and photobleaching dynamics of single light-harvesting complexes. *Proc. Natl. Acad. Sci. U. S. A.* **94**, 10630–5 (1997).

81. Tietz, C. *et al.* Single molecule spectroscopy on the light-harvesting complex II of higher plants. *Biophys. J.* **81**, 556–562 (2001).

82. Liu, Z. *et al.* Crystal structure of spinach major light-harvesting complex at 2.72 Å resolution. *Nature* **428**, 287–292 (2004).

83. BEDDARD, G. S. & PORTER, G. Concentration quenching in chlorophyll. *Nature* **260**, 366–367 (1976).

84. Ishizaki, A., Calhoun, T. R., Schlau-Cohen, G. S. & Fleming, G. R. Quantum coherence and its interplay with protein environments in photosynthetic electronic energy transfer. *Phys. Chem. Chem. Phys.* **12**, 7319–7337 (2010).

85. van Amerongen, H., van Grondelle, R. & Valkunas, L. *Photosynthetic Excitons*. *Photosynthetic Excitons* (WORLD

SCIENTIFIC, 2012). doi:10.1142/3609

86. Szabó, I., Bergantino, E. & Giacometti, G. M. Light and oxygenic photosynthesis: energy dissipation as a protection mechanism against photo-oxidation. *EMBO Rep.* **6**, 629–634 (2005).

87. Hofmann, C., Aartsma, T. J., Michel, H. & Kohler, J. Direct observation of tiers in the energy landscape of a chromoprotein: A single-molecule study. *Proc. Natl. Acad. Sci.* **100**, 15534–15538 (2003).

88. Schlau-Cohen, G. S., Wang, Q., Southall, J., Cogdell, R. J. & Moerner, W. E. Single-molecule spectroscopy reveals photosynthetic LH2 complexes switch between emissive states. *Proc. Natl. Acad. Sci.* **110**, 10899–10903 (2013).

89. Rutkauskas, D. *et al.* Comparative Study of Spectral Flexibilities of Bacterial Light-Harvesting Complexes: Structural Implications. *Biophys. J.* **90**, 2463–2474 (2006).

90. Tietz, C., Chekhlov, O., Dräbenstedt, A., Schuster, J. & Wrachtrup, J. Spectroscopy on Single Light-Harvesting Complexes at Low Temperature. *J. Phys. Chem. B* **103**, 6328–6333 (2002).

91. Scheuring, S. & Sturgis, J. N. Biochemistry: Chromatic adaptation of photosynthetic membranes. *Science (80-.).* **309**, 484–487 (2005).

92. Scheuring, S., Rigaud, J.-L. & Sturgis, J. N. Variable LH2 stoichiometry and core clustering in native membranes of Rhodospirillum photometricum. *EMBO J.* **23**, 4127–4133 (2004).

93. Papiz, M. Z., Prince, S. M., Howard, T., Cogdell, R. J. & Isaacs, N. W. The Structure and Thermal Motion of the B800–850 LH2 Complex from Rps.acidophila at 2.0Å Resolution and 100K: New Structural Features and Functionally Relevant Motions. *J. Mol. Biol.* **326**, 1523–1538 (2003).

94. Monshouwer, R., Abrahamsson, M., van Mourik, F. & van Grondelle, R. Superradiance and Exciton Delocalization in Bacterial

Photosynthetic Light-Harvesting Systems. *J. Phys. Chem. B* **101**, 7241–7248 (2002).

95. Andersson, B. & Anderson, J. M. Lateral heterogeneity in the distribution of chlorophyll-protein complexes of the thylakoid membranes of spinach chloroplasts. *Biochim. Biophys. Acta - Bioenerg.* **593**, 427–440 (1980).

96. Niyogi, K. K. & Truong, T. B. Evolution of flexible non-photochemical quenching mechanisms that regulate light harvesting in oxygenic photosynthesis. *Curr. Opin. Plant Biol.* **16**, 307–314 (2013).

97. Ruban, A. V., Johnson, M. P. & Duffy, C. D. P. The photoprotective molecular switch in the photosystem II antenna. *Biochim. Biophys. Acta - Bioenerg.* **1817**, 167–181 (2012).

98. Duffy, C. D. P. & Ruban, A. V. Dissipative pathways in the photosystem-II antenna in plants. *Journal of Photochemistry and Photobiology B: Biology* **152**, 215–226 (2015).

99. Krüger, T. P. J. *et al.* Controlled Disorder in Plant Light-Harvesting Complex II Explains Its Photoprotective Role. *Biophys. J.* **102**, 2669–2676 (2012).

100. Gwizdala, M., Berera, R., Kirilovsky, D., van Grondelle, R. & Krüger, T. P. J. Controlling Light Harvesting with Light. *J. Am. Chem. Soc.* **138**, 11616–11622 (2016).

101. Tutkus, M., Chmeliov, J., Rutkauskas, D., Ruban, A. V. & Valkunas, L. Influence of the Carotenoid Composition on the Conformational Dynamics of Photosynthetic Light-Harvesting Complexes. *J. Phys. Chem. Lett.* **8**, 5898–5906 (2017).

102. Alboresi, A., Ballottari, M., Hienerwadel, R., Giacometti, G. M. & Morosinotto, T. Antenna complexes protect Photosystem i from Photoinhibition. *BMC Plant Biol.* **9**, 71 (2009).

103. Krüger, T. P. J., Novoderezhkin, V. I., Ilioaia, C. & Van Grondelle, R. Fluorescence spectral dynamics of single LHCII trimers. *Biophys. J.*

98, 3093–3101 (2010).

104. Šanda, F. & Mukamel, S. Anomalous continuous-time random-walk spectral diffusion in coherent third-order optical response. *Phys. Rev. E* **73**, 011103 (2006).

105. Gruber, J. M. *et al.* Photophysics in single light-harvesting complexes II: from micelle to native nanodisks. in *Single Molecule Spectroscopy and Superresolution Imaging IX* (eds. Enderlein, J., Gregor, I., Gryczynski, Z. K., Erdmann, R. & Koberling, F.) **9714**, 97140A (2016).

106. Wollman, A. J. M., Miller, H., Zhou, Z. & Leake, M. C. Probing DNA interactions with proteins using a single-molecule toolbox: inside the cell, in a test tube and in a computer. *Biochem. Soc. Trans.* **43**, 139–145 (2015).

107. Cai, Y.-H. & Huang, H. Advances in the study of protein–DNA interaction. *Amino Acids* **43**, 1141–1146 (2012).

108. Duzdevich, D., Redding, S. & Greene, E. C. DNA dynamics and single-molecule biology. *Chem. Rev.* **114**, 3072–3086 (2014).

109. Farooq, S., Fijen, C. & Hohlbein, J. Studying DNA-protein interactions with single-molecule Förster resonance energy transfer. *Protoplasma* **251**, 317–332 (2014).

110. Xie, X. S., Choi, P. J., Li, G.-W., Lee, N. K. & Lia, G. Single-Molecule Approach to Molecular Biology in Living Bacterial Cells. *Annu. Rev. Biophys.* **37**, 417–444 (2008).

111. Myong, S., Rasnik, I., Joo, C., Lohman, T. M. & Ha, T. Repetitive shuttling of a motor protein on DNA. *Nature* **437**, 1321–1325 (2005).

112. Rasnik, I., Myong, S., Cheng, W., Lohman, T. M. & Ha, T. DNA-binding Orientation and Domain Conformation of the E.coli Rep Helicase Monomer Bound to a Partial Duplex Junction: Single-molecule Studies of Fluorescently Labeled Enzymes. *J. Mol. Biol.* **336**, 395–408 (2004).

113. Lee, J., Finkelstein, I. J., Arciszewska, L. K., Sherratt, D. J. & Greene, E. C. Single-Molecule Imaging of FtsK Translocation Reveals Mechanistic Features of Protein-Protein Collisions on DNA. *Mol. Cell* **54**, 832–843 (2014).

114. Blanchard, S. C., Gonzalez, R. L., Kim, H. D., Chu, S. & Puglisi, J. D. tRNA selection and kinetic proofreading in translation. *Nat. Struct. Mol. Biol.* **11**, 1008–1014 (2004).

115. Lee, T.-H., Blanchard, S. C., Kim, H. D., Puglisi, J. D. & Chu, S. The role of fluctuations in tRNA selection by the ribosome. *Proc. Natl. Acad. Sci.* **104**, 13661–13665 (2007).

116. Cornish, P. V., Ermolenko, D. N., Noller, H. F. & Ha, T. Spontaneous Intersubunit Rotation in Single Ribosomes. *Mol. Cell* **30**, 578–588 (2008).

117. Fei, J., Kosuri, P., MacDougall, D. D. & Gonzalez, R. L. Coupling of Ribosomal L1 Stalk and tRNA Dynamics during Translation Elongation. *Mol. Cell* **30**, 348–359 (2008).

118. Geggier, P. *et al.* Conformational Sampling of Aminoacyl-tRNA during Selection on the Bacterial Ribosome. *J. Mol. Biol.* **399**, 576–595 (2010).

119. Frank, J. & Gonzalez, R. L. Structure and Dynamics of a Processive Brownian Motor: The Translating Ribosome. *Annu. Rev. Biochem.* **79**, 381–412 (2010).

120. Munro, J. B. *et al.* Spontaneous formation of the unlocked state of the ribosome is a multistep process. *Proc. Natl. Acad. Sci.* **107**, 709–714 (2010).

121. Munro, J. B., Altman, R. B., Tung, C.-S., Sanbonmatsu, K. Y. & Blanchard, S. C. A fast dynamic mode of the EF-G-bound ribosome. *EMBO J.* **29**, 770–781 (2010).

122. Christian, T. D., Romano, L. J. & Rueda, D. Single-molecule measurements of synthesis by DNA polymerase with base-pair resolution. *Proc. Natl. Acad. Sci.* **106**, 21109–21114 (2009).

123. Hwang, H., Kim, H. & Myong, S. Protein induced fluorescence enhancement as a single molecule assay with short distance sensitivity. *Proc. Natl. Acad. Sci.* **108**, 7414–7418 (2011).

124. Markiewicz, R. P., Vrtis, K. B., Rueda, D. & Romano, L. J. Single-molecule microscopy reveals new insights into nucleotide selection by DNA polymerase i. *Nucleic Acids Res.* **40**, 7975–7984 (2012).

125. Santoso, Y. *et al.* Conformational transitions in DNA polymerase I revealed by single-molecule FRET. *Proc. Natl. Acad. Sci.* **107**, 715–720 (2010).

126. Hohlbein, J. *et al.* Conformational landscapes of DNA polymerase I and mutator derivatives establish fidelity checkpoints for nucleotide insertion. *Nat. Commun.* **4**, 2131 (2013).

127. Berezhna, S. Y., Gill, J. P., Lamichhane, R. & Millar, D. P. Single-Molecule Förster Resonance Energy Transfer Reveals an Innate Fidelity Checkpoint in DNA Polymerase I. *J. Am. Chem. Soc.* **134**, 11261–11268 (2012).

128. Santoso, Y., Torella, J. P. & Kapanidis, A. N. Characterizing Single-Molecule FRET Dynamics with Probability Distribution Analysis. *ChemPhysChem* **11**, 2209–2219 (2010).

129. Lamichhane, R., Berezhna, S. Y., Gill, J. P., Van der Schans, E. & Millar, D. P. Dynamics of Site Switching in DNA Polymerase. *J. Am. Chem. Soc.* **135**, 4735–4742 (2013).

130. Kapanidis, A. N. *et al.* Initial transcription by RNA polymerase proceeds through a DNA-scrunching mechanism. *Science (80-.).* **314**, 1144–1147 (2006).

131. Tang, G.-Q., Roy, R., Bandwar, R. P., Ha, T. & Patel, S. S. Real-time observation of the transition from transcription initiation to elongation of the RNA polymerase. *Proc. Natl. Acad. Sci.* **106**, 22175–22180 (2009).

132. Tang, G.-Q., Roy, R., Ha, T. & Patel, S. S. Transcription Initiation in a Single-Subunit RNA Polymerase Proceeds through DNA

Scrunching and Rotation of the N-Terminal Subdomains. *Mol. Cell* **30**, 567–577 (2008).

133. Kim, H., Tang, G.-Q., Patel, S. S. & Ha, T. Opening–closing dynamics of the mitochondrial transcription pre-initiation complex. *Nucleic Acids Res.* **40**, 371–380 (2012).

134. Cordes, T. *et al.* Sensing DNA Opening in Transcription Using Quenchable Förster Resonance Energy Transfer. *Biochemistry* **49**, 9171–9180 (2010).

135. Chakraborty, A. *et al.* Opening and closing of the bacterial RNA polymerase clamp. *Science (80-.).* **337**, 591–595 (2012).

136. Ramanathan, S. P. *et al.* Type III restriction enzymes communicate in 1D without looping between their target sites. *Proc. Natl. Acad. Sci.* **106**, 1748–1753 (2009).

137. Lee, G., Bratkowski, M. A., Ding, F., Ke, A. & Ha, T. Elastic Coupling Between RNA Degradation and Unwinding by an Exoribonuclease. *Science (80-.).* **336**, 1726–1729 (2012).

138. Ha, T. *et al.* Single-molecule fluorescence spectroscopy of enzyme conformational dynamics and cleavage mechanism. *Proc. Natl. Acad. Sci.* **96**, 893–898 (1999).

139. Deniz, A. A. *et al.* Single-pair fluorescence resonance energy transfer on freely diffusing molecules: observation of Förster distance dependence and subpopulations. *Proc. Natl. Acad. Sci. U. S. A.* **96**, 3670–5 (1999).

140. Moerner, W. E. & Fromm, D. P. Methods of single-molecule fluorescence spectroscopy and microscopy. *Rev. Sci. Instrum.* **74**, 3597–3619 (2003).

141. Axelrod, D., Burghardt, T. P. & Thompson, N. L. Total internal reflection fluorescence. *Annu. Rev. Biophys. Bioeng.* **13**, 247–268 (1984).

142. Rasnik, I., McKinney, S. A. & Ha, T. Nonblinking and long-lasting single-molecule fluorescence imaging. *Nat. Methods* **3**, 891–893

(2006).

143. Vogelsang, J. *et al.* A reducing and oxidizing system minimizes photobleaching and blinking of fluorescent dyes. *Angew. Chemie - Int. Ed.* **47**, 5465–5469 (2008).

144. Cordes, T., Vogelsang, J. & Tinnefeld, P. On the mechanism of trolox as antiblinking and antibleaching reagent. *J. Am. Chem. Soc.* **131**, 5018–5019 (2009).

145. Ha, T. & Tinnefeld, P. Photophysics of Fluorescent Probes for Single-Molecule Biophysics and Super-Resolution Imaging. *Annu. Rev. Phys. Chem.* **63**, 595–617 (2012).

146. Zheng, Q. *et al.* Ultra-stable organic fluorophores for single-molecule research. *Chem. Soc. Rev.* **43**, 1044–1056 (2014).

147. Sisamakis, E., Valeri, A., Kalinin, S., Rothwell, P. J. & Seidel, C. A. M. Accurate Single-Molecule FRET Studies Using Multiparameter Fluorescence Detection. in *Methods in Enzymology* **475**, 455–514 (Elsevier Inc., 2010).

148. LANG, E., BAIER, J. & KOHLER, J. Epifluorescence, confocal and total internal reflection microscopy for single-molecule experiments: a quantitative comparison. *J. Microsc.* **222**, 118–123 (2006).

149. Vácha, M., Yokoyama, H., Tokizaki, T., Furuki, M. & Tani, T. Laser scanning microscope for low temperature single molecule and microscale spectroscopy based on gradient index optics. *Rev. Sci. Instrum.* **70**, 2041–2045 (1999).

150. Maruo, M. *et al.* Three-dimensional laser-scanning confocal reflecting microscope for multicolor single-molecule imaging at 1.5K. *Chem. Phys. Lett.* **591**, 233–236 (2014).

151. Felekyan, S. *et al.* Full correlation from picoseconds to seconds by time-resolved and time-correlated single photon detection. *Rev. Sci. Instrum.* **76**, 1–14 (2005).

152. Kumazaki, S. *et al.* A line-scanning semi-confocal multi-photon fluorescence microscope with a simultaneous broadband spectral

acquisition and its application to the study of the thylakoid membrane of a cyanobacterium Anabaena PCC7120. *J. Microsc.* **228**, 240–254 (2007).

153. Hofmann, C. *et al.* Single-Molecule Study of the Electronic Couplings in a Circular Array of Molecules: Light-Harvesting-2 Complex from Rhodospirillum Molischianum. *Phys. Rev. Lett.* **90**, 4 (2003).

154. Huang, F. *et al.* Video-rate nanoscopy using sCMOS camera-specific single-molecule localization algorithms. *Nat. Methods* **10**, 653–658 (2013).

155. Diekmann, R. *et al.* Characterization of an industry-grade CMOS camera well suited for single molecule localization microscopy - High performance super-resolution at low cost. *Sci. Rep.* **7**, 1–10 (2017).

156. Brooks Shera, E., Seitzinger, N. K., Davis, L. M., Keller, R. A. & Soper, S. A. Detection of single fluorescent molecules. *Chem. Phys. Lett.* **174**, 553–557 (1990).

157. Li, L. & Davis, L. M. Single photon avalanche diode for single molecule detection. *Rev. Sci. Instrum.* **64**, 1524–1529 (1993).

158. Denvir, D. J. & Coates, C. G. Electron-multiplying CCD technology: application to ultrasensitive detection of biomolecules. in *Biomedical Nanotechnology Architectures and Applications* (eds. Bornhop, D. J. et al.) **4626**, 502–512 (2002).

159. Ueno, H. *et al.* Simple dark-field microscopy with nanometer spatial precision and microsecond temporal resolution. *Biophys. J.* **98**, 2014–2023 (2010).

160. Dale, R. E., Eisinger, J. & Blumberg, W. E. The orientational freedom of molecular probes. The orientation factor in intramolecular energy transfer. *Biophys. J.* **26**, 161–193 (1979).

161. Levene, H. J. *et al.* Zero-mode waveguides for single-molecule analysis at high concentrations. *Science (80-.).* **299**, 682–686 (2003).

162. Holzmeister, P., Acuna, G. P., Grohmann, D. & Tinnefeld, P. Breaking the concentration limit of optical single-molecule detection. *Chem. Soc. Rev.* **43**, 1014–1028 (2014).

163. Hohlbein, J., Craggs, T. D. & Cordes, T. Alternating-laser excitation: single-molecule FRET and beyond. *Chem. Soc. Rev.* **43**, 1156–1171 (2014).

164. Kapanidis, A. N. *et al.* Fluorescence-aided molecule sorting: Analysis of structure and interactions by alternating-laser excitation of single molecules. *Proc. Natl. Acad. Sci.* **101**, 8936–8941 (2004).

165. Miller, H., Zhou, Z., Shepherd, J., Wollman, A. J. M. & Leake, M. C. Single-molecule techniques in biophysics: A review of the progress in methods and applications. *Reports Prog. Phys.* **81**, (2018).

166. Holden, S. J. *et al.* Defining the limits of single-molecule FRET resolution in TIRF microscopy. *Biophys. J.* **99**, 3102–3111 (2010).

167. Martens, K. J. A. *et al.* An open microscopy framework suited for tracking dCas9 in live 1 bacteria. *arXiv* 1–49 (2018).

168. Terentyeva, T. G. *et al.* Dynamic Disorder in Single-Enzyme Experiments: Facts and Artifacts. *ACS Nano* **6**, 346–354 (2012).

169. Watkins, L. P. & Yang, H. Detection of Intensity Change Points in Time-Resolved Single-Molecule Measurements. *J. Phys. Chem. B* **109**, 617–628 (2005).

170. Kalafut, B. & Visscher, K. An objective, model-independent method for detection of non-uniform steps in noisy signals. *Comput. Phys. Commun.* **179**, 716–723 (2008).

171. Tsekouras, K., Custer, T. C., Jashnsaz, H., Walter, N. G. & Pressé, S. A novel method to accurately locate and count large numbers of steps by photobleaching. *Mol. Biol. Cell* **27**, 3601–3615 (2016).

172. Schörner, M., Beyer, S. R., Southall, J., Cogdell, R. J. & Köhler, J. Multi-Level, Multi Time-Scale Fluorescence Intermittency of Photosynthetic LH2 Complexes: A Precursor of Non-Photochemical Quenching? *J. Phys. Chem. B* **119**, 13958–13963 (2015).

173. CICHOS, F., VONBORCZYSKOWSKI, C. & ORRIT, M. Power-law intermittency of single emitters. *Curr. Opin. Colloid Interface Sci.* **12**, 272–284 (2007).

174. Moerner, W. E. & Basché, T. Optical Spectroscopy of Single Impurity Molecules in Solids. *Angew. Chemie Int. Ed. English* **32**, 457–476 (1993).

175. Löhner, A., Ashraf, K., Cogdell, R. J. & Köhler, J. Fluorescence-excitation and emission spectroscopy on single FMO complexes. *Sci. Rep.* **6**, 31875 (2016).

176. Swoboda, M. *et al.* Enzymatic oxygen scavenging for photostability without ph drop in single-molecule experiments. *ACS Nano* **6**, 6364–6369 (2012).

177. Dave, R., Terry, D. S., Munro, J. B. & Blanchard, S. C. Mitigating unwanted photophysical processes for improved single-molecule fluorescence imaging. *Biophys. J.* **96**, 2371–2381 (2009).

178. Altman, R. B. *et al.* Cyanine fluorophore derivatives with enhanced photostability. *Nat. Methods* **9**, 68–71 (2012).

179. Cogdell, R. J. *et al.* How carotenoids protect bacterial photosynthesis. *Philos. Trans. R. Soc. London. Ser. B Biol. Sci.* **355**, 1345–1349 (2000).

180. Pereira, M. J. B. *et al.* Single VS Ribozyme Molecules Reveal Dynamic and Hierarchical Folding Toward Catalysis. *J. Mol. Biol.* **382**, 496–509 (2008).

181. Manley, S., Gillette, J. M. & Lippincott-Schwartz, J. Single-Particle Tracking Photoactivated Localization Microscopy for Mapping Single-Molecule Dynamics. in *Methods in Enzymology* **475**, 109–120 (2010).

182. Novoderezhkin, V. I., Rutkauskas, D. & Van Grondelle, R. Dynamics of the emission spectrum of a single LH2 complex: Interplay of slow and fast nuclear motions. *Biophys. J.* **90**, 2890–2902 (2006).

183. Pirchi, M. *et al.* Single-molecule fluorescence spectroscopy maps the folding landscape of a large protein. *Nat. Commun.* **2**, 493 (2011).

184. Tyagi, S. *et al.* Continuous throughput and long-term observation of single-molecule FRET without immobilization. *Nat. Methods* **11**, 297–300 (2014).

185. Fazio, T., Visnapuu, M. L., Wind, S. & Greene, E. C. DNA curtains and nanoscale curtain rods: High-throughput tools for single molecule imaging. *Langmuir* **24**, 10524–10531 (2008).

186. Granéli, A., Yeykal, C. C., Prasad, T. K. & Greene, E. C. Organized arrays of individual DNA molecules tethered to supported lipid bilayers. *Langmuir* **22**, 292–299 (2006).

187. Cisse, I., Okumus, B., Joo, C. & Ha, T. Fueling protein DNA interactions inside porous nanocontainers. *Proc. Natl. Acad. Sci.* **104**, 12646–12650 (2007).

188. Collins, B. E., Ye, L. F., Duzdevich, D. & Greene, E. C. DNA curtains: Novel tools for imaging protein-nucleic acid interactions at the single-molecule level. *Methods Cell Biol.* **123**, 217–234 (2014).

189. Lemke, E. A. *et al.* Microfluidic device for single-molecule experiments with enhanced photostability. *J. Am. Chem. Soc.* **131**, 13610–13612 (2009).

190. Shi, X., Lim, J. & Ha, T. Acidification of the oxygen scavenging system in single-molecule fluorescence studies: In situ sensing with a ratiometric dual-emission probe. *Anal. Chem.* **82**, 6132–6138 (2010).

191. Valeur, B. Molecular Fluorescence. in *digital Encyclopedia of Applied Physics* 477–531 (Wiley-VCH Verlag GmbH & Co. KGaA, 2010). doi:10.1002/3527600434.eap684

192. Rutkauskas, D. *et al.* Restriction enzyme Ecl18kI-induced DNA looping dynamics by single-molecule FRET. *J. Phys. Chem. B* **118**, 8575–8582 (2014).

193. Katiliene, Z., Katilius, E. & Woodbury, N. W. Single molecule detection of DNA looping by NgoMIV restriction endonuclease.

Biophys. J. **84**, 4053–4061 (2003).

194. Pandit, A. *et al.* Assembly of the major light-harvesting complex II in lipid nanodiscs. *Biophys. J.* **101**, 2507–2515 (2011).

SANTRAUKA

Įvadas

Baltymų konformacinė dinamika, atsirandanti dėl baltymų struktūros lankstumo, yra būtina sąlyga sėkmingam paties baltymo ir visos ląstelės funkcionavimui. Konformacinė dinamika leidžia individualiam baltymui prisitaikyti konkrečių funkcijų vykdymui. Paminėtini tokio prisitaikymo pavyzdžiai apima šias funkcijas: 1) skirtingos baltymo konformacinės būsenos pritaikytos skirtingai funkcijai atlikti[1], 2) alosteriniai efektai[2], 3) aktyvacijai skirti struktūros pokyčio sklidimo keliai (katalizė, taikinio atpažinimas, stabilumas ir t.t.), 4) sąveikos partnerių atpažinimas arba atmetimas[3]. Konformacinė baltymų dinamika leidžia ląstelėms reaguoti į aplinkos sąlygų pokyčius. Tokio reguliavimo žinomas pavyzdys yra nefotocheminio gesinimo (NPQ) reiškinys, kurio metu augalų šviesą sugeriančių baltyminių pigmentinių kompleksų (LHCs) konformacinė dinamika yra tiesiogiai pasitelkiama sistemos adaptacijos prie skirtingų apšvitos sąlygų reguliavimui[4].

Kiekvienas baltymas, nepaisant to, ar jis yra membranoje įsiterpęs (membraninis), ar randamas ląstelės citozolyje (vandenyje tirpus), konkrečių funkcijų vykdymui adaptuoja įvairias galimas konformacines struktūras. Minėtos baltymų klasės skiriasi priklausomai nuo jų natūralios aplinkos ir nuo ląstelėje atliekamų funkcijų. Šiame darbe mes pasirinkome tyrinėti šiuos minėtų baltyminių klasių atstovus: transmembraninius baltyminius pigmentinius kompleksus iš antrosios fotosistemos (LHCII) ir vandenyje tirpius baltymus sąveikaujančius su nukleorūgštimis – DNR Restrikcijos endonukleazes (REases). Pirma, LHCII yra pagrindiniai šviesą sugeriantys fotosintetiniai kompleksai, esantys žaliųjų augalų tilakoidų membranose, kurie yra esminiai minėto NPQ proceso reguliatoriai. Antra, REases yra tipiškai randamos bakterijų citozolyje, kur atlieka apsaugos prieš virusus funkciją. Šiame darbe pristatomoje literatūros apžvalgoje pateikiama abiejų minėtų baltymų klasių pavienių molekulių (SM) lygio tyrimų pasiekimai. Taip pat pristatomos dabartinės mokslo žinios, kurias pavyko pasiekti SM lygio tyrimais.

Konformacinės dinamikos ir individualių LHCII kompleksų fluorescencijos kitimo ryšys buvo ne kartą pademonstruotas[12]. LHCII karotenoidų sudėties įtaka šio komplekso fluorescencijos kitimui (taipogi ir konformacinei dinamikai) yra labai minimali. Todėl mes nusprendėme pasitelkti ypač jautrią pavienių molekulių TIRF mikroskopiją iki šiol SM lygyje netyrinėtiems LHCII mutantams, kurie nefluorescuoja ir dėl šios priežasties yra sunkiai išmatuojami kitais SM metodais. Taip pat mes atlikome bendrus SM ir ansamblio lygio matavimus, kurie leido ištirti periferinio LHCII karotenoido molekulės rolę fluorescencijos gesinimui pakeitus pH ir detergento koncentracijos vertes (t. y. keičiant apšvitos sąlygas).

Yra daug mokslinių publikacijų, kuriose pristatoma SM lygio su DNR sąveikaujančių baltymų tyrimų rezultatai, kurie sėkmingai leido atskleisti jų konformacinę dinamiką. Tačiau kompleksiškesni, su DNR sąveikaujantys baltymai, susidedantys iš kelių domenų arba turintys daug skirtingų būsenų yra vis dar neužtektinai ištyrinėti. Tyrimams dažniausiai trukdo sunkumai, kylantys atliekant šių baltymų žymėjimą, bei jų tyrimai, reikalaujantys labiau specifinių metodų. Šiame darbe mes parodėme, kad vienu metu atliekamas dviejų SM lygio signalų matavimas leidžia atskleisti seniau paslėptą, su DNR sąveikaujančių baltymų ir DNR komplekso dinamiką. Pirma, mes tyrėme DNR ir Ecl18kI restrikcijos endonukleazės komplekso dinamiką. Šių tyrimų rezultatai atskleidė tris galimas DNR ir baltymo komplekso konformacijas ir su jomis susijusią dinamiką[13]. Antra, mes ištyrinėjome tetramerinės restrikcijos endonukleazės NgoMIV ir DNR sąveiką. Šie tyrimai parodė, kad NgoMIV baltymas sąveikauja su DNR labai heterogeniškai ir sąveikos dinamika priklauso nuo baltymo koncentracijos[14].

Baltymų konformacinė dinamika susieja biologiją su fizika[5], ypač – su SM fluorescecncijos (SMF) spektroskopija. Šie metodai yra reikšmingi, nes baltymų konformacinė dinamika paprastai yra sunkiai išskiriama kitokiuose matavimuose dėl ansamblio vidurkinimo. Taigi, darytina išvada, kad ši dinamika gali būti stebima tik pasitelkiant SM metodus. Įvairūs fluorescencija paremti metodai buvo išvystyti biomolekulių dinamikos matavimams nanoskalėje. SM Forsterio rezonansinės energijos pernašos (smFRET) metodo pritaikymas biomolekulių dinamikos tyrimams buvo pats sėkmingiausias, praplėtęs daugelio biologinių sistemų supratimą[6]. Taip pat buvo išvystytos ir kitos molekulinės „liniuotės“, leidžiančios tirti biomolekulių dinamiką vykstančią ir trumpesniuose atstumuose, ne tik tuose, kurie pasiekiami naudojant FRET metodą. Tarp jų tai – baltymo indukuojamas fluorescencijos stiprinimas (PIFE), fluorescencijos gesinimas arba tamsiuoju gesikliu arba metalo jonais[7]. Taip pat kitomis fluorescencijos savybėmis paremti metodai, tokie kaip poliarizacinė SMF detekcija, buvo išvystyti ir sėkmingai pasitelkti stebėti biomolekulių dinamiką[8]. Visi šie metodai reikalauja biomolekulių žymėjimo ir tai nėra triviali užduotis[9]. Kiti baltymai, tokie kaip LHCII, yra natūraliai fluorescuojantys ir ši jų savybė buvo daug kartų pasitelkta tiriant šių baltymų elgseną SM lygyje[10,11].

Šiame darbe mes atlikome minėtus LHCII ir DNR-baltymų sąveikos matavimus bei papildomai išvystėme du naujus metodus, skirtus tirti transmembraniniams baltymų ir pigmentų kompleksams, taipogi su DNR sąveikaujantiems baltymams. Pirmasis metodas leido tirti liposomoje įsiterpusius LHCII kompleksus vienos liposomos lygyje[15]. Ši metodologija yra pažangesnė už seniau tokiems tyrimams taikytą metodiką tuo, kad leidžia patikrinti, ar matuojamas LHCII kompleksas yra tikrai įsiterpęs į liposomą[16]. Ji taip pat leidžia imobilizuoti proteoliposomas ant modifikuoto stiklo paviršiaus nedarant neigiamos įtakos pačioms liposomoms ar baltymams bei leidžia tiesiogiai išmatuoti kiekvienos individualios liposomos dydį. Antras metodas, kurį išvystėme šiame darbe, leido imobilizuoti biotinilintas DNR molekules ant paviršinių struktūrų – nanometrinių matmenų streptavidino linijų, suformuotų ant dengiamojo stiklelio paviršiaus – ir ištiesti jas visu ilgiu naudojant buferio tėkmę. Taikyta metodologija palengvino SM lygio DNR ir baltymų sąveikos vizualizaciją. Šiame darbe pateikiama apžvalga taip pat yra skirta ir metodologiniams proveržiams, susijusiems su mikroskopijos sistemomis bei bandinių paruošimu. Į darbe pateikiamą literatūros apžvalgą taip pat yra įtraukta ir iki šiol išvystytų bei mūsų darbe konkrečiai naudotų SMF metodų aptarimas.

Mūsų pavienių baltyminių pigmentinių kompleksų ir su DNR sąveikaujančių baltymų konformacinės dinamikos tyrimų rezultatai suteikė esminių įžvalgų. Taip pat abu iš mūsų išvystytų metodų buvo sėkmingai pritaikyti ir bus naudingi tolimesniems įvairių su DNR sąveikaujančių baltymų ir kitų pigmentinių baltyminių kompleksų tyrimams. Vertinant pasiektus rezultatus bei galimybes jų tolimesniame taikyme, šio darbo paskutinėje literatūros apžvalgos dalyje pateikiamos mūsų tyrimų srities ateities perspektyvos.

Disertacijos tikslai

Norėdami ištyrinėti ir suprasti konformacinę dinamiką, vykstančią skirtinguose ląsteliniuose procesuose, mes pasirinkome baltymus iš dviejų skirtingų baltymų klasių: transmembraninius baltiminius pigmentinius kompleksus (LHCII) ir citozolines DNR restrikcijos endonukleazes. Šių dviejų baltymų klasių atstovai buvo tyrinėti ansamblio lygyje, bet anksčiau buvo labai mažai arba visai netyrinėti pavienių molekulių lygyje. LHCII pigmentų sudėtis gali turėti įtakos šio baltymo konformacinei dinamikai ir tai, tikėtina, gali turėtų poveikį NPQ vyksmams. Konformaciniai pokyčiai, vykstantys DNR ir restrikcijos endonukleazių kompleksų dinamikoje, yra nevisiškai suprasti ir, gali būti, kad jie skiriasi tarp skirtingų restrikcijos endonukleazių tipų. Taigi, šio darbo tikslai yra tokie:

- Išsiaiškinti galimą karotenoidų vaidmenį LHCII fluorescencijos gesinimo procesuose;
- Atskleisti ir charakterizuoti dviejų skirtingų tipų DNR restrikcijos endonukleazių kompleksų sudaromų su DNR dinamiką pavienių molekulių lygyje.

Disertacijos uždaviniai

Tyrimuose galima pritaikyti panašų matavimo metodą – SMF mikroskopiją, tačiau mums reikia skirtingų bandinio paruošimo metodikų skirtingiems eksperimentams. LHCII tyrimams mes naudojame baltymo ištirpinimą detergente ir įterpimą į liposomas, o DNR restrikcijos endonukleazėms – DNR substrato, turinčio du REases taikinius, žymėjimą fluoroforais ir imobilizaciją ant paviršiaus. Norint pasiekti anksčiau nustatytus disertacijos tikslus, nustatomi tokie uždaviniai:

○ Išvystyti ir pasinaudoti pavienių molekulių fluorescencinės mikroskopijos metodais siekiant ištirti LHCII, turinčio įvairias karotenoidų sudėtis, konformacinę dinamiką detergento aplinkoje;

○ Išvystyti ir pritaikyti pavienių molekulių fluorescencinės mikroskopijos metodus, leidžiančius atskleisti ir charakterizuoti DNR ir baltymo sudaromo komplekso dinamiką dviejų skirtingų tipų restrikcijos endonukleazėms.

Ginamieji teiginiai

○ Vienu metu vykstantis FRET ir pririšto fluoroforo judėjimo signalų sekimas mums leido atskleisti iki šiol paslėptą DNR ir baltymo komplekso dinamiką dviem skirtingo tipo DNR restrikcijos endonukleazėms;

○ LHCII karotenoidų sudėtis periferijoje neturi įtakos nei gesinimo efektyvumui nei conformacinei dinamikai. Tačiau, LHCII mutantas, turintis zeaksantiną kaip vienintelį karotenoidą, rodė pakitusią konformacinę dinamiką bei buvo stipriai prigesintas;

○ SMF mikroskopijos metodai ir fluorescentiškai žymėtų LHCII proteoliposomų paviršiaus imobilizacija mums leido atskleisti žymų kiekį LHCII, kuris lieka neįsiterpęs į liposomas bei platų LHCII tankio proteoliposomose heterogeniškumą.

Darbo naujumas ir aktualumas

Moksliniuose darbuose ir tyrimuose jau yra išvysta įvairių fluorescencija paremtų metodų, skirtų matuoti biomolekulių dinamiką. Pavyzdžiui, su DNR sąveikaujantys baltymai buvo intensyviai tyrinėjami naudojantis pavienių molekulių FRET metodu. Tačiau įvairių signalų, matuojamų pavienių molekulių lygyje, naujos kombinacijos dar ir dabar padeda atskleisti iki šiol paslėptas tokio tipo baltymų dinamikas. LHCII ir kiti pigmentiniai baltyminiai kompleksai buvo tyrinėjami pavienių molekulių lygyje naudojantis konfokaline mikroskopija ir esant santykinai intensyviam žadinimui. Tačiau iki šiol praktiškai nebuvo atlikta tyrimų, kuriuose LHCII būtų buvęs tyrinėtas naudojant pavienių molekulių TIRF mikroskopiją. Ši mikroskopijos sistema yra naudinga tuo, kad turi ypač aukštą signalo ir triukšmo santykį, o tai leidžia tyrinėti netgi ypač stipriai prislopintus pigmentinius baltyminius kompleksus, esant santykinai žemam žadinimo intensyvumui. Bendrai, mūsų tiriamiesiems baltymams galime pritaikyti panašų matavimo metodą – SMF mikroskopiją, bet mums reikia skirtingų bandinio paruošimo metodų kiekvienam skirtingam eksperimentui. Taigi, darbo naujumas parodomas pasitelkiant šiuos teiginius:

○ Tirti LHCII konformacinei dinamikai pavienių molekulių lygyje, esant labai žemam žadinimo intensyvumui, šiame darbe buvo pirmą kartą pasitelkta TIRF mikroskopija. Šie eksperimentai mums leido atskleisti naują karotenoidų daromos įtakos baltymo konformacinei dinamikai efektą.

○ Tyrimo metu buvo išvystytas naujas metodas – kombinacija smFRET ir pririšto fluoroforo judėjimo evanescenciniame lauke. Šis metodas buvo pritaikytas tirti DNR ir Ecl18kI REases komplekso dinamikai, kas mums leido atskirti visas įmanomas DNR ir Ecl18kI komplekso konformacijas ir jų kitimo dinamiką. Panaši strategija buvo pirmąsyk pritaikyta siekiant atskleisti skirtingas NgoMIV Reases ir DNR dinaminės sąveikos modas.

Metodika

Šiame darbe buvo patelktos dvi fluorescencinės mikroskopijos rūšys: objektyvo tipo visiško vidaus atspindžio ir įprastas skenuojantis konfokalinis. Taip pat darbe buvo pritaikyti arba išvystyti net keli bionanotechnologiniai metodai: DNR žymėjimas FRET dažiklių pora ir jos biotinilinimas, DNR imobilizacija ant silanizuoto ir PEGilizuoto stiklo paviršiaus per Neutravidiną, t.t. Be to, darbe buvo išvystyti ir duomenų analizės metodai, skirti pavienių molekulių signalų nustatymui iš mikroskopijos vaizdų, bei jų chrakterizavimui.

Diskusija ir išvados

Fluorescencinės mikroskopijos metodų vystymasis yra svarbus kitoms tyrimų kryptims – biotechnologijai, molekulinei biologijai, biochemijai. Šie metodai taip pat yra pritaikomi siekiant suprasti fundamentines gyvybės mokslų problemas, pastebėtina, kad jie tam ypač tinka, nes yra biologiškai nežalingi, suteikiantys galimybes tirti bandinį neinvaziniu būdu ir realiu laiku[191].

Šiame tekste pristatomi darbai yra skirti baltymų konformacinės dinamikos tyrimams. Baltymus pasirinkome iš dviejų skirtingų sričių: vandenyje tirpūs (citozoliniai) su DNR sąveikaujantys baltymai ir transmembraniniai (vandenyje netirpūs) fotosintetiniai pigmentiniai baltyminiai kompleksai. Mūsų tyrimuose abiejų šių klasių atstovai buvo tyrinėti taikant SM metodus. Be baltymų konformacinės dinamikos tyrimų, šiame darbe mes taip pat išvystėme naują technologiją ir pritaikėme du naujus metodus. Išvystytoji technologija yra naudinga nustatant su DNR sąveikaujančių baltymų dinamiką bei elgseną SM lygyje. Pirmasis iš išvystytų metodų yra pritaikomas tirti su DNR sąveikaujančių baltymų kompleksų konformacinę dinamiką ir kitas sąveikos savybes. Antrasis iš metodų buvo pritaikytas tirti tikrai į liposomas įterptus LHCII bei ateityje gali pasitarnauti tiriant kitus pigmentinius baltyminius kompleksus.

Per paskutinius 20 metų smFRET metodas tapo pagrindiniu įrankiu siekiant nustatyti biomolekulių konformacinę dinamiką, jis buvo ypač plačiai pritaikomas tiriant su DNR sąveikaujančių baltymų konformacinę dinamiką[24,27]. Šiuo metu, norint gauti daugiau informacijos apie tyrinėjamą biologinę molekulinę sistemą, yra bandoma pasitelkti kelių pavienių molekulių lygio signalų (pvz. smFRET ir SM anizotropija) matavimus. Šie kombinuoti metodai buvo naudingi siekiant atskirti skirtingas biomolekulių populiacijas, esančias viename mėginyje, arba skirtingas reakcijos tarpines grandis. Procesas buvo taikomas tiek su imobilizuotomis tiek su laisvai difunduojančiomis biomolekulėmis.

Šiame darbe, siekdami ištyrinėti Ecl18kI su DNR sudaromo komplekso dinamiką, mes pirmąkart panaudojome tokio tipo vienu metu vykstančių dviejų signalų iš pavienių molekulių registravimą. Šie du signalai buvo smFRET ir prie DNR pririšto fluoroforo judėjimas evanescenciniame lauke[13]. Minėtuose eksperimentuose mes, naudodami biotino ir netravidino sąveiką, imobilizavome FRET pora pažymėtas biotinilintas DNR molekules, turinčias du REases prisijungimo taikinius, ant modifikuoto stiklo paviršiaus. Tirpale esant Ca^{2+} jonams, Ecl18kI grįžtamai ir pasikartojančiai jungėsi prie DNR, o ši sąveika lėmė DNR kilpos susidarymą. Šis baltymas, atpažindamas palindorminę DNR seką, suformuodavo dviejų tipų kilpas (lygiagrečią ir nelygiagrečią). Mūsų išvystyta technologija leido atskleisti visas skirtingas galimas DNR ir baltymo komplekso konformacijas bei su jomis susijusias kinetikas, kurios anksčiau buvo neprieinamos[192].

Mes taip pat atskleidėme DNR ir NgoMIV (stabilus tetrameras) sudaromo komplekso dinamiką SM lygyje[14]. Šiems eksperimentams mes pasitelkėme strategiją, kuri buvo panaši į jau naudotą Ecl18kI eksperimentuose. Ankstesnės šio baltymo konformacinės dinamikos studijos buvo atliktos taip pat SM lygyje, tačiau jos nesuteikė detalesnio supratimo[193]. Tai galėjo sąlygoti problemos, susijusios su baltymo agregacija. Šis baltymas gali suformuoti vieno tipo DNR kilpą, bet, nepaisant to, mūsų eksperimentuose buvo stebima du skirtingi FRET efektyvumo lygiai ir bent jau dviejų tipų dinamikos – greita ir lėta. Šis heterogeniškumas buvo susietas su galimybe ant vienos DNR molekulės turėti du veikiančius NgoMIV baltymus – vienas prisijungia abu taikinius ir taip suformuoja DNR kilpą, o kitas, ieškodamas laisvo taikinio, skenuoja DNR. Tai mums leido suformuoti **pirmąjį disertacijos teiginį**: vienu metu vykstantis FRET ir pririšto fluoroforo judėjimo signalų sekimas mums leido atskleisti iki šiol paslėptą DNR ir baltymo komplekso dinamiką dviem skirtingo tipo DNR restrikcijos endonukleazėms.

Nuo pirmų dienų SMF metodai buvo pasitelkiami tyrinėjant įvairius pigmentinius baltyminius kompleksus iš fotosintezę vykdančių sistemų[140]. LHCII baltymas, kuris yra esminis NPQ proceso dalyvis, taip pat buvo tirtas SM lygiu. Tačiau TIRF mikroskopija iki šiol niekad nebuvo pasitelkta šio baltymo tyrimams SM lygiu. Šiame darbe mes tyrėme laukinio tipo LHCII ir keletą jo mutantinių versijų (skirtingos pigmentų sudėties), ištirpintų detergente ir imobilizuotų ant stiklo paviršiaus. TIRF mikrsokopija, lyginant su skenuojančia konfokaline, yra geresnė, nes leidžia pasiekti aukštesnį signalo ir triukšmo santykį bei suteikia galimybę registruoti duomenis lygiagrečiu būdu. Mūsų tyrimų rezultatai parodė, kad skirtingi karotenoidai turi įtakos konformacinei baltymo dinamikai, bei vidutiniam baltymo fluorescencijos intensyvumui. Tačiau tamsinės konformacijos savybės liko nepakitusios.

Taip pat buvo neištirta, ar karotenoidai, esantys LHCII komplekso periferijoje, dalyvauja fluorescencijos gesinimo procese. Anksčiau vykdyti SM lygio tyrimai parodė žymų gesinimą, bet juose nebuvo atliktas gesinimo efekto palyginimas, pasiekiamas ansamblio ir SM lygio matavimuose. Taip pat tuose eksperimentuose bandinys nebuvo ypač grynas. Šiame darbe mes palyginome Vio ir Zea praturtintų LHCII SM ir ansamblio lygių matavimų rezultatus. Šis palyginimas atskleidė, kad gesinimo efektas, pasiekiamas ansamblio matavimuose, yra didesnis nei SM lygio matavimuose. Gautų rezultatų skirtumas yra sietinas su tuo, kad ansamblio matavimuose LHCII yra neimobilizuoti ir todėl, siekiant pamatyti gesinimo efektą, gali suformuoti agregatus, o SM lygio matavimuose LHCII yra imobilizuoti ir šiuo atveju agregatai nesusidaro. Ansambliniai matavimai atskleidė, kad gesinimo indukcijos kinetikos yra greitesnės Zea praturtintam LHCII nei Vio praturtintam, bet pasiekiamas gesinimo efektyvumas abiem bandiniams yra vienodas. Greitesnės gesinimo indukcijos kinetikos tikriausiai atsiranda dėl greitesnės Zea praturtintų LHCII agregacijos. Šie rezultatai mums leido suformuoti **antrąjį disertacijos teiginį**: karotenoidai, esantys LHCII baltymo viduje, turi įtakos šio baltymo konformacinei dinamikai. Kita vertus, karotenoidai, esantys LHCII baltymo išorinėje dalyje, neturi įtakos jo konformacinei dinamikai, bet gali turėti poveikį kontroliuojant LHCII agregaciją.

Iki šiol buvo keletas publikuotų tyrimų, susijusių su LHCII esančių panašioje į natūralią terpę (liposomos, nanodiskai ir pan.) aplinkoje. Tokie tyrimai yra naudingi, nes leidžia kontroliuoti lipidų sudėtį, baltymų ir lipidų santykį, membranos kreivumą, pH gradiento efektą. Pirmasis toks publikuotas rezultatas buvo gautas nagrinėjant LHCII, esantį nanodiskuose[194]. SMF matavimai parodė, kad LHCII tokiuose nanodiskuose yra natūralios būsenos. Antrasis rezultatas buvo gautas patalpinus LHCII liposomose, kas suteikė galimybę tirti LHCII kiekį vienoje liposomoje[16]. Šiuose tyrimuose buvo parodyta, kad LHCII, esantys liposomose, turinčiose mažą baltymų ir lipidų santykį, turi panašią į natūralią būseną. Kaip bebūtų, šiuose eksperimentuose liposomos nebuvo žymėtos ir todėl nebuvo aišku, ar tirti LHCII yra išties įsiterpę į liposomas. Šiame darbe mes parodėme, kad tokie LHCII proteoliposomų bandiniai, net ir po gradientinio centrifugavimo, turi gana daug į liposomas neįsiterpusių LHCII baltymų[15], todėl atliekant tokius tyrimus yra kritiškai svarbu įvertinti baltymų ir liposomų kolokalizaciją. Taip pat paviršiaus modifikacija, naudota anksčiau publikuotame darbe, galėjo turėti įtakos liposomų stabilumui bei deformacijai, o tai galėjo turėti įtakos galutinių matavimų rezultatams. Tai mums leido suformuoti **trečiąjį disertacijos teiginį:** SMF mikroskopijos metodai ir fluorescentiškai žymėtų LHCII proteoliposomų paviršiaus imobilizacija mums leido atskleisti žymų kiekį LHCII, kuris lieka neįsiterpęs į liposomas, bei platų LHCII tankio proteoliposomose heterogeniškumą.

Publikacijos darbo tema

1. M. Tutkus, T. Marčiulionis, G. Sasnauskas, D. Rutkauskas. DNA-Endonuclease Complex Dynamics by Simulataneous FRET and Fluorophore Intensity in Evanescent Field. Biophysical Journal, 2017, 112 (5), 850-858.
2. M. Tutkus, G. Sasnauskas, D. Rutkauskas. Probing the dynamics of restriction endonuclease NgoMIV-DNA interaction by single-molecule FRET. Biopolymers, 2017, 107 (12), e23075.
3. M. Tutkus, J. Chmeliov, D. Rutkauskas, A. V. Ruban, L. Valkunas. Influence of the Carotenoid Composition on the Conformational Dynamics of Photosynthetic Light-Harvesting Complexes. J. Phys. Chem. Lett., 2017, 8 (23), 5898-5906.
4. M. Tutkus, P. Akhtar, J. Chmeliov, F. Gorfol, G. Trinkūnas, P. H. Lambrev, L. Valkunas. Fluorescence Microscopy of Single Liposomes with Incorporated Pigment-Proteins. Langmuir, 2018, 34 (47), 14410-14418.
5. M. Tutkus, F. Saccon, J. Chmeliov, O. Venckus, I. Čiplys, A. V. Ruban, L. Valkunas. Single-molecule microscopy studies of LHCII enriched in Vio or Zea. BBA-Bioenergetics, 2019, just accepted manuscript.
6. M. Tutkus, T. Rakickas, A. Kopūstas, Š. Ivanovaitė, O. Venckus, V. Navikas, M. Zaremba, E. Manakova, R. Valiokas. Fixed DNA

Molecule Arrays for High-Throughput Single DNA-Protein Interaction Studies. Langmuir, 2019, 35 (17), 5921-5930.

Autoriaus indelis:

Šio darbo autorius yra eksperimentatorius. Jis buvo atsakingas už DNR ruošimą, paviršiaus paruošimo darbus, duomenų surinkimą ir analizę bei dalyvavo rašant mokslines publikacijas. Baltymai naudoti šiuose eksperimentuose buvo suteikti mūsų kolegų iš Vilniaus Universiteto, Queen Mary Universiteto Londone ir Szegedo „Biological research center“.

Autoriaus publikacijos neįtrauktos į disertaciją:

1. M. Li, S. K. Jorgensen, D. G. G. McMillan, L. Krzeminski, N. N. Daskalakis, R. H. Partanen, M. Tutkus, R. Tuma, D. Stamou, N. S. Hatzakis, L. J. C. Jeuken. Single Enzyme Experiments Reveal a Long-Lifetime Proton Leak State in a Heme-Copper Oxidase. JACS, 2015.

Šio darbo rezultatai buvo pristatyti šiose konferencijose:

1. Lithuanian national physics conference 2015, Vilnius. Oral presentation “Restriction enzyme Ecl18kI induced DNA looping dynamics studied at the single-molecule level by TIRF FRET microscopy”.
2. FizTech conference 2015, Vilnius. Oral presentation: “Tethered fluorophore motion in the evanescent field combined with FRET reveals dynamics of parallel and anti-parallel DNA loop formation by Ecl18kI restriction endonuclease at the single-molecule level”.
3. EMBO course “Single molecule and single cell fluorescence Å/nm/µm/mm-scopy”, 2015, Heidelberg. Poster presentation: “Restriction enzyme Ecl18kI induced DNA looping dynamics studied at the single-molecule level by TIRF FRET microscopy”.
4. The Swiss NanoConvention, 2016, Basel. Poster presentation: “Revealing parallel and anti-parallel DNA loop dynamics by simultaneous monitoring of FRET and TFM in evanescent field”.
5. FizTech conference 2016, Vilnius. Oral presentation: “Studies of transmembrane light-harvesting protein complexes in native-like and artificial environment using single-molecule microscopy”.
6. Lithuanian national physics conference 2017, Vilnius. Oral presentation “Single-molecule fluorescence and FRET microscopy for DNA-protein interaction studies”.
7. 19-th IUPAB and 11-th EBSA congress 2017, Edinburgh. Poster presentation: ‘Studies of transmemebrane LH complexes in a

natural-like environment at the single-liposome level".

8. QUEBS conference, 2018, Vilnius. Oral presentation: "Single-molecule fluorescence and FRET microscopy for DNA-protein interaction studies".
9. Apropos 16 conference, 2018, Vilnius. Oral presentation: "DNA curtains – nanoscale platform for studying of DNA-protein interactions at the single-molecule level".
10. Baltic Biophysics Conference, 2018, Kaunas. Oral presentation: "nanoscale platform for DNA-protein interaction studies at the single-molecule level".
11. 9th young scientists conference (Interdisciplinary research of physical and technological sciences) 2019, Vilnius. Oral presentation: "DNA Curtains – nanoscale platform for DNA-protein interaction studies at the SM level".
12. Single-molecule Sensors and NanoSystems International Conference 2019, Munich. Oral presentation: "Protein lift-off micro-contact printing for fabrication of fixed DNA Curtains platform".

Apie autorių

Marijonas Tutkus gimė 1987 metais Anykščiuose. 2006 metais baigė Anykščių Jono Biliūno gimnaziją. 2010 metais baigė Biofizikos bakalauro studijų programą Vilniaus Universiteto Gamtos mokslų fakultete. 2012 metais baigė Fizikos magistrantūros studijų programą Kopenhagos Universitete. 2014 metais buvo priimtas į doktorantūros studijas Fizinių ir technologijos mokslų centre. 2018 metais stažavosi Bordo Universitete.

About the author

Marijonas Tutkus was born in 1987 in Anykščiai, Lithuania. In 2010 he received his Biophysics bachelor degree at Vilnius University. In 2012 he received his Physics masters degree at Copenhagen University.

LIST OF PUBLICATIONS, AUTHOR'S CONTRIBUTION AND COPIES OF PUBLICATIONS

This thesis is based upon the results that have been published in scientific papers:

1. M. Tutkus, T. Marčiulionis, G. Sasnauskas, D. Rutkauskas. DNA-Endonuclease Complex Dynamics by Simulataneous FRET and Fluorophore Intensity in Evanescent Field. Biophysical Journal, 2017, 112 (5), 850-858.
2. M. Tutkus, G. Sasnauskas, D. Rutkauskas. Probing the dynamics of restriction endonuclease NgoMIV-DNA interaction by single-molecule FRET. Biopolymers, 2017, 107 (12), e23075.
3. M. Tutkus, J. Chmeliov, D. Rutkauskas, A. V. Ruban, L. Valkunas. Influence of the Carotenoid Composition on the Conformational Dynamics of Photosynthetic Light-Harvesting Complexes. J. Phys. Chem. Lett., 2017, 8 (23), 5898-5906.
4. M. Tutkus, P. Akhtar, J. Chmeliov, F. Gorfol, G. Trinkūnas, P. H. Lambrev, L. Valkunas. Fluorescence Microscopy of Single Liposomes with Incorporated Pigment-Proteins. Langmuir, 2018, 34 (47), 14410-14418.
5. M. Tutkus, F. Saccon, J. Chmeliov, O. Venckus, I. Čiplys, A. V. Ruban, L. Valkunas. Single-molecule microscopy studies of LHCII enriched in Vio or Zea. BBA-Bioenergetics, 2019, just accepted manuscript.
6. M. Tutkus, T. Rakickas, A. Kopūstas, Š. Ivanovaitė, O. Venckus, V. Navikas, M. Zaremba, E. Manakova, R. Valiokas. Fixed DNA Molecule Arrays for High-Throughput Single DNA-Protein Interaction Studies. Langmuir, 2019, 35 (17), 5921-5930.

Author's contribution:

The author of this thesis is an experimentalist. He was responsible for surface preparation work, data acquisition and analysis, and participated in writing of scientific papers. In some cases he also contributed in designing of experiments. Proteins used in these experiments were provided by our colleagues from Vilnius University, Queen Mary University in London, and Szeged Biological research center.

Scientific publication that were not included into the thesis:

1. M. Li, S. K. Jorgensen, D. G. G. McMillan, L. Krzeminski, N. N. Daskalakis, R. H. Partanen, M. Tutkus, R. Tuma, D. Stamou, N. S. Hatzakis, L. J. C. Jeuken. Single Enzyme Experiments Reveal a Long-Lifetime Proton Leak State in a Heme-Copper Oxidase. JACS, 2015.

The results of the thesis were presented at the following conferences:

1. Lithuanian national physics conference 2015, Vilnius. Oral presentation “Restriction enzyme Ecl18kI induced DNA looping dynamics studied at the single-molecule level by TIRF FRET microscopy”.
2. FizTech conference 2015, Vilnius. Oral presentation: “Tethered fluorophore motion in the evanescent field combined with FRET reveals dynamics of parallel and anti-parallel DNA loop formation by Ecl18kI restriction endonuclease at the single-molecule level”.
3. EMBO course “Single molecule and single cell fluorescence Å/nm/µm/mm-scopy”, 2015, Heidelberg. Poster presentation: “Restriction enzyme Ecl18kI induced DNA looping dynamics studied at the single-molecule level by TIRF FRET microscopy”.
4. The Swiss NanoConvention, 2016, Basel. Poster presentation: “Revealing parallel and anti-parallel DNA loop dynamics by simultaneous monitoring of FRET and TFM in evanescent field”.
5. FizTech conference 2016, Vilnius. Oral presentation: “Studies of transmembrane light-harvesting protein complexes in native-like and artificial environment using single-molecule microscopy”.
6. Lithuanian national physics conference 2017, Vilnius. Oral presentation “Single-molecule fluorescence and FRET microscopy for DNA-protein interaction studies”.
7. 19-th IUPAB and 11-th EBSA congress 2017, Edinburgh. Poster presentation: ‘Studies of transmemebrane LH complexes in a natural-like environment at the single-liposome level”.
8. QUEBS conference, 2018, Vilnius. Oral presentation: “Single-molecule fluorescence and FRET microscopy for DNA-protein interaction studies”.
9. Apropos 16 conference, 2018, Vilnius. Oral presentation: “DNA curtains – nanoscale platform for studying of DNA-protein interactions at the single-molecule level”.
10. Baltic Biophysics Conference, 2018, Kaunas. Oral presentation: “nanoscale platform for DNA-protein interaction studies at the single-molecule level”.
11. 9th young scientists conference (Interdisciplinary research of physical and technological sciences) 2019, Vilnius. Oral

presentation: “DNA Curtains – nanoscale platform for DNA-protein interaction studies at the SM level”.

12. Single-molecule Sensors and NanoSystems International Conference 2019, Munich. Oral presentation: “Protein lift-off micro-contact printing for fabrication of fixed DNA Curtains platform”.

Biophysical Journal
Article

Biophysical Society

DNA-Endonuclease Complex Dynamics by Simultaneous FRET and Fluorophore Intensity in Evanescent Field

Marijonas Tutkus,[1] Tomas Marciulionis,[1] Giedrius Sasnauskas,[2] and Danielis Rutkauskas[1,*]
[1]Institute of Physics, Center for Physical Sciences and Technology, Vilnius, Lithuania; and [2]Institute of Biotechnology, Vilnius University, Vilnius, Lithuania

ABSTRACT The single-molecule Förster resonance energy transfer (FRET) is a powerful tool to study interactions and conformational changes of biological molecules in the distance range from a few to 10 nm. In this study, we demonstrate a method to augment this range with longer distances. The method is based on the intensity changes of a tethered fluorophore, diffusing in the exponentially decaying evanescent excitation field. In combination with FRET it allowed us to reveal and characterize the dynamics of what had been inaccessible conformations of the DNA-protein complex. Our model system, restriction enzyme Ecl18kI, interacts with a FRET pair-labeled DNA fragment to form two different DNA loop conformations. The DNA-protein interaction geometry is such that the efficient FRET is expected for one of these conformations—“antiparallel” loop. In the alternative “parallel” loop, the expected distance between the dyes is outside the range accessible by FRET. Therefore, “antiparallel” looping is observed in a single-molecule time trajectory as discrete transitions to a state of high FRET efficiency. At the same time, transitions to a high-intensity state of the directly excited acceptor fluorophore on a DNA tether are due to a change of its average position in the evanescent field of excitation and can be associated with a loop of either “parallel” or “antiparallel” configuration. Simultaneous analysis of FRET and acceptor intensity trajectories then allows us to discriminate different DNA loop conformations and access the average lifetimes of different states.

INTRODUCTION

In the recent past, fluorescence microscopy of single molecules has become a common mode of experimentation to study molecular interactions and conformational changes, where the unsynchronized behavior of many molecules renders the conventional ensemble measurements insufficient (1,2). Among the different single-molecule (SM) microscopy techniques the Förster resonance energy transfer (FRET) approach is one of the most fruitful (3–5). In a smFRET experiment, a biomolecule of interest is labeled with a donor and an acceptor fluorophore at specific sites. Because the FRET efficiency (E_{FRET}) depends on the distance between the fluorophores according to $E_{FRET} = 1/(1 + (R/R_0)^6)$, changes of the distance translate into changes of measurable spectroscopic quantities, such as the ratio of acceptor and donor intensities (6). R_0 (the Förster radius), depending on the combination of the donor and acceptor labels, is 5–7 nm (7), implying that the interval of interdye distances that can be probed by FRET is in the range from a few to ~10 nm. This range was extended to shorter distances by exploiting the phenomenon of self-quenching of identical fluorophores (8), quenching by radical (9), quenching through the electron transfer with a tryptophan or tyrosine residue (10,11), or the protein-induced fluorescence enhancement (PIFE) (12). FRET was also combined with PIFE to gain a concomitant information about molecular interactions on different distance scales (13). There were also attempts of nanoscopic ruling at distances exceeding the upper FRET limit by using the interaction of two metallic nanoparticles (14) or a metallic particle and a fluorophore (15). A relatively simple alternative to the latter approaches to study the large-scale conformational changes of surface-immobilized biomolecules is the tethered particle motion (TPM) technique (16). In a regular TPM, a single nano- or microparticle is tethered by the target molecule to the surface and the radius of diffusion of this particle serves as an indicator of the molecular conformation. To eliminate the distorting particle effects on biomolecular interaction this method was elaborated by

---

Submitted September 15, 2016, and accepted for publication January 24, 2017.

*Correspondence: danielis@ar.fi.lt

Editor: Anatoly Kolomeisky.
http://dx.doi.org/10.1016/j.bpj.2017.01.017

substituting the particle with a fluorophore (tethered fluorophore motion—TFM) to observe the changes of the width of the fluorescence image (17). In our study, we exploit a different aspect of the TFM approach, namely, the dependence of the excitation intensity of a fluorophore on its position in the axial direction (18). In the TFM scheme, fluorophores of surface-immobilized biomolecules are excited by the evanescent electromagnetic field created by the total internal reflection (TIR) of the laser light off the glass-water interface (19). Because the intensity of this field decays exponentially with the distance from the glass surface with the exponent factor being of the order of a few hundreds of nanometers, only a shallow near-surface layer is excited, thus ensuring a better signal-to-noise ratio compared with a regular wide-field excitation (20). At the same time, this exponential field strength distance-dependence implies that the rate of excitation of a fluorophore should depend on its distance from the surface. We exploit this fact with the aim of augmenting the range of molecular distances accessible to FRET and demonstrate that in combination with FRET it can be utilized to discriminate different DNA-protein complex conformations. Because many proteins exist that mediate the site-specific DNA looping, monitoring the dynamics of formation of the different loop conformations in these systems is of potential interest. Moreover, because the proposed method is a natural add-on to a regular TIR fluorescence microscope, it could be an obvious choice for a researcher studying complex dynamics of DNA-protein interactions.

MATERIALS AND METHODS

Protein and DNA fragments

Ecl18kI was purified as described previously (21). Protein concentrations are expressed in terms of dimer.

We have synthesized three DNA fragments with different distances between Ecl18kI recognition sequences: 247, 514, and 1000 bp. The scheme for the fragment synthesis was the same as described previously (22), and the specific details are provided in the Supporting Material. In short, FRET-pair-labeled DNA fragments were synthesized using labeled primers in the PCR. This guaranteed a complete specificity of labeling at respective positions in a DNA fragment.

Sample preparation

The sample chamber was assembled from a six-channel Sticky-Slide VI 0.4 (Ibidi, Planegg, Germany) and a PEG-coated cover slip (Menzel Glaser, Braunschweig, Germany). The procedure of the cover slip modification with PEG derivatives was adapted from Diao et al. (23) The sample chamber was incubated with 5 μg/mL of neutravidin (A-26666, Molecular Probes, Waltham, MA) in the reaction buffer (RB) (33 mM Tris (pH 7.9) at 20°C, 66 mM K-acetate, 1.5 μM BSA) for 3 min, washed with RB, incubated with 1–10 pM DNA in RB for 3 min, and washed with RB. For the measurement of the DNA-protein interactions the cell was infused with 4 nM Ecl18kI in the RB supplemented with 10 mM of $CaCl_2$, 15 units/mL of glucose oxidase (G6125, Sigma-Aldrich, Taufkirchen, Germany), 1% of glucose (G0047, TCI Europe, Zwijndrecht, Belgium), 120 units/mL of catalase (C9322, Sigma-Aldrich), and 2.5 mM of UV-treated Trolox (238813, Sigma-Aldrich).

Single-molecule data acquisition

The objective-type total internal reflection fluorescence (TIRF) microscope (7) with alternating laser excitation (ALEX) (24) was used for single-molecule fluorescence movie acquisition (the optical scheme of the setup is presented in Fig. S1). In short, 532 and 635 nm laser (Crystalaser, Reno, NV) beams were combined by a dichroic mirror zt532rdc-UF2 (Chroma, Bellows Falls, VT), expanded 13×, and guided into an oil-immersion objective (100×, NA 1.4, Nikon, Tokyo, Japan). Laser powers were ~2 mW after the objective. To improve the uniformity of the field of excitation, the laser beam was raster-scanned before the expanding telescope. ALEX was achieved by interlocking lasers with TTL. The fluorescence was filtered with the quadruple-band interference filter FF01-446/510/581/703 (Semrock, Rochester, NY), split by T640lpxr-UF2 (Chroma), and imaged onto EMCCD (DU-897E-CS0-UVB, Andor, Belfast, UK) with 100 ms integration time. The magnification of the fluorescence image on EMCCD was 150×.

Data analysis

In microscopy movies, fluorescent molecules were identified and intensity trajectories extracted using the custom analysis package (available upon request) written in Igor Pro (Wavemetrics, Portland, OR). Acceptor and donor channels were aligned using image registration coefficients (*x*/*y* shift, *x*/*y* skewing) calculated from a reference image. Fluorescence movies with ALEX were acquired with the first image under the 635 nm excitation. To identify immobilized FRET-pair-labeled DNA, first, an image was obtained by averaging 10 frames from the beginning of an image series. The average donor channel image was created from images with the 532 nm excitation, and the average acceptor image was created from images with the 635 nm excitation. Both images were filtered to enhance fluorescent spots and converted to images of fluorescent spot probabilities (25). Spots with probability above a set value were fit with a two-dimensional (2D) symmetrical Gaussian function $f(x,y) = Z0 + A \bullet \exp(-(((x - X0)/W)^2 + ((y - Y0)/W)^2))$ to extract precise center positions and widths (Fig. S2). Initial guesses for the 2D Gaussian fit (*x*-center, *y*-center, width) were calculated from an ellipse that best fits each particle from the particle probability image (using the ImageAnalyzeParticles function from Igor Pro). An average of major and minor ellipse axes was the initial guess for the width of the Gaussian. Fits were performed in a square region of interest (ROI) (half-size 5 pixels) centered at the initial guess center position of each spot. Spots with the fitting error for either amplitude or width exceeding 20% of the parameter value were rejected. Further, the colocalization procedure was performed: accepted spots from the donor channel having a corresponding single spot within a defined distance (<3 pixels) in the acceptor channel were identified (Fig. S3). Intensities for all colocalizing spots in every image from the ALEX image series in both channels were extracted using the 2D symmetric Gaussian. A fast signal extraction was achieved by performing the fitting on multiple CPU cores (one core per spot). Unless stated otherwise, the center and width of the Gaussian fit were fixed. The single molecule intensity was expressed as (amplitude) × $(\text{width})^2$ of the Gaussian fit. Three different fluorescence intensity time trajectories were obtained: I_d^{532} (donor), I_a^{532} (acceptor with the 532 nm excitation), and I_a^{635} (acceptor with the 635 nm excitation). The trajectory of E_{FRET} was calculated as $E_{FRET} = I_a^{532}/(I_a^{532} + I_d^{532})$. Time trajectories were screened to exhibit characteristic single-molecule FRET features: clear donor-acceptor anticorrelated intensity changes, a typical single-molecule fluorescence intensity, and a single bleaching step.

For transition densities and kinetic analysis, I_a^{635} and E_{FRET} trajectories were idealized using the intensity change point (ICP) detection algorithm with clustering based on (26), except that the amplitude of the ICP is constant. This algorithm scans a trajectory point by point with an eight-point window, takes an average of the first four points and the last four points within the window, and calculates a step amplitude (difference between the averages). In the case the step amplitude is higher than a defined value, the center position of this window is recorded as a putative ICP. To be accepted, an ICP has to fulfill the criteria for the durations and slopes of the states it separates. Both states have to be not shorter than half of the scanning window length. The sum of the absolute slope values of the line fits of the states has to be smaller than a set value. We define the ranges of low and high I_a^{635} and E_{FRET} values. Detected states are clustered: if the average values of the neighboring states are within the same defined range, they are combined by removing the ICP. For I_a^{635} of 1000 bp DNA we have defined three ranges: −0.2 to 0.5 (bleached Cy5 state), 0.5–1.2 (unlooped DNA state), and 1.2–3 (looped state).

Average dwell times for the different DNA states were estimated by the bootstrap averaging.

RESULTS

Our model system is the restriction enzyme Ecl18kI. This site-specific endonuclease recognizes a pseudopalindromic DNA sequence 5′-CCNGG-3′ and in the presence of Mg^{2+} ions cuts both DNA strands before the first "C." Substitution of Ca^{2+} for Mg^{2+} precludes the DNA cleavage by Ecl18kI but retains its ability to bind the cognate sequence. Ecl18kI is a homodimer in solution containing a single DNA binding cleft. However, for optimal catalytic activity, two DNA-bound Ecl18kI dimers must associate into a transient tetramer. In the case of a two-site DNA substrate, simultaneous binding of two enzyme dimers to different target sites and their association into a tetramer through conformational DNA diffusion results in a DNA loop (27). Since Ecl18kI is a dimer of two identical subunits and its recognition sequence is symmetric, there can be two different conformations of the protein-DNA complex: the so-called "parallel" and "antiparallel" loop (Fig. 1 *A*) (28).

In our assay, the DNA fragment is labeled with a FRET pair of fluorophores—Cy3 (donor) and Cy5 (acceptor)—18 bp from the respective recognition sequences of Ecl18kI. The labels are at such positions that appreciable FRET is expected upon the formation of the "antiparallel" loop (Fig. 1 *A*). The proper placement of the dye labels on DNA was determined from the crystal structure of the DNA-Ecl18kI complex (22,29) by using the tool for FRET-restrained positioning and screening (30) to simulate the distances between the geometrically accessible volumes (AV) of the two dyes. No FRET is expected in a "parallel" loop configuration where the interdye distance is above the range accessible to FRET (Fig. 1 *A*). In our DNA construct (Fig. 1 *B*), the Cy3 label and the corresponding recognition sequence are more than 200 bp from the surface immobilization point to avoid possible surface interference. The Cy5 label is close to the DNA end distal from the surface and is, therefore, on a tether a few hundreds of nanometers long and can diffuse within the range permitted by the tether. The occurrence of FRET for this construct was previously observed in ensemble experiments (22).

The fluorescence measurements were conducted using the conventional dual-view approach in the TIR mode with ALEX (examples of dual-view images are presented in Fig. S3). Because we used raw signal intensities, E_{FRET} is not the physical FRET efficiency but rather a relative proximity ratio. The I_a^{635} trajectory serves as an independent indicator of the acceptor fluorescence. More importantly, however, it provides the means of accessing the average (during the integration time) position of the fluorophore in the axial direction—the dye is in the evanescent excitation field whose intensity depends in the exponential manner on the distance from the surface as follows:

$$I = I_0 \times \exp(-z/d), \tag{1}$$

where I_0 is the intensity at the surface, z is the distance from the surface, and d is characteristic penetration depth. Consequently, the fluorophore intensity also depends on its distance from the surface. It was expected, therefore, that the

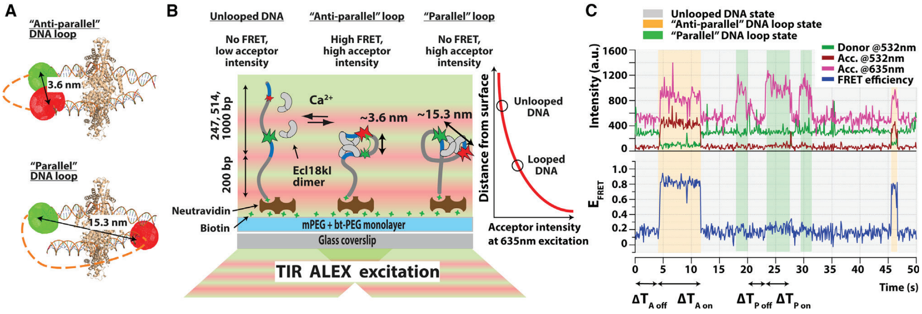

FIGURE 1 (*A*) Ecl18kI tetramer-DNA structure (PBD entry 2GB7) with simulated AV clouds of Cy3 (*green*) and Cy5 (*red*) for "antiparallel" (*top*) and "parallel" (*bottom*) loop conformations. The indicated distances are those between the centers of the AV clouds. DNA extensions with dotted lines denote its topology in the two-loop conformations. (*B*) Experimental scheme of DNA fragment surface-immobilization and excitation through TIR with ALEX is shown; different signals corresponding to various DNA conformations are illustrated. (*C*) Representative single-molecule fluorescence intensity and E_{FRET} time traces in the presence of 4 nM of Ecl18kI and 10 mM of $CaCl_2$ are shown.

measurement of the Cy5 intensity should allow us to monitor looping dynamics since looping of any conformation reduces the effective acceptor tether length and brings it closer to the surface. Thus, the E_{FRET} trajectory contains the dynamics of "antiparallel" loop formation, whereas changes in the I_a^{635} trajectory are associated both with "parallel" and "antiparallel" loops. In combination, the trajectories of E_{FRET} and I_a^{635} should allow us to discriminate the dynamics of different DNA loop conformations.

Fig. 1 *C* illustrates a typical result of the ALEX measurement of Ecl18kI-induced looping of DNA with the 1000 bp intertarget distance. I_d^{532} and I_a^{532} traces exhibit anticorrelated intensity changes characteristic of FRET process (more examples in Fig. S4). Both, E_{FRET} and I_a^{635} display transitions between two levels. The low E_{FRET} of 0.15 ± 0.05 (peak position of the Gaussian fit ± half-width) is associated with unlooped DNA or "parallel" looping and is not equal to zero since even in the absence of FRET, the acceptor is directly excited by the 532 nm excitation and the donor bleads through into the acceptor channel. High E_{FRET} of 0.77 ± 0.07 (peak position of the Gaussian fit ± half-width) is due to the "antiparallel" loop. High E_{FRET} coincides with high I_a^{635}: the acceptor intensity expectedly increases upon "antiparallel" looping. At the same time, high I_a^{635} does not necessarily correspond to high E_{FRET}—the situation indicative of the "parallel" DNA loop.

Verification that the changes of I_a^{635} are due to looping was obtained by performing the measurement on three DNA constructs with different intertarget distances of 1000, 514, and 247 bp (Fig. 2). It was expected that if the observed Cy5 intensity changes were looping-associated then a larger intertarget distance should be connected with a greater effect of the intensity modulation since a larger change of DNA tether length should span more of the evanescent field gradient. Histograms of I_a^{635} from individual traces exhibit two peaks. We fit these intensity distributions with a double Gaussian function to obtain two peak positions: I_L (low intensity, corresponding to unlooped DNA state) and I_H (high intensity, corresponding to the looped state). As control, the I_a^{635} signal recorded in the absence of $CaCl_2$, where the DNA-protein interaction is precluded, shows a stable low intensity (Fig. 2 *A*). To enable collective analysis of I_a^{635} trajectories from different experiments and different locations of the field of view, I_a^{635} signals are normalized to I_L. Then we build 2D histograms of all I_a^{635}/E_{FRET} points from many measured trajectories for the different DNA fragments (Fig. 2 *B*). These plots exhibit three distinct populations: low E_{FRET}/low I_a^{635} (unlooped DNA), low E_{FRET}/high I_a^{635} ("parallel" DNA loop), and high E_{FRET}/high I_a^{635} ("antiparallel" DNA loop). Expectedly, high E_{FRET} correlates strongly with high I_a^{635}, since "antiparallel" looping (manifested by high E_{FRET}) should result in high I_a^{635}. For the 1000 bp DNA fragment the correlation between $I_a^{635} > 1.2$ and $E_{FRET} > 0.45$ is >90%. This alone is a strong sign that the observed I_a^{635} changes were associated with the looping reaction. For a quantitative analysis, parts of 2D distributions with E_{FRET} ranging from 0 to 0.4 and from 0.4 to 0.9 are projected onto I_a^{635} axis to obtain regular, one-dimensional (1D) histograms of the I_a^{635} average over many time trajectories. The I_a^{635} distribution corresponding to the lower E_{FRET} range exhibits two peaks

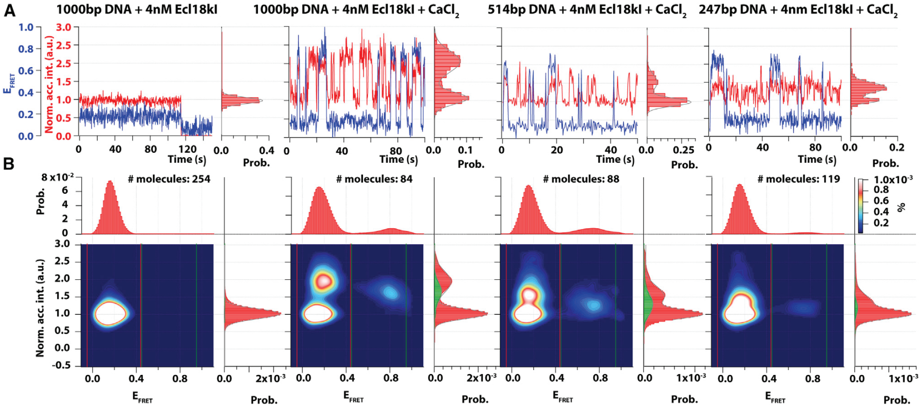

FIGURE 2 (*A*) Normalized I_a^{635} (*red*) and E_{FRET} (*blue*) trajectories and corresponding histograms of I_a^{635} with double Gaussian fits for DNA fragments with 247, 514, and 1000 bp intertarget distances interacting with 4 nM Ecl18kI in the presence of $CaCl_2$. For DNA with 1000 bp intertarget distance a trajectory without $CaCl_2$ is also shown. (*B*) 2D histograms of I_a^{635}/E_{FRET} points are collected from many time trajectories. 1D histograms along the intensity axis are projections of parts of the 2D distributions with E_{FRET} ranging from 0 to 0.4 (*red*) and from 0.4 to 0.9 (*green*).

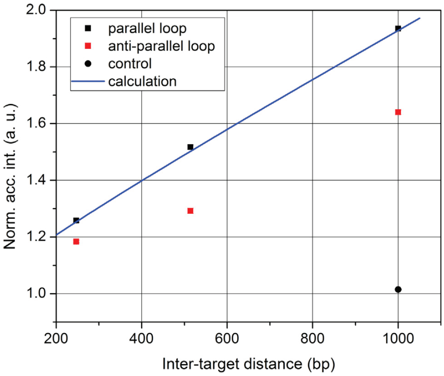

FIGURE 3 Mean I_a^{635} of different DNA loop states for the DNA fragments with different intertarget distances. This value for the "parallel" loop is the higher peak position of the two Gaussian fit of the corresponding 1D histogram in Fig. 2 *B*. For the "antiparallel" loop, it is the peak position of a single Gaussian fit of the corresponding 1D histogram in Fig. 2 *B*. Error bars are the SE of the peak position. For the 1000 bp fragment, a point from the measurement without $CaCl_2$ (control) is also presented. The calculated curve was obtained as detailed in the text with the penetration depth of the evanescent field of 200 nm. The numbers of the measurements in each point are the same as in Fig. 2. To see this figure in color, go online.

corresponding to the unlooped DNA and a "parallel" loop. It is fit with a two Gaussian function to obtain two peak positions. The I_a^{635} distribution corresponding to the higher E_{FRET} range exhibits a single peak corresponding to the "antiparallel" loop and is fit with a single Gaussian function.

The peak positions corresponding to the different loops show a clear dependence on the intertarget distance (Fig. 3): the extent of the I_a^{635} increase upon, e.g., the "parallel" looping increases from ~1.3 to 1.9 with lengthening of the intertarget distance from 247 to 1000 bp. Notably, the increase of I_a^{635} upon the "antiparallel" loop formation is from 8% to 30% smaller than that associated with the "parallel" loop—possibly because of the difference of the polarization effects of fluorophore excitation in the two-loop conformations (2,31,32). The expected I_a^{635} modulation upon looping was estimated by assuming the worm-like chain (WLC) model of DNA flexibility. The WLC model is a special case of the freely rotating ideal (not interacting with itself) chain model for a very small value of the bond angle, and it is a good model for stiff polymers, such as double-stranded DNA. According to this model the rms end-to-end distance of the WLC is $\langle R \rangle = (2l_pL - 2l_p^2(1 - \exp(-L/l_p)))^{1/2}$ (33), here $l_p = 50$ nm is the persistence length, and L is DNA contour length. To calculate the fluorophore intensity, this expression with L being the DNA contour length between the surface attachment point and the fluorophore is substituted for z in Eq. 1. The experimental values qualitatively reproduce the calculated quasi-linear dependence of the looping-associated modulation of the fluorescence intensity on the intertarget distance providing, therefore, another indication that the observed I_a^{635} changes were indeed associated with looping.

For comparison, we analyzed the recorded fluorescence movies without fixing the 2D Gaussian width, to obtain the possible looping-associated changes of the fluorescence image width—the parameter, chosen as an indicator of the DNA conformational state in (17). Analogous to Fig. 2 *B*, the obtained 2D histogram of the acceptor fluorescence image width (FIW) associated with E_{FRET} for 1000 bp DNA is shown in Fig. S5. The difference of FIW in the unlooped and either of the looped states is ~30%. Obviously, it is a smaller effect than the obtained nearly twofold looping-associated change of the acceptor intensity.

A control that the observed I_a^{635} changes were due to looping was obtained by comparing the number of transitions associated with the high-intensity states in the presence of 4 nM Ecl18kI with and without $CaCl_2$. For this, normalized intensity traces from the two experiments were idealized with an ICP algorithm with the same parameter values (see above in Data Analysis). Transitions between different states in the idealized trajectories from many measured single-molecule time traces were pooled into 2D transition density histograms representing probabilities of transitions of different magnitude (Fig. 4). The histogram from the measurement with $CaCl_2$ exhibits two peaks of transitions associated with the intensity range of 1.2–3 defining the higher I_a^{635} states. In the absence of $CaCl_2$, where looping is precluded, there are virtually no transitions to or from the higher I_a^{635} states, and only transitions from the unlooped to bleached state can be observed, which corroborates the notion that the detected I_a^{635} changes in the actual experiment must be due to looping.

Having demonstrated that the I_a^{635} changes are a reliable indication of DNA looping, we performed quantitative analysis of the kinetics of the system in the case of the DNA fragment with the 1000 bp intertarget distance. To calculate the average lifetimes of unlooped and looped states for the two kinds of DNA loops for the 1000 bp DNA fragment, the I_a^{635} traces were analyzed with the ICP detection algorithm. Then, the dwells in the I_a^{635} trajectory were partitioned between the "parallel" and "antiparallel" loops (Fig. 1 *C*). High I_a^{635} dwells with the corresponding average E_{FRET} value >0.4 represent "antiparallel" loop durations (ΔT_{Aon}), and low I_a^{635} dwells preceding them are the durations of the unlooped state before the "antiparallel" loop formation (ΔT_{Aoff}). The rest of the dwells in the I_a^{635} trajectory, correspondingly, are "parallel" loop durations (ΔT_{Pon}) and durations before the "parallel" loop formation (ΔT_{Poff}). The average dwell times of the different states are calculated by the bootstrap averaging and presented in Table 1 along with the state occurrences.

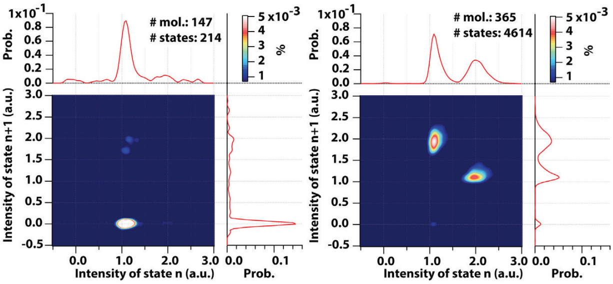

FIGURE 4 Transition density 2D histograms normalized to PDF for DNA with 1000 bp intertarget distance: with 4 nM Ecl18kI (*left*), and with 4 nM Ecl18kI and $CaCl_2$ (*right*). The number of molecules and the number of states contributing to these plots are indicated. To see this figure in color, go online.

DISCUSSION

In this work, we demonstrated that TFM in the exponentially decaying evanescent excitation field could be used to monitor large-scale molecular movements and in combination with FRET could be exploited to detect different conformations of the DNA-protein complex. As an example, we investigated the looping reaction of immobilized DNA fragments by the restriction enzyme Ecl18kI. We exploited the fact that the average distance of the tethered acceptor fluorophore from the surface is different in the looped and unlooped states, and because the strength of the TIR excitation field is exponentially dependent on the distance from the surface, the fluorescence intensity of the directly excited acceptor fluorophore I_a^{635} should be dependent on the looping state. This was observed as a clear two-state character in the I_a^{635} time trajectories during DNA interaction with Ecl18kI. That these intensity changes of the acceptor fluorescence were due to the DNA looping reaction was supported by the fact that under conditions where looping is precluded, virtually no transitions between different states could be observed. The notion is further corroborated by a clear dependence of the magnitude of fluorescence intensity modulation on the DNA intertarget distance since a stronger modulation is expected for a larger intertarget distance as it should span more of the evanescent field gradient.

From the different intertarget distances we probed, the modulation of the I_a^{635} trajectory is most clearly pronounced for the 1000 bp DNA fragment and on the average is equal to ~1.9. The distributions of acceptor intensities from many single-molecule trajectories in the looped and unlooped states are clearly separate (Figs. 2 and 3), and we, therefore, could attempt a quantitative assessment of the kinetic rate parameters governing the dynamics in the system. A simultaneous analysis of idealized acceptor intensity traces and raw E_{FRET} traces allows us to partition between the dynamics of different loop conformations since high E_{FRET} is associated with "antiparallel" loop only, whereas high acceptor intensity states are associated with either loop conformation. Such analysis for the 1000 bp DNA fragment yields all relevant time durations similar and of the order of a few seconds. It is not surprising that the durations of different loop conformers are alike since the loop stability should only depend on the microscopic details of specific protein association with DNA that are the same in both loop geometries. On the other hand, the time it takes to form a loop should depend on the mechanics of the DNA bending and twisting and could potentially be different for the two loop conformations with different energetic costs of the loop formation (34). $\langle \Delta T_{Aoff} \rangle$ of ~2 s for the "antiparallel" loop is a few orders of magnitude longer than it would take for the juxtaposition of the two target sites on DNA with the 1000 bp intertarget distance (35). Therefore, at least the "antiparallel" loop formation is not DNA diffusion, but rather Ecl18kI dimer-dimer reaction-limited. Similar formation rates of different loops suggest that the "parallel" looping is also reaction-limited and $\langle \Delta T_{Poff} \rangle$ is dominated by the time it takes for the DNA-bound Ecl18kI dimers to assemble into a tetramer. In any case, irrespective of the underlying microscopic details, at least with the 1000 bp intertarget distance that we used, both protein-bound DNA loop conformations appear to form at a similar velocity suggesting in general that a possibility of different loop conformations has to be considered when studying the dynamic behavior of similar systems. It is noteworthy that the probability of the "parallel" loop formation is ~6-fold greater than that for the "antiparallel" loop (Table 1). If the system were described by a kinetic scheme with both looped states connected to a common unlooped state, the equality of velocities of formation of loops of both kinds would also require the equality of probabilities of their formation. That this is not the case points to that the observed dynamics in

TABLE 1 State Occurrences and Dwell Times for DNA with the 1000 bp Intertarget Distance Calculated by the Bootstrap Averaging

State	Dwell Time ± SE	Fractional Occurrence
ΔT_{Aon}	2.15 ± 0.1	0.07
ΔT_{Aoff}	2.33 ± 0.2	0.06
ΔT_{Pon}	1.64 ± 0.04	0.47
ΔT_{Poff}	1.61 ± 0.05	0.40

the system cannot be interpreted by such a simple kinetic scheme with a single unlooped state.

To quantify the statistical significance of the effect of the acceptor modulation upon DNA reaction with Ecl18kI, we performed a *t*-test between the control (no $CaCl_2$) acceptor intensity distribution of the 1000 bp DNA fragment and distributions of the antiparallel DNA loop for all three experimentally measured intertarget distances. The distributions in the looped and unlooped states were found to be statistically different with the confidence level of 95% for all three intertarget distances.

In the same fashion, to assess the limits of our approach, we performed the *t*-test analysis on the simulated distributions of the acceptor intensity in the looped and unlooped states for different intertarget distances. For this, we simulated a Gaussian distribution with the peak position at 1 and the width of 0.4, equal to the width of the experimentally measured distribution of the acceptor intensities in the looped state. Distributions in the looped state for different intertarget distances were obtained by multiplying the intensity values in the modeled distribution with the intensity modulation factor calculated as detailed earlier assuming the WLC model of DNA flexibility and taking into account the exponential dependence of the strength of the exciting field on the distance from the surface with the penetration depth $d = 200$ nm. Then the *t*-test was performed between the modeled distributions for various intertarget distances and the experimentally measured control (without $CaCl_2$) distribution for the 1000 bp fragment. The shortest intertarget distance resulting in a statistically significant difference was ~16 nm, which is a few times less than the DNA persistence length, meaning that, even with the shortest intertarget distances at which DNA could still be looped, the acceptor intensity modulation due to looping should result in a discernible difference between the distributions in the looped and unlooped states.

The observed effect of I_a^{635} modulation upon the looping reaction can be enhanced with a few modifications. First, the exponential decay factor or the penetration depth of the evanescent field d depends on the angle of incidence (θ) of the exciting laser according to $d = \lambda/4\pi(n_1^2\sin^2\theta - n_2^2)^{1/2}$ (19), here n_1 and n_2 are the higher and lower refraction indexes at the interface, respectively. Thus, larger θ yields smaller d (Fig. 5 *inset*) and, therefore, a sharper dependence of the evanescent field strength on the distance from the surface. The effect of d on the strength of I_a^{635} modulation upon looping is simulated in the same manner as above for a few experimentally measured DNA intertarget distances (Fig. 5). It is clear that reducing d increases the change of I_a^{635}. Consequently, increasing θ should enhance the observed difference of the fluorescence intensity between unlooped and looped DNA states. In our setup, we used an objective with NA = 1.4. With this, in theory, the half angle of the acceptance cone and, therefore, also the maximum achievable incidence angle should be 68° and the corresponding penetration depth should be115 nm. For the 1000 bp intertarget distance this would result in the fluorescence intensity modulation significantly larger (Fig. 5) than it could actually be observed. In practice, the maximum achievable angle of incidence is limited by the finite size of the back aperture of the objective and is only marginally larger than the critical angle (where the sample excitation intensity is maximum). Therefore, it would be advantageous to substitute for a specialized TIRF objective for which larger incidence angles and shallower penetration depths can be obtained (36).

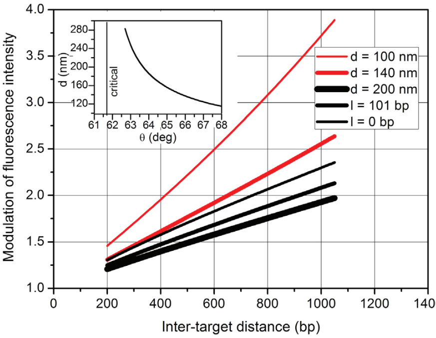

FIGURE 5 Dependences of the ratio of fluorescence intensities of Cy5 fluorophore in looped and unlooped DNA conformations on the intertarget distance with different evanescent field penetration depths and different spacings of the DNA loop from the surface (*l*). The thickness of the line corresponds to the magnitude of the corresponding parameter. The lines with different penetration depths were obtained with $l = 205$, whereas the lines with different spacings were obtained with $d = 200$ nm. The inset shows the dependence of the penetration depth on the angle of incidence. To see this figure in color, go online.

Secondly, in our DNA construct, both dye labels are attached to DNA at some distance from the surface. Upon looping the change of the effective acceptor tether length is roughly from the full DNA length to the DNA length between the anchoring point and the donor label. The same effective change of the tether length would correspond to a larger change of the evanescent field strength if it occurred to zero tether length (Fig. 5). In our case this could not be done, since the DNA-protein interaction kinetics was clearly affected by the close proximity of the surface (data not shown), but in more surface-tolerant experimental systems bringing of the recognition sequence with the donor label closer to the surface would further enhance the observed signal.

CONCLUSIONS

We have demonstrated that the dependence of the fluorophore intensity in the evanescent excitation field on the distance from the immobilization surface can be exploited to monitor large-scale conformational motions of biological molecules. In the case of the DNA looping by the restriction enzyme Ecl18kI with our experimental arrangement, changes of the DNA conformation larger than about a few tens of nanometers were predicted to be detectable and should, therefore, allow us to monitor the smallest of the physically feasible DNA loops. In combination with the FRET measurement, which is sensitive to the distance changes from a few to ~10 nm, the measurement of the acceptor fluorophore intensity revealed two different loop conformations and allowed the quantitative assessment of the average lifetimes of different states governing these complex dynamics.

SUPPORTING MATERIAL

Supporting Discussion and five figures are available at http://www.biophysj.org/biophysj/supplemental/S0006-3495(17)30112-1.

AUTHOR CONTRIBUTIONS

M.T. designed the research; M.T. and T.M. performed the measurements and analyzed the data; G.S. designed the DNA fragments; D.R. implemented the experimental setup, analyzed the data, and wrote the manuscript; and all authors discussed and interpreted the results.

ACKNOWLEDGMENTS

We would like to thank Dr. Gintautas Tamulaitis for Ecl18kI sample.

This research was funded by a grant (No. MIP-43/2013) from the Research Council of Lithuania.

REFERENCES

1. Deniz, A. A., S. Mukhopadhyay, and E. A. Lemke. 2008. Single-molecule biophysics: at the interface of biology, physics and chemistry. *J. R. Soc. Interface.* 5:15–45.
2. Joo, C., H. Balci, …, T. Ha. 2008. Advances in single-molecule fluorescence methods for molecular biology. *Annu. Rev. Biochem.* 77:51–76.
3. Borgia, A., P. M. Williams, and J. Clarke. 2008. Single-molecule studies of protein folding. *Annu. Rev. Biochem.* 77:101–125.
4. Brunger, A. T., P. Strop, …, K. R. Weninger. 2011. Three-dimensional molecular modeling with single molecule FRET. *J. Struct. Biol.* 173:497–505.
5. Preus, S., and L. M. Wilhelmsson. 2012. Advances in quantitative FRET-based methods for studying nucleic acids. *ChemBioChem.* 13:1990–2001.
6. Sisamakis, E., A. Valeri, …, C. A. M. Seidel. 2010. Accurate single-molecule FRET studies using multiparameter fluorescence detection. *Methods Enzymol.* 475:455–514.
7. Roy, R., S. Hohng, and T. Ha. 2008. A practical guide to single-molecule FRET. *Nat. Methods.* 5:507–516.
8. Zhou, R., S. Kunzelmann, …, T. Ha. 2011. Detecting intramolecular conformational dynamics of single molecules in short distance range with subnanomolar sensitivity. *Nano Lett.* 11:5482–5488.
9. Zhu, P., J.-P. Clamme, and A. A. Deniz. 2005. Fluorescence quenching by TEMPO: a sub-30 A single-molecule ruler. *Biophys. J.* 89:L37–L39.
10. Doose, S., H. Neuweiler, and M. Sauer. 2009. Fluorescence quenching by photoinduced electron transfer: a reporter for conformational dynamics of macromolecules. *ChemPhysChem.* 10:1389–1398.
11. Yang, H., G. Luo, …, X. S. Xie. 2003. Protein conformational dynamics probed by single-molecule electron transfer. *Science.* 302:262–266.
12. Hwang, H., H. Kim, and S. Myong. 2011. Protein induced fluorescence enhancement as a single molecule assay with short distance sensitivity. *Proc. Natl. Acad. Sci. USA.* 108:7414–7418.
13. Lerner, E., E. Ploetz, …, S. Weiss. 2016. A quantitative theoretical framework for protein-induced fluorescence enhancement-Förster-type resonance energy transfer (PIFE-FRET). *J. Phys. Chem. B.* 120:6401–6410.
14. Reinhard, B. M., M. Siu, …, J. Liphardt. 2005. Calibration of dynamic molecular rulers based on plasmon coupling between gold nanoparticles. *Nano Lett.* 5:2246–2252.
15. Seelig, J., K. Leslie, …, V. Sandoghdar. 2007. Nanoparticle-induced fluorescence lifetime modification as nanoscopic ruler: demonstration at the single molecule level. *Nano Lett.* 7:685–689.
16. Yin, H., R. Landick, and J. Gelles. 1994. Tethered particle motion method for studying transcript elongation by a single RNA polymerase molecule. *Biophys. J.* 67:2468–2478.
17. May, P. F. J., J. N. M. Pinkney, …, A. N. Kapanidis. 2014. Tethered fluorophore motion: studying large DNA conformational changes by single-fluorophore imaging. *Biophys. J.* 107:1205–1216.
18. Lee, K. S., H. Balci, …, T. Ha. 2013. Direct imaging of single UvrD helicase dynamics on long single-stranded DNA. *Nat. Commun.* 4:1878.
19. Axelrod, D., T. P. Burghardt, and N. L. Thompson. 1984. Total internal reflection fluorescence. *Annu. Rev. Biophys. Bioeng.* 13:247–268.
20. Mattheyses, A. L., S. M. Simon, and J. Z. Rappoport. 2010. Imaging with total internal reflection fluorescence microscopy for the cell biologist. *J. Cell Sci.* 123:3621–3628.
21. Tamulaitis, G., A. S. Solonin, and V. Siksnys. 2002. Alternative arrangements of catalytic residues at the active sites of restriction enzymes. *FEBS Lett.* 518:17–22.
22. Rutkauskas, D., M. Petkelyte, …, V. Siksnys. 2014. Restriction enzyme Ecl18kI-induced DNA looping dynamics by single-molecule FRET. *J. Phys. Chem. B.* 118:8575–8582.
23. Diao, J., Y. Ishitsuka, …, T. Ha. 2012. A single vesicle-vesicle fusion assay for in vitro studies of SNAREs and accessory proteins. *Nat. Protoc.* 7:921–934.
24. Kapanidis, A. N., N. K. Lee, …, S. Weiss. 2004. Fluorescence-aided molecule sorting: analysis of structure and interactions by alternating-laser excitation of single molecules. *Proc. Natl. Acad. Sci. USA.* 101:8936–8941.
25. Yang, L., R. Parton, …, W. Lu. 2010. An adaptive non-local means filter for denoising live-cell images and improving particle detection. *J. Struct. Biol.* 172:233–243.
26. Krüger, T. P. J., C. Ilioaia, and R. van Grondelle. 2011. Fluorescence intermittency from the main plant light-harvesting complex: resolving shifts between intensity levels. *J. Phys. Chem. B.* 115:5071–5082.
27. Zaremba, M., A. Owsicka, …, V. Siksnys. 2010. DNA synapsis through transient tetramerization triggers cleavage by Ecl18kI restriction enzyme. *Nucleic Acids Res.* 38:7142–7154.
28. Semsey, S., K. Virnik, and S. Adhya. 2005. A gamut of loops: meandering DNA. *Trends Biochem. Sci.* 30:334–341.
29. Bochtler, M., R. H. Szczepanowski, …, V. Siksnys. 2006. Nucleotide flips determine the specificity of the Ecl18kI restriction endonuclease. *EMBO J.* 25:2219–2229.
30. Kalinin, S., T. Peulen, …, C. A. M. Seidel. 2012. A toolkit and benchmark study for FRET-restrained high-precision structural modeling. *Nat. Methods.* 9:1218–1225.

31. Warshaw, D. M., E. Hayes, …, C. Berger. 1998. Myosin conformational states determined by single fluorophore polarization. *Proc. Natl. Acad. Sci. USA*. 95:8034–8039.
32. Adachi, K., R. Yasuda, …, K. Kinosita, Jr. 2000. Stepping rotation of F1-ATPase visualized through angle-resolved single-fluorophore imaging. *Proc. Natl. Acad. Sci. USA*. 97:7243–7247.
33. Rubinstein, M., and R. H. Colby. 2010. Polymer Physics. Oxford University Press, New York.
34. Swigon, D., B. D. Coleman, and W. K. Olson. 2006. Modeling the Lac repressor-operator assembly: the influence of DNA looping on Lac repressor conformation. *Proc. Natl. Acad. Sci. USA*. 103:9879–9884.
35. Jun, S., J. Bechhoefer, and B.-Y. Ha. 2003. Diffusion-limited loop formation of semiflexible polymers: Kramers theory and the intertwined time scales of chain relaxation and closing. *Europhys. Lett*. 64:420–426.
36. Burghardt, T. P. 2012. Measuring incidence angle for through-the-objective total internal reflection fluorescence microscopy. *J. Biomed. Opt*. 17:126007.

Received: 19 June 2017 | Revised: 22 September 2017 | Accepted: 4 October 2017
DOI: 10.1002/bip.23075

WILEY Biopolymers

ORIGINAL ARTICLE

Probing the dynamics of restriction endonuclease NgoMIV-DNA interaction by single-molecule FRET

Marijonas Tutkus[1] | **Giedrius Sasnauskas**[2] | **Danielis Rutkauskas**[1]

[1]Institute of Physics, Center for Physical Sciences and Technology, Savanoriu 231, Vilnius 02300, Lithuania

[2]Institute of Biotechnology, Vilnius University, Sauletekio av. 7, Vilnius 10257, Lithuania

Funding information
Research Council of Lithuania, Grant Number: No. MIP-43/2013

Abstract

Many type II restriction endonucleases require two copies of their recognition sequence for optimal activity. Concomitant binding of two DNA sites by such an enzyme produces a DNA loop. Here we exploit single-molecule Förster resonance energy transfer (smFRET) of surface-immobilized DNA fragments to study the dynamics of DNA looping induced by tetrameric endonuclease NgoMIV. We have employed a DNA fragment with two NgoMIV recognition sites and a FRET dye pair such that upon protein-induced DNA looping the dyes are brought to close proximity resulting in a FRET signal. The dynamics of DNA-NgoMIV interactions proved to be heterogeneous, with individual smFRET trajectories exhibiting broadly different average looped state durations. Distinct types of the dynamics were attributed to different types of DNA-protein complexes, mediated either by one NgoMIV tetramer simultaneously bound to two specific sites ("slow" trajectories) or by semi-specific interactions of two DNA-bound NgoMIV tetramers ("fast" trajectories), as well as to conformational heterogeneity of individual NgoMIV molecules.

KEYWORDS
DNA looping, heterogeneity, kinetic scheme, PIFE, rate constant

1 | INTRODUCTION

Restriction endonucleases (REases) are key components of restriction-modification systems that protect host bacteria and archaea cells against bacteriophage infections. The best known REases are the Type II enzymes used as molecular scissors for various *in vitro* DNA manipulations. They recognize 4-8 base pair (bp) DNA sequences, and cleave both DNA strands within or near this sequence in reactions that normally require only Mg^{2+} as a cofactor.[1] Despite a similar function, Type II REases differ in their oligomeric structure and mechanisms of DNA cleavage. Orthodox type II enzymes are homodimers that bind and cleave a single recognition site. In contrast, type IIF and IIE enzymes need to interact with two copies of their recognition site for efficient DNA cleavage. The former cleave both sites in a concerted manner,[2,3] whereas the latter cut only one target site with the other serving as an allosteric effector.[4] Simultaneous interaction of a Type IIF or Type IIE restriction enzyme with two sites on the same DNA molecule leads to DNA looping, a process also observed in various other biological phenomena, including regulation of gene expression, DNA replication, and recombination.[5,6] Due to relative simplicity, Type IIE and Type IIF enzymes are convenient model systems for the studies of DNA looping. In the case of REases it has been studied with various biochemical assays,[7] atomic force microscopy,[8] and more recently—single-molecule (SM) technique of tethered particle motion (TPM), where the protein-induced DNA looping was detected through the apparent shortening of the effective DNA tether length.[9–11] In our own work, we have employed SM fluorescence microscopy to explore the DNA looping by a dimeric REase Ecl18kI.[12,13] The topic of the present work is quantitative characterization of the real-time dynamics of interaction between DNA and a well-characterized homotetrameric type IIF REase—NgoMIV,[14,15] capable of simultaneous binding of two 5′-GCCGGC-3′ target sites via two identical DNA-binding surfaces. Since NgoMIV tetramer contains two DNA-binding clefts, compared to Ecl18kI[12] it presents a more complex example of interactions with a two-target DNA described by a branched kinetic scheme. NgoMIV-induced DNA looping has been studied previously by measuring inhibition of Tn21 resolvase reaction, but the loops were found to be too unstable to be characterized by this method.[7] NgoMIV interaction with DNA was also addressed by Katiliene et al. using SM fluorescence correlation spectroscopy,[16] where the authors have determined diffusion properties of DNA-protein complexes in solution. In this work, we have employed SM Förster resonance energy transfer (smFRET) and total internal reflection fluorescence (TIRF) microscopy to monitor the dynamics of interaction between NgoMIV and surface-immobilized FRET pair-labeled DNA fragments. The dye labels were attached to DNA close to the REase recognition sites at such positions that upon the target bridging by a REase, the distance between the fluorophores becomes favorable for efficient FRET. High temporal resolution of the assay allowed us to detect NgoMIV-induced loops of different stability. Also, unlike TPM, our approach does not suffer from the distorting effects of a relatively bulky DNA-attached microparticle. In conjunction with smFRET used to monitor the REase-mediated DNA looping/unlooping, we have also exploited the effect of the protein-induced fluorescence enhancement (PIFE)[17] to characterize the dissociation rate of NgoMIV-DNA complexes. By combining these techniques, we were able to determine the rate constants for DNA unlooping and protein dissociation in the kinetic scheme of NgoMIV-DNA interactions. The dynamics of NgoMIV interaction with DNA proved to be highly heterogeneous exhibiting broadly different loop stabilities—the feature that was not detected in our previous work on DNA interactions with dimeric REase Ecl18kI.[12,13] The observed diversity is attributed to the different forms of NgoMIV-induced DNA loops connected with the fact that NgoMIV is a tetrameric protein and also to the conformational heterogeneity of individual NgoMIV molecules.

2 | MATERIALS AND METHODS

2.1 | Protein

The protein concentration was determined using an extinction coefficient of 22 920 M^{-1} cm^{-1} calculated for the NgoMIV monomer by the ProtParam tool at http://web.expasy.org/protparam/. Protein concentrations are expressed in terms of tetramer.

2.2 | DNA fragments

The general strategy of DNA fragment preparation was the same as that used in our previous work.[12] Specific details of synthesis are presented in the Supporting Information.

2.3 | Sample cell preparation

The flow cell for microscopy was assembled from a six-channel Sticky-Slide VI 0.4 (80608, Ibidi) and a functionalized 24 × 60 mm #1.5 coverslip (Menzel Glaser). Liquids were inserted through a 1 mL pipette tip and sucked out with a 1 mL plastic syringe through a 0.5 mm ID and 1.6 mm OD Halar tube (4020L, Upchurch Scientific). The tip and the tube were attached to a slide through ~1 cm long pieces of silicone tube with 0.8 mm ID and 4 mm OD (CH24.1, Roth) inserted into the inlet and outlet of a channel. The volume of the cell including the inlet and outlet bits of tubing was about 70 μL.

The protocol of coverslip cleaning and functionalization with PEG derivatives was adapted from Diao et al.[18] (see the Supporting Information for details).

2.4 | SM assay

For biotin-labeled DNA fragment immobilization the flow cell was incubated with 5 μg mL^{-1} of Neutravidin (A-26666, Molecular probes) in the RB (33 mM Tris pH 7.9 at 20°C, 66 mM K-acetate) for 3 min, washed with RB, incubated with 1-10 pM DNA in RB for 3 min, washed with RB. For the measurement of the protein-DNA interactions the cell was infused with NgoMIV in the RB supplemented with 10 mM of $CaCl_2$, 15 U mL^{-1} of glucose oxidase (G6125, Sigma-Aldrich), 1% of glucose (G0047, TCI Europe) and 2.5 mM Trolox (238813, Sigma-Aldrich). Trolox was treated with UV light for 25 min following the recipe by Cordes et al.[19]

Alternatively, preparation with α-casein passivation was obtained by prior incubation of the sample cell with unfunctionalized cleaned coverslip with 0.1 mg mL^{-1} of biotin–BSA (A8549, Sigma-Aldrich) and 1 mg mL^{-1} of α-casein (C6780, Sigma-Aldrich) in the RB for 5 min and then washing the cell with RB.

2.5 | SM fluorescence microscopy

We used a custom-built single-molecule fluorescence microscopy setup described in detail previously.[12,13] In brief, the setup is based on a commercial inverted Nikon Eclipse Ti-U microscope, equipped with 100× 1.4 Oil Plan Apo VC objective, EMCCD detector (DU-897E-CS0-UVB, Andor) and 25 mW 532 and 635 nm diode-pumped solid state and diode lasers, respectively (Crystalaser). The 532 nm excitation intensity after the objective was 4.6 mW, 635 nm—0.6 mW. The integration time was 50 ms.

2.6 | Fluorescence movie analysis

Fluorescence movies were analyzed with the custom-written program (available upon direct request from the author) in Igor Pro environment (Wavemetrics).

Since the acceptor channel with the 635 nm excitation exhibits less background fluorescence than the donor channel with the 532 nm excitation, in addition to the actual movies with the 532 nm excitation we first acquired short movies with the 635 nm excitation on the same sample area for bright spot identification. A number of frames at the beginning of the 635 nm excitation movie are averaged. The acceptor channel of the resulting average image is transformed to align with the donor channel by applying the shifting and skewing whose coefficients were obtained from a calibration image measured on a dilute sample of surface-immobilized fluorescent polystyrene microspheres (F8806, Invitrogen). The obtained image is convoluted with the Gaussian kernel and converted to a fluorescent spot probability image.[20] Spots with probability exceeding the set threshold are fitted to the 2D symmetrical Gaussian to determine the center positions and widths of spots in the acceptor channel that should correspond to spots in the donor channel. Spots with fitting error exceeding a set threshold are rejected.

The same procedure of image averaging and spot detection is performed on the donor channel of the 532 nm excitation movie. The detected spots are screened to singularly colocalize within 3 pixels with spots in the acceptor channel calculated from the 635 nm excitation movie. Then the donor and corresponding acceptor traces are extracted,

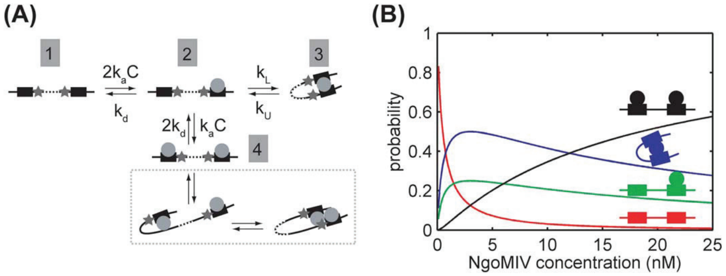

FIGURE 1 NgoMIV interactions with a two-site DNA. A, The kinetic scheme. The target sites are represented by rectangles, NgoMIV tetramers by circles, fluorophores by stars. k_a is the second order enzyme-DNA association rate constant, C is the tetramer concentration, k_d is the enzyme-DNA dissociation rate constant, k_L is the looping rate constant, k_U is the unlooping rate constant. B, Probabilities of different reaction species (depicted by cartoons colored in the same colours as the respective plot curves) depending on the NgoMIV concentration calculated from the steady-state conditions of the reaction scheme in panel (A). In the calculation $k_d = 0.003\ s^{-1}$—estimated from the PIFE measurements, $k_L = 2\ s^{-1}$ and $k_U = 1\ s^{-1}$—inverses of characteristic durations of unlooped and "antiparallel" looped state dwell durations of DNA494 with 10 nM NgoMIV and Ca^{2+}, respectively; $k_a = 1 \times 10^5\ M^{-1}s^{-1}$ was chosen to yield the concentration dependences compatible with the measured ones

respectively, from the donor and transformed acceptor channels of a 532 nm excitation movie by 2D Gaussian fitting with constrained center position and width at all determined donor and corresponding acceptor positions. For faster data processing the fitting of different spots was distributed over multiple CPU cores. The obtained Gaussian amplitude is the fluorescence intensity. Trajectories of proximity ratio (PR) as a measure of FRET efficiency are calculated using a conventional definition: $PR = F_5/(F_3 + F_5)$, where F_5 is the acceptor intensity and F_3 is the donor intensity, without correcting for the direct excitation of the acceptor or bleedthrough of the donor signal into the acceptor channel. *PR* trajectories are screened by manually selecting the signals with anticorrelated changes of the donor/acceptor intensities, typical single-molecule fluorescence intensity and a single step bleaching behavior.

2.7 | Ensemble FRET

The measurements of DNA fragment interactions with NgoMIV in solution were performed with the custom-built fluorimeter,[12] which is an extension of the single-molecule setup with a Shamrock SR-303i polychromator (Andor) with 53–310R grating (Newport) and the same EMCCD camera as used for the dual image acquisition. DNA solution was excited in a regular wide-field mode through a CFI S Plan Fluor ELWD 40× objective (Nikon) with a 532 nm laser at 50 μW. The polychromator entrance slit was set to 50 μm width. Integration time was 0.5, the number of accumulations—100. Fluorescence spectra were background-subtracted and corrected for the spectral detection sensitivity. DNA and NgoMIV concentrations were ~10 nM. The reaction was carried out in the RB supplemented with 10 mM of $CaCl_2$.

3 | RESULTS

3.1 | NgoMIV interactions with a two-site DNA

The dynamics of interactions of two-site DNA with NgoMIV is conveniently summarized by a kinetic scheme depicting conversions between possible reaction species (Figure 1A). Since NgoMIV is a stable tetramer in solution (the large monomer surface area buried upon tetramerization, ~4200 Å^2, makes dissociation of NgoMIV into primary dimers or monomers highly unlikely[15]), four different species resulting from specific interactions are considered in the scheme: bare DNA (1), DNA with one NgoMIV tetramer attached (2), looped DNA, where a single tetramer binds to both DNA targets simultaneously (3), and DNA with both of its recognition sequences occupied by different tetramers (4). Also NgoMIV interacting with DNA semi-specifically is shown to branch off (boxed) the specific species of both DNA target sites occupied by different NgoMIV tetramers.

The mechanism in Figure 1A predicts that concentration of the looped DNA complex (species "3" in Figure 1A), which is proportional to the concentration of the 2-site DNA fragment with a single bound NgoMIV tetramer (species "2"), increases with protein concentration to a maximal value, and then decreases at higher protein concentrations due to the formation of species "4", the 2-site DNA fragment with 2 NgoMIV tetramers (Figure 1B). It is known that the looped complex, formed by a single NgoMIV tetramer bound to two specific DNA sites via two identical DNA binding surfaces (species "3") is required for NgoMIV catalysis.[15] On the other hand, complex "4", predominant at high protein concentrations, contains two NgoMIV tetramers bound to separate specific sites via one of the two DNA binding clefts, leaving one DNA binding surface of each tetramer DNA free. These NgoMIV tetramers might use the binding clefts unoccupied by specific DNA for nonspecific interactions with the DNA, thereby bridging one specific and one nonspecific DNA site via a semi-specific loop (Figure 1A boxed).

3.2 | Design and characterization of DNA fragments

To decipher the dynamics of NgoMIV-induced DNA looping, we have prepared DNA constructs with Cy3 and Cy5 FRET dye labels 6 bp from the NgoMIV recognition sites so that upon simultaneous binding

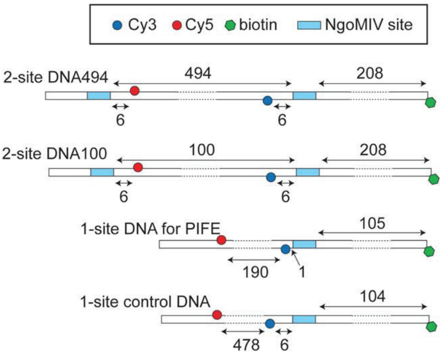

FIGURE 2 DNA constructs with lengths in base pairs

of NgoMIV to both sites, the donor and acceptor are brought to close proximity, resulting in appreciable FRET (Figure 2). The probability of DNA looping depends on the loop contour length and the helical phasing between the DNA sites bridged by the protein.[21] For optimal looping we have chosen an intertarget distance close to the optimal DNA length for cyclization—494 bp (DNA494). To duplicate the measurements on DNA494, but also expecting a different—slower speed of loop formation due to the bending rigidity of the DNA, we have also prepared a DNA construct with a much shorter—100 bp inter-site distance—DNA100. The occurrence of FRET and, hence, the correctness of the dye label positions on DNA was established through the comparison of the solution fluorescence spectra of DNA alone and interacting with NgoMIV (Figure 3). For both DNA fragments the intensity of the Cy5 component relative to that of Cy3 clearly increases upon the addition of about equimolar concentration of NgoMIV, providing an unequivocal indication of FRET between the dyes.

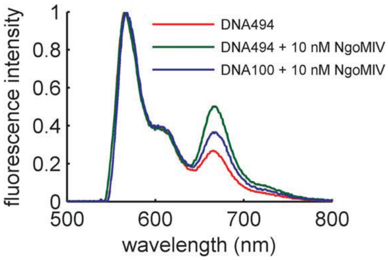

FIGURE 3 Bulk fluorescence spectra of fragments with two different intersite distances interacting with NgoMIV. The spectrum of DNA494 without NgoMIV is presented for comparison. The spectrum of DNA100 without NgoMIV is identical to that of DNA494 and is not shown. All spectra are normalized to the maximum of the Cy3 fluorescence intensity

Enzymatic activity of NgoMIV on DNA494 was tested in solution under standard conditions for DNA cleavage, and also in our reaction buffer (RB) supplemented with Mg^{2+}. In both cases, DNA494 was nearly fully digested (Supporting Information Figure S1). The activity of NgoMIV was also tested in our single-molecule setup, where NgoMIV digested up to 60% of DNA molecules (Supporting Information Figure S2).

3.3 | PR trajectories of NgoMIV-mediated DNA looping

To study the NgoMIV-induced DNA looping, we have obtained PR trajectories of DNA494 interacting with NgoMIV in the presence of Ca^{2+} (Ca^{2+} ions permit specific DNA binding by NgoMIV, but, unlike Mg^{2+}, do not support DNA cleavage) by recording the two-channel fluorescence movies (Supporting Information Figure S3), extracting the corresponding donor and acceptor intensity traces and calculating the resulting PR. Then we chose the trajectories exhibiting clear anticorrelated changes of the donor and acceptor intensities indicative of the energy transfer (Figure 4).

The obtained PR records for DNA494 exhibit diverse temporal evolutions (Figure 4). There exist traces, where high PR dwells are uniformly short (Figure 4B,C). Other traces contain dwells of different longer durations (Figure 4D). There are also traces, where PR remains constant during the whole ~50 s record (Figure 4E,F). To test that this heterogeneity is not specific to DNA494, we have performed identical measurements with DNA100. They resulted in a collection of traces with similar temporal characteristics of high PR (Supporting Information Figure S4), and at the same time longer durations of dwells of low PR, which is likely to be due to the shorter and less flexible DNA construct.

With DNA494 we have also used a range of NgoMIV concentrations and tested a different immobilization surface using passivation with α-casein instead of PEG (Supporting Information Figure S5), but these modifications did not alter the overall pattern of different PR behaviors. Control measurements performed with NgoMIV on a DNA fragment with one recognition site (Supporting Information Figure S6), and on regular DNA494 excluding Ca^{2+} (Figure 4A) produced no trajectories with PR different from the baseline level with anti-correlated donor/acceptor behavior. This confirmed that all types of PR dynamics observed with DNA494 are due to specific NgoMIV interaction with two recognition sequences, and that higher than the baseline PR must be associated with looping.

3.4 | Distinct configurations of NgoMIV-DNA loops

To interpret the observed dynamics, first, we have obtained the average characteristics of the different observed PR levels. To do so, we have pooled the PR trajectories obtained in the 10 nM NgoMIV measurement with Ca^{2+} together (Figure 5A-C) and averaged the resulting 2D histograms of PR occurrence depending on time within the first 5 s (Figure 5D). Fitting the obtained average PR occurrences with a double Gaussian function yielded the values of the PR level positions and standard deviations: for DNA494—0.21 (0.12) and 0.62 (0.06), for DNA100—0.16 (0.07) and 0.62 (0.06). The same procedure with a

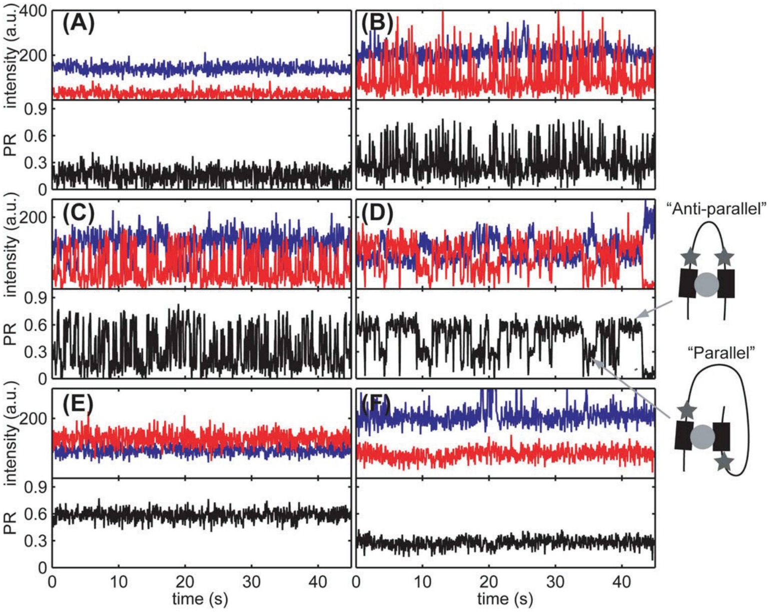

FIGURE 4 Examples of PR and corresponding Cy3 and Cy5 intensity trajectories of DNA494 interacting with 10 nM of NgoMIV. Trajectory (A) was obtained with NgoMIV but without Ca^{2+}; trajectories (B-F) were obtained with Ca^{2+}. B and C are examples of "fast", D-F are examples of "slow" trajectories. Cartoons depict two possible loop conformations corresponding to different PR levels

single Gaussian fit performed on the selected trajectories from a control of DNA494 with NgoMIV but without Ca^{2+} (Figure 5B) yielded the baseline PR of 0.15 (0.07) corresponding to unlooped DNA. It is not equal to zero since PR was calculated without correcting for the direct excitation of the acceptor and the bleedthrough of the donor signal into acceptor channel. Clearly, the lower PR level in the actual (DNA494 with Ca^{2+}) measurement is broader and has a higher value than the control (DNA494 without Ca^{2+}) experiment. Inspection of individual trajectories indicates that it consists of the baseline level and a level of an intermediate PR (Figure 4D). Since experiment with single-target DNA confirmed that all nonbaseline PR is due to looping, this intermediate level and the highest PR level of 0.62 must be associated with different types of DNA loops resulting from NgoMIV tetramer bridging its DNA recognition sequences. One possibility is different loop configurations due to the global twist of the DNA molecule (different values of δ by Zhang et al.[22]) with the same REase-DNA site attachment geometry. However, with the relatively close attachment of the dye labels to the DNA sites (6 bp distance) the global twist would not be sufficient for the observed large difference of the measured FRET efficiency values. Alternatively, the different observed PR

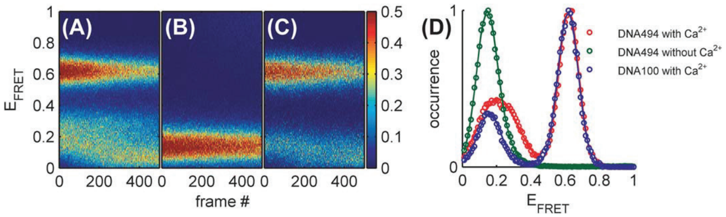

FIGURE 5 Pooled traces and their averages in time. A, DNA494 in the presence of 10 nM of NgoMIV with Ca^{2+}. B, DNA494 in the presence of 10 nM of NgoMIV without Ca^{2+}. C, DNA100 in the presence of 10 nM of NgoMIV with Ca^{2+}. D, Normalized time-averages of images of pooled traces within the first 5 s with the Gaussian fits

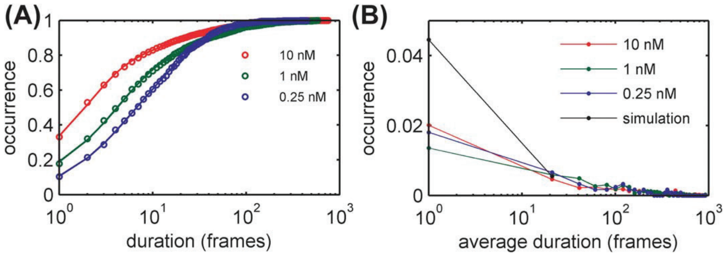

FIGURE 6 PR = 0.62 state dwell durations of DNA494 with different NgoMIV concentrations. A, Cumulative distributions of state dwell durations with three-exponent fits. B, Distributions of the number of traces with an average state dwell duration. Distribution from data simulated in QuB with a two-state model with looping and unlooping rates equal to the reciprocal of the middle time constant of 15 frames (Table 1) is shown for comparison. Distributions are normalized to unit area. Bin size is 20 frames

could be due to the different geometries of REase-DNA attachment. Since DNA recognition sequence of NgoMIV is symmetric, REase tetramer can form the loop in two configurations: the so-called "parallel" and "antiparallel" loops.[23] Then the higher PR of 0.62 should result from DNA forming the "antiparallel" loop, since the dye labels are placed for maximum FRET in this configuration, whereas the lower nonbasal PR—from the "parallel" loop, where the dye labels are across the bound protein (cartoons in Figure 4). The attribution of high PR levels to looping is reinforced by the measurement on control DNA fragments with known interdye distances of 6, 16, and 26 bp corresponding to the PR values of 0.89, 0.36, and 0.17, respectively (Supporting Information Figure S7). Comparison of average fluorescence intensities of Cy3 on 1-site control DNA fragment with/without NgoMIV indicates that Cy3 at 6 bp from the endonuclease target on DNA is not subject to PIFE effect (Supporting Information Figure S8). Moreover, upon the addition of Ca^{2+}, the stability of the intensity traces of both dyes remains unaffected (Supporting Information Figure S9). To rule out possible artefacts of limited dye mobility because of their attachment to DNA, we have also performed control measurements of the donor and acceptor fluorescence anisotropy decays (Supporting Information Figure S10). Since the anisotropy decays occur with rates comparable to rotation correlation times of these dyes in solution,[24] we conclude that rotational motions are not hindered by the dye coupling to DNA or possible interaction with the protein. Furthermore, if the intermediate PR level was a consequence of limited dye mobility, it should be pronounced in both DNA constructs. However, as can be seen from the comparison of the time averages of pooled traces of the control DNA494 and DNA100 (Figure 5D), intermediate PR is absent in the case of DNA100. This is expected if it was due to looping in "parallel", since due to the short (shorter than the DNA persistence length) intertarget distance, DNA100 should be unable to form the more twisted "parallel" loop.

3.5 | Dynamics of NgoMIV-mediated DNA looping

To determine the unlooping rate constant, we first idealized the PR traces using HMM in QuB software (Supporting Information Figure S11) with the values of PR level positions and standard deviations determined above for DNA494 with 10 nM NgoMIV and Ca^{2+}. Traces were loaded to QuB as different segments, and idealization was done using the segmental K-means algorithm with a two-state model with the state amplitudes fixed. Then we have built cumulative distributions of the number of different "antiparallel" looped state dwell durations (Figure 6A), and approximated them with an exponential model in order to find the rate constant of unlooping. However, at least three exponential components appear to be required to reasonably approximate the distributions (Table 1). This indicates that the looped state is heterogeneous, and features different NgoMIV-induced loop stabilities.

We further notice that this heterogeneity is associated with the heterogeneity among individual traces. For each idealized trace we calculated the average dwell duration of the PR = 0.62 state as a parameter to characterize the dynamics in a trace. In this calculation, the beginning and end dwells in a trace were not removed in order to retain the instances of traces containing only one or two possibly long-lived PR = 0.62 edge dwells. The distributions of the average looped state dwell durations (Figure 6B) demonstrate that there is a significant spread of dynamic behaviors among the individual PR trajectories with the average looped state duration extending over a few orders of magnitude, from a few to a few hundred frames. For comparison, a distribution simulated assuming a single exponential process with an unlooping rate reciprocal to 15 frames fits into two bins of the histogram.

Distribution analysis quantitatively confirms that heterogeneity is also present for a different DNA construct—DNA100, and a different chemistry of surface passivation (Supporting Information Figure S12), suggesting that it is not an experimental artefact of surface-immobilization or DNA synthesis. Juxtaposition of histograms for DNA494 reveals that the spread of dynamics is pertinent also for a range of NgoMIV concentrations (Figure 6).

To test enzyme concentration dependencies following from our kinetic model, we divide all traces into two groups. Traces with the average PR = 0.62 state duration shorter than the shortest exponential rate constant of 5 frames we call "fast" traces while the rest—"slow" traces. Then we consider the relative numbers of "fast" and "slow" trajectories as well as the overall occurrences of dynamic traces for

TABLE 1 Exponential fits of the cumulative distributions of state dwell durations of DNA494 (with 95% confidence intervals). Time constants are expressed in frames

NgoMIV concentration (nM)	A_1	τ_1	A_2	τ_2	A_3	τ_3
10	0.685 ± 0.006	1.87 ± 0.03	0.210 ± 0.003	15.0 ± 0.3	0.066 ± 0.001	103 ± 2
1	0.636 ± 0.007	3.79 ± 0.08	0.244 ± 0.006	22.0 ± 0.9	0.090 ± 0.003	116 ± 3
0.25	0.38 ± 0.02	3.6 ± 0.2	0.57 ± 0.01	16.1 ± 0.6	0.079 ± 0.009	63 ± 4

different DNA constructs and NgoMIV concentrations (Table 2). There is a clear increase of the number of dynamic traces with the protein concentration, both for DNA494 and DNA100. At the same time, the number of dynamic traces for DNA100 is smaller than that for DNA494. Furthermore, the occurrence of "fast" traces relative to that of "slow" increases with increasing of NgoMIV concentration both for DNA494 and DNA100.

3.6 | Dissociation rate of the NgoMIV-DNA complex

Since the distribution of the low PR dwell times cannot be interpreted straightforwardly to extract the rate constants for looping, and protein association/dissociation, we obtained an independent estimate of the NgoMIV-DNA dissociation rate constant (k_d in Figure 1A) using the PIFE approach. To this end we have employed a DNA construct with the Cy3 label only 1 bp from a sole copy of NgoMIV recognition site so that specific binding of NgoMIV enhanced the Cy3 fluorescence. The single-molecule (Supporting Information Figure S13) and quasi-ensemble (Supporting Information Figure S14) measurement of NgoMIV-DNA dissociation demonstrated that NgoMIV dissociation is slow in comparison to the ~1 min time scale of our SM measurements. Thus, all individual PR trajectories observed in smFRET experiments must result from specific interactions of a DNA fragment with specific copies of one or two tightly bound NgoMIV tetramers. Also, the equilibrium concentrations of different kinetic species (Figure 1B) must correspond to the probabilities of different types of PR trajectories.

4 | DISCUSSION

The smFRET measurement of DNA-NgoMIV interactions yielded PR trajectories indicating very different stabilities of the looped state of the DNA. Furthermore, the number of trajectories corresponding to the transient loops increased with increasing of the NgoMIV concentration. To account for this heterogeneity and concentration dependence of the looping dynamics, in addition to specific DNA loops mediated by a single NgoMIV tetramer simultaneously bound to both recognition sites either in "parallel" or "antiparallel" arrangement, we must consider the existence of alternative DNA loops, mediated by two NgoMIV tetramers. One possibility is direct protein-protein interaction between the two DNA-bound NgoMIV tetramers. However, such interactions are not documented for NgoMIV, and are highly unlikely based on the function and the available structure of NgoMIV.[15] A more likely model is depicted in the boxed region in Figure 1A. Here, two NgoMIV tetramers, each tightly bound to one specific recognition sequence via one DNA binding surface (the average life time of such an interaction according to PIFE exceeds 5 min, Figure S14), transiently bind to nonspecific DNA sequence via the second DNA binding surface. Such semispecific complexes may be analogs to the target search intermediates of a single NgoMIV bound to its recognition site on a two-site DNA fragment. It is known that NgoMIV displays optimal catalytic activity upon simultaneous interaction with two specific sites, and only residual activity when bound to a single DNA site.[15] Thus, in order to protect host bacteria from an invading bacteriophage, the enzyme must be able to rapidly locate, bridge and cleave two cognate sites among a vast excess of noncognate DNA. Since NgoMIV has two DNA binding surfaces, its target search may be facilitated by all mechanisms involving the surrounding nonspecific DNA sequences, originally proposed by von Hippel and colleagues, namely, intersegmental transfer, sliding, and dissociation/association between distant or adjacent DNA sites (jumping/hopping).[25] Upon location of the first target site, the NgoMIV is "locked" on this site via one of the DNA-binding clefts, while the second DNA-binding cleft may continue

TABLE 2 Statistics of traces with different dynamics

Fragment	NgoMIV concentration (nM)	# traces	Fraction of dynamic traces	Fraction of "fast" traces[a]
DNA494	0.25	925	0.07	0.08
	2.5	1362	0.14	0.14
	10	1388	0.50	0.26
	25	1428	0.43	0.68
DNA100	2.5	1001	0.03	0
	10	1236	0.19	0.03

[a] The fraction of the "fast" traces was calculated relative to the number of dynamics traces.

the target search via sliding on nonspecific DNA and/or multiple association-dissociation events with noncognate DNA. Such semi-specific DNA looping may result in a myriad of possible loop configurations, some of which might bring into close proximity the two NgoMIV tetramers with adjacent FRET dyes, resulting in high PR values, as depicted in Figure 1A. Since interactions leading to the excitation energy transfer in this case would be nonspecific, they are expected to be short-lived and, hence, result in the "fast" trace-like time dependence of PR. In this context, the "slow" looping dynamics is attributed to looping/unlooping of DNA with a single specifically-bound NgoMIV tetramer.

The steady-state analysis (Figure 1B) shows that the occurrence of DNA with two NgoMIV tetramers relative to that of DNA with one tetramer (and hence, the fraction of "fast" looping dynamics relative to "slow") should increase with NgoMIV concentration. As predicted, experimentally we observe an increase of the number of "fast" traces relative to that of "slow" traces at higher NgoMIV concentrations with both DNA494 and DNA100 substrates (Table 2), supporting the idea that the "fast" dynamics is indeed associated with semi-specific DNA looping mediated by two NgoMIV tetramers bound to the same two-site DNA fragment. This model is also consistent with the measurements on DNA100. The relative number of dynamic traces, and the fraction of the "fast" traces for DNA100 is lower than that for DNA494 at the same NgoMIV concentration (Table 2). This can be attributed to smaller association constant and lesser likelihood of semi-specific loops with the FRET labels in close proximity on the shorter and less flexible fragment.

We also note that no looping events were detected on the single-site DNA fragment, whose design is compatible with the formation of the semi-specific loops. Presumably, in the case of such a semi-specific loop formed by a single NgoMIV molecule, transient proximity of the FRET dyes is too short-lived (less than 50 ms, a single movie frame) to be detected in our experimental setup. At the same time, on a two-site DNA, favorable disposition of fluorescence labels may be stabilized by the two NgoMIV tetramers acting as mutual brakes for their movement on nonspecific DNA, as depicted in the boxed section of Figure 1A.

Interestingly, heterogeneity of NgoMIV-induced DNA loop stabilities observed in the current work was not encountered in our previous study on another type IIF REase—Ecl18kI.[12,13] Unlike homotetrameric NgoMIV, Ecl18kI is a homodimer in the DNA-free form, and Ecl18kI-mediated DNA looping occurs through two Ecl18kI homodimers bound to specific recognition sequences associating to form a tetramer bridging the two cognate sites.[9] As Ecl18kI dimer contains a sole DNA-binding cleft, once it is occupied by the interactions with a recognition sequence, the Ecl18kI lacks the ability to mediate the formation of semi-specific loops in the manner of NgoMIV. Thus, the absence of "fast" traces in the case of Ecl18kI is consistent with the proposed model of semi-specific looping for NgoMIV.

Despite the fact that different looping modes provide a qualitative interpretation for the existence and enzyme concentration dependence of the occurrence of the "fast" and "slow" NgoMIV looping trajectories, they do not explain the observed heterogeneity within the subset of "slow" traces (wide distribution of average looped state durations in Figure 6B and two slow exponential components of cumulative histogram of looped state durations in Figure 6A), nor do they account for the "fast" looping dynamics at the lowest enzyme concentrations. Indeed, calculation in Figure 1B predicts that at low protein concentration the predominant species are bare DNA and DNA with a single NgoMIV monomer, with virtually no DNA fragments with two NgoMIV tetramers (e.g., if 60% of DNA fragments contain no bound protein, >99% of the remaining 40% DNA fragments contain a single NgoMIV tetramer). Under these conditions one would expect only the "slow" looping behavior, associated with a single NgoMIV tetramer bridging two specific sites. At 0.25 nM NgoMIV, the lowest enzyme concentration tested in our experiments (Table 2), the predominant species was bare DNA (only 7% of all traces displayed PR dynamics). Nevertheless, a significant fraction (8%) of all dynamic PR trajectories recorded under these conditions fell within the category of "fast" behavior. Thus, semi-specific loops mediated by two NgoMIV tetramers cannot account for the observed "fast" looping dynamics at low NgoMIV concentration. We assign the extra heterogeneity among individual "slow" looping trajectories, and the quantitative discrepancy between the calculation in Figure 1B and experimental data obtained at low enzyme concentrations to the static heterogeneity among the individual DNA-bound NgoMIV molecules. Heterogeneity of enzyme properties has been observed with single-molecule methods before in the case of many enzymes, including lactate dehydrogenase,[26] alkaline phosphatase,[27] cholesterol oxidase,[28] and β-galactosidase.[29,30] Here, we do not monitor the activity of the enzyme since it was precluded by the substitution of the Ca^{2+} ions for Mg^{2+}. Instead, we observe different dynamics of the REase-DNA interaction, which is a prerequisite for the DNA cleavage reaction. It would be interesting to trace whether the heterogeneity in the stability of NgoMIV complexes with two specific DNA sites formed in the presence of Ca^{2+} is functionally significant for the efficiency of DNA cleavage by individual NgoMIV molecules in the presence of Mg^{2+}. This would, however, require a different experimental arrangement and could be a topic for further investigation.

5 | CONCLUSIONS

In this work, we have applied the smFRET technique for the mechanistic studies of NgoMIV-DNA interaction dynamics. Our experimental strategy allowed us a prolonged observation of the NgoMIV-induced DNA looping, and discrimination between distinct DNA-protein binding configurations with different distances between the fluorophore labels. The temporal behavior of the NgoMIV-induced loops proved to be heterogeneous. We attribute this diversity in looping dynamics to the conformational heterogeneity of individual NgoMIV molecules and different types of looped DNA complexes: loops mediated by NgoMIV bridging two specific target sites or one specific and one nonspecific DNA sequence. We propose that the latter loops may represent target search intermediates of NgoMIV, which were not detected before using alternative experimental techniques. The applied experimental approach, thus, could be utilized to decipher complex DNA-protein interactions in the case of other DNA-binding proteins.

ACKNOWLEDGMENTS

We thank E. Manakova for the NgoMIV sample. We also would like to gratefully acknowledge R. Augulis for the help with the measurements of the decays of fluorescence anisotropy. This research was funded by a grant (No. MIP-43/2013) from the Research Council of Lithuania.

ORCID

Danielis Rutkauskas http://orcid.org/0000-0003-4705-2222

REFERENCES

[1] A. Pingoud, M. Fuxreiter, V. Pingoud, W. Wende, *Cell Mol Life Sci.* **2005**, *62*, 685.

[2] L. M. Wentzell, S. E. Halford, *J Mol Biol.* **1998**, *281*, 433.

[3] M. Zaremba, G. Sasnauskas, C. Urbanke, V. Siksnys, *J Mol Biol.* **2005**, *348*, 459.

[4] G. Tamulaitis, G. Sasnauskas, M. Mucke, V. Siksnys, *J Mol Biol.* **2006**, *358*, 406.

[5] K. S. Matthews, *Microbiol Rev.* **1992**, *56*, 123.

[6] R. Schleif, *Annu Rev Biochem.* **1992**, *61*, 199.

[7] S. E. Milsom, S. E. Halford, M. L. Embleton, M. D. Szczelkun, *J Mol Biol.* **2001**, *311*, 515.

[8] L. S. Shlyakhtenko, J. Gilmore, A. Portillo, G. Tamulaitis, V. Siksnys, Y. L. Lyubchenko, *Biochemistry* **2007**, *46*, 11128.

[9] M. Zaremba, A. Owsicka, G. Tamulaitis, G. Sasnauskas, L. S. Shlyakhtenko, A. Y. Lushnikov, Y. L. Lyubchenko, N. Laurens, B. van den Broek, G. J. L. Wuite, V. Siksnys, *Nucleic Acids Res.* **2010**, *38*, 7142.

[10] N. Laurens, S. R. W. Bellamy, A. F. Harms, Y. S. Kovacheva, S. E. Halford, G. J. L. Wuite, *Nucleic Acids Res.* **2009**, *37*, 5454.

[11] B. van den Broek, F. Vanzi, D. Normanno, F. S. Pavone, G. J. L. Wuite, *Nucleic Acids Res.* **2006**, *34*, 167.

[12] D. Rutkauskas, M. Petkelyte, P. Naujalis, G. Sasnauskas, G. Tamulaitis, M. Zaremba, V. Siksnys, *J Phys Chem B* **2014**, *118*, 8575.

[13] M. Tutkus, T. Marciulionis, G. Sasnauskas, D. Rutkauskas, *Biophys J.* **2017**, *112*, 850.

[14] M. L. Embleton, V. Siksnys, S. E. Halford, *J Mol Biol.* **2001**, *311*, 503.

[15] M. Deibert, S. Grazulis, G. Sasnauskas, V. Siksnys, R. Huber, *Nat Struct Biol.* **2000**, *7*, 792.

[16] Z. Katiliene, E. Katilius, N. W. Woodbury, *Biophys J.* **2003**, *84*, 4053.

[17] H. Hwang, H. Kim, S. Myong, *Proc Natl Acad Sci USA* **2011**, *108*, 7414.

[18] J. Diao, Y. Ishitsuka, H. Lee, C. Joo, Z. Su, S. Syed, Y.-K. Shin, T.-Y. Yoon, T. Ha, *Nat Protoc.* **2012**, *7*, 921.

[19] T. Cordes, J. Vogelsang, P. Tinnefeld, *J Am Chem Soc.* **2009**, *131*, 5018.

[20] L. Yang, R. Parton, G. Ball, Z. Qiu, A. H. Greenaway, I. Davis, W. Lu, *J Struct Biol.* **2010**, *172*, 233.

[21] J. P. Peters, J. L. Maher, *Q Rev Biophys.* **2010**, *43*, 23.

[22] Y. Zhang, A. E. McEwen, D. M. Crothers, S. D. Levene, *Biophys J.* **2006**, *90*, 1903.

[23] S. Semsey, K. Virnik, S. Adhya, *Trends Biochem Sci.* **2005**, *30*, 334.

[24] M. E. Sanborn, B. K. Connolly, K. Gurunathan, M. Levitus, *J Phys Chem B* **2007**, *111*, 11064.

[25] R. B. Winter, O. G. Berg, P. H. von Hippel, *Biochemistry* **1981**, *20*, 6961.

[26] Q. Xue, E. S. Yeung, *Nature* **1995**, *373*, 681.

[27] D. B. Craig, E. A. Arriaga, J. C. Y. Wong, H. Lu, N. J. Dovichi, *J Am Chem Soc.* **1996**, *118*, 5245.

[28] H. P. Lu, L. Xun, X. S. Xie, *Science* **1998**, *282*, 1877.

[29] A. C. Dyck, D. B. Craig, *Luminescence* **2002**, *17*, 15.

[30] D. M. Rissin, H. H. Gorris, D. R. Walt, *J Am Chem Soc.* **2008**, *130*, 5349.

SUPPORTING INFORMATION

Additional Supporting Information may be found online in the supporting information tab for this article.

How to cite this article: Tutkus M, Sasnauskas G, Rutkauskas D. Probing the dynamics of restriction endonuclease NgoMIV-DNA interaction by single-molecule FRET. *Biopolymers*. 2017; e23075. https://doi.org/10.1002/bip.23075

THE JOURNAL OF PHYSICAL CHEMISTRY Letters

Letter

Cite This: J. Phys. Chem. Lett. 2017, 8, 5898-5906

pubs.acs.org/JPCL

Influence of the Carotenoid Composition on the Conformational Dynamics of Photosynthetic Light-Harvesting Complexes

Marijonas Tutkus,[†] Jevgenij Chmeliov,[†,‡] Danielis Rutkauskas,[†] Alexander V. Ruban,[§] and Leonas Valkunas*[,†,‡]

[†]Department of Molecular Compound Physics, Center for Physical Sciences and Technology, Saulėtekio Avenue 3, LT-10257 Vilnius, Lithuania

[‡]Institute of Chemical Physics, Faculty of Physics, Vilnius University, Saulėtekio Avenue 9, LT-10222 Vilnius, Lithuania

[§]The School of Biological and Chemical Sciences, Queen Mary, University of London, Mile End Road, London E1 4NS, United Kingdom

S *Supporting Information*

ABSTRACT: Nonphotochemical quenching (NPQ) is the major self-regulatory mechanism of green plants, performed on a molecular level to protect them from an overexcitation during the direct sunlight. It is believed that NPQ becomes available due to conformational dynamics of the light-harvesting photosynthetic complexes and involves a direct participation of carotenoids. In this work, we perform a single-molecule microscopy on major light-harvesting complexes (LHCII) from different *Arabidopsis thaliana* mutants exhibiting various carotenoid composition. We show how the distinct carotenoids affect the dynamics of the conformational switching between multiple coexisting light-emitting states of LHCII and demonstrate that properties of the quenched conformation are not influenced by the particular carotenoids available in LHCII. We also discuss the possible origin of different conformational states and relate them to the fluorescence decay kinetics observed during the bulk measurements.

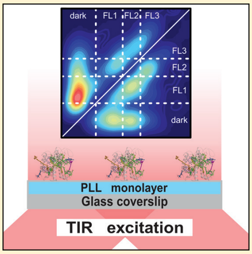

The importance of photosynthesis and its role in the Earth's ecosystem is difficult to overestimate: it is the key physiological process performed by green plants, algae, and some bacteria that is responsible for the initial step of biomass production and refilling the atmosphere with oxygen. To efficiently perform this task, distinct photosynthetic organisms have developed various photosynthetic apparatuses, different in structure but similar in design. Their "photosynthetic factories" comprise a huge number of pigment molecules, usually bound to a protein scaffold and distributed over a photosynthetic membrane.[1,2] Both the mutual arrangement of the pigments and their spectroscopic properties have been carefully adjusted by Nature to optimize an overall efficiency of the photosynthetic light-harvesting antenna: up to 99% of the absorbed photons are successfully utilized during the primary processes of photosynthesis.[1−4] While such an efficiency helps photosynthetic organisms to survive and to function at very low illumination conditions (like underwater environment or deep continuous shadow), bright sunlight might result in an overexcitation of the light-harvesting antenna and lead to the formation of highly reactive singlet oxygen species. In order to avoid any possible photodamage, over ages of evolution, plants have developed various self-regulatory mechanisms. The most efficient one, operating on a molecular level and dissipating the excess excitation as heat, reversibly forms and relaxes within several seconds to minutes and is commonly known as an energy-dependent (qE) part of nonphotochemical quenching (NPQ).[5] Many studies aiming to reveal the molecular origin of NPQ have been carried out over the last two decades (see, e.g., the recent review by Ruban et al.[5]), but the final answer is still to be found, although more evidence for the direct involvement of the carotenoid (Car) molecules appears.[6−11]

The larger part of the photosynthetic antenna of plants is built from the trimeric major light-harvesting complexes (LHCIIs) that bind more than 50% of all the terrestrial chlorophyll (Chl) molecules.[1] These complexes, however, are known not only for the efficient light harvesting, but also for participation in various regulatory processes. First, depending on the spectral composition of the incoming light, LHCII trimers can diffuse through the thylakoid membrane between different photosynthetic units to optimize their relative absorption cross-sections.[12] Besides that, LHCII complexes participate in the dynamic variation of the antenna size during high light conditions[13] and are also supposed to be the most probable location for the NPQ traps.[5]

The crystal structure of the LHCII complexes, known with a sub-3 Å resolution,[14] reveals the mutual arrangement of 8 Chl *a* and 6 Chl *b* molecules as well as 4 Car pigments: 2 luteins (Lut), 1 neoxanthin (Neo), and 1 xanthophyll cycle carotenoid (either violaxanthin (Vio) or zeaxanthin (Zea)) per each

Received: October 5, 2017
Accepted: November 15, 2017
Published: November 15, 2017

DOI: 10.1021/acs.jpclett.7b02634
J. Phys. Chem. Lett. 2017, 8, 5898−5906

monomeric subunit (see Figure 1a for schematic view). Neo, the most polar and asymmetric of these Cars, is found on a Chl *b*-rich peripheral side of LHCII. The xanthophyll cycle Car is located at the interface between the two monomeric subunits of the LHCII trimer. Exposure to high light results in a reversible de-epoxidation of Vio into Zea, which promotes the clustering of the LHCII complexes, leading to a more efficient excitation energy quenching.[5] Finally, the remaining two Cars, luteins, are arranged in a cross pattern and assist in holding the LHCII complex together.[14] This Car is also known to be responsible for the trimerization of LHCII;[15] therefore lutein-deficient plants are able to form only monomeric light-harvesting complexes.[16] Moreover, one of these luteins, namely Lut1, is located close to the so-called chlorophyll terminal emitter—the cluster of 3 Chl molecules of the lowest site energies, which makes it a favorable candidate to govern NPQ.[8]

To study the role of each carotenoid in light harvesting and self-regulation, the targeted mutagenesis of various photosynthetic antenna complexes has been widely applied.[6,16−22] By blocking the specific paths of Car biosynthesis, LHCIIs with different xanthophyll composition can be obtained, causing specific structural variations that affect the overall excitation energy dynamics in the light-harvesting antenna.[16] In this work, we utilize the methods of single molecule (SM) microscopy to examine fluorescence (FL) intensity fluctuations in single monomeric LHCII subunits from the lutein-deficient *Arabidopsis thaliana* mutants. In particular, we study the double mutant *npq1lut2*,[17] which is incapable of synthesizing either Zea or Lut and therefore accumulates only Vio and Neo, and the triple mutants *aba4npq1lut2*[20] and *npq2lut2*,[23] accumulating Vio and Zea, respectively, as the only carotenoid. The Car composition of these mutants is also summarized in Table 1. For reference, isolated trimeric LHCII complexes from unaffected wild-type (WT) *Arabidopsis thaliana* were also analyzed.

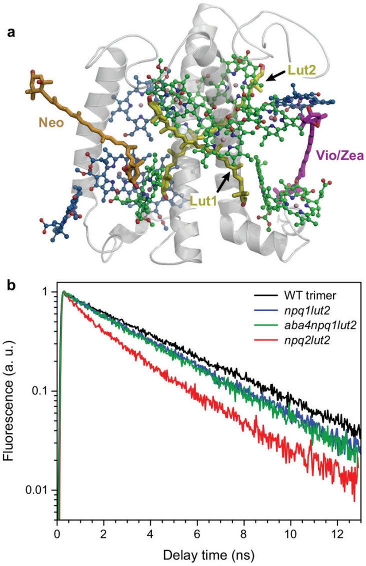

Figure 1. (a) Crystal structure of LHCII monomer and carotenoid binding sites (Lut1, Lut2, Neo, and Vio/Zea).[14] Chls *a* are indicated with green, Chls *b* with blue, both luteins with dark yellow, Vio with magenta, Neo with orange, and protein helices with gray. (b) Fluorescence decay kinetics in the detergent-solubilized LHCII complexes from WT *Arabidopsis thaliana* as well as *npq1lut2* (containing Vio and Neo carotenoids), *aba4npq1lut2* (binding Vio as the only Car), and *npq2lut2* (binding Zea as the only Car) mutants, measured at 273 K.

Fluorescence decay kinetics in the mentioned bulk solubilized LHCII samples, measured with a streak-camera at 273 K temperature, are shown in Figure 1b. Those in all mutants clearly demonstrate somewhat faster decay behavior compared to the WT species. Thus, replacement of the lutein pigments by the xanthophyll cycle carotenoid (either Vio or Zea) possibly opens some additional weak channel for excitation quenching, not available in wild-type LHCIIs. Since Neo is located in the Chl *b*-rich region of the LHCII monomer (cf. Figure 1a), its replacement by the Vio pigment in the *aba4npq1lut2* mutant does not influence the mean relaxation rate of the Chls *a* (mean excitation lifetimes in the *npq1lut2* and *aba4npq1lut2* mutants are 3.3 and 3.2 ns, respectively). Meanwhile, *npq2lut2* mutant, incapable of synthesizing any carotenoid except Zea, shows huge qualitative difference in the fluorescence decay kinetics, clearly exhibiting a strongly biexponential decay behavior contrary to all three of the other samples, demonstrating almost single-exponential decay (see Table S1 for lifetimes and their amplitudes). The appearance of the additional fast decay component of 0.8 ns strongly suggests that a new conformational state of the protein scaffold, notably enhancing excitation quenching, becomes available in this mutant. To perform further analysis of the intrinsic conformational states and their dynamics, we continued with SM microscopy measurements of single LHCII complexes, immobilized on the PLL modified glass coverslips in detergent micelles.

For our measurements, we used total internal reflection (TIR) objective-based microscope setup equipped with the EM-CCD camera working at 30 ms integration time and 635 nm laser excitation.[24] This method allowed us to subject LHCII complexes to the continuous <1 W/cm^2 illumination, which is considerably lower than typical intensities utilized in confocal microscopy,[25−30] thus we completely avoid any singlet−singlet and singlet−triplet annihilation (taking into account the absorption cross-section of an LHCII trimer of $\sigma = 1.4 \times 10^{-15}$ cm^2,[31] the probability of simultaneous generation of two singlet excited states is negligible, and the probability of accumulating a triplet state[32] is less than 1%). Nevertheless, such low illumination conditions are quite close to the mean natural solar radiation hitting the Earth surface during a sunny day. In addition, by using TIR microscopy, we excite only a

Table 1. Carotenoid Composition in the LHCII Samples Studied in This Work

sample	bound carotenoids
WT	Lut, Vio, and Neo
npq1lut2	Vio and Neo
aba4npq1lut2	Vio
npq2lut2	Zea

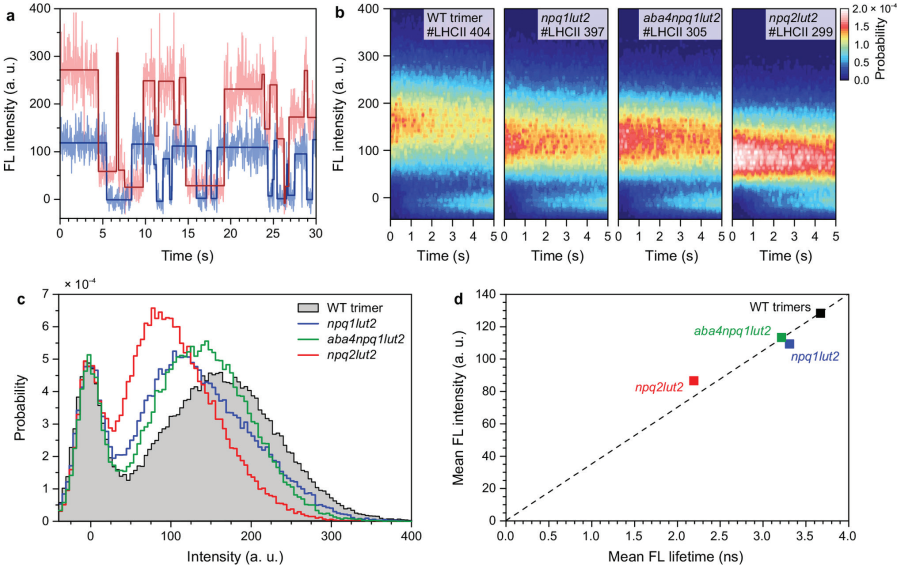

Figure 2. Fluorescence measurements in single LHCII complexes. (a) Two representative time traces of the fluorescence intensity fluctuations, measured for two different wild-type LHCII trimers (0 FL intensity level is set as the mean intensity value of the dark state). Dark step lines represent resolved intensity levels. (b) Color-coded distribution of the fluorescence intensities at different time delays, measured in WT LHCII trimers and LHCII monomers from *npq1lut2*, *aba4npq1lut2*, and *npq2lut2* mutants. These distributions were acquired by collecting fluorescence time traces similar to those shown in panel a, obtained from 300−400 (the exact number is indicated in each case) single LHCII complexes. (c) Total distribution of the resolved fluorescence intensity levels in four different LHCII samples shown in panel b. These distributions are normalized to unit area. (d) Correlation between the mean fluorescence intensities in the SM spectroscopy measurements, obtained from the FL intensity distributions shown in panel c, and the mean fluorescence lifetimes in the mentioned samples, obtained from the FL decay kinetics in the solubilized LHCIIs presented in Figure 1b.

small distance (~15 nm) perpendicular to the glass coverslip, which gives negligible background signal and enables much better signal-to-noise ratio than confocal microscopy. Since the signal from all the LHCII complexes is monitored mostly simultaneously, the whole measurement takes less time and guarantees that all of the measured complexes were exposed to very similar conditions. And finally, TIR setup is equipped with an EM-CCD camera, which has very high detection sensitivity (quantum efficiency about 80% in the region of LHCII emission), low noise, and excellent detection stability.

The acquired fluorescence signal coming from the single LHCII complexes exhibited a well-known blinking behavior,[25−30] when FL intensity switches quickly and reversibly between several stable emission levels as a result of the conformational variations of the protein scaffold[33] (see Figure 2a for the FL intensity fluctuations in two distinct wild-type LHCII trimers). Such time traces of the fluorescence intensity fluctuations were collected for 404 distinct WT LHCII trimers, and the time-dependent distribution of all the obtained emission levels is shown in the left panel of Figure 2b as a color-coded two-dimensional fluorescence map. This map reveals that the intensities of the highly emitting states are broadly distributed around the intensity level of ~160 a.u., whereas the second much narrower peak at ~0 a.u. represents nonfluorescing, or quenched, LHCII complexes (if the switching to this state was reversible) or, alternatively, the complexes being completely bleached (when the switching to the dark state was irreversible). Since only those single LHCII complexes initially being in their light-emitting conformational state were detected, there was a relatively small number of dark states detected during the first second. Later on, more complexes reversibly switch to the dark state, thus the zero-intensity level becomes populated more often. After ~25 s of continuous illumination, the majority of the detected complexes were bleached (cf. Figure S1). Only the part of the FL time trace prior to photobleaching of each LHCII complex was considered in any further analysis.

In order to compare the statistical properties of the fluorescence blinking in different LHCII samples, analogous measurements were also performed for LHCII monomers from three lutein-deficient mutants mentioned above. The obtained results are summarized in Figure 2b and qualitatively resemble those collected from the WT LHCII trimers. The most apparent difference is the decrease of the mean FL intensity of the fluorescing state in all the mutants compared to that in the WT samples. This difference becomes even clearer in Figure 2c, where the overall distribution of the resolved emission levels is demonstrated. Interestingly, FL intensity in the LHCII monomers from the mutants does not exhibit a 3-fold drop compared to the wild-type LHCII trimers: while in the wild-

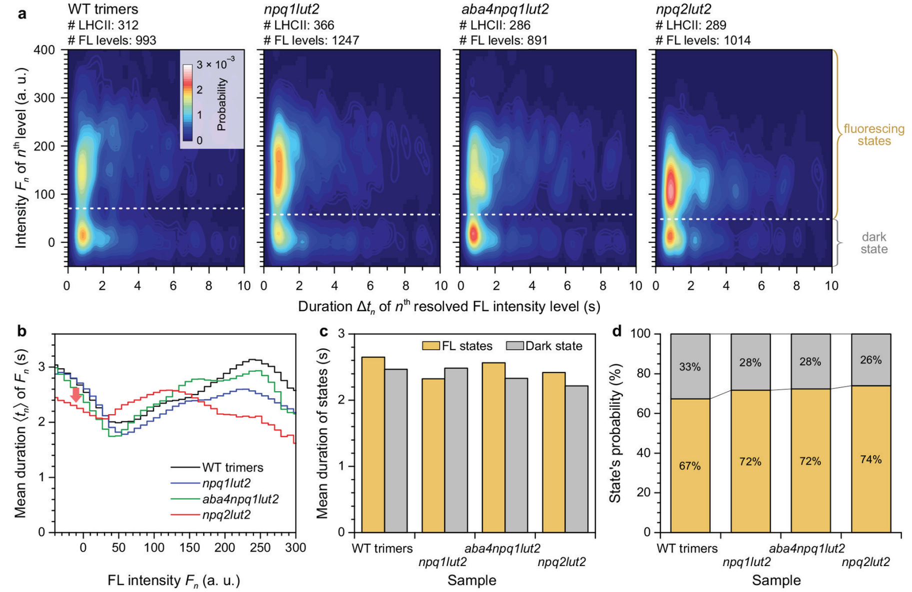

Figure 3. (a) Color-coded correlation between the fluorescence intensity level (vertical axis) and the duration of detected states (horizontal axis), obtained for wild-type LHCII trimers as well as monomeric LHCIIs from the *npq1lut2*, *aba4npq1lut2*, and *npq2lut2* mutants. The number of LHCII complexes analyzed and the number of the resolved FL intensity levels is indicated separately in each case. The assignment of the distinct FL intensity levels to the dark and fluorescing states is indicated with horizontal white dashed lines. (b) Mean durations of various FL intensity levels in the single LHCII complexes from different samples, obtained from the correlation maps in panel a by averaging them over horizontal axis. Red arrow indicates a notable drop in the mean duration of the quenched state in the *npq2lut2* mutant. (c) Overall mean duration of the fluorescing and dark states of single LHCII complexes from various samples. (d) The relative probabilities of the dark and fluorescing conformational states of various LHCII samples, obtained by integrating correlation maps in panel a over both vertical and horizontal axes within the domains separated by the white dashed lines.

type LHCII complexes the emission intensities of the highly fluorescing states are distributed around 160 a.u., the corresponding peak intensity dropped by ∼ one-quarter in the *npq1lut2* and *aba4npq1lut2* mutants (115 and 130 a.u., respectively). This indicates that, under our illumination conditions, the probability to absorb three photons per trimer while all its monomeric subunits are in the high-emitting state, might be rather low (see also Methods), although the possibility for trimeric and monomeric complexes to experience slightly different environments (e.g., they can be differently orientated during their immobilization on the PLL glass coverslip) also cannot be disregarded.

Distributions of FL intensities in both *npq1lut2* and *aba4npq1lut2* mutants are very similar, again demonstrating that the replacement of the Neo with Vio in the latter one does not significantly change the overall excitation dynamics in LHCII. Meanwhile, in the LHCII monomers from *npq2lut2* mutant, the drop in observed FL intensities was even more pronounced and exceeded 45% in these complexes—the dominating fluorescence intensity decreased down to 85 a.u. In all the mutants, not only the maximum position of the band of the FL intensities of the strongly fluorescing states shifted toward lower intensities (comparing to the WT samples), but also the amplitude of this band (i.e., the number of occurrences of the corresponding FL levels) increased, while the width of this band decreased accordingly. Interestingly, neither the amplitude nor the width of the band corresponding to the nonfluorescing state exhibited any differences between different LHCII samples, suggesting the same physical origin of the dark state in all the cases. Indeed, distribution of intensities around this dark state was fitted with a Gaussian function, and its width within the fitting error was the same as for the bleached spot intensity distributions shown in Figure S1b (20.4 ± 1.9 and 20.6 ± 0.48 a.u., respectively). By taking an average of the whole distribution shown in Figure 2c, including the quenched and fluorescing states, the mean fluorescence intensities in different samples were calculated. These mean intensities correlate with the mean FL lifetimes observed during the bulk measurements, as shown in Figure 2d. Thus, we can conclude that the FL decay kinetics, reflecting excitation dynamics that occurs within the complex on a nanosecond time scale, is strongly related to the conformational dynamics of the complex as a single unit, taking place on a time scale from milliseconds to several seconds.

All four LHCII samples studied in this work exhibited a very broad distribution of the intensity levels of the fluorescing states. Thus, several distinct conformational states of the light-harvesting complexes, each corresponding to some specific

DOI: 10.1021/acs.jpclett.7b02634
J. Phys. Chem. Lett. 2017, 8, 5898−5906

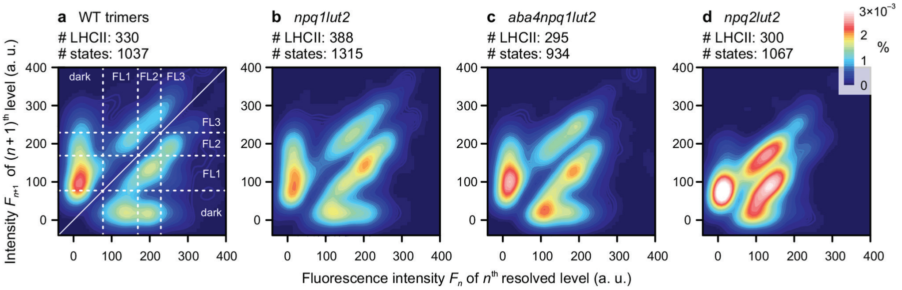

Figure 4. Transitions between different conformational states. (a) Two-dimensional transition density (TD) histogram plot for WT LHCII trimers, showing correlation between the mean intensity F_n of nth state (horizontal axis) and the mean intensity F_{n+1} of the following $(n + 1)$th state (vertical axis). The number of single LHCII trimers and the numbers of the resolved FL intensity levels are indicated at the top. The TD map is normalized to 1, and the color scale on the right indicates the probability of the corresponding transition $F_n \rightarrow F_{n+1}$. The observed cross-peaks correspond to the conformational switching between different states of LHCII, denoted as "dark", "FL1", "FL2" and "FL3" and separated with white dashed lines. LHCII monomers from the carotenoid mutants exhibit qualitatively similar correlation maps (b−d).

dominating fluorescence intensity, might coexist, as suggested previously.[25,29] To address this issue and to characterize the possible conformational states, we have first evaluated the correlation between each resolved FL intensity level (F_n) and the time duration Δt_n that each LHCII complex was fluorescing with that particular intensity before a transition to another intensity level (F_{n+1}) occurred. The resulting two-dimensional histogram plots are shown in Figure 3a and demonstrate that the wide distribution of the intensities of the active (highly fluorescing) LHCII state in Figure 2c indeed has some intrinsic structure. For example, in the case of WT LHCII species, we can identify at least two distinct fluorescing states: one with the dominating fluorescence intensity around 150 a.u. and another around 230 a.u. The former state is more probable, but its duration on average is shorter. Qualitatively similar correlation pattern is obtained in LHCII mutants, although the dominating fluorescence intensities of the bright states are reduced.

Most of the detected FL intensity levels had a duration from several hundreds of milliseconds to ~3 s, but longer-living states were also observed, in accordance with the well-known power-law distribution.[25,26] By averaging the correlation maps in Figure 3a over the horizontal axis, we obtain the mean durations $\langle \Delta t_n(F_n) \rangle$ of each resolved FL intensity level F_n, as shown in Figure 3b. While the mean duration of the FL intensity levels corresponding to the dark states (those around $F_n = 0$) in both *npq1lut2* and *aba4npq1lut2* mutants remain the same as in WT LHCII trimers, those in the *npq2lut2* exhibit a notable drop, as indicated by the red arrow in Figure 3b. On average, the dark conformation survives for 2.5 s in both WT trimers and *npq1lut2* mutants, its mean duration then decreased to 2.3 s in *aba4npq1lut2* and further dropped down to 2.2 s in the *npq2lut2* mutant (see Figure 3c). The description of the fluorescing states is complicated by the coexistence of multiple distinct conformations, thus only the mean duration of all these fluorescing conformational states can be reliably evaluated: while being 2.7 s in WT complexes, it decreases by 0.4, 0.1, and 0.3 s in *npq1lut2, aba4npq1lut2*, and *npq2lut2*, respectively. This results in slightly faster conformational dynamics in all the mutants compared to the wild-type LHCII trimers.

Finally, by integrating correlation maps shown in Figure 3a over both vertical and horizontal axes within the domains corresponding to the emitting and quenched states and separated by the white dashed lines, we can evaluate the overall probabilities of fluorescing and dark states, as demonstrated in Figure 3d. Counterintuitively, we see the stabilization of the fluorescing states (manifesting itself via 57% increase in probability) in all the mutants compared to the WT samples, despite the fact that the drop in the overall mean FL intensity and mean excitation lifetime, observed in the mutants and discussed above, would suggest an opposite effect. This could indicate that replacement of luteins by either Vio or Zea pigments results in more pronounced switching between different fluorescing conformational states and, accordingly, less frequent "visiting" of the quenched conformation.

To check this suggestion and to highlight the conformational dynamics between different conformational states of the LHCII complex, we have also calculated the correlation pattern of the intensities of two detected subsequent fluorescence levels (F_n and F_{n+1}). The resulting two-dimensional transition density (TD) histogram, describing probabilities of different transitions between the detected states (F_n) in the single-molecule fluorescence intensity traces from WT trimeric LHCIIs, is presented in Figure 4a. This TD map shows a complex landscape and further reveals the hidden structure of the main emission intensity band. Indeed, we can clearly distinguish several cross-peaks corresponding to various transitions between different conformational states: one such state is readily attributed to the aforementioned dark state (with FL intensity around 0 a.u.). However, we can also resolve at least three distinct fluorescing states corresponding to the fluorescence intensities of ~100−130 a.u., ~200 a.u., and ~250 a.u. (denoted in Figure 4a as FL1, FL2, and FL3, respectively). We can also note the asymmetry between different transition pathways: the most dominating transition corresponds to the conformational switch of the LHCII complex from the dark state into FL1 state, whereas the repopulation of the dark state occurs from both FL1 and FL2 states. Somewhat less probable transitions occur between FL2 and FL1 states as well as FL3 and FL2 states. Moreover, the elongation of the cross-peaks along the main diagonal rather reveals a high level of inhomogeneity of FL emission in different single LHCII complexes (see also FL time traces in

Figure 2a, exhibiting various FL intensities of the fluorescing states for distinct LHCIIs).

The corresponding TD maps, obtained for the lutein-deficient LHCII complexes, are shown in Figure 4b−d. Both *npq1lut2* and *aba4npq1lut2* mutants exhibit very similar transition pattern as the wild-type samples, except for the general drop in FL intensity. However, one can also note more frequent switching between distinct fluorescent states (represented by the increased amplitude of the cross-peaks at $F_n \approx 200$ and $F_{n+1} \approx 150$ a.u. and vice versa), thus supporting the suggestion made above. This effect is even more pronounced in the case of *npq2lut2*, shown in Figure 4d. In this mutant, only the emitting state corresponding to the *lowest* FL intensity is involved in the reversible transitions to/from the quenched state, whereas the conformational states attributed to higher FL intensity participate only in the switching to/from other emitting states.

Based on our measurements, several conclusions regarding conformational dynamics of LHCII complexes can be drawn. First of all, the mean fluorescence intensity, observed during the SM measurements and related to protein conformation dynamics, correlates with the time scale of fluorescence decay kinetics, representing excitation energy transfer and relaxation within the complex. Next, SM microscopy revealed a rather high level of heterogeneity of single LHCII complexes and quite complex conformational energy landscape. In particular, besides the quenched state, the coexistence of at least three distinct fluorescing conformational states, attributed to different FL intensity levels and experiencing strongly asymmetric switching between themselves, was revealed. Each such state might correspond to slightly different mutual arrangements of the pigment molecules within the LHCII complex and, as suggested earlier,[29] result in different time scales of excitation energy dynamics between the pigment molecules. Therefore, partially quenched, but still fluorescing state(s) might explain any nonexponentiality observed during the time-resolved fluorescence measurements.

We have also demonstrated that the replacement of the lutein pigments with either Vio or Zea, preventing the formation of tightly bound trimeric complexes, results in faster conformational dynamics compared to that observed in WT LHCII trimers. This explains why such monomeric pigment−protein complexes are more sensitive to a varying environment such as lumen protons, as was previously observed during the *in vitro* experiments.[34] Meanwhile, the fact that all the samples exhibited fluorescence blinking behavior and the observed properties of the dark conformational state were rather similar regardless of the carotenoid compositions reveals the identical nature of the quenching mechanism in all these LHCII complexes. Our observations suggest that not a particular carotenoid but rather a carotenoid that is bound to a specific binding locus acts as quenchers. Hence, the variability of LHCII carotenoid types is less critical than their environment. This result indirectly supports the model, attributing NPQ to the incoherent excitation energy transfer from Chl molecule to the optically dark short-lived S_1 state of the available carotenoid.[8] Indeed, the coherent mixing of the Car and Chl excitonic states or, alternatively, the formation of the Car−Chl charge-transfer state would be very sensitive to the exact position of the Car S_1 energy level (with respect to the site energies of the nearby chlorophylls) and therefore would lead to different results in different samples. On the other hand, very broad density-of-states distribution of the Car S_1 transition results in very weak effect of both the Car S_1 site energy and small variations in the Chl−Car couplings (expected to take place in our different samples with various carotenoid composition) on the rate of the incoherent Chl → Car excitation transfer.[35,36]

Nevertheless, the carotenoid composition does have some effect on the conformational switching of the LHCII complex between different emitting states. That is not surprising since carotenoids are essential structural elements of the light-harvesting complexes and, as such, they can affect the overall structure that, in its turn, influences the blinking behavior. However, transition density patterns, shown in Figure 4, reveal that the replacement of the luteins with Vio in both *npq1lut2* and *aba4npq1lut2* mutants results in very subtle structural variations that do not change the overall conformational dynamics of the LHCII monomer, but makes switching between the strongly and moderately fluorescing states more probable than in the WT samples. As a result, we observe somewhat smaller mean fluorescence intensity (Figure 2c) and slightly faster excitation decay kinetics (Figure 1b). Very similar results, obtained for both these mutants, also confirm that the Neo binding site in the Chl *b*-rich peripheral side participates neither in fluorescence quenching nor in the conformational dynamics of the pigment protein complex as a whole. On the other hand, the *npq2lut2* LHCII monomers, containing Zea as the only carotenoid, demonstrated even more pronounced switching between fluorescing and partially quenched states, which is in line with the observed nonexponentiality in fluorescence decay kinetics. The qualitative differences, observed for this mutant both in the bulk measurements (see Figure 1b) and by means of single-molecule microscopy (see Figures 3b and 4d), suggest that (at lest in this mutant) the mentioned partially quenching state cannot be simply the result of very fast switching between the fully quenched and fluorescing conformations, occurring within the binning time. Rather, some additional factors should be involved. The physical origin of this partially quenched conformational state could be related to the formation of Chl−Zea charge transfer state; the signatures of the presence of a Zea^+ radical cation were indeed observed earlier in the Zea-enriched photosynthetic antenna.[6,21] All these properties again demonstrate very flexible and highly adaptable self-regulation of plants, in general capable to dissipate the excess excitation energy using any carotenoids available and, if needed, also being prone to further fine-tuning by utilizing xanthophyll cycle to produce Zea and the corresponding partially quenched conformational state of the protein scaffold.

■ METHODS

Sample Preparation. Unstacked thylakoids were prepared from 100 g of dark-adapted *Arabidopsis thaliana* leaves with the midrib removed. Leaves were homogenized in 300 mL of icy grinding medium (0.33 Msorbitol, 10 mM Na4P2O7·H2O and 130 mg D-iso-ascorbate; pH 6.5) and the homogenate filtered through a bilayer of muslin cloth, followed by a secondary filtration through four layers of muslin interlaid with cotton wool. Thylakoids were then centrifuged (4000 × *g*) for 10 min and the pellet gently resuspended in washing medium (0.33 M sorbitol and 10 mM MED) before additional centrifugation. The pellet was then resuspended in resuspension medium (0.33 M sorbitol, 1 mM EDTA, 50 mM HEPES; pH 7.6) and osmotically shocked by mixing in 50 mL of break medium (10 mM HEPES; pH 7.6). After 30 s, osmotic potential was returned to normal with the addition of 50 mL of osmoticum medium (0.66 M sorbitol, 40 mM MES; pH 6.5) and thylakoids centrifuged (4000 × g) for 10 min. The final pellet was resuspended in resuspension medium, and aliquots were frozen immediately in liquid nitrogen. The major LHCII complex was isolated from unstacked *Arabidopsis thaliana* thylakoids using isoelectric focusing.[37] The protein band corresponding to LHCII was collected and eluted in elution buffer containing 0.01% n-dodecyl β-D-maltoside (~200 μM), then followed by size exclusion purification to remove ampholites (PD-10 columns, GE Healthcare). Aliquots of LHCII prepared at the same concentration (OD = 6) were immediately frozen in liquid nitrogen for later use in fluorescence analyses. While studying WT samples, we preferred not to use any additional artificial treatments of the isolated trimeric LHCII complexes, such as phospholipase, which is crucial for the monomerization of the trimers. Hence, we can compare the conformational dynamics in the naturally occurring WT LHCII trimers with that in the naturally occurring monomers of the mutant plants.

Streak Camera Measurements. Time-resolved fluorescence dynamics of the samples were measured by means of Hamamatsu C5680 streak camera with M5677 single-sweep module coupled to a spectrometer. Femtosecond Yb:KGW oscillator (Pharos, Light Conversion Ltd.) with a frequency doubler (HIRO, Light Conversion Ltd.) producing 515 nm sub-100 fs pulses at a 76 MHz repetition rate was employed, and a pulse picker was used to reduce the repetition rate to 20 kHz for nanosecond time scales. The beam was attenuated down to about 100 pJ per pulse and focused into about 100 μm spot on the sample. No intensity dependence was observed when increasing the pulse energies by an order of magnitude or during the measurement process. The temporal resolution of the whole system was ~100 ps. All the measurements were performed at 273 K in a fused silica cell of 0.1 mm optical path. The obtained fluorescence decay kinetics, shown in Figure 1b, were independent of the detection wavelength (see Figure S2 for details).

Single-Molecule Microscopy Measurements. Buffer Solution: Buffer1: 10 mM Hepes (>99.5 Buffer grade, Carl-Roth Art.-Nr: HN07.1), 1 mM MgCl2 (>99 Cell pure, Carl-Roth Art.-Nr: HN78.2), 0.03% w/v Ÿ-DM (Lauryl-β-D-maltoside, > 99% for biochemistry, Art. CN26.2), pH = 7.8

Cleaning of Coverslips: Glass coverslips (Menzel-glaser #1.5) were placed in a staining jar and rinsed 3 times with ultrapure water (LaboStar, Siemens). Water was exchanged with 1% Alconox detergent solution (Alconox powdered precision cleaner) and the jar sonicated for 10 min (Ultrasonic Cleaning Unit RK 102H, Bandelin). Detergent solution was discarded from the jar and rinsed four times with ultrapure water. Water was exchanged with isopropanol (2-propanol ≥99.5%, art.no.:9866.6 Carl-Roth). Isopropanol was discarded, and the jar with coverslips was vacuumed in the plasma machine (PDC-002, Harric plasma) for 20 min, then plasma etched at ~400 mTorr pressure using maximal power for 5 min.

Surface Modification of Coverslips and Flow Cell Assembling: Clean glass coverslips were incubated with 0.01% of PLL (P4707 Sigma) for 10 min, then rinsed with Milli-Q, dried and assembled into the flow cell (sticky-slide VI 0.4, 80608, IBIDI) with the PLL modified side facing the sticky slide. Tubings were inserted into the inlet and outlet port of the cell and channel was filled with buffer1.

LHCII Immobilization and Imaging: 1.5e+05 diluted LHCII (2 μg/mL) dissolved in buffer1 were injected into the flow cell channel and incubated for 3 min. 300 μL of the buffer1 was injected to wash out the excess of unbound LHCII. For microscopy 100 μL of buffer1 containing 15 units/ml glucose oxidase (from *Aspergillus niger*, G6125, Sigma-aldrich), 1% glucose (Ÿ-D-Glucose, G0047,TCI AMERICA). Measurements were performed at 23 °C.

SM TIRF Microscopy: The SM fluorescence microscopy setup used in this study was essentially the same as described previously except for a few important improvements.[38] All the dichroic mirrors in the setup were replaced with 2 mm thick TIRF flat parts glued in metal filter cubes (91032, Chroma). The 635 nm continuous-wave laser beam is expanded 66x. The laser beam was reflected off and the resulting fluorescence was transmitted through a zt532/635rps-XT (Chroma) dual-band dichroic mirror. The excitation light was filtered off by a quadruple-band interference filter FF01-446/510/581/703 (Semrock). The fluorescence image was split into two spectral components by T640lpxr-UF2 (Chroma) dichroic mirror. The 635 nm excitation intensity behind the objective was 0.6 mW and exposure time was 30 ms. In TIRF microscopy, light beam after passing the objective enters the sample with the high angle of incidence, so that at the interface of the regions with two different refractive indexes the evanescence field is generating, and technically it is difficult to measure its exact intensity.[39] However, according to our estimations, it should be far less than 1 W/cm^2, which corresponds to less than ~3 × 10^{18} photons per second per cm^2. Hence taking into account the mean absorption cross-section of the LHCII trimer, $\sigma = 1.4 \times 10^{-15}$ cm^2,[31] we conclude that the absorption rate should not exceed ~4500 photons per second per LHCII trimer.

In the EM-CCD camera used in this work, one detected photon corresponds to ~34 counts. The signal intensity (denoted in this work with a.u.) represents the amplitude of the 2D Gaussian fit, whose width was held constant and on average was equal to $s = 1.33$ pixels for all the detected spots. Therefore, one detected photon corresponds to the $34/(2\pi s^2)$ a.u. = 3 a.u.

Data Analysis. All data analysis procedures were performed and graphs prepared in Igor Pro (Wavemetrics) program using a custom written analysis package (available upon direct request to the author or under the link: http://www.igorexchange.com/project/TEA_MT). To detect immobilized LHCII, fluorescent spots were detected in images acquired using 635 nm laser. To make this detection more reliable, several frames from the beginning of the image series were averaged. From this averaged image a filtered image, enhancing the fluorescent spots, was generated and converted into a fluorescent spot probability image.[40] Spots having the probability above the manually defined value were fitted to the 2D symmetrical Gaussian to extract precise center position and width. Spots having higher than manually defined fitting error and center positions closer than 3 pixels were rejected. Intensity-versus-time dependency was extracted for all accepted spots from the series of images acquired at 635 nm excitation using 2D symmetrical Gaussian fit (center position and width was held constant). SM intensity was expressed by an amplitude of the 2D Gaussian fit. When LHCII switches into the dark state or bleaches out, the intensity of the local background becomes similar or sometimes even higher than in the center of the previously fluorescing spot. Therefore, sometimes intensity that we record becomes negative (i.e., the amplitude of the 2D Gaussian becomes less than 0). Hence in Figures 2−4, the 0 a.u. level can be treated as the mean intensity of the dark state. Finally, manual check and selection of those signals showing

DOI: 10.1021/acs.jpclett.7b02634
J. Phys. Chem. Lett. 2017, 8, 5898−5906

characteristic single-molecule features (typical single-molecule fluorescence intensity and a single bleaching step) was performed. Only that selected data was used to make plots. SM fluorescence intensity traces were idealized using a custom-made intensity change point (ICP) detection algorithm without clustering. This algorithm is similar to a previously published method,[25] except that amplitude of the ICP is a constant and predefined by the user. Basically, it scans a trace point-by-point with an 8 point window, takes an average of the first 4 points and the last 4 points within the window and calculates a step amplitude (the difference between the averages) that is then compared with some threshold value. The latter was found empirically by testing different numerical values. Value of 40 a.u. for WT LHCII was high enough not to find any steps in the bleached part of the signal and low enough not to miss any significant steps in the active part of the signal. Next, we calculated step amplitude thresholds for mutant samples by multiplying the step amplitude of WT LHCII with a ratio between mean fluorescence intensity of WT and each of the mutant samples (Figure 2d). For example, for the *npq1lut2* and *aba4npq1lut2* mutants, 40/(125/110) = 35 a.u., and for *npq2lut2*, 40/(125/80) = 25 a.u. In the case where the step amplitude is higher than this threshold value, the center position of this window is recorded as a putative ICP. To be accepted, an ICP has to fulfill the criteria for the durations and slopes of the states it separates. Both states have to be not shorter than half of the scanning window length. The sum of the absolute slope values of the line fits of the states has to be smaller than a set value of 10.

■ ASSOCIATED CONTENT

Supporting Information

The Supporting Information is available free of charge on the ACS Publications website at DOI: 10.1021/acs.jpclett.7b02634.

> Biexponential description of the fluorescence decay kinetics shown in Figure 1b, distributions of the fluorescence intensities at different time delays, demonstrating the bleaching of the observed single LHCII complexes, and fluorescence decay kinetics in various samples, detected at different wavelengths during the bulk streak camera measurements (PDF)

■ AUTHOR INFORMATION

Corresponding Author

*E-mail: leonas.valkunas@ff.vu.lt.

ORCID

Marijonas Tutkus: 0000-0002-5795-1347
Jevgenij Chmeliov: 0000-0002-7591-1373
Danielis Rutkauskas: 0000-0003-4705-2222

Notes

The authors declare no competing financial interest.

■ ACKNOWLEDGMENTS

We would like to acknowledge Prof. Luca Dall'Osto for providing us with the seeds of *aba4npq1lut2* mutant, Dr. Petra Ungerer for providing the samples, Egidijus Songaila for the streak-camera fluorescence measurements, and Oskaras Venckus for help with the data analysis. J.C. and L.V. were supported by the Research Council of Lithuania (LMT Grant No. MIP-080/2015). A.R. was supported by The Royal Society Wolfson Research Merit Award and U.K. BBSRC Grant BB/L019027/1.

■ REFERENCES

(1) van Amerongen, H.; Valkunas, L.; van Grondelle, R. *Photosynthetic Excitons*; World Scientific: Singapore, 2000.

(2) Blankenship, R. E. *Molecular Mechanisms of Photosynthesis*, 2nd ed.; Wiley Blackwell: Chichester, U.K., 2014.

(3) Fleming, G. R.; Schlau-Cohen, G. S.; Amarnath, K.; Zaks, J. Design Principles of Photosynthetic Light-Harvesting. *Faraday Discuss.* **2012**, *155*, 27−41.

(4) Croce, R.; van Amerongen, H. Natural Strategies for Photosynthetic Light Harvesting. *Nat. Chem. Biol.* **2014**, *10*, 492−501.

(5) Ruban, A. V.; Johnson, M. P.; Duffy, C. D. P. The Photoprotective Molecular Switch in the Photosystem II Antenna. *Biochim. Biophys. Acta, Bioenerg.* **2012**, *1817*, 167−181.

(6) Holt, N. E.; Zigmantas, D.; Valkunas, L.; Li, X. P.; Niyogi, K. K.; Fleming, G. R. Carotenoid Cation Formation and the Regulation of Photosynthetic Light Harvesting. *Science* **2005**, *307*, 433−436.

(7) Pascal, A. A.; Liu, Z. F.; Broess, K.; van Oort, B.; van Amerongen, H.; Wang, C.; Horton, P.; Robert, B.; Chang, W. R.; Ruban, A. Molecular Basis of Photoprotection and Control of Photosynthetic Light-Harvesting. *Nature* **2005**, *436*, 134−137.

(8) Ruban, A. V.; Berera, R.; Ilioaia, C.; van Stokkum, I. H. M.; Kennis, J. T. M.; Pascal, A. A.; van Amerongen, H.; Robert, B.; Horton, P.; van Grondelle, R. Identification of a Mechanism of Photoprotective Energy Dissipation in Higher Plants. *Nature* **2007**, *450*, 575−578.

(9) Ahn, T. K.; Avenson, T. J.; Ballottari, M.; Cheng, Y. C.; Niyogi, K. K.; Bassi, R.; Fleming, G. R. Architecture of a Charge-Transfer State Regulating Light Harvesting in a Plant Antenna Protein. *Science* **2008**, *320*, 794−797.

(10) Staleva, H.; Komenda, J.; Shukla, M. K.; Šlouf, V.; Kaňa, R.; Polívka, T.; Sobotka, R. Mechanism of Photoprotection in the Cyanobacterial Ancestor of Plant Antenna Proteins. *Nat. Chem. Biol.* **2015**, *11*, 287−291.

(11) Chmeliov, J.; Gelzinis, A.; Songaila, E.; Augulis, R.; Duffy, C. D. P.; Ruban, A. V.; Valkunas, L. The Nature of Self-Regulation in Photosynthetic Light-Harvesting Antenna. *Nat. Plants* **2016**, *2*, 16045.

(12) Allen, J. F. Protein Phosphorylation in Regulation of Photosynthesis. *Biochim. Biophys. Acta, Bioenerg.* **1992**, *1098*, 275−335.

(13) Belgio, E.; Kapitonova, E.; Chmeliov, J.; Duffy, C. D. P.; Ungerer, P.; Valkunas, L.; Ruban, A. V. Economic Photoprotection in Photosystem II That Retains a Complete Light-Harvesting System with Slow Energy Traps. *Nat. Commun.* **2014**, *5*, 4433.

(14) Liu, Z. F.; Yan, H. C.; Wang, K. B.; Kuang, T. Y.; Zhang, J. P.; Gui, L. L.; An, X. M.; Chang, W. R. Crystal Structure of Spinach Major Light-Harvesting Complex at 2.72 Å Resolution. *Nature* **2004**, *428*, 287−292.

(15) Bishop, N. I. The *β,ε*-Carotenoid, Lutein, is Specifically Required for the Formation of the Oligomeric Forms of the Light Harvesting Complex in the Green Alga, *Scenedesmus obliquus*. *J. Photochem. Photobiol., B* **1996**, *36*, 279−283.

(16) Fuciman, M.; Enriquez, M. M.; Polívka, T.; Dall'Osto, L.; Bassi, R.; Frank, H. A. Role of Xanthophylls in Light Harvesting in Green Plants: A Spectroscopic Investigation of Mutant LHCII and Lhcb Pigment−Protein Complexes. *J. Phys. Chem. B* **2012**, *116*, 3834−3849.

(17) Niyogi, K. K.; Shih, C.; Chow, W. S.; Pogson, B. J.; DellaPenna, D.; Björkman, O. Photoprotection in a Zeaxanthin- and Lutein-Deficient Double Mutant of Arabidopsis. *Photosynth. Res.* **2001**, *67*, 139−145.

(18) Bode, S.; Quentmeier, C. C.; Liao, P.-N.; Hafi, N.; Barros, T.; Wilk, L.; Bittner, F.; Walla, P. J. On the Regulation of Photosynthesis by Excitonic Interactions between Carotenoids and Chlorophylls. *Proc. Natl. Acad. Sci. U. S. A.* **2009**, *106*, 12311−12316.

(19) Müller, M. G.; Lambrev, P.; Reus, M.; Wientjes, E.; Croce, R.; Holzwarth, A. R. Singlet Energy Dissipation in the Photosystem II Light-Harvesting Complex Does Not Involve Energy Transfer to Carotenoids. *ChemPhysChem* **2010**, *11*, 1289−1296.

(20) Ware, M. A.; Dall'Osto, L.; Ruban, A. V. An In Vivo Quantitative Comparison of Photoprotection in Arabidopsis Xanthophyll Mutants. *Front. Plant Sci.* **2016**, *7*, 841.

(21) Dall'Osto, L.; Cazzaniga, S.; Bressan, M.; Paleček, D.; Židek, K.; Niyogi, K. K.; Fleming, G. R.; Zigmantas, D.; Bassi, R. Two Mechanisms for Dissipation of Excess Light in Monomeric and Trimeric Light-Harvesting Complexes. *Nat. Plants* **2017**, *3*, 17033.

(22) Tian, L.; Xu, P.; Chukhutsina, V. U.; Holzwarth, A. R.; Croce, R. Zeaxanthin-Dependent Nonphotochemical Quenching Does Not Occur in Photosystem I in the Higher Plant *Arabidopsis thaliana*. *Proc. Natl. Acad. Sci. U. S. A.* **2017**, *114*, 4828−4832.

(23) Havaux, M.; Dall'Osto, L.; Cuiné, S.; Giuliano, G.; Bassi, R. The Effect of Zeaxanthin as the Only Xanthophyll on the Structure and Function of the Photosynthetic Apparatus in Arabidopsis thaliana. *J. Biol. Chem.* **2004**, *279*, 13878−13888.

(24) Tutkus, M.; Marciulionis, T.; Sasnauskas, G.; Rutkauskas, D. DNA-Endonuclease Complex Dynamics by Simultaneous FRET and Fluorophore Intensity in Evanescent Field. *Biophys. J.* **2017**, *112*, 850−858.

(25) Krüger, T. P. J.; Ilioaia, C.; van Grondelle, R. Fluorescence Intermittency from the Main Plant Light-Harvesting Complex: Resolving Shifts between Intensity Levels. *J. Phys. Chem. B* **2011**, *115*, 5071−5082.

(26) Krüger, T. P. J.; Ilioaia, C.; Valkunas, L.; van Grondelle, R. Fluorescence Intermittency from the Main Plant Light-Harvesting Complex: Sensitivity to the Local Environment. *J. Phys. Chem. B* **2011**, *115*, 5083−5095.

(27) Krüger, T. P. J.; Wientjes, E.; Croce, R.; van Grondelle, R. Conformational Switching Explains the Intrinsic Multifunctionality of Plant Light-Harvesting Complexes. *Proc. Natl. Acad. Sci. U. S. A.* **2011**, *108*, 13516−13521.

(28) Krüger, T. P. J.; Ilioaia, C.; Johnson, M. P.; Ruban, A. V.; Papagiannakis, E.; Horton, P.; van Grondelle, R. Controlled Disorder in Plant Light-Harvesting Complex II Explains Its Photoprotective Role. *Biophys. J.* **2012**, *102*, 2669−2676.

(29) Schlau-Cohen, G. S.; Yang, H.-Y.; Krüger, T. P. J.; Xu, P.; Gwizdala, M.; van Grondelle, R.; Croce, R.; Moerner, W. E. Single-Molecule Identification of Quenched and Unquenched States of LHCII. *J. Phys. Chem. Lett.* **2015**, *6*, 860−867.

(30) Kondo, T.; Pinnola, A.; Chen, W. J.; Dall'Osto, L.; Bassi, R.; Schlau-Cohen, G. S. Single-Molecule Spectroscopy of LHCSR1 Protein Dynamics Identifies Two Distinct States Responsible for Multi-Timescale Photosynthetic Photoprotection. *Nat. Chem.* **2017**, *9*, 772−778.

(31) Krüger, T. P. J.; Novoderezhkin, V. I.; Ilioaia, C.; van Grondelle, R. Fluorescence Spectral Dynamics of Single LHCII Trimers. *Biophys. J.* **2010**, *98*, 3093−3101.

(32) Gruber, J. M.; Chmeliov, J.; Krüger, T. P. J.; Valkunas, L.; van Grondelle, R. Singlet-Triplet Annihilation in Single LHCII Complexes. *Phys. Chem. Chem. Phys.* **2015**, *17*, 19844−19853.

(33) Gwizdala, M.; Berera, R.; Kirilovsky, D.; Van Grondelle, R.; Krüger, T. P. Controlling Light Harvesting with Light. *J. Am. Chem. Soc.* **2016**, *138*, 11616−11622.

(34) Ruban, A. V.; Young, A. J.; Horton, P. Dynamic Properties of the Minor Chlorophyll *a*/*b* Binding Proteins of Photosystem II, an *in vitro* Model for Photoprotective Energy Dissipation in the Photosynthetic Membrane of Green Plants. *Biochemistry* **1996**, *35*, 674−678.

(35) Balevičius, V.; Gelzinis, A.; Abramavicius, D.; Mančal, T.; Valkunas, L. Excitation Dynamics and Relaxation in a Molecular Heterodimer. *Chem. Phys.* **2012**, *404*, 94−102.

(36) Fox, K. F.; Balevičius, V.; Chmeliov, J.; Valkunas, L.; Ruban, A. V.; Duffy, C. D. P. The Carotenoid Pathway: What is Important for Excitation Quenching in Plant Antenna Complexes? *Phys. Chem. Chem. Phys.* **2017**, *19*, 22957−22968.

(37) Ruban, A. V.; Young, A. J.; Pascal, A. A.; Horton, P. The Effects of Illumination on the Xanthophyll Composition of the Photosystem II Light-Harvesting Complexes of Spinach Thylakoid Membranes. *Plant Physiol.* **1994**, *104*, 227−234.

(38) Rutkauskas, D.; Petkelyte, M.; Naujalis, P.; Sasnauskas, G.; Tamulaitis, G.; Zaremba, M.; Siksnys, V. Restriction Enzyme Ecl18kI-Induced DNA Looping Dynamics by Single-Molecule FRET. *J. Phys. Chem. B* **2014**, *118*, 8575−8582.

(39) Martin-Fernandez, M.; Tynan, C.; Webb, S. A 'Pocket Guide' To Total Internal Reflection Fluorescence. *J. Microsc.* **2013**, *252*, 16−22.

(40) Yang, L.; Parton, R.; Ball, G.; Qiu, Z.; Greenaway, A. H.; Davis, I.; Lu, W. An Adaptive Non-Local Means Filter for Denoising Live-Cell Images and Improving Particle Detection. *J. Struct. Biol.* **2010**, *172*, 233−243.

LANGMUIR
Article
Cite This: Langmuir XXXX, XXX, XXX−XXX
pubs.acs.org/Langmuir

Fluorescence Microscopy of Single Liposomes with Incorporated Pigment−Proteins

Marijonas Tutkus,[†] Parveen Akhtar,[§] Jevgenij Chmeliov,[†,‡] Fanni Görföl,[§] Gediminas Trinkunas,[†] Petar H. Lambrev,[§] and Leonas Valkunas*[,†,‡]

[†]Department of Molecular Compound Physics, Centre for Physical Sciences and Technology, Saulėtekio Avenue 3, LT-10257 Vilnius, Lithuania
[‡]Institute of Chemical Physics, Faculty of Physics, Vilnius University, Saulėtekio Avenue 9-III, LT-10222 Vilnius, Lithuania
[§]Biological Research Centre, Hungarian Academy of Sciences, Temesvári körút 62, 6726 Szeged, Hungary

Ⓢ *Supporting Information*

ABSTRACT: Reconstitution of transmembrane proteins into liposomes is a widely used method to study their behavior under conditions closely resembling the natural ones. However, this approach does not allow precise control of the liposome size, reconstitution efficiency, and the actual protein-to-lipid ratio in the formed proteoliposomes, which might be critical for some applications and/or interpretation of data acquired during the spectroscopic measurements. Here, we present a novel strategy employing methods of proteoliposome preparation, fluorescent labeling, purification, and surface immobilization that allow us to quantify these properties using fluorescence microscopy at the single-liposome level and for the first time apply it to study photosynthetic pigment−protein complexes LHCII. We show that LHCII proteoliposome samples, even after purification with a density gradient, always contain a fraction of nonreconstituted protein and are extremely heterogeneous in both protein density and liposome sizes. This strategy enables quantitative analysis of the reconstitution efficiency of different protocols and precise fluorescence spectroscopic study of various transmembrane proteins in a controlled nativelike environment.

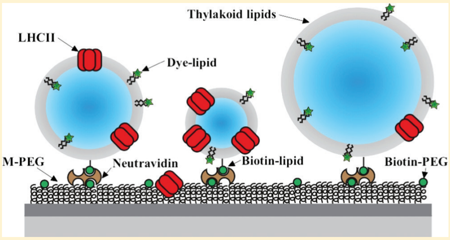

■ INTRODUCTION

Photosynthesis is the natural process utilized by plants, algae, and some bacteria to collect solar energy and store it in the form of chemical bonds. In green plants, the light reactions of photosynthesis occur in the pigment−protein supercomplexes embedded into the thylakoid membranes of the chloroplast. The process starts with the absorption of a photon of sunlight by a pigment molecule bound to the light-harvesting proteins, followed by the transfer of generated electronic excitation energy to the reaction center (RC). There the excitation energy initiates an electron transfer process to build up an electrochemical potential across the thylakoid membrane that fuels chemical reactions producing energy-rich complex carbohydrates.[1] Besides this primary function, multiple-level self-regulatory processes occur in the thylakoid membrane aiming to optimize the photosynthesis efficiency under varying light conditions. This optimization involves continuous rebuild of the pigment−protein complexes, diffusion of the antenna complexes through the membrane during the state transition, dynamic variation of the size of the light-harvesting antenna attached to the RC, or dissipation of the excess excitation energy via nonphotochemical quenching (NPQ) that is reversibly activated during strong sunlight.[2−4]

Due to the presence of two types of photosystems within the membrane as well as two types of excitation quenchers (RCs and NPQ-traps), the spectroscopic signatures of various parallel processes occurring in the thylakoid membrane are not easily resolved,[5−9] which severely complicates the detailed direct investigation of the molecular mechanisms involved. Instead, different photosynthetic units or just pigment−protein complexes are usually extracted from the thylakoid membrane and then are studied separately either in the detergent-solubilized form utilizing conventional bulk spectroscopy methods[10−17] or being immobilized on some surface while applying the single-molecule microscopy techniques.[18−22] Such treatment in the non-native environment allows much more straightforward analysis of the collected data but does not ensure that all of the observations directly correspond to the in vivo processes and not to the side effect of the detergent micelle environment. This drawback, however, may be overcome by studying isolated pigment−protein complexes embedded into liposomes—artificial lipid bilayers that mimic

Received: July 9, 2018
Revised: October 31, 2018
Published: November 1, 2018

DOI: 10.1021/acs.langmuir.8b02307

natural thylakoid membranes.[14,23−26] Liposomes are useful model systems for reconstitution of the transmembrane- and membrane-related proteins, which allow studying their properties in a nativelike environment bypassing their complex cellular surrounding. Reconstitution of proteoliposomes permits a high level of flexibility achieved by varying lipid and protein composition as well as lipid-to-protein (L/P) ratio.[14,15] On the other hand, reproduction of proteoliposomes with fixed L/P ratio, independent of the liposome size, remains a great challenge.[23,27−29] Therefore, the variability of the mentioned parameters in the studied sample might play a significant role in proteoliposome's fluorescence quenching, sensitive to protein lateral aggregation, conformational switches, and protein−lipid interactions, possibly skewing the ensemble-type measurement results or even leading to their misinterpretation.

Recent studies of the proteoliposomes reconstituted with the major light-harvesting complex of photosystem II from plants (LHCII) revealed several valuable insights. First of all, quantum yield (QY) of LHCII fluorescence in liposomes is generally lower than that of the ones solubilized in detergent micelles.[30] Second, QY could be varied by changing the L/P ratio affecting the number of LHCII complexes per liposome (high L/P ratio results in QY similar to that of the unquenched LHCII in detergent micelles). Finally, the fluorescence quenching in these proteoliposomes appears to be driven by protein−protein interactions and not by a specific thylakoid lipid microenvironment.[31,32]

It is important to mention that the typical protocol for LHCII reconstitution into liposomes, utilized in currently reported works, does not entirely rule out the possibility that free (nonreconstituted) LHCII complexes might remain in the sample. This reconstitution protocol relies on detergent removal, and it is known that at low detergent concentrations, LHCIIs forms aggregate.[33] Thus, after reconstitution, there may still possibly be the aggregates in the solvent or on the surface, contributing to the observed reduction of the total QY. That would also result in the effective L/P ratio in the proteoliposomes being different from the bulk stoichiometry used during the sample preparation, which could explain a large mismatch between the reported magnitude of fluorescence quenching and the L/P ratios.[30,32] Finally, a rather wide distribution in the sizes of the formed liposomes additionally increases the uncertainty of the L/P ratio, thus further complicating the straightforward interpretation of the results obtained during the ensemble-type experiments.[34] Performing density gradient centrifugation and using specific fractions for further analysis[35] allows one to reduce but not entirely avoid this uncertainty. Therefore, it is highly critical to develop a method to directly reveal the correct L/P ratio of the proteoliposomes and measure their heterogeneity, thus characterizing the efficiency of LHCII reconstitution into the liposomes.

Here, we report a novel method for preparation of LHCII proteoliposomes from native lipid composition that allowed us to address the issues specified above by combining several spectroscopic techniques. First, we employ very sensitive total internal reflection fluorescence (TIRF) microscopy and novel data analysis methods[36] to detect single proteoliposomes and characterize the actual L/P ratio and number of LHCII complexes per liposome. Also, we utilize previously published approach combining dynamic light scattering (DLS) and confocal microscopy methods[37] to characterize the liposome size. A critical methodological characteristic of the present work is the use of a lipophilic dye[38] as a reporter to label single liposomes. We have also employed improved surface modification methods to maintain intact immobilized proteoliposomes on the surface for long periods of time.[39,40] The obtained results clearly indicate that a substantial number of LHCII complexes remain nonreconstituted into the liposomes, suggesting that at least some of the previously reported conclusions on LHCII proteoliposomes might/should be revisited in the future studies. Our reported methods can also be directly applied to study other proteoliposomes on a single-liposome level.

■ MATERIALS AND METHODS

Isolation of LHCII. LHCII was isolated from 14-day-old pea (*Pisum sativum*) plants by solubilization of PSII-enriched membranes with *n*-dodecyl-*β*-D-maltoside (*β*-DDM, Cube Biotech, Germany).[41,42] The LHCII trimer bands were collected and concentrated (Amicon Ultra, Millipore); the chlorophyll (Chl) concentration was measured according to published procedure,[43] and the samples were frozen in liquid N_2 and stored at −80 °C until use.

Preparation of Liposomes. Liposomes were prepared from plant thylakoid lipids by using previously published protocol[10] with modifications. A chloroform/methanol solution mixture of isolated plant thylakoid lipids monogalactosyldiacylglycerol, digalactosyldiacylglycerol, phosphatidylglycerol, and sulfoquinovosyldiacylglycerol (Avanti Polar Lipids) was prepared at a molar ratio of 5:3:1:1. The lipophilic fluorescent dye DiI (Invitrogen) was added to the mixture at a lipid-to-dye ratio of 50:1. DiI was used as a probe to estimate the lipid/protein ratio in reconstituted proteoliposomes. Biotinylated lipid (1,2-distearoyl-*sn*-glycero-3-phosphoethanolamine-*N*-[biotinyl(poly-(ethylene glycol))-2000]) (Avanti Polar Lipids) was added into the mixture at a ratio of 250:1 (lipids/biotin-lipid).

The chloroform−methanol lipid mixture was slowly dried in a vacuum rotatory evaporator to form a thin film of lipids on the wall of a round-bottom glass vial. After completely drying the solvent, the lipid film was hydrated with a buffer containing 10 mM Tris−aminomethane (pH 7.8) and 10 mM NaCl (henceforth termed reconstitution buffer) to a total lipid concentration of 5 mg/mL. The suspension was vortexed for approximately 40−50 min and subsequently subjected to 10 freeze−thaw cycles and then extruded through a 100 nm pore membrane (Avanti Polar Lipids). After centrifugation on the Ficoll gradient, a sharp band representing empty liposomes was observed, while no free DiI were detected in the supernatant, which demonstrate very high (close to unity) efficiency of the implemented liposome labeling by DiI.

Reconstituted LHCII Membranes. Isolated LHCII complexes were inserted into DiI liposomes to form reconstituted LHCII membranes (proteoliposomes) as previously described[10] with slight modifications. The DiI liposomes were destabilized by adding 0.05% detergent (*β*-DDM). The trimeric LHCII complexes dissolved in *β*-DDM were added dropwise to a suspension of liposomes at concentration of 5 mg/mL, while agitating continuously, to obtain a mixture of desired molar L/P ratio (from 100:1 to 1500:1). The L/P ratio of this reconstitution mixture ($L/P^{(rm)}$) was estimated taking into account that LHCII trimer contains 14 Chls per monomer. The lipid−protein mixture was incubated at room temperature for 30 min in the dark. The detergent was then removed by repeated incubation of the sample with absorbent beads (Bio-Beads SM2, Bio-Rad)—a total of 240 mg/mL beads were added in three 80 mg portions incubating for 1 h, overnight, and 2 h, respectively. This method removes almost all detergent in the suspension.[44] The samples were further diluted several-fold during the next purification steps, so any remaining free detergent was eventually removed.

Separation of Proteoliposomes by Density. Proteoliposome fractions of different densities and lipid/protein ratios were separated by density gradient ultracentrifugation. Discontinuous (step) gradients were prepared by adding 2 mL layers of 7, 14, 21, and

DOI: 10.1021/acs.langmuir.8b02307
Langmuir XXXX, XXX, XXX−XXX

28% Ficoll PM-400 (GE Healthcare) dissolved in reconstitution buffer. The proteoliposome sample was loaded on the gradient and centrifuged for 18 h at 200 000g and 4 °C. Four to five colored band fractions of different densities were collected.

Absorption Spectroscopy. Absorption spectra in the visible region were recorded at room temperature with a Nicolet Evolution 500 dual-beam UV−Vis spectrophotometer (Thermo Fisher Scientific). The sample and reference solution were placed in 1 cm path length optical glass cuvettes, and absorption was measured with 1 nm spectral resolution. The spectra were analyzed and graphed using the Spectr-O-Matic software.

Quantification of the L/P Ratio in Bulk. To quantify the L/P ratio in bulk (Supporting Information (SI) Table S2), first, we determined the apparent molar absorption coefficients of Chl in LHCII and of DiI in control liposomes at 674 and 553 nm. The apparent Chl absorption coefficients were determined from the absorption spectra of LHCII of known total Chl concentration (Chl a + b), which were estimated from pigment extracts in 80% acetone (SI Table S1).[43] The molar concentration of Chl (a + b) and DiI in the LHCII proteoliposomes was estimated from absorption spectra using the following formula: $C_{\mathrm{Chl}} = A_{674}/\in'_{674}$, $C_{\mathrm{DiI}} = (A_{553} - \in'_{553}\cdot C_{\mathrm{Chl}})/\in''_{553}$, where A_{553} and A_{674} are the measured absorbances and $\in'$ and $\in''$ are the apparent molar absorption coefficients of Chl and DiI, respectively (SI Table S1). The molar L/P ratio = $(C_{\mathrm{DiI}}\cdot\mathrm{LDR})/(C_{\mathrm{Chl}}/14)$, where LDR is the lipid-to-DiI ratio of the liposomes and 14 is the number of Chls per LHCII monomer.

Immobilization of Proteoliposomes for Microscopy Experiments. Silanized and PEGylated (methoxy-PEG and biotin−PEG) glass slides (#1.5, Menzel Glaser) were prepared in the same way as described previously.[45] These glass slides were assembled into the six-channel flow cells (sticky-Slide VI 0.4, IBIDI, Germany). Next channel was filled with the reconstitution buffer (300 μL) and incubated with neutravidin (nAv, A-26666, Molecular Probes) solution (0.02 mg/mL) for at least 3 min. Free nAv was removed by washing the channel with the reconstitution buffer (300 μL). Next, proteoliposomes were injected into the channel at low concentration and incubated until sufficient liposome density was achieved. Free proteoliposomes were removed by washing the channel with the reconstitution buffer (300 μL). After this step, the sample was ready for microscopy measurements. During fluorescence microscopy measurements, liposomes were immobilized and washed thoroughly with detergent-free buffer. Therefore, there was low probability to have detergent in the solution during the microscopy experiment.

Microscopy Measurements. We have employed TIRF microscopy and confocal microscopy setups to collect various information of the obtained LHCII proteoliposome samples. TIRF microscopy was used to analyze the co-localization of liposomes and LHCII complexes: this method does not involve intensity characterization of the observed fluorescent spots, but instead checks for spatial overlap of the spots detected in the DiI and LHCII channels (Figure 2d). Being a fast technique allowing one to collect sufficient statistics with good signal-to-noise ratio, TIRF microscopy was also used to estimate the number of LHCII per liposomes from the bleaching traces of the LHCII complexes. Meanwhile, confocal setup provides even excitation of different size liposomes and therefore it was employed to characterize liposome sizes and protein densities.

TIRF Microscopy. Our home-built setup was previously described.[22,45] For these measurements, a beam expander, mounted before the focusing lens, was changed into 7×, which allowed us to optimize the evenness of the illumination field. Laser power before the objective was set to 2.5 mW for both 532 and 632 nm lasers (20 mW both, Crystalazer). That resulted in a laser power density of ~12 W/cm^2 at the plane of the sample. Exposure time of the EMCCD camera (Ixon3 Andor) was set to 50 ms. In the TIRF microscopy images, we have detected no signal of DiI in the LHCII channel under 532 nm excitation and also no signal of LHCII in the DiI channel under 635 nm excitation (data not shown). The penetration depth of the evanescent field was set to ~300 nm for both wavelengths of excitation.

Confocal Microscopy. Our home-built confocal microscope uses the same excitation part as the TIRF microscope, except that for the red channel excitation, we have used a pulsed diode laser (635 nm wavelength, 50 MHz, Becker & Hickl, Germany). Laser power at the plane of the sample was set to ~0.21 μW (10 W/cm^2) for the red laser and ~0.9 μW (180 W/cm^2) for the green laser. The fluorescence emission was collected with the same objective as in TIRF (100×, 1.4 NA, Nikon), passed through a four-band emission filter (446/510/581/703 nm, Semrock), and then directed to the dichroic mirror where the light was split into green and red components. The intensity of the green component was measured with one avalanche photodiode (APD) (tau-SPAD, PicoQuant, Germany), and the intensity of the red component was measured with a second identical APD. Intensity counts from the APDs were read out by an NI card (SCB-68, NI) connected to the FPGA card (PCIe-7851R, NI). Sample was scanned with the piezo stage (P-733.2CD, PI, Germany) with the controller (E-712.3CDA, PI, Germany). Control of the scanning and readout was achieved by custom-written Lab-View (NI) software. Pixel dwell time was set to 5 ms, and size of the image was set to 200 × 200 pixels.

Image Analysis. Image analysis was performed using custom-written software (Igor Pro 6.37) as described previously.[22,45] To extract the integrated fluorescence intensity, the intensity of the detected spots was fitted with a two-dimensional symmetric Gaussian function. To calculate the number of LHCII trimers per liposome, we analyzed their photobleaching traces as described previously.[36] Briefly, bleaching movies of LHCII under continuous excitation with 635 nm laser were acquired in TIRF mode. In these movies, we have detected fluorescent spots and extracted the bleaching traces (see Supporting Information Figure S2). The number of LHCII molecules per bleaching trace was calculated using the recently published model fitting algorithm.[36] It must be noted that although single LHCII trimer exhibits multiple fluorescence intensity levels changing over time,[18,19,22] its bleaching is a single-step process. Also, individual bleaching steps, recorded in bleaching traces under the described imaging conditions, are short-lasting and protein does not show much fluorescence blinking before it bleaches out. Therefore, although the fluorescence intensity fluctuations complicate the analysis, the algorithm accounts just for the difference in the mean fluorescence intensity between individual bleaching steps in the bleaching trace, thus enabling us to correctly evaluate the number of LHCII per liposome. Another aspect of the photobleaching analysis is its assumption that every fluorophore was subjected to similar excitation intensity. This assumption complicates the analysis because in larger liposomes, due to the exponentially decaying excitation field in the Z direction, LHCIIs located in different parts of the liposome may be exposed to different excitation intensities. Therefore, the estimated number of proteins per liposome has some uncertainty that approximately exponentially depends on the liposome size. For the liposomes that are smaller than 100 nm in diameter, this uncertainty is less than 10%, and for those that are ~300 nm in diameter, it reaches ~30%. Thus, this uncertainty becomes significant only for the liposomes whose size is similar to or larger than the penetration depth of TIRF, and in our samples, the majority of proteoliposomes are below this value. Also, our method enables selection of proteoliposomes based on their size; therefore, one can analyze only those proteoliposomes that are below the penetration depth of TIRF system.

DLS and Size Calibration. To convert liposome intensities into diameter in nanometers, we have followed a previously described procedure.[37] We have measured average liposome sizes of the control liposome sample without protein, which was prepared in the same way as proteoliposomes, using DLS (Zetasizer μV, Malvern Analytical). Our control liposomes had an average diameter of 106 nm. On our microscope setups, we have imaged the same control liposomes as in DLS, obtained integrated intensities, took square root of the intensities, and calculated average of these distributions. The average diameter obtained from DLS and average square root intensity allowed us to obtain a numeric conversion factor of 10.5 to

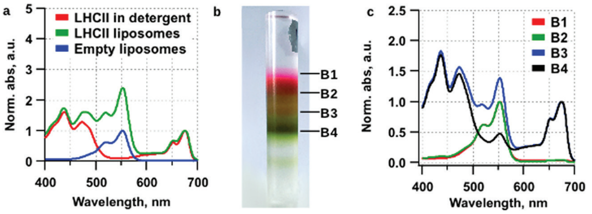

Figure 1. LHCII proteoliposome fractions and their absorption spectra. (a) Absorption spectra of control liposomes, LHCII trimers in detergent micelles, and LHCII proteoliposomes at L/P ratio of the reconstitution mixture being 500:1. The latter two spectra are normalized at 674 nm. (b) Separation of LHCII liposome fractions by gradient density. Differently colored bands of increasing density in ficoll are denoted as B1−B4. (c) Absorption spectra of proteoliposome sample bands B1−B4 from reconstitution mixture with L/P ratio of 1500:1. The spectra of B3−B4 bands are normalized at 674 nm.

convert from fluorescence intensity of liposome into diameter in nanometers.

We note that, although being high, DiI labeling efficiency is not identical in all liposomes and might exhibit up to ∼30% error, which however strongly depends on the lipid used.[28] This effect gives a particular uncertainty for the liposome size calculation, which previously was estimated to be around 20%, and, due to the Poisson noise of the small number of chromophores, it is more pronounced for the small liposomes.[28,46] However, there is no good way to precisely correct for this minor effect, and therefore, we did not perform any additional correction for determined liposome size.

For TIRF microscopy, the liposomes sizes were determined in the same way as with the confocal microscopy. It must be noted that TIRF microscopy might produce a somewhat biased estimation of the liposome diameter because of the excitation unevenness in the direction perpendicular to the glass surface.[47] Nevertheless, we observed a similar trend results obtained by both microscopy types.

■ RESULTS

Bulk Spectroscopy. Reconstitution of the LHCII complexes into liposomes is a rather complicated process involving detergent removal from the solution comprising solubilized pigment−protein complexes and liposomes. As a result, two competing processes are initiated—LHCII aggregation within the solution[48] and LHCII insertion into the liposomes.[49] Therefore, before performing any detailed analysis of the obtained data, it is critical to determine the reconstitution level and evaluate the correct L/P ratio in the produced proteoliposomes.

LHCIIs are trimeric complexes comprising 42 chlorophyll (Chl) pigments, and therefore, they are naturally fluorescent. Contrarily, liposomes do not exhibit any fluorescence signal and are not suitable for the direct quantitative spectroscopic analysis. To overcome this issue, we have employed the lipophilic stain DiI (see Supporting Information Figure S1) during the liposome production. DiI is a very stable membrane dye that, due to its spectral characteristics, is perfectly suitable for labeling LHCII proteoliposomes. Indeed, the absorption spectrum of LHCII complexes is characterized by two absorption bands (Figure 1a). The 650−700 nm wavelength region manifests the strong Q_y transitions of chlorophylls (the Chl *a* and Chl *b* pigments). The absorption band in the 400−500 nm spectral region corresponds to the Soret band of the Chls and the absorption band of the carotenoid pigments.[1] Meanwhile, the DiI dyes in the control liposomes (prior to LHCII reconstitution) exhibit a strong absorption band around 550 nm—exactly at the minimum of the LHCII absorption spectrum (Figure 1a). The absorption spectrum of LHCII proteoliposomes, formed by using the 500:1 lipid-to-protein ratio of the reconstitution mixture (denoted below as $L/P^{(rm)}$), is also presented in Figure 1a and clearly exhibits the additive nature of its sub-bands.

The reconstitution of protein into liposomes depends on many factors,[49] and typically proteins are not evenly incorporated.[34,50] Depending on the reconstitution conditions, there could remain empty liposomes (those without LHCII complexes) as well as free LHCIIs (aggregated, nonaggregated, or both). As the first step to separate empty liposomes and free LHCIIs from proteoliposomes, we performed density gradient ultracentrifugation. Density gradients were prepared with Ficoll 400 that is a high-molecular-weight polymer of sucrose having low osmotic pressure to keep the liposomes intact.

After centrifugation, several gradient bands of different colors were observed and collected as separate fractions (see Figure 1b). The lowest-density gradient band (B1 in Figure 1b) had a distinct pink color and showed the absorption spectrum of pure DiI (peaking at 553 nm) without any Chl (at 674 nm), indicating that it consists entirely of empty liposomes (Figure 1c). This fraction was excluded from further analysis. Bands of higher density (B2−B4) had orange-brown to green color and exhibited increasing relative absorption in the Chl region at the expense of DiI absorption, indicating progressively higher protein and lower lipid content. It could correspond to either lower abundance of unoccupied liposomes or lower L/P content of the proteoliposomes.

The differences in the molar absorption coefficients of the Chls and DiI dyes at various wavelengths (shown in Supporting Information Table S1) allowed us to estimate the mean lipid-to-protein ratio in these distinct gradient bands ($L/P^{(gb)}$); see Materials and Methods for details. By varying the lipid-to-protein ratio of the initial reconstitution mixture ($L/P^{(rm)}$), we found that in all of the samples, the $L/P^{(gb)}$ ratio of the B2 was about 2−3 times larger than that of the initial mixture (see Supporting Information Table S2). Meanwhile, the $L/P^{(gb)}$ ratio of the higher-density bands was spread over a broad range of values. In most cases, the fractions containing the largest amount of Chl had $L/P^{(gb)}$ considerably lower than the corresponding $L/P^{(rm)}$. Only rarely the two quantities were of similar magnitude, and there was no clear correlations between them. As a result, there is no practical way to predict the L/P ratio in the proteoliposomes a priori by varying the concentration of the reconstitution mixture. Moreover, even the separation of the proteoliposomes into distinct gradient

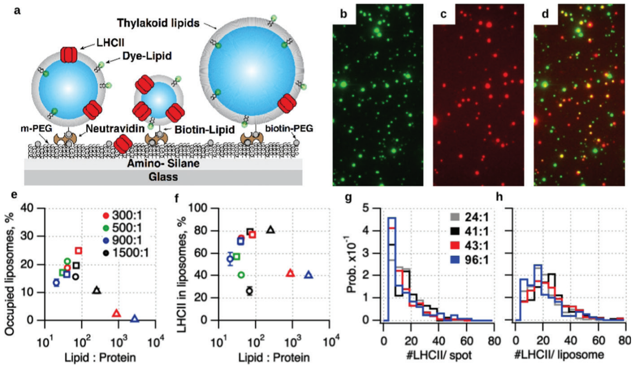

Figure 2. TIRF microscopy of single LHCII proteoliposomes. (a) Experimental scheme showing immobilization of the proteoliposomes of various sizes that contain both DiI dyes and biotin-lipids on the silanized and PEGylated (10% biotin−PEG) glass coverslip via neutravidin. (b−d) TIRF images obtained via the (b) DiI channel at 532 nm excitation, (c) LHCII channel at 635 nm, and (d) both channels overlaid. (e) Percentage of the occupied liposomes vs lipid/protein ratio of the gradient band. Colors indicate L/P$^{(rm)}$ of the reconstitution mixture, symbols—different gradient bands: B2 (triangles), B3 (squares), and B4 (circles). (f) Percentage of reconstituted LHCII complexes vs L/P$^{(gb)}$ of the gradient band. Color in symbol notation is the same as for panel (e). (g, h) Statistical distribution of the number of LHCII complexes per spot representing the (g) free surface-bound LHCIIs and (h) per liposome in the TIRF image, calculated from bleaching traces for four distinct L/P$^{(gb)}$ ratios shown in the legend.

bands does not entirely rule out the possibility of coexistence of empty liposomes and free LHCIIs in the same band.

TIRF Microscopy of Single Proteoliposomes. To address the issue of possible heterogeneity of the LHCII proteoliposomes and to characterize the reconstitution efficiency, we have used fluorescence microscopy and employed proteoliposome anchoring strategy on a surface at low densities (shown schematically in Figure 2a).[34,39,40,51,52] Particularly, during the production of the liposomes, we have included the biotinylated lipids that served as an anchor of the liposomes onto the silanized and PEGylated glass surface via neutravidin (see Materials and Methods for details). Under these anchoring conditions, liposomes remain intact and maintain permeability to ions.[39] Thus, they still reflect the natural membrane conditions for the embedded proteins. Besides that, the mentioned glass surface modification ensures low nonspecific binding of both liposomes and proteins.

For the measurements, we have employed TIRF microscopy that provided high sensitivity and the possibility to image the massive amount of proteoliposomes in a parallel manner. In these experiments, we recorded images of two fluorescence channels (red for LHCII and green for DiI) under different excitation conditions: excitation of DiI dyes at 532 nm wavelength and excitation of LHCII at 635 nm (see Figure 2b−d). Next, the fluorescent diffraction-limited spots observed in the acquired images were analyzed using custom-written automated software to detect the co-localized spots. This procedure allowed distinguishing the spots that correspond to the proteoliposomes containing successfully embedded LHCII complexes (when both signals coincide) from just empty liposomes (no signal in the Chl channel) or nonreconstituted LHCIIs that were nonspecifically bound to the surface (no signal in the DiI channel).

The performed co-localization analysis revealed that no gradient bands were devoid of empty liposomes or non-reconstituted protein. The percentage of liposomes incorporating LHCII was rather low in all of the examined samples and does not exceed 25% of the total number of liposomes (see Figure 2e and Supporting Information Table S3). In higher-density bands (B3, B4), it increases with the L/P$^{(gb)}$ ratio (albeit exhibits no general trend with the L/P$^{(rm)}$) and reaches the maximal value of 25% at L/P$^{(gb)}$ ≈ 100:1. We see therefore that, counterintuitively, the gradient bands with the lower L/P (thus higher amount of LHCII) exhibit substantially higher percentage of empty liposomes. A rather low percentage of occupied liposomes was observed in the low-density gradient band (B2), which confirms our previous assumption based on the absorption spectrum.

In addition to the percentage of LHCII incorporating liposomes, the co-localization analysis also provided us a piece of information about the surface-bound free LHCII. Notably, we found that in some gradient bands, up to 75% of fluorescing spots detected in the LHCII channel images correspond to the nonreconstituted LHCIIs (see Figure 2f and Supporting Information Table S3). Overall, in different samples, the efficiency of the LHCII incorporation into the liposomes varied between 25 and 80%, but no strict dependency on neither L/P$^{(gb)}$ nor L/P$^{(rm)}$ was observed. In the similar studies of ß2AR protein, it was demonstrated previously that by using this method of liposome labeling, it is impossible to observe such a vast amount of free proteins because of merely insufficient liposome labeling.[34] These results, therefore, demonstrate the importance of our employed co-localization assay, as it allows direct monitoring of the LHCIIs embedded into the liposomes.

By analyzing the fluorescence bleaching traces of the spots from TIRF microscopy images corresponding to the LHCII complexes, we were able to evaluate the number of the LHCII trimers fluorescing at that specific spot (assuming no excitation energy transfer between LHCIIs within the same spot; see Materials and Methods for details). We obtained statistical distributions of the cluster sizes for several distinct L/P$^{(gb)}$

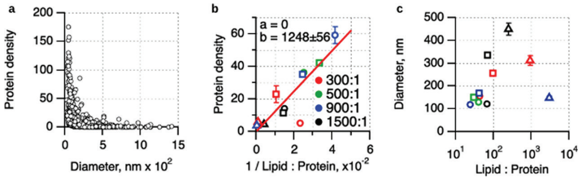

Figure 3. Confocal microscopy of single LHCII proteoliposomes. (a) Relation between the protein density in the proteoliposome (the ratio of fluorescence intensity of LHCII and liposome dyes) and the liposome diameter. (b) Linear correlation between the mean protein density in the proteoliposome and the inverted L/P$^{(gb)}$ ratio of the gradient band. (c) Average liposome diameter vs L/P of the gradient band.

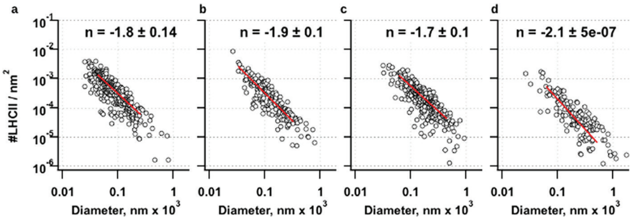

Figure 4. Distribution of the LHCII mean surface concentration (the number of LHCII trimers per unit surface area of the proteoliposome) for liposomes of various sizes. The panels correspond to different lipid/protein ratios of the B3 and B4 gradient bands from different reconstitution mixtures: L/P$^{(gb)}$ = 24:1 (a), 41:1 (b), 43:1 (c), and 96:1 (d). The red lines demonstrate the power-law description, $y \propto x^n$, and the exponent n is indicated in each case.

ratios, which revealed that the free surface-bound LHCII complexes formed mostly small clusters comprising about 10–13 LHCII trimers per spot, albeit several larger aggregates of up to 50 LHCIIs were also detected (Figure 2g). On the other hand, the number of LHCII trimers embedded into the liposome exhibited a much wider distribution, varying from just a few complexes up to 80 trimers per liposome for different spots (see Figure 2h). In principle, this broad distribution indicates either widespread of liposome sizes or heterogeneous distribution of the LHCII density in various liposomes or both.

Confocal Microscopy of Single Proteoliposomes. To access the liposome sizes in nanometers, we performed confocal microscopy studies of the same samples as in the previously described TIRF microscopy, measuring the two fluorescence intensity signals following excitation at 532 nm (DiI dyes) and 635 nm (LHCII complexes) (see Supporting Information Figure S3 for the obtained images). Again, automated spot detection software allowed us to perform the co-localization of the liposomes and LHCIIs analysis. By measuring the fluorescence intensity of control empty liposomes (see Supporting Information Figure S4) and comparing their intensity distributions with the dynamic light scattering data of the same sample, we were able to calibrate the measurement results and convert the liposome's fluorescence intensity into its diameter expressed in nanometers.[37,40] The same conversion factor was also used for other samples containing proteoliposomes.

The ratio of fluorescence intensities of LHCII and liposome dyes at each co-localized spot, reflecting the protein density in a particular detected single liposome, demonstrated a strong dependence on the liposome size (Figure 3a). The protein density in the individual proteoliposome exhibited a broad distribution for liposomes smaller than ~200 nm in diameter, and reduced severely in larger liposomes. On the other hand, as expected, the evaluated mean protein density of the proteoliposomes scaled linearly with the inverse of the L/P$^{(gb)}$ ratio of the corresponding gradient band (Figure 3b). Meanwhile, the mean diameters of the proteoliposomes detected in different gradient bands did not exhibit any correlation with the L/P$^{(gb)}$ ratio of that band (see Figure 3c). It is also noteworthy to mention that both liposome sizes and protein density per liposome demonstrated a very inhomogeneous distribution within each gradient band, indicating that the spectroscopic information obtained from ensemble measurements on the proteoliposomes might not be sufficient for proper interpretation, and treating both parameters on a single-liposome level is highly critical.

■ DISCUSSION

Reconstitution of membrane proteins into liposomes is a widely used approach to study the structure and function of various proteins in the conditions mimicking natural environment. In this work, we have demonstrated that the usage of the lipophilic DiI dye during the preparation of LHCII proteoliposomes has proven to be a suitable method for labeling liposomes. It allowed them to be studied at the single-liposome level using TIRF and confocal microscopy. By implementing TIRF microscopy, we addressed efficiency of LHCII reconstitution into liposomes while by applying confocal microscopy, we were able to quantify the size of individual liposomes and the relative protein density therein. Particularly, the obtained results revealed that each of the density bands, which was supposed to be purified to some extend from free LHCII, still remained a highly heterogeneous mixture of empty liposomes, proteoliposomes of various sizes, and free LHCIIs. We found no gradient band consisting entirely of proteoliposomes. In any of given gradient density band, only up to 25% of all liposomes incorporated LHCII, as well as at least 20% of the LHCII complexes formed clusters with no detectable lipid. Also, judging from the bulk fluorescence lifetime results and the CD spectra (SI Figure S5), there were no evidences for remaining detergent-solubilized LHCII (no ~4 ns lifetime, and no aggregation signature bands at 436 and 484 nm) and for LHCII monomerization (loss of CD amplitude at 473 nm) found in samples, which were used for microscopy. This implies severe difficulties while interpreting bulk spectroscopic measurements when the signals from all of these subpopulations are mixed, suggesting that some previously reported results might have to be revisited.

The single-vesicle TIRF microscopy analysis enabled us also to determine another important structural parameter—the protein surface concentration, i.e., the absolute number of the LHCII trimers per unit surface area of the liposome (see Materials and Methods for details). Although exhibiting wide scatter, this parameter showed striking dependence on the liposome diameter—smaller liposomes tended to demonstrate higher protein concentration (see Figure 4). This trend spans over almost 6 orders of magnitude and exhibits a power-law dependence. Interestingly, in all of the examined samples, the exponent of this power-law dependence was close to −2, which means that the absolute number of LHCII complexes per liposome is independent of the liposome diameter. Indeed, a wide scatter of the data points in Figure 4 reveals that the reconstituted proteoliposomes with statistically almost equal probability can contain from several to ~50 LHCII complexes. Such behavior might seem as a rather surprising result contradicting the intuitive assumption that larger liposomes should on average accumulate a larger number of protein complexes. It is expected, however, that the balance between the elastic and hydrophobic forces acting on the LHCII complexes, embedded into lipid bilayer, thermodynamically favors their reconstitution into the small liposomes rather than into the larger ones.[53] The combined effect of these two opposing factors indeed results in our observation that the number of the LHCII complexes incorporated into the liposome in principle does not depend on the liposome size or the $L/P^{(gb)}$.

To summarize, we have shown quantitatively that the liposome formation and subsequent reconstitution of the LHCII complexes into them result in by-all-means heterogeneous systems: in terms of the liposome size, the number of pigment−protein complexes embedded into individual proteoliposomes and, consequently, the protein surface density. More importantly, the resulting L/P ratio in these proteoliposomes cannot be predicted a priori by varying sample preparation conditions. We have also determined that the process of reconstitution itself is not efficient: at least 75% of the liposomes remained empty in different gradient bands, while, at the same time, 20−75% of the LHCII complexes remained liposome-free. The spectroscopic signal of the latter might severely interfere with one coming from proteoliposomes, complicating therefore the interpretation of the results of simple bulk measurements. In contrast, liposome labeling with specific dyes and the application of the single-molecule techniques provide a unique tool to clarify this uncertainty and study membrane-related proteins and their function in a controlled nativelike environment.

■ ASSOCIATED CONTENT

Ⓢ Supporting Information

The Supporting Information is available free of charge on the ACS Publications website at DOI: 10.1021/acs.langmuir.8b02307.

> Chemical structure of the lipophilic dye DiI; bleaching traces of sample; confocal images; bulk characterization results; molar absorption coefficients of Chl; distribution of LHCII in proteoliposomes fraction (PDF)

■ AUTHOR INFORMATION

Corresponding Author

*E-mail: leonas.valkunas@ff.vu.lt.

ORCID

Marijonas Tutkus: 0000-0002-5795-1347
Jevgenij Chmeliov: 0000-0002-7591-1373
Gediminas Trinkunas: 0000-0002-3624-0239
Petar H. Lambrev: 0000-0001-5147-153X
Leonas Valkunas: 0000-0002-1356-8477

Notes

The authors declare no competing financial interest.

■ ACKNOWLEDGMENTS

This work was supported by Lithuanian-Ukrainian grant (P-LU-18-64) and by a grant from the Hungarian Ministry for National Economy (GINOP-2.3.2-15-2016-00001) and the National Research, Development and Innovation Office (NKFIH NN-124904). The authors thank D. Rutkauskas for help on setting up the confocal microscope and participation in the initial discussion on the project; M. Vengris for lending hardware and help with the signal acquisition software; and O. Venckus and I. Ciplys for participation in performing several TIRF and confocal microscopy measurements.

■ REFERENCES

(1) Blankenship, R. E. *Molecular Mechanisms of Photosynthesis*; Blankenship, R. E., Ed.; Blackwell Science Ltd: Oxford, U.K., 2002.

(2) Horton, P.; Ruban, A. V.; Walters, R. G. Regulation of Light Harvesting in Green Plants. *Annu. Rev. Plant Physiol. Plant Mol. Biol.* **1996**, *47*, 655−684.

(3) Ruban, A. V.; Johnson, M. P.; Duffy, C. D. P. The Photoprotective Molecular Switch in the Photosystem II Antenna. *Biochim. Biophys. Acta, Bioenerg.* **2012**, *1817*, 167−181.

(4) Duffy, C. D. P.; Valkunas, L.; Ruban, A. V. Light-Harvesting Processes in the Dynamic Photosynthetic Antenna. *Phys. Chem. Chem. Phys.* **2013**, *15*, 18752.

(5) Haferkamp, S.; Haase, W.; Pascal, A. A.; van Amerongen, H.; Kirchhoff, H. Efficient Light Harvesting by Photosystem II Requires an Optimized Protein Packing Density in Grana Thylakoids. *J. Biol. Chem.* **2010**, *285*, 17020−17028.

(6) Johnson, M. P.; Brain, A. P. R.; Ruban, A. V. Changes in Thylakoid Membrane Thickness Associated with the Reorganization of Photosystem II Light Harvesting Complexes during Photoprotective Energy Dissipation. *Plant Signaling Behav.* **2011**, *6*, 1386−1390.

(7) Kiss, A. Z.; Ruban, A. V.; Horton, P. The PsbS Protein Controls the Organization of the Photosystem II Antenna in Higher Plant Thylakoid Membranes. *J. Biol. Chem.* **2008**, *283*, 3972−3978.

(8) Akhtar, P.; Lingvay, M.; Kiss, T.; Deák, R.; Bóta, A.; Ughy, B.; Garab, G.; Lambrev, P. H. Excitation Energy Transfer between Light-Harvesting Complex II and Photosystem i in Reconstituted Membranes. *Biochim. Biophys. Acta, Bioenerg.* **2016**, *1857*, 462−472.

(9) Farooq, S.; Chmeliov, J.; Wientjes, E.; Koehorst, R.; Bader, A.; Valkunas, L.; Trinkunas, G.; van Amerongen, H. Dynamic Feedback of the Photosystem II Reaction Centre on Photoprotection in Plants. *Nat. Plants* **2018**, *4*, 225−231.

(10) Akhtar, P.; Dorogi, M.; Pawlak, K.; Kovács, L.; Bóta, A.; Kiss, T.; Garab, G.; Lambrev, P. H. Pigment Interactions in Light-Harvesting Complex II in Different Molecular Environments. *J. Biol. Chem.* **2015**, *290*, 4877−4886.

(11) Borch, J.; Hamann, T. The Nanodisc: A Novel Tool for Membrane Protein Studies. *Biol. Chem.* **2009**, *390*, 805−814.

(12) Bell, A. J.; Frankel, L. K.; Bricker, T. M. High Yield Non-Detergent Isolation of Photosystem I-Light-Harvesting Chlorophyll II Membranes from Spinach Thylakoids: Implications for the Organization of the PS I Antennae in Higher Plants. *J. Biol. Chem.* **2015**, *290*, 18429−18437.

(13) Liguori, N.; Roy, L. M.; Opacic, M.; Durand, G.; Croce, R. Regulation of Light Harvesting in the Green Alga *Chlamydomonas reinhardtii*: The c-Terminus of Lhcsr Is the Knob of a Dimmer Switch. *J. Am. Chem. Soc.* **2013**, *135*, 18339−18342.

(14) Zhou, F.; Liu, S.; Hu, Z.; Kuang, T.; Paulsen, H.; Yang, C. Effect of Monogalactosyldiacylglycerol on the Interaction between Photosystem II Core Complex and Its Antenna Complexes in Liposomes of Thylakoid Lipids. *Photosynth. Res.* **2009**, *99*, 185−193.

(15) Yang, C.; Boggasch, S.; Haase, W.; Paulsen, H. Thermal Stability of Trimeric Light-Harvesting Chlorophyll a/b Complex (LHCIIb) in Liposomes of Thylakoid Lipids. *Biochim. Biophys. Acta, Bioenerg.* **2006**, *1757*, 1642−1648.

(16) Wardak, A.; Brodowski, R.; Krupa, Z.; Gruszecki, W. I. Effect of Light-Harvesting Complex II on Ion Transport across Model Lipid Membranes. *J. Photochem. Photobiol., B* **2000**, *56*, 12−18.

(17) Chmeliov, J.; Gelzinis, A.; Songaila, E.; Augulis, R.; Duffy, C. D. P.; Ruban, A. V.; Valkunas, L. The Nature of Self-Regulation in Photosynthetic Light-Harvesting Antenna. *Nat. Plants* **2016**, *2*, No. 16045.

(18) Schlau-Cohen, G. S.; Wang, Q.; Southall, J.; Cogdell, R. J.; Moerner, W. E. Single-Molecule Spectroscopy Reveals Photosynthetic LH2 Complexes Switch between Emissive States. *Proc. Natl. Acad. Sci. U.S.A.* **2013**, *110*, 10899−10903.

(19) Krüger, T. P. J.; Ilioaia, C.; van Grondelle, R. Fluorescence Intermittency from the Main Plant Light-Harvesting Complex: Resolving Shifts between Intensity Levels. *J. Phys. Chem. B* **2011**, *115*, 5071−5082.

(20) Gruber, J. M.; Chmeliov, J.; Krüger, T. P. J.; Valkunas, L.; van Grondelle, R. Singlet−Triplet Annihilation in Single LHCII Complexes. *Phys. Chem. Chem. Phys.* **2015**, *17*, 19844−19853.

(21) Kondo, T.; Pinnola, A.; Chen, W. J.; Dall'Osto, L.; Bassi, R.; Schlau-Cohen, G. S. Single-Molecule Spectroscopy of LHCSR1 Protein Dynamics Identifies Two Distinct States Responsible for Multi-Timescale Photosynthetic Photoprotection. *Nat. Chem.* **2017**, *9*, 772−778.

(22) Tutkus, M.; Chmeliov, J.; Rutkauskas, D.; Ruban, A. V.; Valkunas, L. Influence of the Carotenoid Composition on the Conformational Dynamics of Photosynthetic Light-Harvesting Complexes. *J. Phys. Chem. Lett.* **2017**, *8*, 5898−5906.

(23) Rigaud, J.-L.; Lévy, D. Reconstitution of Membrane Proteins into Liposomes. In *Methods in Enzymology*; Academic Press, 2003; Vol. *372*, pp 65−86.

(24) Barros, T.; Kühlbrandt, W. Crystallisation, Structure and Function of Plant Light-Harvesting Complex II. *Biochim. Biophys. Acta, Bioenerg.* **2009**, *1787*, 753−772.

(25) Schaller, S.; Latowski, D.; Jemioła-Rzemińska, M.; Dawood, A.; Wilhelm, C.; Strzałka, K.; Goss, R. Regulation of LHCII Aggregation by Different Thylakoid Membrane Lipids. *Biochim. Biophys. Acta, Bioenerg.* **2011**, *1807*, 326−335.

(26) Wilk, L.; Grunwald, M.; Liao, P.-N.; Walla, P. J.; Kuhlbrandt, W. Direct Interaction of the Major Light-Harvesting Complex II and PsbS in Nonphotochemical Quenching. *Proc. Natl. Acad. Sci. U.S.A.* **2013**, *110*, 5452−5456.

(27) Niu, S. L.; Doctrow, B.; Mitchell, D. C. Rhodopsin Activity Varies in Proteoliposomes Prepared by Different Techniques. *Biochemistry* **2009**, *48*, 156−163.

(28) Larsen, J.; Hatzakis, N. S.; Stamou, D. Observation of Inhomogeneity in the Lipid Composition of Individual Nanoscale Liposomes. *J. Am. Chem. Soc.* **2011**, *133*, 10685−10687.

(29) Walsh, S. M.; Mathiasen, S.; Christensen, S. M.; Fay, J. F.; King, C.; Provasi, D.; Borrero, E.; Rasmussen, S. G. F.; Fung, J. J.; Filizola, M.; et al. Single Proteoliposome High-Content Analysis Reveals Differences in the Homo-Oligomerization of GPCRs. *Biophys. J.* **2018**, *115*, 300−312.

(30) Moya, I.; Silvestri, M.; Vallon, O.; Cinque, G.; Bassi, R. Time-Resolved Fluorescence Analysis of the Photosystem II Antenna Proteins in Detergent Micelles and Liposomes. *Biochemistry* **2001**, *40*, 12552−12561.

(31) Natali, A.; Gruber, J. M.; Dietzel, L.; Stuart, M. C. A.; Van Grondelle, R.; Croce, R. Light-Harvesting Complexes (LHCs) Cluster Spontaneously in Membrane Environment Leading to Shortening of Their Excited State Lifetimes. *J. Biol. Chem.* **2016**, *291*, 16730−16739.

(32) Crisafi, E.; Pandit, A. Disentangling Protein and Lipid Interactions That Control a Molecular Switch in Photosynthetic Light Harvesting. *Biochim. Biophys. Acta, Biomembr.* **2017**, *1859*, 40−47.

(33) Petrou, K.; Belgio, E.; Ruban, A. V. PH Sensitivity of Chlorophyll Fluorescence Quenching Is Determined by the Detergent/Protein Ratio and the State of LHCII Aggregation. *Biochim. Biophys. Acta, Bioenerg.* **2014**, *1837*, 1533−1539.

(34) Mathiasen, S.; Christensen, S. M.; Fung, J. J.; Rasmussen, S. G. F.; Fay, J. F.; Jorgensen, S. K.; Veshaguri, S.; Farrens, D. L.; Kiskowski, M.; Kobilka, B.; et al. Nanoscale High-Content Analysis Using Compositional Heterogeneities of Single Proteoliposomes. *Nat. Methods* **2014**, *11*, 931−934.

(35) Cowell, G. M.; Tranum-Jensen, J.; Sjöström, H.; Norén, O. Topology and Quaternary Structure of Pro-Sucrase/Isomaltase and Final-Form Sucrase/Isomaltase. *Biochem. J.* **1986**, *237*, 455−461.

(36) Tsekouras, K.; Custer, T. C.; Jashnsaz, H.; Walter, N. G.; Pressé, S. A Novel Method to Accurately Locate and Count Large Numbers of Steps by Photobleaching. *Mol. Biol. Cell* **2016**, *27*, 3601−3615.

(37) Kunding, A. H.; Mortensen, M. W.; Christensen, S. M.; Stamou, D. A Fluorescence-Based Technique to Construct Size Distributions from Single-Object Measurements: Application to the Extrusion of Lipid Vesicles. *Biophys. J.* **2008**, *95*, 1176−1188.

(38) Gullapalli, R. R.; Demirel, M. C.; Butler, P. J. Molecular Dynamics Simulations of DiI-C18(3) in a DPPC Lipid Bilayer. *Phys. Chem. Chem. Phys.* **2008**, *10*, 3548.

(39) Diao, J.; Ishitsuka, Y.; Lee, H.; Joo, C.; Su, Z.; Syed, S.; Shin, Y. K.; Yoon, T. Y.; Ha, T. A Single Vesicle-Vesicle Fusion Assay for in Vitro Studies of Snares and Accessory Proteins. *Nat. Protoc.* **2012**, *7*, 921−934.

(40) Bendix, P. M.; Pedersen, M. S.; Stamou, D. Quantification of Nano-Scale Intermembrane Contact Areas by Using Fluorescence Resonance Energy Transfer. *Proc. Natl. Acad. Sci. U.S.A.* **2009**, *106*, 12341−12346.

(41) Caffarri, S.; Croce, R.; Breton, J.; Bassi, R. The Major Antenna Complex of Photosystem II Has a Xanthophyll Binding Site Not Involved in Light Harvesting. *J. Biol. Chem.* **2001**, *276*, 35924−35933.

(42) Berthold, D. A.; Babcock, G. T.; Yocum, C. F. A Highly Resolved, Oxygen-Evolving Photosystem II Preparation from Spinach Thylakoid Membranes. EPR and Electron-Transport Properties. *FEBS Lett.* **1981**, *134*, 231−234.

(43) Porra, R. J.; Thompson, W. A.; Kriedemann, P. E. Determination of Accurate Extinction Coefficients and Simultaneous Equations for Assaying Chlorophylls a and b Extracted with Four Different Solvents: Verification of the Concentration of Chlorophyll Standards by Atomic Absorption Spectroscopy. *Biochim. Biophys. Acta, Bioenerg.* **1989**, *975*, 384−394.

(44) Lambert, O.; Levy, D.; Ranck, J. L.; Leblanc, G.; Rigaud, J. L. A New "gel-like" Phase in Dodecyl Maltoside-Lipid Mixtures:

Implications in Solubilization and Reconstitution Studies. *Biophys. J.* **1998**, 918.

(45) Tutkus, M.; Marciulionis, T.; Sasnauskas, G.; Rutkauskas, D. DNA-Endonuclease Complex Dynamics by Simultaneous FRET and Fluorophore Intensity in Evanescent Field. *Biophys. J.* **2017**, *112*, 850−858.

(46) Larsen, J. B.; Jensen, M. B.; Bhatia, V. K.; Pedersen, S. L.; Bjørnholm, T.; Iversen, L.; Uline, M.; Szleifer, I.; Jensen, K. J.; Hatzakis, N. S.; et al. Membrane Curvature Enables N-Ras Lipid Anchor Sorting to Liquid-Ordered Membrane Phases. *Nat. Chem. Biol.* **2015**, *11*, 192−194.

(47) Axelrod, D. Evanescent Excitation and Emission in Fluorescence Microscopy. *Biophys. J.* **2013**, *104*, 1401−1409.

(48) Ruban, A. V.; Horton, P. Mechanism of ΔpH-Dependent Dissipation of Absorbed Excitation Energy by Photosynthetic Membranes. I. Spectroscopic Analysis of Isolated Light-Harvesting Complexes. *Biochim. Biophys. Acta, Bioenerg.* **1992**, *1102*, 30−38.

(49) Rigaud, J. L.; Paternostre, M. T.; Bluzat, A. Mechanisms of Membrane Protein Insertion into Liposomes during Reconstitution Procedures Involving the Use of Detergents. 2. Incorporation of the Light-Driven Proton Pump Bacteriorhodopsin. *Biochemistry* **1988**, *27*, 2677−2688.

(50) Hatzakis, N. S.; Bhatia, V. K.; Larsen, J.; Madsen, K. L.; Bolinger, P.-Y.; Kunding, A. H.; Castillo, J.; Gether, U.; Hedegård, P.; Stamou, D. How Curved Membranes Recruit Amphipathic Helices and Protein Anchoring Motifs. *Nat. Chem. Biol.* **2009**, *5*, 835−841.

(51) Stamou, D.; Duschl, C.; Delamarche, E.; Vogel, H. Self-Assembled Microarrays of Attoliter Molecular Vessels. *Angew. Chem., Int. Ed.* **2003**, *42*, 5580−5583.

(52) Boukobza, E.; Sonnenfeld, A.; Haran, G. Immobilization in Surface-Tethered Lipid Vesicles as a New Tool for Single Biomolecule Spectroscopy. *J. Phys. Chem. B* **2001**, No. 12165.

(53) Lasic, D. D. A Molecular Model for Vesicle Formation. *Biochim. Biophys. Acta* **1982**, *692*, 501−502.

DOI: 10.1021/acs.langmuir.8b02307
Langmuir XXXX, XXX, XXX−XXX

LANGMUIR Cite This: *Langmuir* 2019, 35, 5921−5930
Article
pubs.acs.org/Langmuir

Fixed DNA Molecule Arrays for High-Throughput Single DNA−Protein Interaction Studies

Marijonas Tutkus,[‡] Tomas Rakickas,[†] Aurimas Kopūstas,[§] Šarūnė Ivanovaitė,[‡] Oskaras Venckus,[‡] Vytautas Navikas,[†,∥] Mindaugas Zaremba,[§] Elena Manakova,[§] and Ramūnas Valiokas*[,†]

[†]Departments of Nanoengineering and [‡]Molecular Compound Physics, Center for Physical Sciences and Technology, Savanorių 231, Vilnius LT-02300, Lithuania

[§]Vilnius University, Life Sciences Center, Institute of Biotechnology, Sauletekio av. 7, Vilnius LT-10257, Lithuania

Supporting Information

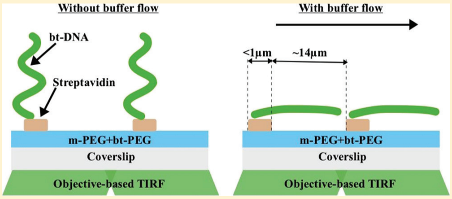

ABSTRACT: The DNA Curtains assay is a recently developed experimental platform for protein−DNA interaction studies at the single-molecule level that is based on anchoring and alignment of DNA fragments. The DNA Curtains so far have been made by using chromium barriers and fluid lipid bilayer membranes, which makes such a specialized assay technically challenging and relatively unstable. Herein, we report on an alternative strategy for DNA arraying for analysis of individual DNA−protein interactions. It relies on stable DNA tethering onto nanopatterned protein templates via high affinity molecular recognition. We describe fabrication of streptavidin templates (line features as narrow as 200 nm) onto modified glass coverslips by combining surface chemistry, atomic force microscopy (AFM), and soft lithography techniques with affinity-driven assembly. We have employed such chips for arraying single- and double-tethered DNA strands, and we characterized the obtained molecular architecture: we evaluated the structural characteristics and specific versus nonspecific binding of fluorescence-labeled DNA using AFM and total internal reflection fluorescence microscopy. We demonstrate the feasibility of our DNA molecule arrays for short single-tethered as well as for lambda single- and double-tethered DNA. The latter type of arrays proved very suitable for localization of single DNA−protein interactions employing restriction endonucleases. The presented molecular architecture and facile method of fabrication of our nanoscale platform does not require clean room equipment, and it offers advanced functional studies of DNA machineries and the development of future nanodevices.

INTRODUCTION

Protein−nucleic acid interactions is a very important field of modern molecular biology. The recent advances in microscopy and fluorescent labeling of biological macromolecules have opened new perspectives for this field by revealing interaction details at the level of single molecules.[1−3] Single-molecule (SM) techniques are indispensable, for example, in studying transient multiprotein complexes and their interaction with the nucleic acid substrate. However, most of the SM microscopy techniques require immobilization of the object of interest on a planar surface,[4,5] coupling to a bead[6] or combination of both[7] to study the molecular events for an extended period of time. Biotinylated DNA (bt-DNA) immobilization via biotin−streptavidin (sAv) interaction on a modified glass surface has been used for SM fluorescence measurements as a common approach.[8] In such an approach, glass is typically covered with biotinylated bovine serum albumin (BSA-bt), poly-L-lysine grafted with biotinylated polyethylene glycol (PLL-PEG-bt), or modified with silane-PEG-biotin. To facilitate detection of the DNA molecules (appearing as individual fluorescent spots), they can be randomly positioned on the modified glass surface at small densities. However, this strategy is challenging in advanced biophysical and molecular biology experiments with larger quantities of molecules and long DNA substrates, or when the reactions themselves are inefficient, or when they involve rare intermediates.

The recently developed so-called DNA Curtains offer a methodological breakthrough in terms of solving the statistical issues and deriving extra information from the SM experiments.[9,10] In this experimental platform, the DNA molecules are extended by a buffer flow perpendicularly to nanofabricated barriers on a glass surface otherwise covered with a supported lipid bilayer (SLB). This way, the termini of the DNA fragments are aligned with respect to each other, and the molecules themselves are oriented in a single direction, while their orientation is defined with respect to the nucleotide sequence. A number of previous studies have focused on developing this platform and they described the double-tethered DNA Curtains,[11,12] parallel arrays of double-tethered

Received: October 11, 2018
Revised: March 22, 2019
Published: April 8, 2019

DOI: 10.1021/acs.langmuir.8b03424
Langmuir 2019, 35, 5921−5930

isolated DNA molecules,[13] crisscrossed curtains,[14] and single-stranded DNA (ssDNA) curtains.[15]

An important advantage of the DNA Curtains platform (e.g., in comparison to DNA stretching by optical or magnetic tweezers) is simultaneous observation of a high number of DNA molecules within a single experiment. It proved to be very useful in specific protein−DNA interaction studies on the level of individual molecules under the equilibrium conditions, without the shear force introduced by the buffer flow, or at low local DNA concentrations.[13,16] However, the DNA Curtains systems reported to date rely on nanofabricated physical (metallic) barriers surrounded by a fluid SLB. The DNA molecules are tethered to biotinyl-labeled lipids and diffuse laterally in the lipid bilayer. Preparation of the SLB-based system creates experimental risks in terms of defect control and stability. For example, single-end tethered DNA strands tend to diffuse away from the barrier when the buffer flow is off.

In this paper, we present an alternative approach for obtaining oriented and aligned DNA molecules for studies of individual protein−nucleic acid interactions. Instead of using nanofabricated chips containing metallic barriers[9] and forming fluid SLB, we have employed desk-top fabrication and surface chemistry for docking and alignment of single DNA fragments. Previously, soft lithography techniques have attracted a lot of attention for their simplicity and versatility in fabrication of biomolecular architectures.[17] Therefore, we have explored a combination of scanning probe lithography (SPL) and liftoff micro-contact printing (liftoff μCP)[18] for obtaining sAv templates on chemically modified, protein-repellent glass substrates. Such an architecture is essentially flat and sAv patterns function as high-affinity molecular interaction sites for formation of fixed DNA molecule arrays from biotinylated DNA fragments. We have achieved the positioning, alignment, and orientation of the DNA fragments in a fashion resembling the DNA Curtains platform. The employed fabrication strategy provides additional experimental versatility because it is suitable for stable DNA positioning in arbitrary layouts having any desired shape and dimensions and it is fast and relatively cheap. Our study paves the way for broader applications of SM techniques in functional studies of DNA−protein interactions.

■ MATERIALS AND METHODS

Chemicals and Materials. Silicone elastomer Sylgard 184 (Dow Corning, Midland, MI, USA) was used for liftoff μCP stamp production. Ethanol (99.9%, Merck KGaA, Germany) was additionally distilled and stored in a glass bottle prior to use. Ultrapure water was taken directly from a Synergy 185 UV water purification system (Millipore) and was used for washing and preparation of solutions. Nitrogen gas, purity of 99.999% (ElmeMesser Lit, Lithuania), was used for drying. Gold-coated silicon wafers (a 20 nm-thick Au film and a 2 nm Ti adhesion layer, Ssens BV, The Netherlands) were used for Si master structure production. Substrate cleaning was performed in SC-1 solution: ultrapure water, 30% hydrogen peroxide (Carl Roth GmbH, Germany), 25% ammonia solution (Carl Roth GmbH, Germany) at 5:1:1 v/v/v, respectively. Wet chemical etching solution for Au: 20 mM $Fe(NO_3)_3 \cdot 9\ H_2O$ (Fluka, Switzerland), 30 mM thiourea (Fluka, Switzerland), and 1 mM HCl (Sigma-Aldrich, USA) dissolved in ultrapure water saturated with octanol (Sigma-Aldrich, USA). DNA primers were synthesized and purified by Iba-lifesciences (Germany) or Metabion (Germany). Streptavidin (SERVA, Germany), HEPES (Carl Roth GmbH, Germany), Tris-acetate (Sigma-Aldrich, USA), and NaCl (Carl Roth GmbH, Germany) were also obtained. Buffer solutions: (A) 33 mM Tris-acetate, 66 mM K-acetate (pH = 7.9, at 25 °C), (B) 40 mM Tris (pH = 7.8 at 25 °C), (C) 20 mM HEPES, 150 mM NaCl (pH = 7.5, at 25 °C).

Production of DNA. Biotinylated oligonucleotides were annealed to the overhang (cos sequences) at either the left or both ends of bacteriophage λ DNA (ThermoFisher Scientific). The sequences of the oligonucleotides: 5′-AGGTCGCCGCCC-TEG-Biotin (right end) and 5′-GGGCGGCGACCT-TEG-Biotin (left end) (Metabion). These biotinylated oligonucleotides were phosphorylated at the 5′-end using standard PNK kinase reaction (1 μM of the respective oligonucleotide, 10× diluted PNK enzyme, 10× diluted 10× PNK buffer, 0.1 mM ATP) at 37 °C for 30 min. Then, to deactivate the enzyme, they were kept at 95 °C for 5 min. The λ DNA and the oligonucleotide were mixed at a molar ratio of 1:10, heated to 80 °C, and slowly cooled to room temperature (RT). Subsequently, T4 DNA ligase (ThermoFisher Scientific) was added, and the reaction mixture was incubated at RT for 2 h. For the DNA substrates that were biotinylated at both ends, an additional round of annealing and ligation was performed using a 50-fold molar excess of the second oligonucleotide. After the reactions were complete, the DNA ligase was inactivated by heating to 70 °C for 10 min, the excess oligonucleotide was removed using a CHROMA SPIN TE-1000 column (Clontech, USA), and the purified DNA was stored at −20 °C.

Biotinylated 5 kb long DNA was synthesized by PCR using phiX174 RF1 DNA (ThermoFisher Scientific) as a template and oligonucleotides 5′ biotin-CGAAGTGGACTGCTGGCGG-3′ and 5′-CGTAAACAAGCAGTAGTAATTCCTGCTTTATCAAG-3′. Then, it was purified using the GeneJET PCR Purification Kit (ThermoFisher Scientific). Biotinylated 350 bp long dsDNA with the Atto647N dye was prepared using a two-step PCR reaction and ligation with the biotinylated DNA leg in the same way as described previously.[19] The protocol is presented in detail in the Supporting Information file.

Flowcells. Microfluidic flowcells were fabricated from a 25 × 25 × 5 mm^3 ($L \times W \times H$) poly(methyl methacrylate) (PMMA) transparent substrate, double-sided tape, and a coverslip glass. The inlet and outlet holes were drilled through the PMMA substrate approximately 10 mm apart by employing a regular drill bit for metal (4 mm o.d.). To clean the PMMA substrate, it was rinsed with a 1% (w/v) detergent solution (Alconox, USA) supplemented with ∼0.1% (v/v) of an antifoaming agent (neodisher antifoaming agent S, Carl-Roth GmbH, Germany), thoroughly rinsed with ultrapure water, and etched using air plasma (∼500 mTorr, high-power mode, PDC-002, Harrick, USA). Next, a 25 × 25 mm^2 modified glass coverslip (#1.5, Menzel-Galsser, Germany) with printed protein structures was glued to the cleaned PMMA substrate using double-sided tape 25 × 25 mm^2 (0.2 mm thick, 9088, 3M, USA) with a channel cut along its center by a scalpel blade. This glass coverslip was placed so that the printed protein structures would be in the central part of the channel of the flowcell. An inlet port was made by inserting a 1 ml disposable pipette tip into a ∼10 mm long silicone tubing (4 mm o.d., CH24.1, Carl-Roth GmbH, Germany) firmly inserted into the inlet of the PMMA substrate. Accordingly, the outlet port was made by inserting a tubing (0.51 mm i.d., 0.91 mm wall, TYGON R3607, ISMATEC, Germany) of the peristaltic pump into the ∼10 mm long silicone tubing (4 mm o.d., Carl-Roth GmbH, Germany) firmly inserted into the outlet port of the PMMA substrate. The dimensions of the sample channel were 4 × 10 × 0.2 mm^3 ($L \times W \times H$). The total volume of the flowcell was ∼10 μL. A peristaltic pump (6 rollers, REGLO, ISMATEC, Germany) working in a suction mode was used to control the buffer delivery to the flowcell. In case of open loop circulation, the outlet end of the peristaltic pump tubing was placed into a glass beaker, and in case of closed-loop circulation − the outlet end was placed into the inlet port of the flowcell (Figure S1). After the experiment, the flowcell was disassembled by immersing it into isopropanol until the coverslip fell apart, and this way the PMMA substrate was reused multiple times. Upon reusing, the PMMA substrate was carefully washed in clean isopropanol, Alconox, and the ultrapure water, respectively.

Fabrication and Characterization of a Silicon Master. Before use, the Au-coated Si wafers were cut to the required size, rinsed and sonicated in ethanol for 2 min twice, and then cleaned in the SC-1 solution at 85 °C for 15 min. Subsequently, they were thoroughly rinsed in ultrapure water, rinsed and sonicated in ethanol for 1 min, and dried under a N_2 gas stream. Immediately after cleaning, the substrates were immersed into a 40 μM solution of 1-eicosanethiol (HS-C_{20}, Alfa Aesar) in ethanol and incubated for at least 14 h to form a self-assembled monolayer (SAM), acting as a resist layer in wet chemical etching of Au.[20−22] After incubation, the substrates were rinsed and sonicated in ethanol for 5 min twice and dried with N_2 gas. The substrates coated with the SAM were employed in surface patterning by the nanoshaving lithography technique using an atomic force microscope (AFM, NanoWizard3, JPK Instruments AG, Germany). The latter was operating in the contact mode and using probes (Tap190DLC, BudgetSensors, Bulgaria) coated with diamond-like carbon.[23,24] Line feature engraving in the surface was repeated three times, at a typical writing speed of 10 μm s^{-1} and a force of about 6400−10 000 nN. After lithography, the samples were sonicated in ethanol for 2 min and Au was gently etched to remove any debris inside the line features and to slightly increase the line width. Wet chemical etching of Au was performed in the Au etching solution.[20−22] Etching of Au was monitored with an optical microscope and was stopped once the scratched lines became clearly visible. The typical Au etching times were 4−10 min. Then, the etching of Si substrate was performed in 50% KOH solution (Carl Roth GmbH, Germany) upon sonication in an ultrasonic bath (RK100H, Bandelin Sonorex, Germany) at approximately 25−30 °C, typically for about 80 min.[25] Temperature was kept at 25 °C in the ultrasonic bath. After every 20 min of etching, the sample was rinsed with ultrapure water and the depth of the features was measured with the AFM. The etching process was stopped once the desired depth was obtained. Then, the samples were thoroughly rinsed in ultrapure water and the remaining Au layer was removed by immersing them into the Au etching solution without addition of octanol, for at least 1 h.

The morphology of the fabricated master structures was analyzed by an upright optical microscope BX51 (Olympus, Japan), equipped with a motorized sample stage (Prior Scientific Instruments Ltd., United Kingdom). For the Si master structure and glass surface characterization, the same NanoWizard3 AFM was used. The topography measurements of the etched Si master structures were made in air in the AC mode using the Tap190DLC, ARROW-NCR, or RTESPA probes. The width and morphology of the printed protein line features on the glass surface were analyzed in buffer C. For this purpose, the samples were mounted into the ECCel (JPK Instruments AG, Berlin, Germany) liquid cell with perfusion. To minimize the probe interaction forces on the proteins, the QI-Advanced mode was used. The measurements were performed using the HQ:NSC35/Cr-Au BS (nominal spring constant 5.4 N m^{-1}, MikroMasch, Bulgaria) probes. Before each measurement, the probe sensitivity and spring constant were calibrated using the contact-free calibration routine (based on the thermal spectrum of cantilever oscillations) built into the AFM software. The setpoint for measurements was set to 1.5−2 nN tip pushing force.

Protein Nanopatterning by Liftoff μCP. Sylgard 184 silicone elastomer kit was used to produce flat polydimethylsiloxane (PDMS) elastomer stamps for protein liftoff μCP. The prepolymer and curing agent were mixed in a 10:1 ratio w/w and thoroughly mixed. The mixture was degassed in a vacuum desiccator for 30 min to remove any trapped air bubbles; then, it was poured into a plastic Petri dish and cured in an oven at 65 °C for 14 h. The thickness of the cast PDMS elastomer was ~2 mm. The PDMS side that was in contact with the Petri dish was treated as the flat one.

The liftoff μCP was performed according to the published procedure.[18] For this purpose, the Si master and PDMS elastomer (cut to 5 × 5 mm^2 dimensions) were cleaned in this sequence: rinsing with isopropanol solution (30% v/v in ultrapure water), rinsing with ultrapure water, and drying under N_2 gas stream. The Si master surface was further cleaned by air plasma (~500 mTorr, high-power mode, PDC-002, Harrick, USA) for 5 min. To homogeneously cover the PDMS surface with a film of the protein ink, the PDMS stamp was placed in a clean plastic Petri dish with its flat side facing up. Then, a 60 μL drop of 0.2 mg/mL (unless stated otherwise) streptavidin solution (in buffer A) was placed on the PDMS surface and kept for 10 min. After incubation with the protein ink, the PDMS stamp was washed with 5 mL of buffer A using a 1 mL pipette, ~50 mL ultrapure water using a wash bottle, and dried under N_2 gas stream. To transfer the original pattern from the Si master to the modified glass coverslip, the dried PDMS stamp was first placed into contact with the plasma-cleaned Si surface containing the master structures for ~15 s using tweezers. Subsequently, the PDMS stamp was transferred from the Si surface onto the silanized and PEGylated (methoxy-PEG-SVA and biotin-PEG-SVA, Lyasan Bio, USA) glass coverslip (25 × 25 mm^2, #1.5, Menzel Glaser) and kept for 1 min, and again to establish contact its corners were gently pressed using the tip of the tweezer. The surface of the glass coverslips was modified in the same way as described previously,[26] and the biotin-PEG/methoxy-PEG ratio was 4:10 w/w, unless stated otherwise. Next, the PDMS stamp was peeled off the glass coverslip using the tweezers and discarded. The patterned glass coverslip was assembled into the flowcell (see above). The Si masters were reused for the liftoff μCP multiple times and in between the experiments they were stored in 30% isopropanol solution.

Total Internal Reflection Fluorescence Microscopy. The employed home-build total internal reflection fluorescence (TIRF) microscopy setup was described previously.[26] For TIRF measurements, we installed an additional 488 nm wavelength laser (20 mW, Crystalaser, USA). The laser was coupled into the common optical path via a 488 nm single-band dichroic mirror (zt488RDC, AHF, Germany) downstream to the dichroic mirror combining the green and red lasers into the common optical path. These combined beams were directed to the objective (100×, 1.4NA, Nikon) using a quad-line dichroic mirror (zt405/488/532/640rpc, Chroma Technology Corp), which was placed in the upper filter cube turret installed in the microscope body (Nikon Eclipse Ti-U). The laser power before the objective was set to 2.5 mW for both 532 and 632 nm lasers and to 0.1 mW for the 488 nm laser, respectively. The exposure time of the EMCCD camera (Ixon3, Andor) was set to 100 ms. The microscopy images represented in the article and in the Supporting Information file were averaged over 10 consecutive frames, thus improving the signal-to-noise ratio. The penetration depth of the evanescent field was set to ~300 nm for both wavelengths of excitation. This setup was equipped with a piezo Z stage (PI), on which the objective was mounted. Also, it had an infrared diode laser, which beam was totally reflected from the glass−water interface. This infrared diode laser was directed to the objective via a dedicated dichroic mirror (T800dcsp, Chroma Technology Corp) placed in the lower filter cube turret. Position of the reflected beam was monitored by a CCD camera (WAT-902H3 SUPREME, Watec, The Netherlands). Position of the objective was controlled via a PI controller (E-712.3CDA, PI, Germany). Dedicated custom-written software (Lab-View, NI) was used to establish feed-back control of the beam position on the camera and the Z piezo stage movement to compensate the Z-axis drift of the sample, so that the latter was kept stably in focus.

Fluorescence Characterization. The average line quality factor (QF) was calculated using the formula—QF = avg$((I_{\text{line}} - I_{\text{bckg}})/(I_{\text{interline}} - I_{\text{bckg}}))$. Here, I_{line}—average intensity of the structure, which was calculated by taking a horizontal line-profile 8 pixels wide (orange line in Figure S2). The average intensity of the area between the structures $I_{\text{interline}}$—was calculated by taking a horizontal line-profile of the width equal to the interline width (the yellow area in Figure S2). These intensities were calculated for at least 10 different lines in at least 3 images taken in different positions of the sample. The average intensity of the global background—I_{bckg} was estimated by taking the average of the ROI intensity in several different positions in the image, where clearly no fluorescent spot was found (the green ROI in Figure S2). Thus, the QF was calculated by dividing the background-subtracted I_{line} by the background-subtracted $I_{\text{interline}}$ value of the neighboring area, and an average of this ratio together with the standard deviation (SD) was taken over all positions. TIRF microscopy has an uneven excitation profile and this may skew the QF. Therefore, only those structures that were close to the center of the excitation peak were taken into consideration.

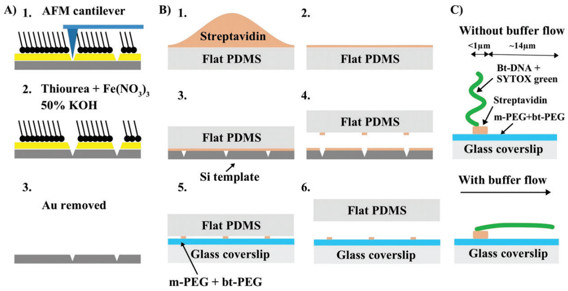

Figure 1. Schematics explaining the main steps of fixed DNA molecule array fabrication. (A) Fabrication of a reusable Si master: (1) AFM nanoshaving of a SAM and Au layer on a Si substrate; (2) deepening of the inscribed patterns by sequential treatment with thiourea and Fe$(NO_3)_3$, and then with 50% KOH solution; (3) final removal of Au by wet chemical etching. (B) Protein liftoff micro-contact printing (μCP): (1) inking of a planar PDMS stamp with streptavidin (sAv) ink; (2) drying of PDMS under a stream of N_2 gas; (3−4) selective subtraction of sAv by contacting the Si master with the inked PDMS followed by a liftoff; (5−6) μCP of sAv onto a glass coverslip modified with methoxy-PEG and biotin-PEG mixture. (C) Immobilization and alignment of biotinylated DNA on the fabricated sAv templates.

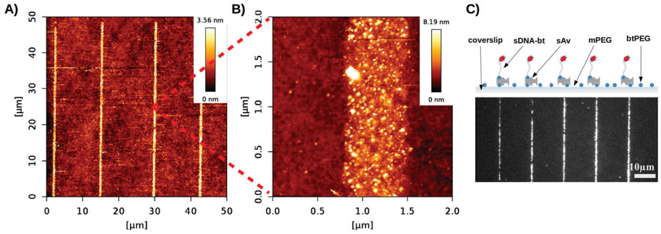

Figure 2. Characterization of streptavidin (sAv) patterns on a PEGylated glass coverslip surface obtained by replicating a Si master with line features having a width of 600 nm (see text for details). (A) AFM topography micrograph of typical sAv features. (B) Zoomed view of the micrograph in panel (A). (C) TIRF microscopy image and an explanatory schematic showing biotinylated and Atto647N-labeled, 350 bp-long dsDNA immobilized on an sAv template fabricated using the same Si master as in panels (A,B). Excitation was at 635 nm, QF = 26.2 ± 5.6 (±SD), the TIRF image is an average of 10 consecutive frames.

DNA Immobilization and Interaction with Restriction Enzyme BfiI. First, the channel of the flowcell was filled by injecting buffer B. Next the biotinylated DNA (~30 pM, in buffer B) was added and incubated for at least 15 min. The excess of unbound DNA was washed out with ~300 μL of buffer A. Then, DNA was labeled with the DNA intercalating green fluorescent dye—SYTOX green (ThermoFisher Scientific) at a concentration of ~10 pM (in buffer B). SYTOX green was present during the entire time of the experiment. In case of close-loop circulation, the loop was first filled with 160 μL of buffer B, and then 4 μL of DNA was added (this resulted in ~30 pM concentration, in buffer B) and incubated for at least 15 min. The pump was set to the ~0.1 mL/min rate for this period. Next, to reveal the bound DNA, 1 μL of SYTOX green was added (this resulted in ~10 pM concentration, in buffer B). For BfiI DNA cleavage studies, this enzyme was added at 1 nM final concentration (in buffer A + 10 mM $MgCl_2$). After the BfiI reaction step, we washed the flowcell with 7 M urea solution. This step was introduced to remove any bound protein from DNA after cleavage reaction. BfiI was purified according to the previously published procedure.[27] BfiI acts at an asymmetric 5′-ACTGGG-3′ sequence and cleaves the top and bottom DNA strands five and four nucleotides downstream of the recognition sequence.[28] All experiments were carried out at RT. We excluded from the statistical analysis of DNA fragment length those DNA molecules that did not stretch or formed loops with buffer flow applied.

■ RESULTS AND DISCUSSION

Nanofabrication of Templates and DNA Immobilization. For stable DNA molecule array assembly via high affinity molecular interactions, we fabricated nanoscopic sAv templates on glass coverslips. For this purpose, we combined SPL and protein liftoff μCP. Schematics shown in Figure 1 explain the main steps of the DNA molecule array fabrication process (see also Supporting Information file Figure S3).

First, we used Au-coated silicon wafers modified with a SAM of HS-C_{20} as the substrates for nanofabrication of the master structures in Si for protein liftoff μCP (hereafter—masters, Figure 1A). First, we patterned the SAM/Au surface by inscribing lines features by the nanoshaving technique using an AFM. Subsequent chemical treatment of the patterned Au surface slightly widened the inscribed line features in the Au coating. Then, we obtained Si surface reliefs by etching the patterned chip in KOH solution. In such a treatment, the intact SAM/Au zones acted as an etch resist, whereas the patterns generated by the AFM tip transferred into the Si substrate and appeared as surface depressions. In the final step, we removed the remaining Au layer entirely by chemical etching. This simple fabrication process allowed obtaining Si masters having relatively large surface areas, which contained hundreds of line features, within several hours. Note that such a desk-top process requires neither the use of any specialized nanolithographic/cleanroom equipment nor costly intermediate products, like lithography masks. Typical Si masters contained intruding line features having a width of ~600 nm and a depth of ~400 nm and they were well suited for the liftoff μCP (Figure S6). For comparison, we changed the feature depth in the range from 140 to 500 nm and this had no significant influence on the quality of the resulting DNA molecule arrays. Also, we tested the effect of reusing the same Si master by characterizing it with AFM immediately after Au etching and after its multiple use as described below (see Figure S7). The AFM analysis showed no evidence of any significant degradation of the master that we reused tens of times.

We performed liftoff μCP with a homogeneously inked and dried flat PDMS stamp (see explanation of the process in Figure 1B), which we brought manually into contact with the master and subsequently transferred onto the PEGylated glass surface. We tested several biotin-binding proteins as inks for the protein liftoff μCP procedure (sAv, neutravidin, avidin, all at 0.2 mg/mL). Our results showed that protein templates on glass produced from the sAv ink performed best in terms of specific biotinylated DNA binding (Figure S8).

To measure the exact width of the printed sAv template (the line width was ~600 nm on the Si master), we carried out AFM topography measurements in solution. The results of the measurements showed that the width of the printed sAv line features was ~600 nm; thus, they also matched the Si master very well (see Figures 2A,B, S6 and S9 for comparison). Also, the printed sAv features on glass mostly had heights matching a single layer of sAv molecules, with occasional higher spots, which we interpreted as sAv aggregates. The amount of sAv detected in the nonpatterned areas of the samples was negligibly low.

To characterize binding of a biotinylated dsDNA to the sAv template features, we employed TIRF microscopy. First, we injected a 350 bp long dsDNA into the flowcell and incubated the chip. The DNA fragment was biotinylated at its 5′ end and had the other end labeled with an organic fluorophore-ATTO647N. The excess unbound DNA was removed by washing the chip with buffer B. Images of this sample acquired using a TIRF microscope at the 635 nm excitation and in the red fluorescence channel showed a high contrast between the template features for DNA binding and the nonpatterned surface areas, respectively (Figure 2C). According to the employed intensity-based characterization approach, the average difference between the template features and the nonstructured areas was above 26:1 (QF).

Most of the bound DNA molecules were forming a single straight line on the sAv template, indicating that the designed structure width of ~600 nm was sufficient to achieve a narrow distribution of the DNA pinning points, as observed in optical microscopy. In contrast, we noted that a structure width of ~1 μm was too large and analysis clearly showed that the bound DNA was forming a curved line structure (see Figure S10A). We also tested sAv templates having lines of a smaller width (~200 nm) that may be useful for even better alignment of biotinylated DNA (Figure 10B). Based on the performed comparisons, we can state that 600 nm-wide lines allow for studying substrates longer than 1700 bp, while 200 nm-wide lines allow studying DNA as short as 600 bp. However, in our experiments, an alignment precision better than 600 bp was not practical because of the employed TIRF system.

Optimization of the Molecular Composition of the DNA Molecule Array. We optimized the composition of the array template features in terms of nonspecific DNA binding as well as the overall SM fluorescence detection conditions. First, we tested the effect of different surface concentrations of biotin-PEG on the amount of bound DNA to the sAv line features and the nonstructured areas, respectively. For this purpose, we changed biotin-PEG fractions in the PEGylation solution using several biotin-PEG to methoxy-PEG ratios: 0.5:10, 1:10, 4:10, and 8:10 w/w. We fabricated patterns from sAv (0.2 mg/mL) and analyzed binding of 5 kb long biotinylated dsDNA stained with the SYTOX green. Figure 3 shows the images of bound DNA acquired using a TIRF microscope under 488 nm excitation. These results suggested that glass substrates modified using 1:10 and 4:10 biotin-PEG/methoxy-PEG ratios (Figure 3B,C and Table 1) displayed a similar quality of protein line features (serving as an array template) and performed equally well in terms of DNA specific versus nonspecific binding (QFs of ~19:1 and 14:1 respectively). The lowest biotin-PEG to methoxy-PEG ratio surface (Figure 3A and Table 1) displayed a poorer quality of

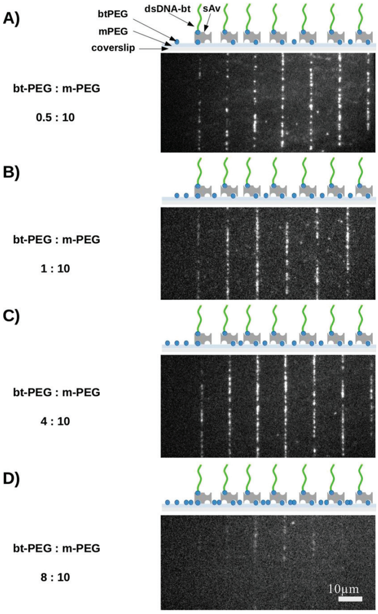

Figure 3. TIRF microscopy images showing the effect of biotin-PEG-SVA to methoxy-PEG-SVA ratio in the PEG monolayer formed on an amino-functionalized glass coverslip. Biotin-PEG/methoxy-PEG ratios (w/w): (A) 0.5:10, (B) 1:10, (C) 4:10, and (D) 8:10. Concentration of streptavidin ink for patterning was kept the same for all the experiments ~0.2 mg/mL. After immobilization, DNA was stained with SYTOX green. The patterns were fabricated using a Si master with 200 nm-wide, ~160 nm-deep lines, interline spacing was ~14 μm. Images (excitation at the 488 nm wavelength) are averages of 10 consecutive frames.

Table 1. Summary of the Average QF of Line Feature Intensity vs Interline Intensity Characterization for Various Biotin-PEG/Methoxy-PEG Ratios Used for Glass Surface Modification (Figure 3), as Well as at Various sAv Concentrations in the Ink Solution Used for Liftoff μCP (Figure 4)

biotin-PEG/methoxy-PEG (w/w), fixed sAv concentration of 0.2 mg/mL	QF ± SD	sAv [mg/mL], fixed biotin-PEG/methoxy-PEG ratio of 4:10	QF ± SD
0.5:10	4.2 ± 1.6	0.03	3.2 ± 0.6
1:10	19.1 ± 8	0.1	9.5 ± 3.4
4:10	14.5 ± 6.1	0.2	14.5 ± 6.1
8:10	3 ± 0.8	0.4	2 ± 0.8

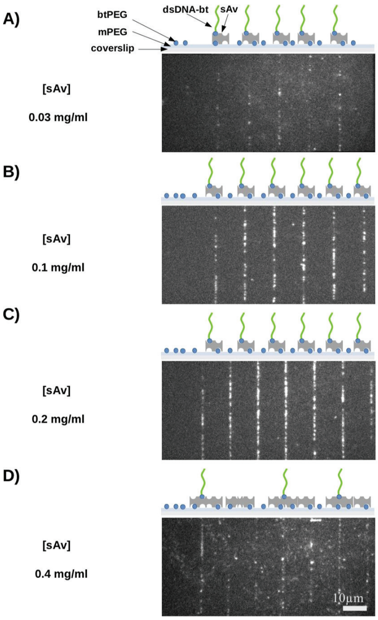

Figure 4. TIRF microscopy images showing the effect of concentration of streptavidin (sAv) ink used for protein patterning on glass coverslips coated with biotin-PEG/methoxy-PEG at the ratio 4:10. Streptavidin concentrations: (A) 0.03, (B) 0.1, (C) 0.2, and (D) 0.4 mg/mL. The line features in the original Si master had a width of 200 nm, a depth of around 160 nm, and the interline spacing was close to 14 μm. After immobilization DNA fragments were stained with SYTOX green. Corresponding schematics explain the strategy for preparing the surface. Each of the images (recorded at the excitation wavelength at 488 nm) is an average of 10 consecutive frames.

the line features, likely because of a lower surface concentration of sAv bound during transferring the pattern from the PDMS stamp. The highest biotin-PEG to methoxy-PEG ratio on the surface (Figure 3D and Table 1) resulted in a very low biotinylated DNA binding onto the sAv template structures. This could be rationalized by the fact that at such a high biotin concentration on the surface binding of sAv—biotin might be sterically hindered. Such an effect of an effective window of surface biotin concentration has been previously reported by different studies on SAM-based molecular interaction systems.[29,30] Based on these results, we conclude that biotin-PEG to methoxy-PEG ratios of 1:10 and 4:10 are both well suited for dense biotinylated DNA immobilization.

Concentration of sAv in the ink solution prepared for PDMS stamp inking may also affect the quality of the printed lines. To estimate this effect, we selected the modified glass surface with 4:10 biotin-PEG to methoxy-PEG ratio and fabricated array templates (protein line features) using different concentrations of sAv in the PDMS stamp ink solution: 0.03, 0.1, 0.2, and 0.4 mg/mL. To evaluate biotinylated DNA binding, we immobilized 5 kb long biotinylated dsDNA stained by SYTOX green. Images of bound DNA acquired using the TIRF microscope under 488 nm excitation (Figure 4 and Table 1) showed that the best quality of lines (yielding the highest amount of DNA bound to the protein templates vs nonstructured glass surface areas) was for 0.2 mg/mL sAv concentration (Figure 4B,C and Table 1). For comparison, 0.1 mg/mL sAv resulted in a slightly lower quality of the DNA molecule array, than 0.2 mg/mL (QF of ~9.5 compared to ~14.5). The lowest concentration of sAv also gave a low binding of DNA (Figure 4A and Table 1), whereas the highest one resulted in both higher DNA binding on the nonstructured surface areas and low binding to the sAv template features (Figure 4D and Table 1). It is likely that at higher concentration sAv molecules after printing pack densely on the PEGylated glass surface, and this affects their orientation so that the binding pockets of the sAv become inaccessible to the biotinylated DNA.[31] Based on these results, 0.2 mg/mL sAv concentration proved to be best suited to achieve the high quality structures, and therefore we used it in our further experiments.

Alignment of Short DNA Fragments. Having optimized the molecular composition of the array templates, we were able to test stretching of $5'$-end biotinylated 5 kb DNA by pinning it to the sAv line features. We stained the immobilized DNA molecules by SYTOX green and acquired the images using the TIRF microscope under 488 nm excitation. During these proof-of-principle experiments, when we repeatedly switched the buffer flow (~1 mL/min) on and off we observed repetitive extension of the DNA molecules perpendicularly to the sAv line features (Figure 5 and Video S1). The measured length of the extended DNA reached ~1.4−1.5 μm and it was close to the theoretical length of an >90% extended 5 kb long dsDNA.[32,33]

Alignment of Single-Tethered Biotinylated λ DNA. Having demonstrated the possibility to stretch relatively short DNA fragments, we employed the same strategy to align single-end biotinylated λ DNA along the buffer flow. We were able to image ~80 single-tethered DNA molecules per chosen field of view ($80 \times 40\ \mu m^2$), Figure 6. Note that by using the full camera chip (i.e., bypassing the dual-view module) for imaging of our fixed DNA molecule array, one would also be able to image twice as high a number per field of view. We compared two different flow rates: 0.2 and 1 mL/min, and in

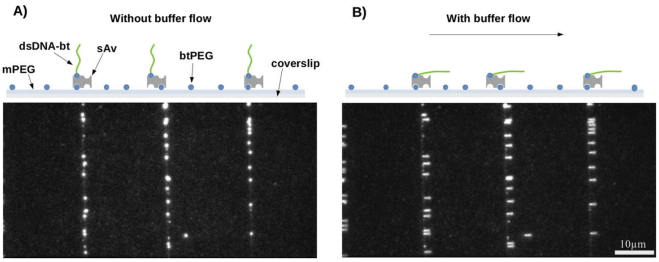

Figure 5. TIRF microscopy images of SYTOX green stained 5 kb length dsDNA molecules immobilized on streptavidin array template: (A) without buffer flow, (B) a buffer flow of ~1 mL/min. The streptavidin template was fabricated using a master with 600 nm-wide lines. Each of the images (excitation at the 488 nm wavelength) is an average of 10 consecutive frames.

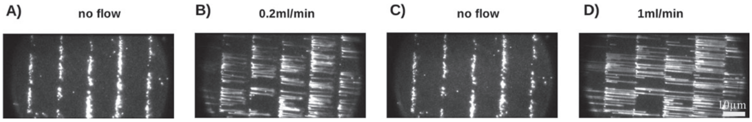

Figure 6. TIRF microscopy images of SYTOX green-stained, single-tethered λ DNA immobilized on a streptavidin array template: (A,C) without flow, (B) at a low flow rate (0.2 mL/min), and (D) at a high flow rate (1 mL/min). One-end biotinylated λ DNA molecules were immobilized on the streptavidin template fabricated using a Si master with 600 nm-wide lines. Each of the images (excitation at the 488 nm wavelength) is an average of 10 consecutive frames.

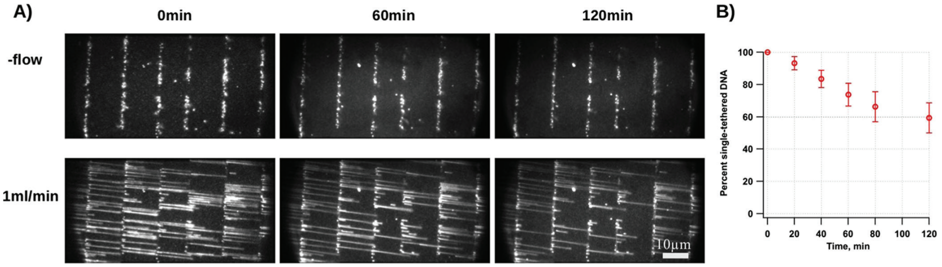

Figure 7. TIRF microscopy images (excitation at the 488 nm wavelength) showing the stability test of single-tethered λ DNA molecule arrays. One-end biotinylated λ DNA molecules were immobilized on a streptavidin array template and stained with SYTOX green. The original Si master contained line features having a width of 600 nm. (A) Images were acquired each 20 min for a period of 2 h. In between acquisition, there was no buffer flow applied. During the acquisition, 50 frames were acquired at a buffer flow of 1 mL/min and 50 frames without the flow. (B) Number of single-tethered DNA molecules that extended to the full length was counted on each line and the average number of the molecules with the corresponding SD is represented graphically.

each case the λ DNA molecules were stably stretched (see Videos S2 and S3). This indicated that our flow delivery system worked well for such an application as it did not introduce the undesired frequent stretching-and-contracting of the immobilized DNA molecules. Also, we did not observe any focus drift upon starting and stopping the flow.

Next, to characterize the stability of the DNA molecules immobilized in the array, we performed a long-term observation experiment. During this experiment, we acquired image series with and without buffer flow, each 20 min (Figure S11). In between these acquisitions, we switched the buffer flow off. To quantify the stability of single-tethered biotinylated λ DNA immobilization, we manually counted the number of SYTOX green-labeled single-tethered λ DNA molecules that were stretched along the buffer flow (Figure 7A). We calculated the average number of these single-tethered DNAs by counting over five sAv lines features of the array template visible in the image and also the corresponding SD. This analysis revealed that around 60% of the immobilized single-tethered λ DNAs remained bound even 2 h after initial imaging (Figure 7B).

Double-Tethered Biotinylated λ DNA. To perform detailed mechanistic studies of DNA−protein interaction, it is necessary to have longer DNA substrates immobilized on the array template (i.e., pinning to the sAv features). Also, it is essential to have the possibility to examine DNA−protein interactions eliminating the eventual effect of the buffer flow. Therefore, we immobilized λ DNA molecules biotinylated at their both ends, one sticking to one sAv line feature and the other end extending to the next line, in the direction of the

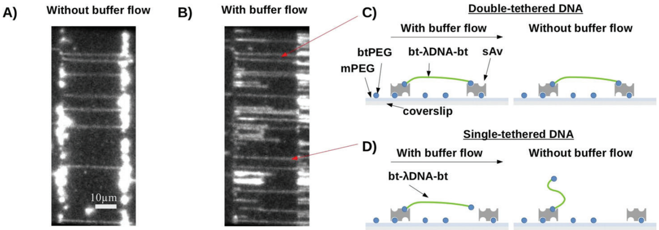

Figure 8. TIRF microscopy images of λ DNA biotinylated at both ends, immobilized on streptavidin (sAv) line patterns and stained with SYTOX green. Such a protein template was fabricated using a Si master having line features with the 600 nm line-width. (A) Only those DNA molecules, which have both ends successfully bridging the neighboring sAv lines, are visible without the buffer flow, (B) only single-end immobilized DNA molecules also appear with the flow. (C) Schematics of DNA immobilized via both ends and (D) explanation of unsuccessful immobilization of the second DNA end. Images (excitation at the 488 nm wavelength) are averages of 10 consecutive frames.

buffer flow. For these experiments, we used a closed loop flow circuit. First, we injected the DNA solution at a slow flow rate (∼0.1 mL/min) to capture the first end. After ∼10 min of incubation, we increased the rate of the buffer flow to ∼1 mL/min to capture the other end onto the next sAv line, and in this fashion we extended the DNA molecules so that they bridged the neighboring sAv line features (Figure 8A,B).

Results have shown that it is possible to immobilize and successfully capture DNA molecules by both ends to the neighboring sAv lines (Figure 8A,B). However, around 65% of the DNAs were tethered only by a single end (Figure 8A,B). This we revealed by stopping the buffer flow and checking if the DNA fragment was contracting or not. The success of this immobilization strategy depends on several factors such as the width of the protein line used as the template and the rate of the buffer flow. The latter we calibrated using different flow speeds, and for the designed array template (sAv line pattern) and the selected DNA length, the optimal buffer flow was at ∼1 mL/min (Figure 9). One drawback of this strategy is that it does not allow predefined orientation of DNA during immobilization, because both ends have the same functional group. On the other hand, it is possible to label DNA with a fluorescent dye in a defined position, and this would allow to digitally rotate the DNA fragments in an image so that they would be all oriented in the same direction. Additionally, digoxigenin (DIG) modification of the second end of the λ DNA molecule, which has its first end biotinylated, may be used as well in combination with biotinylated anti-DIG.

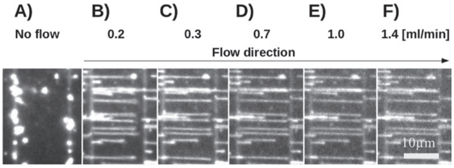

Figure 9. TIRF microscopy images showing extension of single-tethered one-end biotinylated λ DNA, by the shear flow. The DNA molecules were stained with the SYTOX green and the corresponding series of images taken (A) without the flow and (B−F) at flow rates of 0.2, 0.3, 0.7, 1, and 1.4 mL/min. The DNA molecules displayed a mean extension of 11.7 ± 0.34, 12.7 ± 0.26, 13.3 ± 0.22, 13.8 ± 0.4, and 14.1 ± 0.5 μm, respectively (±SD). The original Si master used for printing the streptavidin template contained line features having a width of 600 nm. Images (excitation at the 488 nm wavelength) are averages of 10 frames.

Localization of Single DNA−Protein Interactions. As a proof-of-principle experiment that allowed us to preliminary test the performance of our platform, we tested binding and DNA cleavage by restriction endonuclease BfiI on the single-tethered λ DNA fragments. Restriction endonuclease BfiI recognizes and cleaves DNA sequence ACTGGG downstream of the recognition site.[28,34−40] The employed λ DNA has four recognition sequences of BfiI that are located at 7065, 11 619, 25 702, and 30 328 bp, respectively.

We incubated single-tethered λ DNA fragments with a 1 nM concentration of BfiI, and acquired TIRF microscopy images at the 488 nm excitation wavelength before (Figure 10A) and after DNA treatment with BfiI (Figure 10B). After sample treatment with BfiI, we washed the flowcell with 7 M urea solution. We introduced this step to remove the bound protein from cleaved DNA, and in that way we avoided artificial DNA shortening due to DNA looping (single BfiI can bind to two targets on DNA). We observed successful cleavage of the DNA fragments by BfiI, manifested by shortening of the arrayed DNA molecules. Next, we estimated the lengths of the immobilized single-tethered λ DNA before and after cleavage reaction in images acquired under a flow rate of 1 mL/min (Figure 10C). This characterization revealed that before the reaction the distribution of the length of DNA fragments had a monodispersed appearance with an expected average length ∼13.6 μm (center position of the single Gaussian fit). After the reaction, the fragments clearly shortened, and their length distribution became poly-dispersed with five main peaks. We fitted these peaks using single (for the full length DNA fragments) or double Gaussians (for cleaved DNA fragments) and found that their center positions were located at 1.6, 3.1, 6.7, 8.1, and 13.6 μm. The center positions of these peaks corresponded well to the BfiI target locations of the λ DNA. The peak at 13.6 μm, which was still visible after sample treatment with BfiI, indicated that ∼10% of all immobilized DNA molecules remained intact.

■ CONCLUSIONS

We successfully implemented an alternative strategy for stable arraying of single DNA molecules by combining surface chemistry, molecular patterning, and affinity-based assembly techniques. Our approach does not involve the use of metallic

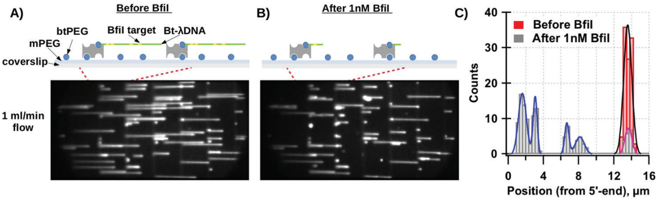

Figure 10. TIRF microscopy monitoring of restriction endonuclease BfiI cleavage position distributions measured on single-tethered bt-λ DNA immobilized in the array. The array template consisting of sAv was printed using a Si master having 600 nm-wide line features. DNA was stained with the SYTOX green. (A) Typical image of single-tethered bt-λ DNA before BfiI treatment. All four possible BfiI binding targets on the λ DNA are indicated in yellow in the schematics. (B) Typical image of single-tethered bt-λ DNA after 1 nM BfiI treatment and wash with 7 M urea. (C) Graph showing measured DNA length before (N: 104) and after (N: 128) DNA treatment with BfiI. Peaks in the DNA length distributions were fitted using single (black and magenta) or double Gaussian (blue) fittings. Images (excitation at the 488 nm wavelength) are averages of 10 frames; the buffer flow rate was set to 1 mL/min.

templates and SLB, thus improving the stability of the assembled arrays, minimizing the nonspecific binding, and extending the time available for the experiments. For fabrication of the nanoscale protein template needed for assembling the array of DNA molecules, we took advantage of the simplicity of soft lithography, which can be readily implemented in any regular chemistry laboratory. Our experimental system allows visualization of more than 100 DNA molecules within a typical field-of-view (80×80 μm^2) of an objective-based TIRF microscope—a setup that potentially could be also used for super-resolution imaging. Our strategy allows obtaining both single- and double-tethered DNA molecule arrays. The smallest line width that we achieved was 200 nm, such narrow templates can be applied for studying DNAs as short as 600 bp. The DNA molecules were immobilized stably – 60% of single-tethered DNA remained immobilized on the protein structures after 2 h without the buffer flow. We also demonstrated that this platform is well suited for functional protein–DNA interaction studies, as the robust array platform is at the same time optimized in terms of specific versus nonspecific interactions. The chosen strategy allows using various complementary chemistries, including PEG–maleimide, PEG–COOH or PEG–NHS, PEG–NTA[41−43] that were previously developed for docking, analysis, and manipulation of biomolecules. Moreover, our strategy is compatible with a wide variety of protein inks, functional surface chemistries and protein nanopatterning techniques that provide a broad versatility for studying and engineering complex protein–nucleic acid assemblies. At the next stage, this platform is promising for SM studies and SM Förster Resonance Energy Transfer (smFRET), because the techniques described in the present study are very similar to those used in smFRET or other SM fluorescence techniques.

■ ASSOCIATED CONTENT

Ⓢ Supporting Information

The Supporting Information is available free of charge on the ACS Publications website at DOI: 10.1021/acs.langmuir.8b03424.

> Repetitive extension of the DNA molecules perpendicularly to the sAv line features, when the buffer flow was switched (~1 mL/min) on and off (AVI)
>
> Stably stretched λ DNA molecules at the flow rate of 0.2 mL/min (AVI)
>
> Stably stretched λ DNA molecules at the flow rate of 1 mL/min (AVI)
>
> DNA synthesis; schematics of the peristaltic pump connected to the flowcell and operating in the closed loop mode; locations of regions of interest used for quality factor calculation; schematic explaining the steps involved in the fabrication process of the Si master using scanning probe nanoshaving and wet chemical etching techniques; optical and AFM micrographs; and TIRF microscopy images (PDF)

■ AUTHOR INFORMATION

Corresponding Author

*E-mail: valiokas@ftmc.lt.

ORCID

Marijonas Tutkus: 0000-0002-5795-1347
Tomas Rakickas: 0000-0002-1231-7545
Aurimas Kopūstas: 0000-0002-2972-1851
Ramūnas Valiokas: 0000-0003-4807-9136

Present Address

[‖]Laboratory of Nanoscale Biology, Institute of Bioengineering, School of Engineering, Ecole Polytechnique Federale de Lausanne (EPFL), 1015 Lausanne, Switzerland.

Notes

The authors declare no competing financial interest.

■ ACKNOWLEDGMENTS

This study was funded by Research Council of Lithuania [S-MIP-17-59 to E.M.].

■ REFERENCES

(1) Kim, H.; Ha, T. Single-Molecule Nanometry for Biological Physics. *Rep. Prog. Phys.* **2013**, *76*, 016601.

(2) Zheng, Q.; Juette, M. F.; Jockusch, S.; Wasserman, M. R.; Zhou, Z.; Altman, R. B.; Blanchard, S. C. Ultra-Stable Organic Fluorophores for Single-Molecule Research. *Chem. Soc. Rev.* **2014**, *43*, 1044–1056.

(3) Farooq, S.; Fijen, C.; Hohlbein, J. Studying DNA–Protein Interactions with Single-Molecule Förster Resonance Energy Transfer. *Protoplasma* **2014**, *251*, 317–332.

(4) Joo, C.; McKinney, S. A.; Nakamura, M.; Rasnik, I.; Myong, S.; Ha, T. Real-Time Observation of RecA Filament Dynamics with Single Monomer Resolution. *Cell* **2006**, *126*, 515–527.

(5) Zawadzki, P.; May, P. F. J.; Baker, R. A.; Pinkney, J. N. M.; Kapanidis, A. N.; Sherratt, D. J.; Arciszewska, L. K. Conformational Transitions during FtsK Translocase Activation of Individual XerCD-

Dif Recombination Complexes. *Proc. Natl. Acad. Sci. U.S.A.* **2013**, *110*, 17302−17307.

(6) Comstock, M. J.; Whitley, K. D.; Jia, H.; Sokoloski, J.; Lohman, T. M.; Ha, T.; Chemla, Y. R. Direct Observation of Structure-Function Relationship in a Nucleic Acid-Processing Enzyme. *Science* **2015**, *348*, 352−354.

(7) Lee, K. S.; Balci, H.; Jia, H.; Lohman, T. M.; Ha, T. Direct Imaging of Single UvrD Helicase Dynamics on Long Single-Stranded DNA. *Nat. Commun.* **2013**, *4*, 1878.

(8) Visnapuu, M.-L.; Duzdevich, D.; Greene, E. C. The Importance of Surfaces in Single-Molecule Bioscience. *Mol. BioSyst.* **2008**, *4*, 394.

(9) Fazio, T.; Visnapuu, M.-L.; Wind, S.; Greene, E. C. DNA Curtains and Nanoscale Curtain Rods: High-Throughput Tools for Single Molecule Imaging. *Langmuir* **2008**, *24*, 10524−10531.

(10) Granéli, A.; Yeykal, C. C.; Prasad, T. K.; Greene, E. C. Organized Arrays of Individual DNA Molecules Tethered to Supported Lipid Bilayers. *Langmuir* **2006**, *22*, 292−299.

(11) Gorman, J.; Fazio, T.; Wang, F.; Wind, S.; Greene, E. C. Nanofabricated Racks of Aligned and Anchored DNA Substrates for Single-Molecule Imaging. *Langmuir* **2010**, *26*, 1372−1379.

(12) Soniat, M. M.; Myler, L. R.; Schaub, J. M.; Kim, Y.; Gallardo, I. F.; Finkelstein, I. J. *Next-Generation DNA Curtains for Single-Molecule Studies of Homologous Recombination*, 1st ed.; Elsevier Inc., 2017; Vol. *592*.

(13) Wang, F.; Redding, S.; Finkelstein, I. J.; Gorman, J.; Reichman, D. R.; Greene, E. C. The Promoter-Search Mechanism of Escherichia Coli RNA Polymerase Is Dominated by Three-Dimensional Diffusion. *Nat. Struct. Mol. Biol.* **2013**, *20*, 174−181.

(14) Gorman, J.; Wang, F.; Redding, S.; Plys, A. J.; Fazio, T.; Wind, S.; Alani, E. E.; Greene, E. C. Single-Molecule Imaging Reveals Target-Search Mechanisms during DNA Mismatch Repair. *Proc. Natl. Acad. Sci. U.S.A.* **2012**, *109*, E3074−E3083.

(15) Gibb, B.; Silverstein, T. D.; Finkelstein, I. J.; Greene, E. C. Single-Stranded DNA Curtains for Real-Time Single-Molecule Visualization of Protein−Nucleic Acid Interactions. *Anal. Chem.* **2012**, *84*, 7607−7612.

(16) Terakawa, T.; Bisht, S.; Eeftens, J. M.; Dekker, C.; Haering, C. H.; Greene, E. C. The Condensin Complex Is a Mechanochemical Motor That Translocates along DNA. *Science* **2017**, *358*, 672−676.

(17) Xia, Y.; Whitesides, G. M. SOFT LITHOGRAPHY. *Annu. Rev. Mater. Sci.* **1998**, *28*, 153−184.

(18) Coyer, S. R.; García, A. J.; Delamarche, E. Facile Preparation of Complex Protein Architectures with Sub-100-Nm Resolution on Surfaces. *Angew. Chem., Int. Ed.* **2007**, *46*, 6837−6840.

(19) Tutkus, M.; Sasnauskas, G.; Rutkauskas, D. Probing the Dynamics of Restriction Endonuclease NgoMIV-DNA Interaction by Single-Molecule FRET. *Biopolymers* **2017**, *107*, e23075.

(20) Geissler, M.; Wolf, H.; Stutz, R.; Delamarche, E.; Grummt, U. W.; Michel, B.; Bietsch, A. Fabrication of Metal Nanowires Using Microcontact Printing. *Langmuir* **2003**, *19*, 6301.

(21) Geissler, M.; Schmid, H.; Bietsch, A.; Michel, B.; Delamarche, E. Defect-Tolerant and Directional Wet-Etch Systems for Using Monolayers as Resists. *Langmuir* **2002**, *18*, 2374.

(22) Drevinskas, R.; Rakickas, T.; Selskis, A.; Rosa, L.; Valiokas, R. Cup-Shaped Nanoantenna Arrays for Zeptoliter Volume Biochemistry and Plasmonic Sensing in the Visible Wavelength Range. *ACS Appl. Mater. Interfaces* **2017**, *9*, 19082−19091.

(23) Liu, G.-Y.; Xu, S.; Qian, Y. Nanofabrication of Self-Assembled Monolayers Using Scanning Probe Lithography. *Acc Chem Res* **2000**, *33*−457. DOI: 10.1021/ar980081s

(24) Rosa, L. G.; Liang, J. Atomic Force Microscope Nanolithography: Dip-Pen, Nanoshaving, Nanografting, Tapping Mode, Electrochemical and Thermal Nanolithography. *J. Phys.: Condens. Matter* **2009**, *21*, 483001.

(25) Seidel, H. Anisotropic Etching of Crystalline Silicon in Alkaline Solutions. *J. Electrochem. Soc.* **1990**, *137*, 3626.

(26) Tutkus, M.; Marciulionis, T.; Sasnauskas, G.; Rutkauskas, D. DNA-Endonuclease Complex Dynamics by Simultaneous FRET and Fluorophore Intensity in Evanescent Field. *Biophys. J.* **2017**, *112*, 850−858.

(27) Zaremba, M.; Siksnys, V. An Engineered SS Bridge Blocks the Conformational Change Required for the Nuclease Activity of BfiI. *Biochemistry* **2015**, *54*, 5340−5347.

(28) Vitkute, J.; Maneliene, Z.; Petrusyte, M.; Janulaitis, A. BfiI, a Restriction Endonuclease from Bacillus Firmus S8120, Which Recognizes the Novel Non-Palindromic Sequence 5’-ACTGGG(N)-(5/4)-3’. *Nucleic Acids Res* **1998**, *26*, 3348.

(29) Seifert, M.; Rinke, M. T.; Galla, H.-J. Characterization of Streptavidin Binding to Biotinylated, Binary Self-Assembled Thiol Monolayers - Influence of Component Ratio and Solvent. *Langmuir* **2010**, *26*, 6386−6393.

(30) Nelson, K. E.; Gamble, L.; Jung, L. S.; Boeckl, M. S.; Naeemi, E.; Golledge, S. L.; Sasaki, T.; Castner, D. G.; Campbell, C. T.; Stayton, P. S. Surface Characterization of Mixed Self-Assembled Monolayers Designed for Streptavidin Immobilization. *Langmuir* **2001**, *17*, 2807−2816.

(31) Roach, P.; Farrar, D.; Perry, C. C. Interpretation of Protein Adsorption: Surface-Induced Conformational Changes. *J. Am. Chem. Soc.* **2005**, *127*, 8168−8173.

(32) Bustamante, C.; Marko, J. F.; Siggia, E. D.; Smith, S. Entropic Elasticity of λ-Phage DNA. *Science* **1994**, *265*, 1599.

(33) Bouchiat, C.; Wang, M. D.; Allemand, J. F.; Strick, T.; Block, S. M.; Croquette, V. Estimating the Persistence Length of a Worm-like Chain Molecule from Force-Extension Measurements. *Biophys. J.* **1999**, *76*, 409.

(34) Golovenko, D.; Manakova, E.; Zakrys, L.; Zaremba, M.; Sasnauskas, G.; Gražulis, S.; Siksnys, V. Structural Insight into the Specificity of the B3 DNA-Binding Domains Provided by the Co-Crystal Structure of the C-Terminal Fragment of BfiI Restriction Enzyme. *Nucleic Acids Res.* **2014**, *42*, 4113−4122.

(35) Sasnauskas, G.; Zakrys, L.; Zaremba, M.; Cosstick, R.; Gaynor, J. W.; Halford, S. E.; Siksnys, V. A Novel Mechanism for the Scission of Double-Stranded DNA: BfiI Cuts Both 3′-5′ and 5′-3′ Strands by Rotating a Single Active Site. *Nucleic Acids Res.* **2010**, *38*, 2399−2410.

(36) Sasnauskas, G.; Connolly, B. A.; Halford, S. E.; Siksnys, V. Template-Directed Addition of Nucleosides to DNA by the BfiI Restriction Enzyme. *Nucleic Acids Res.* **2008**, *36*, 3969−3977.

(37) Sasnauskas, G.; Halford, S. E.; Siksnys, V. How the BfiI Restriction Enzyme Uses One Active Site to Cut Two DNA Strands. *Proc. Natl. Acad. Sci. U.S.A.* **2003**, *100*, 6410−6415.

(38) Lagunavicius, A.; Sasnauskas, G.; Halford, S. E.; Siksnys, V. The Metal-Independent Type IIs Restriction Enzyme BfiI Is a Dimer That Binds Two DNA Sites but Has Only One Catalytic Centre. *J. Mol. Biol.* **2003**, *326*, 1051−1064.

(39) Zaremba, M.; Urbanke, C.; Halford, S. E.; Siksnys, V. Generation of the BfiI Restriction Endonuclease from the Fusion of a DNA Recognition Domain to a Non-Specific Nuclease from the Phospholipase D Superfamily. *J. Mol. Biol.* **2004**, *336*, 81−92.

(40) Grazulis, S.; Manakova, E.; Roessle, M.; Bochtler, M.; Tamulaitiene, G.; Huber, R.; Siksnys, V. Structure of the Metal-Independent Restriction Enzyme BfiI Reveals Fusion of a Specific DNA-Binding Domain with a Nonspecific Nuclease. *Proc. Natl. Acad. Sci. U.S.A.* **2005**, *102*, 15797−15802.

(41) Lv, Z.; Krasnoslobodtsev, A. V.; Zhang, Y.; Ysselstein, D.; Rochet, J.-C.; Blanchard, S. C.; Lyubchenko, Y. L. Direct Detection of α-Synuclein Dimerization Dynamics: Single-Molecule Fluorescence Analysis. *Biophys. J.* **2015**, *108*, 2038−2047.

(42) Schlingman, D. J.; Mack, A. H.; Mochrie, S. G. J.; Regan, L. A New Method for the Covalent Attachment of DNA to a Surface for Single-Molecule Studies. *Colloids Surf., B* **2011**, *83*, 91.

(43) Cha, T.; Quo, A.; Zhu, X. Y. Enzymatic Activity on a Chip: The Critical Role of Protein Orientation. *Proteomics* **2005**, *5*, 416.

BBA - Bioenergetics 1860 (2019) 499–507

Contents lists available at ScienceDirect

BBA - Bioenergetics

journal homepage: www.elsevier.com/locate/bbabio

Single-molecule microscopy studies of LHCII enriched in Vio or Zea

Marijonas Tutkus[a], Francesco Saccon[c], Jevgenij Chmeliov[a,b], Oskaras Venckus[a], Ignas Ciplys[a], Alexander V. Ruban[c], Leonas Valkunas[a,b,*]

[a] *Department of Molecular Compound Physics, Center for Physical Sciences and Technology, Sauletekio Ave. 3, LT-10257 Vilnius, Lithuania*
[b] *Institute of Chemical Physics, Faculty of Physics, Vilnius University, Sauletekio Ave. 9, LT-10222 Vilnius, Lithuania*
[c] *The School of Biological and Chemical Sciences, Queen Mary, University of London, Mile End Road, London E1 4NS, UK*

ABSTRACT

Plants have developed multiple self-regulatory mechanisms to efficiently function under varying sunlight conditions. At high light intensities, non-photochemical quenching (NPQ) is activated on a molecular level, safely dissipating an excess excitation as heat. The exact molecular mechanism for NPQ is still under debate, but it is widely agreed that the direct participation of the carotenoid pigments is involved, one of the proposed candidate being the zeaxanthin. In this work, we performed fluorescence measurements of violaxanthin- and zeaxanthin-enriched major light-harvesting complexes (LHCII), in ensemble and at the single pigment–protein complex level, where aggregation is prevented by immobilization of LHCIIs onto a surface. We show that a selective enrichment of LHCII with violaxanthin or zeaxanthin affects neither the ability of LHCII to switch into a dissipative conformation nor the maximal level of induced quenching. However, the kinetics of the fluorescence decrease due to aggregation on the timescale of seconds are different, prompting towards a modulatory effect of zeaxanthin in the dynamics of quenching.

1. Introduction

Oxygenic photosynthesis is one of the most important physiological processes occurring in Earth biosphere, during which solar energy is stored in a form of chemical bonds and the atmosphere is refilled with oxygen as a by-product of photosynthetic reactions. The photosynthetic apparatus of green plants is highly optimized to perform efficiently under varying environment conditions [1]. The spectral properties and mutual arrangement of chlorophylls (Chls) and carotenoids(Car) within the pigment-protein complexes and of the latter within the photosynthetic units ensure efficient light harvesting in dim light followed by the excitation energy transfer towards the reaction center. Such efficiency, however, might be fraught with the photo-damage to photosystem II (PSII) induced by the over-excitation of the light-harvesting antenna when it is exposed to excess light [1]. Over billions of years of evolution, plants have developed multiple self-regulatory mechanisms to deal with this threat. A fast and efficient one, acting on a molecular level and safely dissipating excess excitation energy as heat, is known as an energy-dependent (qE) component of the non-photochemical quenching (NPQ) [2,3].

The extensive studies performed over the past two decades have revealed that NPQ arises from structural changes in the light harvesting antenna that can be reversibly activated within seconds to minutes in response to the increase of ΔpH across the thylakoid membrane during the bright sunlight [3]. The presence and protonation of the PsbS protein were identified to be required for NPQ activation [3–5], and total NPQ efficiency is enhanced by the conversion of the xanthophyll violaxanthin (Vio) into zeaxanthin (Zea), through the intermediate antheraxanthin, by the Vio de-epoxidase (VDE, the so-called xanthophyll cycle) [6]. The exact molecular mechanism for NPQ is still under debate, but it is widely agreed that the direct participation of the Car pigments is involved [7–11]. The main candidate for the NPQ location is the major light-harvesting complex of photosystem II (LHCII), even though minor antenna complexes have also been considered [3,12,13].

LHCII is a trimeric transmembrane protein rich in chromophores (Fig. 1). Its crystal structure, known with the sub-3 Å resolution [14], reveals that each monomeric subunit contains eighteen pigment molecules: six Chls *b*, eight Chls *a*, and four Cars, namely two luteins (located in Lut1 and Lut2 binding sites), violaxanthin in V1 site, and neoxanthyn (Neo) in N1 site. Both luteins are arranged in a cross pattern in the center of LHCII monomer, assist in holding the whole protein scaffold together and are responsible for the trimerisation of the LHCII [15]. They were also proposed to participate in NPQ via incoherent excitation energy transfer from the nearby Chls to the optically dark short-lived S_1 states of Luts [8,16,17]. On the other hand, Vio is located on a periphery of the LHCII trimer, which makes it easily accessible for the Vio de-epoxidase to convert it into Zea [14,18].

The link between qE and the xanthophyll cycle carotenoids is still one of the most uncertain aspects in the NPQ scenario. The reversible de-epoxidation of violaxanthin to zeaxanthin and its dependency on

---

[*] Corresponding author.
E-mail address: leonas.valkunas@ff.vu.lt (L. Valkunas).

https://doi.org/10.1016/j.bbabio.2019.05.002
Received 23 February 2018; Received in revised form 20 December 2018; Accepted 6 January 2019

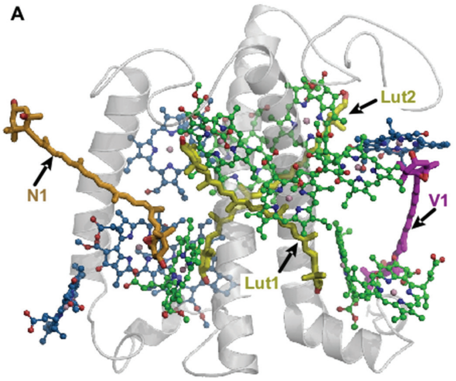

Fig. 1. Crystal structure of LHCII monomer (PDB ID: 1RWT) and carotenoid binding sites (Lut1, Lut2, V1 and N1). Protein scaffold in grey, Chl *a* in green, Chl *b* in blue, both luteins in dark yellow, xanthophyll cycle carotenoid (Vio/Zea) in magenta, Neo in orange. (For interpretation of the references to color in this figure legend, the reader is referred to the web version of this article.)

illumination is a long-known aspect of the photosynthetic membrane [19,20]. However, it was only in the 90s that the work of Demmig-Adams elucidated a link between this physiological trait and the process of non-photochemical quenching of chlorophyll fluorescence [6]. This finding ignited an elegant hypothesis put forward by Frank and coworkers, according to which the de-epoxidation of violaxanthin during high light lowers the energy of the xanthophyll's first excited state so that it becomes accessible for excitation energy transfer from chlorophylls [21]. In this way, zeaxanthin can act directly as a quencher of the excited state of chlorophylls. Later, it was found that the S_1 energy level of both Vio and Zea lies below the energy of chlorophyll S_1, therefore confuting the de-epoxidation as the sole factor for the appearance of the quencher [22]. However, more recently, evidences of a reductive-type of quenching, where Zea cations are formed in illuminated thylakoids, have been found [7,10,23,24]. Snapshot transient absorption data have also suggested that a stronger coupling of Chl and Zea during NPQ conditions allow excitation energy transfer from Chl to Zea to occur [7,23]. Based on these observations, a direct role of Zea in qE was suggested, with the minor antenna proposed as one of the NPQ sites [10,12]. However, it has been questioned the extent to which the formation of Zea^+ cation is correlated with qE and how much minor antenna are involved since neither the presence of Zea or minor antennae are strict requirements for the formation of qE. Observations of the hysteretic correlation between trans-membrane ΔpH and qE in the presence of Vio or Zea have prompted to a particular role of the xanthophyll cycle carotenoids as allosteric regulators of qE [24,25]. It was indeed demonstrated that isolated major LHCII complexes with Zea in the reaction mixture accelerated the drop in fluorescence quantum yield under the NPQ-mimicking conditions, while violaxanthin retarded this process rather than simply inhibiting it [26]. Also, it has been shown that when lumen pH drops below 5, Zea is not prerequisite for qE formation [18]. Therefore, it is possible that in vivo zeaxanthin thermodynamically favors the aggregation of antenna complexes, which in turn stabilizes the quenched conformation of the pigment–-protein complexes [24,27].

As a result, the role of Zea in plant self-regulation is yet to be fully understood: it might be that Zea induces a photo-physical effect, when this carotenoid directly quenches chlorophyll excited state, or a physico-chemical effect, when it indirectly assists the quenching process by stabilizing the corresponding structural changes within the light-harvesting antenna. Similarly, it is still debated whether Zea effect is exerted at the single-molecule or ensemble level [28,29]. To assess these questions and study the role of Zea in excitation energy quenching in the LHCII complexes, targeted mutagenesis has been widely used previously to block biosynthesis of Vio and thus produce LHCII complexes with zeaxanthin in the V1 binding site. Alternative approach is to mimic natural NPQ condition by inducing Vio de-epoxidation in the wild type plants followed by the purification of the pigment–proteins, thus obtaining naturally Zea-enriched LHCII complexes [28,30]. In this work, we used the LHCII trimers obtained in the latter way and performed their fluorescence (FL) measurements, in ensemble and at the single pigment–protein complex level, where aggregation is prevented by immobilization of LHCIIs onto a surface, to compare their quenching ability with the naturally Vio-enriched LHCII complexes. We show that a selective enrichment of LHCII with violaxanthin or zeaxanthin affects neither the intrinsic ability of LHCII to switch into a dissipative conformation nor the maximum quenching inducible. However, the kinetics of the fluorescence decrease due to LHCII aggregation on the time scale of seconds are different, prompting towards a modulatory effect of zeaxanthin in the dynamics of quenching.

2. Methods

2.1. LHCII isolation and characterization

For preparation of unstacked thylakoids, spinach leaves from supermarket were used. Fresh leaf tissue was homogenized in ice-cold grinding medium (330 mM sorbitol, 10 mM $Na_4P_2O_7$, pH 6.5) with a polytron blender. The homogenate was then filtered through four layers of muslin followed by four layers of muslin and one layer of cotton wool. The filtrate was centrifuged for 10 min at 4000 ×*g*, and the chloroplast-enriched pellet was resuspended in wash buffer (330 mM sorbitol, 10 mM MES, pH 6.5), followed by another 10-min centrifugation at 4000 ×*g*. The pellet was then resuspended in a resuspension medium (330 mM sorbitol, 1 mM EDTA, 50 mM HEPES, pH 7.6) and breaking medium (10 mM HEPES, pH 7.6) was added to lyse any remaining intact chloroplasts. After 30 s, an equal volume of osmotic medium (660 mM sorbitol, 40 mM MES, pH 6.5) was added to restore the right osmotic potential. After centrifugation, thylakoids were resuspended in a small volume of resuspension medium.

Induction of maximum de-epoxidation of violaxanthin was performed as described before [31]. Briefly, spinach leaves were treated with 900 μE of light for 1 h, keeping the petioles submersed in cold water with a constant flux of nitrogen. 3 mM D-isoascorbate was added to grinding medium during thylakoid preparation. Thylakoids in resuspension medium where diluted to a chlorophyll concentration of 150 μg/ml, incubated for one hour at room temperature in 330 mM sorbitol, 25 mM HEPES, 25 mM Na-citrate, 40 mM Na-ascorbate, pH 5.5, and centrifuged 10 min at 4000 ×*g*. Thylakoids were then resuspended in a small volume of resuspension medium.

Solubilisation of thylakoid membranes was performed with β-DM detergent, on ice, with occasional mixing, with 25 mM β-DM (β-DM/Chl = ~13). Fractionation of protein complexes was performed with seven steps exponential sucrose gradient, as previously described [30], with a buffer containing 25 mM HEPES, 200 μM β-DM at pH 7.8.

2.2. Quenching induction assay

To monitor fluorescence quenching in solution, isolated LHCII were diluted in a buffer containing 10 mM tri-sodium citrate, 10 mM HEPES, pH 5.5 (final chlorophyll concentration, 3 μg/ml; final detergent concentration, 6 μM). Chlorophyll *a* fluorescence traces were recorded with a Dual-PAM 100 (Walz GmbH, Effeltrich, Germany) as described previously [32]. During this procedure, chlorophyll *a* fluorescence traces (integrated intensity of wavelength range of > 700 nm) were recorded using a 460 nm measuring beam (24 µmol photons $m^{-2} s^{-1}$). The experiments were performed at room temperature under continuous stirring. Data represent the averages of 3 experiments, and are plotted from the moment of injection of the LHCII in the buffer. Normalization was done on the initial maximum of Chl fluorescence.

2.3. Fluorescence lifetime measurements

Fluorescence lifetime values were measured with time-correlated single photon counting (TCSPC), performed using a FluoTime 200 fluorometer (PicoQuant, Germany). Fluorescence lifetime decay kinetics were measured on diluted LHCII (3 µg/ml total chlorophyll content). Excitation was provided by the 468 nm laser diode at 20 MHz repetition rate and 0.6 mW (~30 pJ/pulse) intensity. Fluorescence was detected at 680 nm with 2 nm of slit width.

FluoFit software (PicoQuant, Germany) was used to analyze fluorescence lifetime data by a multi-exponential model with iterative reconvolution of the instrument response function (IRF, 50 ps). The χ^2 parameter and autocorrelation function were used to judge the quality of the fit. Average lifetimes were calculated as $\Sigma_i(A_i \cdot \tau_i) / \Sigma_i A_i$, where A_i is the amplitude of i-th lifetime component and τ_i is the respective fluorescence lifetime value.

2.4. Steady-state spectroscopy

Fluorescence emission spectra of LHCII (3 µg/ml total chlorophyll content) were recorded at 77 K using a Jobin Yvon FluoroMax-3 spectrophotometer equipped with a liquid-nitrogen-cooled cryostat, as previously described [13]. Excitation was performed at 435 nm with 5 nm slit width and the fluorescence spectral resolution was 0.5 nm. Integration time was set to 0.1 s. Every spectrum is the average of 5 scans. Spectra were normalized at their absolute maximum.

Absorption spectra of LHCII (10 µg/ml total chlorophyll content) were recorded with an Aminco DW- 2000 UV/Vis spectrophotometer (Olis Inc., USA), in dual-beam mode as previously described. Slits width was 0.5 mm and the spectral bandwidth 2 nm. Traces were normalized at the maximum of the Soret absorption band of Chl *a*.

2.5. Pigment analysis

Pigment quantification was performed through reversed-phase HPLC, using a LiChrospher 100-RP-18 column (Merck) and a Dionex Summit chromatography system as described previously [24]. Samples were solubilized in 80% ice-cold acetone, centrifuged for 1 min and filtered through a 0.22 µm filter. The solvents used were: acetonitrile, methanol, 0.1 M filtered Tris, pH 8 (A) and 80% methanol, 20% hexane (B). The run profile was: 0–9 min A, 9–12.5 min A/B gradient, 12.5–18 min B. Each peak was integrated using the Chromelion software and pigment concentration was estimated using standards of known concentration.

2.6. Streak camera measurements

Time-resolved fluorescence dynamics of the samples were measured as described previously [33]. Briefly, we used Hamamatsu C5680 streak camera with M5677 single-sweep module coupled to a spectrometer. Femtosecond Yb:KGW oscillator (Pharos, Light Conversion Ltd.) with a frequency doubler (HIRO, Light Con- version Ltd.) producing 515 nm sub-100-fs pulses at a 76 MHz repetition rate was employed, and a pulse picker was used to reduce the repetition rate to 20 kHz for nanosecond timescales. The beam was attenuated down to about 100 pJ per pulse and focused into about 100 µm spot on the sample. The temporal resolution of the whole system was ~90 ps. All the measurements were performed at the room temperature in a fused silica cell of 0.1 mm optical path.

2.7. Sample preparation for microscopy measurements

2.7.1. Buffer solutions

Buffer 1: 10 mM Hepes (> 99.5 Buffer grade, Carl-Roth Art.-Nr: HN07.1), 1 mM $MgCl_2$ (> 99 Cell pure, Carl-Roth Art.-Nr: HN78.2), 0.03% w/v β-DM (Lauryl-β-D-maltoside, > 99% for biochemistry, Art. CN26.2), pH = 7.8. Buffer 2: 10 mM Hepes, 1 mM $MgCl_2$, ~0.001% w/v β-DM, pH = 7.8. Buffer 3: 10 mM Hepes, 1 mM $MgCl_2$, ~6 µM β-DM, pH = 5.

2.7.2. Cleaning of cover slips

Glass coverslips (Menzel-glaser #1.5) were placed in a staining jar and rinsed 3 times with ultrapure water (LaboStar, Siemens). Water was exchanged with 1% Alconox detergent solution (Alconox powdered precision cleaner) and the jar sonicated for 10 min (Ultrasonic Cleaning Unit RK 102H, Bandelin). Detergent solution was discarded from the jar and rinsed 4 times with ultrapure water. Water was exchanged with isopropanol (2-propanol ≥ 99.5%, art.no.: 9866.6 Carl-Roth). Isopropanol was discarded and the jar with coverslips was vacuumed in the plasma machine (PDC-002, Harric plasma) for 20 min, then plasma etched at ~400 mTorr pressure using maximal power for 5 min.

2.7.3. Surface modification of coverslips and flowcell assembling

Clean glass coverslips were incubated with 0.01% of PLL (P4707 Sigma) for 10 min, then rinsed with ultrapure water, dried and assembled into the flowcell (sticky-slide VI 0.4, 80,608, IBIDI) with the PLL modified side facing the sticky slide. Tubings were inserted into the inlet and outlet port of the cell and channel was filled with buffer 1.

2.7.4. LHCII immobilization and imaging

Channel of the flow cell was filled with the buffer 1. ~1e+06 diluted LHCII dissolved in buffer 1 were injected into the flowcell channel and incubated for 3 min. 300 µl of the buffer 1 was injected to wash out the excess of unbound LHCII. For microscopy 100 µl of buffer 1 containing 10 units/ml of pyranose oxidase (P4234, Sigma-Aldrich) and 300 units/ml catalase (C9322, Sigma-Aldrich), 1% glucose (ß-D-glucose, G0047, TCI, AMERICA). When exchanging the buffer conditions 300 µl of either buffer 2 or buffer 3 were injected and then 100 µl of the same buffer supplemented with oxygen scavengers was injected.

2.8. TIRF microscopy

The SM fluorescence microscopy set-up used in this study was essentially the same as described previously [33]. The 635 nm laser beam is expanded 13×. The 635 nm excitation intensity after the objective was 0.15 mW (< 10 W/cm^2 at the sample plane) and exposure time was 50 ms.

As previously, described all data analysis procedures were performed and graphs prepared in Igor Pro 6.37 (Wavemetrics, USA) program using custom written analysis package (available upon direct request to the author or under the link: http://www.igorexchange.com/project/TEA_MT) [33]. Only difference is that for the intensity change point (ICP) detection minimal amplitude now was set to 33 a.u. and the sum of the absolute slope values of the line fits of the states had to be smaller than a set value of 20. Additionally we have employed the *t*-test statistics to reject the putative ICPs – if t-value of the t-test for the ICP under revision was < 1.3, the ICP was rejected.

3. Results

3.1. Bulk fluorescence spectroscopy

Xanthophyll cycle carotenoids were found to be loosely bound to the V1 site of LHCII and to be easily lost upon purification procedures, but a mild solubilisation with the non-ionic detergent dodecyl-D-

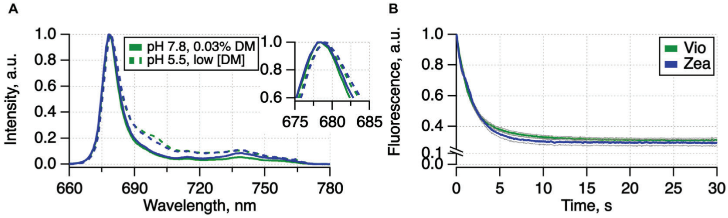

Fig. 2. Bulk fluorescence spectroscopy results of Vio and Zea-enriched LHCII samples and the effect of quenching induction in bulk. A) Fluorescence emission spectra measured at 77 K in high detergent and pH 7.8 (solid lines) as well as low detergent and pH 5.5 (dashed lines) conditions. Inset shows zoomed top of the main peak. B) Quenching induction traces of LHCII – intensity of chlorophyll fluorescence (integral of wavelength range > 700 nm), which was excited with a weak 635 nm light, versus time. Initially at the high detergent concentration and pH 7.8 LHCII solution was resuspended into low detergent and low pH buffer, resulting in the final detergent concentration of 6 μM and pH ~5.5. Maximum achieved quenching – decrease of the fluorescence intensity, was ~70% for both Vio- and Zea-enriched LHCII. The fluorescence traces were normalized at the beginning of the trace. Traces are the means of 4–8 replicates and grey lines represent the boundaries for standard error of means.

Table 1
Pigment composition of LHCII collected from sucrose gradients. DES = de-epoxidation state ((zeaxanthin + ½ antheraxanthin) ∗ 100 / (violaxanthin + zeaxanthin + antheraxanthin)); Presented data is the mean of 3 replicates, and ± indicates st. dev.

Sample	Chl *a*/*b*	DES	%Vio/Car	%Zea/Car
Vio-enriched LHCII	1.48 ± 0.01	0	17.25 ± 0.82	0
Zea-enriched LHCII	1.42 ± 0.00	76.19 ± 1.52	3.84 ± 0.36	12.27 ± 0.29

maltoside can preserve well the intactness of these peripheral xanthophylls [29,30,34]. To isolate LHCII with the maximum amount of xanthophyll cycle carotenoids bound, thylakoids from either dark-adapted or light-treated spinach leaves were solubilized with a carefully determined β-dodecyl-ᴅ-maltoside (β-DM) concentration and loaded on sucrose gradients. The fraction of LHCII trimers (~0.3 M sucrose) was collected and the identity of the proteins was confirmed via absorption measured at room temperature (RT, SI Fig. 1) and low-temperature fluorescence analysis (Fig. 2A, SI Fig. 2). The pigment analysis showed a high de-epoxidation yield in the light-treated samples (around 76%, see Table 1) and a good retention of the xanthophyll cycle pigments in the purification procedure. The Chl *a*/*b* ratio was slightly higher than 8/6 = 1.33, that follows from the crystallographic data [4], because due to the isolation conditions we have also collected some (up to 10%) minor antennae complexes. However, this is a negligible amount of impurity and this procedure allowed us to achieve high de-epoxidation yield.

RT absorption spectra showed small red shift around 505 nm region of Zea sample, which is an independent indication of successful Zea enrichment. Meanwhile, fluorescence spectroscopy performed using streak camera at the RT under high detergent and high pH conditions showed that the fluorescence spectrum of the light-pretreated (Zea-enriched) LHCII trimers exhibits slightly less intense red shoulder of the spectrum (at ~720–740 nm) compared to the dark-pretreated (Vio-enriched) samples (see SI Fig. 3A–C). It was also noticed that the main peak of fluorescence spectrum is composed of two sub-peaks (centered at 686 and 689 nm), with the second sub-peak being more intense in the Zea-enriched LHCII, a characteristic conserved when measuring the emission at 77 K (data not shown). The whole fluorescence spectrum of Zea-enriched sample seems to be redshifted by several nm, compared to Vio-enriched ones. Fluorescence decay kinetics in both samples exhibited no dependence on the detection wavelength (see SI Fig. 3E–H) and were practically indistinguishable between the samples (SI Fig. 3D), with dominating lifetime component of ~3.5 ns and some fraction (~13%) of the faster component of ~0.6–0.8 ns (see SI Fig. 3 caption for the bi-exponential description). This indicates that the presence (or absence) of the red shoulder in the LHCII fluorescence spectrum is not related to the quenching mechanism [11,35].

Early studies on isolated LHCII complexes have shown that xanthophyll cycle carotenoids modulate the quenching induced by low pH, with Vio and Zea having inhibiting or enhancing effects, respectively, on the quenching kinetics [18,26]. This modulation shows conserved features in isolated chloroplasts and in leaves, suggesting that the xanthophyll cycle pool indeed controls the dynamics of qE by modulating the switch of a single antenna complex to a dissipative state. To explicitly determine the effect of different xanthophyll composition on the ability of LHCII complex to switch from a light-harvesting to a dissipative state, we measured intensity of chlorophyll fluorescence emission of LHCII samples versus time by re-suspending both samples, initially prepared at high detergent concentration and high pH buffer, into a buffer with low pH and low detergent concentration. The gradual decrease of the detergent concentration initiated the formation of mostly two-dimensional [11,36] LHCII aggregates, thus mimicking excitation energy transfer through the thylakoid membrane. At the same time, acidification of the buffer solution promoted the conformational switching of LHCIIs into the quenching state [37,38], resulting in the random generation of the NPQ traps within the LHCII aggregate.

The resulting quenching induction traces are shown in Fig. 2B. After ~25 s, the buffer re-suspending resulted in ~6 μM detergent concentration and pH 5.5 of the solution for both samples. This was accompanied by a significant change in the observed fluorescence intensity: initially, the absolute FL emission intensity in the Vio-enriched LHCIIs was by 15% smaller than in the Zea-enriched ones. Later on, during the injection of the buffer with low detergent concentration and low pH, the FL intensity dropped rapidly by (69.16 ± 1.37)% and (70.89 ± 1.97)% in the Vio- and Zea-enriched samples, respectively (± represents standard error from 4 to 8 replicates), indicating that LHCII complexes underwent a fast switch into the dissipative state. As we can see in Fig. 2B, upon normalizing the Fl quenching kinetics at the initial intensity, both samples reached the same final state, but the quenching induction was slightly faster in the Zea-enriched samples: there, the maximal fluorescence quenching was observed after ~10 s, whereas for Vio-enriched LHCIIs it took about 15 s. This difference may be related to the different aggregation rate of Vio- and Zea-enriched LHCII after the change in detergent concentration and pH conditions. This observation is in line with the previously published experimental works [18,25,45,26,27,39–44]. The differences we observed in our measurements were less evident than in the previous studies, because we were working with physiological amounts of xanthophyll cycle Cars bound to the native pocket of LHCII and not with the externally added

Cars. The quenching effect was less obvious and reached a similar extent, both in the Vio- and Zea-enriched LHCI samples. Therefore, Zea is unlikely to be a major quencher in LHCII.

To further investigate the (in)significance of the red shoulder in fluorescence spectrum and its relation to the fluorescence quenching, we also measured the steady-state fluorescence spectra of both samples at 77 K (Fig. 2A) and the fluorescence decay kinetics at the RT (SI Fig. 4) in the high detergent concentration and high pH (corresponding to the conditions at the beginning of the quenching traces shown in Fig. 2B) as well as in the low detergent concentration and low pH conditions (the final condition of the quenching traces). We can notice that the fluorescence spectra in high detergent concentration and high pH conditions exhibit the same features as the streak camera measurements (cf. Fig. 2A and SI Fig. 3C), but upon the change in buffer conditions we have observed an increase in the red shoulder intensity (at ~ 700 nm) for both samples. This is a well-known spectral indicator of the formation of LHCII aggregates [11,27,46,47]. In both aggregated samples, the spectra again are very similar, though the red shoulder is slightly more intense in the Vio-enriched LHCII samples. Also, upon the change in buffer conditions, both samples exhibited a slight red shift of the main peak (see inset in Fig. 2A). The measured fluorescence lifetime kinetics were fitted by the bi-exponential function and upon the change in buffer conditions of both samples they showed the shortening of both time components and increase in the shorter time component amplitude (Table 2). The average fluorescence lifetime decreased from 3.62 ns to 1.4 ns for Vio-enriched samples and from 3.53 ns to 1.55 ns for Zea-enriched ones.

To further investigate the effect of pH and detergent concentration on both Vio- and Zea-LHCII samples, we also studied them by means of single-molecule (SM) fluorescence microscopy. In this way, we were able to retrieve the fluorescence behavior of isolated LHCII in controlled condition while avoiding their aggregation. As a result, this approach allowed us to clarify whether the observed differences in ensembles (Fig. 2B) are due to intrinsic conformational single-protein dynamics or structural rearrangements of several complexes while LHCII aggregate is formed.

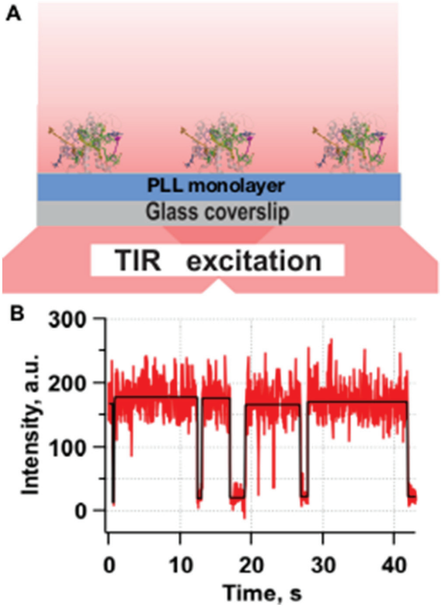

Fig. 3. A) Shematics of LHCII immobilization for SM TIRF microscopy measurements on the PLL coated glass coverslip. B) Illustrative SM trace - fluorescence emission intensity versus time. Horizontal lines indicate the resolved mean FL intensity levels that were used in further analysis.

3.2. Single-molecule microscopy

To investigate the conformational dynamics of single LHCII trimers, we have employed SM Total Internal Reflection Fluorescence (TIRF) microscopy. We have used this method recently to study single monomeric LHCII complexes lacking some particular carotenoids due to mutagenic sample preparation [28]. Here we have examined both Vio- and Zea-enriched LHCII samples solubilized in detergent micelles immobilized on PLL coated-glass coverslip at low densities (Fig. 3A) under the 635 nm wavelength excitation and 50 ms exposition time. From the acquired movies we have extracted fluorescence intensity variations over time and selected those spots representing single LHCII complexes (Fig. 3B). These fluorescence time traces exhibit a well-known blinking behavior [38,48] due to reversible switching of the pigment–protein complexes between the strongly- and weakly-fluorescing states as a result of the conformational dynamics of protein scaffold [37]. By overlapping similar FL time traces measured for 438 distinct LHCII trimers, we obtain the two-dimensional map shown in Fig. 4A and representing time-dependent distribution of various detected FL intensity levels. Since only those LHCII trimers initially being in strongly emitting state were detected, there was relatively small number of quenched complexes during the first second. At later times, due to reversible switching into the non-fluorescent state and irreversible photobleaching the population of zero-intensity level increases. After ~30 s of continuous illumination the majority of LHCII complexes were bleached irreversibly.

The discussed FL intensity map shown in Fig. 4A was obtained from the Vio-enriched LHCII complexes under the buffer conditions mimicking the light-harvesting state (pH 7.8, high detergent concentration). Similar data were also acquired for the Zea-enriched complexes (Fig. 4B) as well as both Vio- and Zea-enriched trimers under buffer condition imitating the high-light acclimation (pH 5.5 and low detergent concentration), see Fig. 4C and D respectively. The intermediate conditions of high pH and low detergent concentration are shown in SI Fig. 5. By visually comparing these FL intensity maps we can note that detergent removal alone produces much smaller effect than when

Table 2
Bi-exponential description ($F(t) = A_1\exp(-t/\tau_1) + A_2\exp(-t/\tau_2)$) of the fluorescence decay kinetics in Vio- and Zea-enriched LHCII trimers before and after quenching induction shown in SI Fig. 4.

Sample	A_1 (%)	τ_1 (ns)	A_2 (%)	τ_2 (ns)	$<\tau>$ (ns)
Vio-enriched LHCII, pH 7.8, 0.03% DM	93	3.78 ± 0.01	7	1.54 ± 0.1	3.62
Zea-enriched LHCII, pH 7.8, 0.03% DM	90	3.74 ± 0.02	10	1.67 ± 0.08	3.53
Vio-enriched LHCII, pH 5.5, low [DM]	63	1.73 ± 0.01	37	0.85 ± 0.02	1.4
Zea-enriched LHCII, pH 5.5, low [DM]	55	1.93 ± 0.02	45	1.08 ± 0.02	1.55

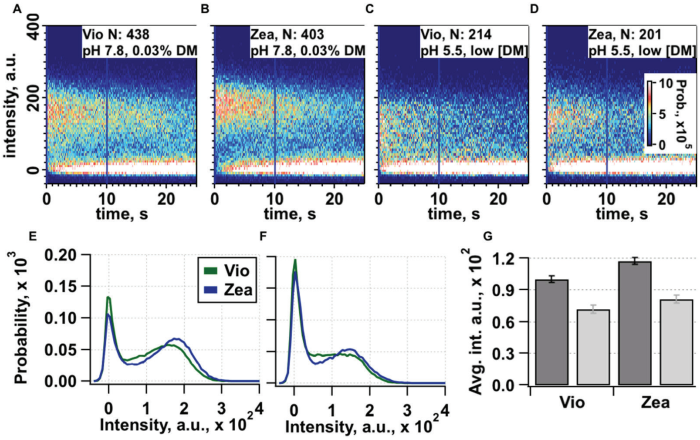

Fig. 4. Single-molecule population emission plots in Vio- and Zea-enriched LHCII trimers (A–D) and their vertical linescans for the initial 10 s (E and F). Panels A, B and E correspond to the high detergent and high pH conditions, panels C, D and F – to the low detergent and low pH conditions. G) Average intensity of population of SM traces from 0 till 10 s. Black – high detergent high pH conditions, grey – low detergent low pH. Number of included molecules in each plot are indicated on the top right corner of panels A–D.

accompanied with the acidification of the buffer solution: while the former factor does not lead to any pronounced re-distribution of the FL intensities, the latter one results in considerably faster photobleaching and, more importantly, the formation of additional conformational states with intermediate FL intensities. That can be easily seen from the FL intensity histograms shown in Fig. 4E–F and SI Fig. 5C that were obtained by integrating FL maps from Fig. 4A–D and SI Fig. 5A–B over the first 10 s, when most of the trimers are still active. By describing these histograms as a sum of Gaussian peaks, each possibly corresponding to a distinct conformational state, we were able to distinguish at least three such states: the non-fluorescent state S1, intermediate fluorescent state S2, and highly fluorescent state S3.

We see from Fig. 4 that under light-harvesting conditions (high detergent concentration and high pH value) Zea-enriched complexes exhibit slightly higher probability to be in the highly fluorescent state compared to the Vio-enriched ones. As already mentioned, reduction of the detergent concentration of the buffer (while still keeping high pH value) does not result in any significant differences in the distribution of FL intensities, suggesting that detergent concentration alone does not influence conformational dynamics of the LHCII complexes. On the other hand, under low detergent concentration and low pH conditions the probability of the highly fluorescent state is notably reduced at the expense of the increased probabilities for both non-fluorescent and intermediate states. These changes are accompanied with the FL intensity shift of the highly fluorescent state towards the lower values. Overall, upon lowering both detergent concentration and pH values there is a considerable (by ~30%) drop in the mean FL intensity in both Vio- and Zea-enriched LHCII complexes (see Fig. 4G). Interestingly, by comparing both samples we can also note that the Vio-enriched complexes exhibit slightly higher probability to be in the non-fluorescent state than the Zea-enriched ones (cf. Fig. 4E–F). As a result, in the light-harvesting-mimicking conditions the mean FL intensity in the Zea-enriched complexes is by ~20% *larger* than in the Vio-enriched trimers (compare dark bars in Fig. 4G). This value is similar to the mentioned ~15% (p-value < 0.05) difference in the absolute FL intensity, observed between Vio- and Zea-enriched samples in bulk measurements. On the other hand, at low pH the difference in mean FL intensities in both samples becomes less pronounced (see light bars in Fig. 4G).

There is a possibility that upon reduction of detergent concentration and pH level some fraction of the surface-immobilized LHCII complexes became permanently strongly quenched and therefore undetectable by the automated analysis. To estimate the percentage of such undetectable complexes, we calculated the average number of fluorescent spots per image in each step of the experiment (SI Fig. 6). Since the sole drop in the detergent concentration does not promote the conformational quenched state of LHCII, we attributed the observed ~ 10% decrease in the average number of the detected spots per image to unbinding of LHCII from the surface due to the washing step. On the other hand, once both detergent concentration and pH level were reduced to mimic NPQ conditions, the number of detected spots per image farther decreased by 25%-that could be the results of either somewhat weaker binding of the LHCII complexes to the PLL surface in acidic environment (and therefore more pronounced washing off) or the switching of these LHCII complexes into long-living strongly quenched state, so that they did not exhibit any conformational dynamics and remained too dim for the detection during the whole measurement. However, even in the later less probable scenario accounting to these undetected LHCII trimers would increase the fluorescence intensity drop observed in our SM analysis to ~ 50%, which is still far from a 70% decrease in fluorescence intensity observed in the aggregated state in bulk.

To further analyze the time traces of FL intensity variations, we have applied the Intensity Change Point (ICP) detection algorithm that allows characterization of the correlation between the detected FL intensity level (state of constant fluorescence emission) and its duration before transition to another intensity level occurs. The resulting correlation maps, obtained for different samples and different buffer conditions are shown in Fig. 5A–D. We see that most probable dwell times between the subsequent transitions were smaller than 2 s, though sometimes LHCII trimer remained at the same FL intensity for as long as 15 s. The mean duration of the dark or dim (FL intensities below 20 a.u.), intermediate (from 20 to 130 a.u.) or highly fluorescing (above 130 a.u.) are presented in Fig. 5E–F and are rather identical for both Vio- and Zea-enriched samples. On average, highly fluorescent states lasted about 3 times shorter than the dim states, and the intermediate states were even shorter. The reduction of detergent concentration and pH level leads mainly to the shortening of the intermediate state and increased probability for the dim state at the expense of highly fluorescing state.

In addition to changes revealed by the state intensity–duration correlation plot, the pathways of the transition between different states could also be affected. These can be accessed by constructing the

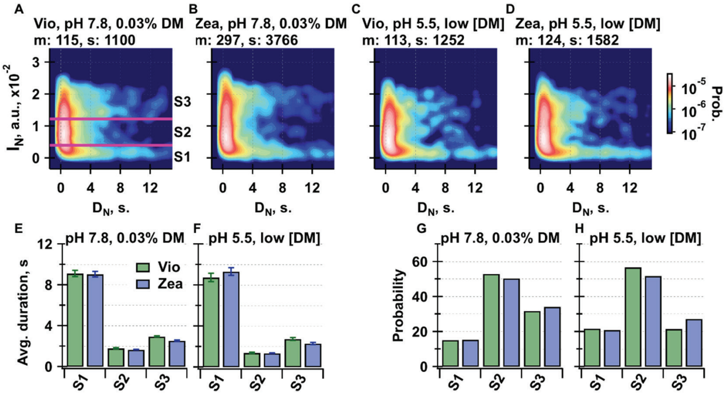

Fig. 5. State intensity versus duration plots. A–B) high detergent high pH, C–D) low detergent low pH. I_N – average intensity of state N, D_N – average duration of state N. Number of included molecules (m) and detected intensity states (s) are indicated at the top of each graph. Plots are normalized to their total area. Logarithmic color scale represents probability density. E–F) average durations and G–H) probabilities of non-fluorescent (S1) and fluorescent (S2 and S3) states.

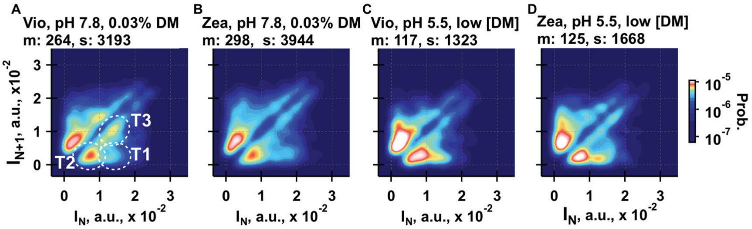

Fig. 6. Transition density plots. A–B) high detergent high pH, C–D) low detergent low pH conditions. I_N – average intensity of state N, I_{N+1} – average intensity of state N + 1. Number of included molecules (m) and states (s) are indicated above each graph. Plots are normalized to probability density function. Logarithmic color scale represents probability.

transition density maps, where the x-axis corresponds to the FL intensity I_N of some resolved level (state of constant fluorescence emission) in the acquired SM fluorescence intensity time trace shown in Fig. 3B, while y-axis—that of the subsequent (in time) intensity level I_{N+1}. The resulting maps for different samples and different buffer conditions are presented in Fig. 6. All of these maps are quite dispersed with several dominating transitions. For example in the Fig. 6A there are three main transitions: T1 – between the strongly fluorescing state and the non-fluorescent state, T2 – between the intermediate intensity state and the non-fluorescent state, T3 – between the high intensity state and intermediate one. Differently from our previously studied monomeric LHCII complexes from the Lut-deficient mutants [33], all these transition maps are essentially symmetrical with respect to the diagonal, meaning that the forward and backward transitions between some particular intensity levels are approximately equally probable. In other word, the free energies of different conformational states corresponding to these intensity levels are very similar. At the high detergent concentration and high pH conditions, both samples showed the mentioned three dominating transitions T1, T2 and T3. The only difference between the samples was the probability of these transitions: T3 transition was more probable in the Vio-enriched sample. Upon the lowering of detergent concentration and pH level, in the Vio-enriched LHCII complexes the probability of T3 transition became similar to T1, while probability of T2 notably increased. Again, the Zea-enriched trimers exhibited almost the same transition density pattern. This property supports that both samples at low pH possess the same quenching ability.

4. Discussion

In this work, we have compared the spectral signatures of LHCII complexes gently isolated from the dark-adapted or light-treated thylakoids, in order to retain the maximum amount of xanthophyll cycle carotenoids (Table 1). Our results show that a selective enrichment of LHCII with violaxanthin or zeaxanthin does not affect the ability of LHCII to switch to a dissipative conformation or the maximum quenching inducible. In these samples, environmental changes that mimic qE conditions (pH decrease and detergent removal) results in the identical ~70% drop in the fluorescence intensity, which suggests that presence of Zea is not essential for the excitation quenching (Fig. 2B). However, the kinetics of the fluorescence decrease due to NPQ induction are different, prompting towards a modulatory effect of zeaxanthin in the dynamics of quenching.

The physical origin of the observed 70%-drop of the fluorescence intensity upon the pH decrease and detergent removal is two-fold: first, variation of the environment conditions naturally affects the conformational dynamics of the pigment–protein, making its quenching state thermodynamically more favorable. Meanwhile, further drop of fluorescence intensity results from the formation of aggregates, which stabilizes the quenched conformation and allows excitation energy transfer through the aggregate towards the LHCII complexes being in the quenched state. In order to distinguish between these two different processes—conformational dynamics and aggregation effects—we have implemented SM microscopy technique and studied single immobilized LHCII complexes. We observed that the mere removal of detergent influence conformational dynamics of the LHCIIs in a much less pronounced way than when accompanied with acidification of the environment (cf. Fig. 3 and SI Fig. 6). In SM experiments LHCIIs are surface-immobilized at low densities and therefore, in contrast to the typical bulk measurements, their aggregation upon removing the detergent is prevented. Another effect that the detergent concentration reduction alone might induce is the conformational change of LHCII. Thus in SM experiments low detergent concentration and high pH control is more beneficial than a high detergent concentration low pH control because it allows decoupling the conformational change effect from aggregation. Moreover, in the SM microscopy measurements we observed ~30%-drop in the mean fluorescence intensity after mimicking NPQ conditions. That means that the remaining 40%-drop detected during the bulk measurements originates from the LHCII aggregation. Therefore, slight increase in the quenching induction rate in the Zea-enriched samples, observed during the bulk fluorescence measurements (Fig. 2B) suggests that Zea, locating the peripheral binding site of the LHCII protein, might play mediating role enhancing the aggregation process. It is worthwhile to mention that these findings agree well with the results of the previously published SM level studies of Vio- and Zea-enriched LHCII, which showed that at the SM level both types of the enriched samples can achieve maximum average fluorescence decrease of ~35% [49].

In addition to these findings, by comparing the steady-state fluorescence spectra and the excitation decay kinetics of Vio- and Zea-enriched LHCII complexes, we can conclude that the presence or absence of the red shoulder in the steady state fluorescence spectrum (see SI Fig. 3C) is not directly related to the quenching state of the LHCII complexes: despite slight spectral differences, both samples exhibited virtually the same excitation decay kinetics (SI Fig. 3D). This is in line with our recent studies, showing that red-shifted emission, originating from chlorophyll-chlorophyll charge transfer states, exhibits a strong temperature dependence and is not linked to the quenching mechanism [11,35].

We have also provided evidence of rather subtle differences of the main Chl fluorescence peak (the presence of two sub-peaks of the top of the main peak, and red-shifting of the whole spectrum) between Zea- and Vio-LHCII. This internal structure of the fluorescence spectra cannot be separated by taking different vertical or horizontal sections of the streak camera images, indicating that these features are convolved. Indeed, complex state-transition patterns revealed by the SM data might be related to this complex internal structure of the fluorescence spectra. In a previous work, excitation fluorescence spectra of thylakoids enriched in zeaxanthin showed that there is a weak coupling between Zea and Chls [50]. It has been recently proposed that structural changes associated with qE bring about a stronger coupling between Chl and Zea, which allow for dissipative processes to occur with the direct participation of Zea [51]. Our findings on the presence of a red-shifted fluorescence emission peak suggest that there is a weak effect of Zea on the terminal emitter site. However, this effect does not change the dynamics of quenched and unquenched states of LHCII, as shown by the single molecule spectroscopy data, suggesting that whether Zea is weakly coupled to chlorophylls or simply its binding provokes slight changes in the arrangement of other pigments, it is probably not involved in the quenching process. The structure of LHCII binding zeaxanthin is currently unavailable, and this result in difficulties in determining its coupling strength to other pigments [16,52].

Finally, we detected that while variations of the buffer condition affect the protein's conformational dynamics, neither the state-duration nor transition density plots showed major differences between the quenching abilities of both Vio- and Zea-enriched LHCII samples, again suggesting that Zea does not directly participates in excitation quenching. Moreover, from Fig. 2C we can see that under typical low-light conditions (i.e. high pH level) the presence of Zea results in stronger fluorescence compared to the Vio-samples, that might even reduce the unnecessary loss of excitation energy.

Together with PsbS protein, zeaxanthin is a crucial modulator of the NPQ process [53]. Our single-molecule study considers the two extremes of unquenched and quenched conformation and shows that there are no differences in the presence of violaxanthin or zeaxanthin. The quenching level observed during the ensemble measurements is in good agreement with these findings, showing that the extent of quenching inducible in isolated LHCII upon acidification and detergent removal is the same. The differences are found in the quenching induction *kinetics*, which show a faster decay of the fluorescence yield of Zea-enriched LHCII and strongly support the role of zeaxanthin as an allosteric modulator of the quenching process. The most likely mechanistic explanation considers a structural effect of zeaxanthin that promotes faster LHCII clustering in virtue of its markedly hydrophobic nature and position at the interface between LHCII trimers [3,25,54]. Aggregation of LHCII in the thylakoid membrane arises as a consequence of a conformational switch of the LHCII and in turn stabilizes the dissipative state [55]. Endogenous levels of either violaxanthin or zeaxanthin were found to inhibit or promote LHCII aggregation, respectively [18]. The marked hydrophobic nature of zeaxanthin could also bring to a change of the pKa of some amino acids important for the conformational switch, making LHCII more sensitive to protonation [25,56].

Whether PsbS and Zea play a synergetic role in the modulation of quenching, is still unclear [57,58]. However, even if both promote the LHCII aggregation in thylakoids during high light [55,59], their role in the relaxation of NPQ is seemingly different [60]. While PsbS is acting as a fast switch that allows for quick kinetics of formation and relaxation of the quencher, the de-epoxidation of violaxanthin has a rather opposite effect, being activated relatively slowly and persisting in the dark, delaying the recovery of chlorophyll fluorescence [53]. The relevance of this difference is to be found in the adaptation of plants to sun-flecks and fast changes in sunlight intensities, when PsbS-mediated prompt response of the regulation of the photosynthetic machinery is essential together with the establishment of a zeaxanthin-induced "memory of illumination history" [25], whereby the photosynthetic membrane is more prone to the dissipation of excess, potentially harmful excitation energy.

Transparency document

The Transparency document associated this article can be found, in online version.

Acknowledgment

This work was supported by the European Union's Horizon 2020 research and innovation programme under the Marie Skłodowska-Curie grant agreement (No. 675006) and Gilibert project funded by Lithuanian Research Council (No. S-LZ-19-3).

Appendix A. Supplementary data

Supplementary data to this article can be found online at https://doi.org/10.1016/j.dummy.2019.01.002.

References

[1] B. Demmig-Adams, G. Garab, W. Adams, Govindjee. Non-Photochemical Quenching and Energy Dissipation in Plants, Algae and Cyanobacteria. 40, Springer,

Netherlands, 2014.

[2] P. Horton, A.V. Ruban, R.G. Walters, Regulation of light harvesting in green plants, Annu. Rev. Plant Physiol. Plant Mol. Biol. 47 (1996) 655–684.

[3] A.V. Ruban, M.P. Johnson, C.D.P. Duffy, The photoprotective molecular switch in the photosystem II antenna, Biochim. Biophys. Acta Bioenerg. 1817 (2012) 167–181.

[4] X.-P. Li, et al., A pigment-binding protein essential for regulation of photosynthetic light harvesting, Nature 403 (2000) 391–395.

[5] C. Funk, et al., The PSII-S protein of higher plants: a new type of pigment-binding protein, Biochemistry 34 (1995) 11133–11141.

[6] B. Demmig-Adams, Carotenoids and photoprotection in plants: a role for the xanthophyll zeaxanthin, BBA-Bioenergetics 1020 (1990) 1–24.

[7] N.E. Holt, et al., Carotenoid cation formation and the regulation of photosynthetic light harvesting. *Science (80-.)*, vol. 307, (2005), pp. 433–436.

[8] A.V. Ruban, et al., Identification of a mechanism of photoprotective energy dissipation in higher plants, Nature 450 (2007) 575–578.

[9] S. Bode, et al., On the regulation of photosynthesis by excitonic interactions between carotenoids and chlorophylls, Proc. Natl. Acad. Sci. 106 (2009) 12311–12316.

[10] T.K. Ahn, et al., Architecture of a charge-transfer state regulating light harvesting in a plant antenna protein. Science (80-.), vol. 320, (2008), pp. 794–797.

[11] J. Chmeliov, et al., The nature of self-regulation in photosynthetic light-harvesting antenna, Nat. Plants 2 (2016) 16045.

[12] L. Dall'Osto, et al., Two mechanisms for dissipation of excess light in monomeric and trimeric light-harvesting complexes, Nat. Plants 3 (2017) 17033.

[13] A.J. Townsend, et al., The causes of altered chlorophyll fluorescence quenching induction in the Arabidopsis mutant lacking all minor antenna complexes, Biochim. Biophys. Acta Bioenerg. 1859 (2018) 666–675.

[14] Z. Liu, et al., Crystal structure of spinach major light-harvesting complex at 2.72 Å resolution, Nature 428 (2004) 287–292.

[15] N.I. Bishop, The β,ϵ-carotenoid, lutein, is specifically required for the formation of the oligomeric forms of the light harvesting complex in the green alga, scenedesmus obliquus, J. Photochem. Photobiol. B Biol. 36 (1996) 279–283.

[16] J. Chmeliov, et al., An ‘all pigment’ model of excitation quenching in LHCII, Phys. Chem. Chem. Phys. 17 (2015) 15857–15867.

[17] K.F. Fox, et al., The carotenoid pathway: what is important for excitation quenching in plant antenna complexes? Phys. Chem. Chem. Phys. 19 (2017) 22957–22968.

[18] A. Ruban, P. Horton, The xanthophyll cycle modulates the kinetics of non-photochemical energy dissipation in isolated light-harvesting complexes, intact chloroplasts, and leaves of spinach, Plant Physiol. 119 (1999) 531–542.

[19] D.I. Sapozhnikov, T.A. Krasovskaya, A.N. Maevskaya, Change in the interrelationship of the basic carotenoids of the plastids of green leaves under the action of light, Dokl Akad Nauk USSR 113 (1957).

[20] H.Y. Yamamoto, T.O.M. Nakayama, C.O. Chichester, Studies on the light and dark interconversions of leaf xanthophylls, Arch. Biochem. Biophys. 97 (1962) 168–173.

[21] H.A. Frank, et al., Photophysics of the carotenoids associated with the xanthophyll cycle in photosynthesis, Photosynth. Res. 41 (1994) 389–395.

[22] T. Polivka, J.L. Herek, D. Zigmantas, H.-E. Akerlund, V. Sundstrom, Direct observation of the (forbidden) S1 state in carotenoids, Proc. Natl. Acad. Sci. 96 (2002) 4914–4917.

[23] S. Park, et al., Chlorophyll-carotenoid excitation energy transfer in high-light-exposed thylakoid membranes investigated by snapshot transient absorption spectroscopy, J. Am. Chem. Soc. 140 (2018) 11965–11973.

[24] P. Horton, A.V. Ruban, M. Wentworth, Allosteric regulation of the light-harvesting system of photosystem II, Philos. Trans. R. Soc. Lond. Ser. B Biol. Sci. 355 (2000) 1361–1370.

[25] A.V. Ruban, M.P. Johnson, Xanthophylls as modulators of membrane protein function, Arch. Biochem. Biophys. 504 (2010) 78–85.

[26] A.V. Ruban, A. Young, P. Horton, Modulation of Chlorophyll Fluorescence Quenching in Isolated Light Harvesting Complex of Photosystem II, *BBA - Bioenerg.* **1186** (1994), pp. 123–127.

[27] A.V. Ruban, D. Phillip, A.J. Young, P. Horton, Carotenoid-dependent oligomerization of the major chlorophyll a/b light harvesting complex of photosystem II of plants, Biochemistry 36 (1997) 7855–7859.

[28] T.P.J. Krüger, C. Ilioaia, M.P. Johnson, A.V. Ruban, R. Van Grondelle, Disentangling the low-energy states of the major light-harvesting complex of plants and their role in photoprotection, Biochim. Biophys. Acta Bioenerg. 1837 (2014) 1027–1038.

[29] P. Xu, L. Tian, M. Kloz, R. Croce, Molecular insights into zeaxanthin-dependent quenching in higher plants, Sci. Rep. 5 (2015).

[30] A.V. Ruban, P.J. Lee, M. Wentworth, A.J. Young, P. Horton, Determination of the stoichiometry and strength of binding of xanthophylls to the photosystem II light harvesting complexes, J. Biol. Chem. 274 (1999) 10458–10465.

[31] D. Rees, et al., pH dependent chlorophyll fluorescence quenching in spinach thylakoids from light treated or dark adapted leaves, Photosynth. Res. 31 (1992) 11–19.

[32] K. Petrou, E. Belgio, A.V. Ruban, PH sensitivity of chlorophyll fluorescence quenching is determined by the detergent/protein ratio and the state of LHCII aggregation, Biochim. Biophys. Acta Bioenerg. 1837 (2014) 1533–1539.

[33] M. Tutkus, J. Chmeliov, D. Rutkauskas, A.V. Ruban, L. Valkunas, Influence of the carotenoid composition on the conformational dynamics of photosynthetic light-harvesting complexes, J. Phys. Chem. Lett. 8 (2017) 5898–5906.

[34] S. Caffarri, R. Croce, J. Breton, R. Bassi, The major antenna complex of photosystem II has a xanthophyll binding site not involved in light harvesting, J. Biol. Chem. 276 (2001) 35924–35933.

[35] A. Gelzinis, J. Chmeliov, A.V. Ruban, L. Valkunas, Can red-emitting state be responsible for fluorescence quenching in LHCII aggregates? Photosynth. Res. 135 (2018) 275–284.

[36] J. Chmeliov, G. Trinkunas, H. van Amerongen, L. Valkunas, Excitation migration in fluctuating light-harvesting antenna systems, Photosynth. Res. 127 (2016) 49–60.

[37] L. Valkunas, J. Chmeliov, T.P.J. Krüger, C. Ilioaia, R. Van Grondelle, How photosynthetic proteins switch, J. Phys. Chem. Lett. 3 (2012) 2779–2784.

[38] T.P.J. Krüger, C. Ilioaia, R. van Grondelle, Fluorescence intermittency from the main plant light-harvesting complex: resolving shifts between intensity levels, J. Phys. Chem. B 115 (2011) 5071–5082.

[39] D. Phillip, A.V. Ruban, P. Horton, A. Asato, A.J. Young, Quenching of chlorophyll fluorescence in the major light-harvesting complex of photosystem II: a systematic study of the effect of carotenoid structure, Proc. Natl. Acad. Sci. 93 (1996) 1492–1497.

[40] A.V. Ruban, D. Phillip, A.J. Young, P. Horton, Excited-state energy level does not determine the differential effect of violaxanthin and zeaxanthin on chlorophyll fluorescence quenching in the isolated light-harvesting complex of photosystem II, Photochem. Photobiol. 68 (1998) 829–834.

[41] M. Wentworth, A.V. Ruban, P. Horton, Chlorophyll fluorescence quenching in isolated light harvesting complexes induced by zeaxanthin, FEBS Lett. 471 (2000) 71–74.

[42] M.P. Johnson, P.A. Davison, A.V. Ruban, P. Horton, The xanthophyll cycle pool size controls the kinetics of non-photochemical quenching in Arabidopsis thaliana, FEBS Lett. 582 (2008) 262–266.

[43] M. Wentworth, A.V. Ruban, P. Horton, Kinetic analysis of nonphotochemical quenching of chlorophyll fluorescence. 2. Isolated light-harvesting complexes, Biochemistry 40 (2001) 9902–9908.

[44] A.V. Ruban, A.J. Young, P. Horton, Dynamic properties of the minor chlorophyll a/b binding proteins of photosystem II, an in vitro model for photoprotective energy dissipation in the photosynthetic membrane of green plants, Biochemistry 35 (1996) 674–678.

[45] A.V. Ruban, D. Rees, A.A. Pascal, P. Horton, Mechanism of ΔpH-dependent dissipation of absorbed excitation energy by photosynthetic membranes. II. The relationship between LHCII aggregation in vitro and qE in isolated thylakoids, BBA-Bioenergetics 1102 (1992) 39–44.

[46] A.V. Ruban, J.P. Dekker, P. Horton, R.V.A.N. Grondelle, Temperature dependence of chlorophyll fluorescence from the light harvesting complex II of higher plants, Photochem. Photobiol. 61 (1995) 216–221.

[47] N.M. Magdaong, M.M. Enriquez, A.M. LaFountain, L. Rafka, H.A. Frank, Effect of protein aggregation on the spectroscopic properties and excited state kinetics of the LHCII pigment–protein complex from green plants, Photosynth. Res. 118 (2013) 259–276.

[48] G.S. Schlau-Cohen, et al., Single-molecule identification of quenched and unquenched states of LHCII, J. Phys. Chem. Lett. 6 (2015) 860–867.

[49] T.P.J. Krüger, et al., The specificity of controlled protein disorder in the photoprotection of plants, Biophys. J. 105 (2013) 1018–1026.

[50] C. Ilioaia, C.D.P. Duffy, M.P. Johnson, A.V. Ruban, Changes in the energy transfer pathways within photosystem II antenna induced by xanthophyll cycle activity, J. Phys. Chem. B 117 (2013) 5841–5847.

[51] S. Park, et al., Snapshot transient absorption spectroscopy of carotenoid radical cations in high-light-acclimating thylakoid membranes, J. Phys. Chem. Lett. 8 (2017) 5548–5554.

[52] C.D.P. Duffy, et al., Modeling of fluorescence quenching by lutein in the plant light-harvesting complex LHCII, J. Phys. Chem. B 117 (2013) 10974–10986.

[53] A.V. Ruban, Nonphotochemical chlorophyll fluorescence quenching: mechanism and effectiveness in protecting plants from photodamage, Plant Physiol. 170 (2016) 1903–1916.

[54] P. Horton, A.V. Ruban, A.J. Young, Regulation of the structure and function of the light harvesting complexes of photosystem II by the xanthophyll cycle, The Photochemistry of Carotenoids, Kluwer Academic Publishers, 2006, pp. 271–291.

[55] M.P. Johnson, et al., Photoprotective energy dissipation involves the reorganization of photosystem II light-harvesting complexes in the grana membranes of spinach chloroplasts, Plant Cell 23 (2011) 1468–1479.

[56] E.L. Mehler, M. Fuxreiter, I. Simon, E. Garcia-Moreno, B. The role of hydrophobic microenvironments in modulating pKa shifts in proteins, Proteins Struct. Funct. Genet. 48 (2002) 283–292.

[57] M. Aspinall-O'Dea, et al., In vitro reconstitution of the activated zeaxanthin state associated with energy dissipation in plants, Proc. Natl. Acad. Sci. 99 (2002) 16331–16335.

[58] V. Daskalakis, Protein–protein interactions within photosystem II under photoprotection: the synergy between CP29 minor antenna, subunit S (PsbS) and zeaxanthin at all-atom resolution, Phys. Chem. Chem. Phys. 20 (2018) 11843–11855.

[59] M.A. Ware, V. Giovagnetti, E. Belgio, A.V. Ruban, PsbS protein modulates non-photochemical chlorophyll fluorescence quenching in membranes depleted of photosystems, J. Photochem. Photobiol. B Biol. 152 (2015) 301–307.

[60] E.J. Sylak-Glassman, et al., Distinct roles of the photosystem II protein PsbS and zeaxanthin in the regulation of light harvesting in plants revealed by fluorescence lifetime snapshots, Proc. Natl. Acad. Sci. 111 (2014) 17498–17503.

FOR NOTES

Vilniaus universiteto leidykla
Universiteto g. 1, LT-01513 Vilnius
El. p. info@leidykla.vu.lt,
www.leidykla.vu.lt
Tiražas 25 egz.